The biophysics of ion-channel forming peptides

Schmitt, Jeffrey Daniel

Award date:
1998

Awarding institution:
University of Bath

THE BIOPHYSICS OF ION-CHANNEL FORMING PEPTIDES

Submitted by **Jeffrey Daniel Schmitt**
for the degree of Ph.D.
at the University of Bath
1998

Jeffrey Daniel Schmitt

ProQuest LLC
789 East Eisenhower Parkway
P.O. Box 1346
Ann Arbor, MI 48106-1346

ACKNOWLEDGMENTS

First, I wish to express the highest gratitude to my spouse Pam Wagner for her unconditional and inexhaustible friendship, humor and support during our time in England.

In addition to his fiscal and intellectual assistance, I am grateful to Dr. Robert Eisenthal for his friendship and willingness to give me the freedom to explore the variety of ideas expressed in this Thesis.

I am greatly indebted to Dr. Mark Sansom for the opportunity to work in his laboratory. Mark's talent, enthusiasm and faith in Science has been a great inspiration. I also wish to extend my thanks to Dr. Ian Kerr and other members of Mark's lab for their stimulating dialogue and hospitality.

I thank Professor George Lunt for his assistance in obtaining my ORS Fellowship and for his useful discussions.

Many thanks to Dr. Chris Dempsy for the collaboration on the melittin analogs and for a number of interesting and useful discussions.

Heartfelt appreciation to Dr. Robert Wykle and Dr. Bill Caldwell for their stimulating (extracurricular) collaboration and long-standing friendship.

My Bath lab-mates Drs. Ed Seravolac and Robin Maytum deserve sincere thanks for helping to get me oriented when I first arrived.

Finally, I thank Drs. Sue Wonnacott, Alan Rayner and the Bio*Art Group for their stimulating conversations and friendship.

DEDICATION

For all the years of unconditional support,

Love and keen guidance -

For all the years of patience

beyond measure -

And for helping to make my

journey a joyous one -

This is for you Mom.

ABSTRACT

This study explores the physical determinants of ion channel formation using novel analogues of alamethicin and melittin. Analogs of these channel forming peptides were synthesized using a variety of solid and liquid phase techniques. Biophysical characterization was conducted using the Planar Lipid Bilayer (PLB) technique at both the macroscopic and single-channel levels.

The first reported synthesis and characterization of redox-active ion channel peptides comprises the first part of this Thesis. Three C-terminus ferrocenoyl derivatives of alamethicin were synthesized by liquid-phase methodologies. Two of these peptides form voltage-sensitive ion channels with marked sensitivity to the ferrocene's redox state. Correlations between channel behavior and physico-chemical properties are also explored.

Next, the solid-phase synthesis of carboxy-alamethicin its N-terminus ferrocenoyl derivative is described. The ferrocenoyl peptide forms ion channels with strikingly different ion selectivity depending on its oxidation state. Preliminary electrostatics calculations of modeled peptide bundles predict this change in selectivity-- Lending substantiating evidence for the helix-bundle model of ion channel formation.

Once we established the validity of structure-function studies that focus on altering the electrostatics, we sought to extend this investigation to a different molecular system. Melittin was chosen because its position among the family of channel forming peptides is rather tenous. Under most conditions this peptide fails to form conductance states that are easy to define within the context of current models of ion channel formation. We hypothesized that melittin could be altered to form

alamethicin-like channels by reducing its cationic character. The last experimental part of this Thesis describes a number of melittin analogs that form channels within the helix bundle regime.

Molecular dynamics simulations are conducted on helix bundle models of the alamethicin and melittin derivatives. Correlations between experimentally observed behavior and the simulations results are discussed. Finally a number of theories, based on this investigation and a literature survey, relevant to ion channel formation are also explored.

PUBLICATIONS OF THE WORK

Schmitt, J. D., Sansom, M.S.P., Kerr, I.D., Lunt, G.G. and Eisentlal, R. (1997) Ferrocenoyl Derivatives of Alamethicin: Redox Active Ion Channels. *Biochemistry* **36**:1112-1115

Schmitt, J.D., Adcock, C., Sansom, M.S.P., Lunt, G.G. and Eisenthal, R. (1998) N-Terminus Ferrocenoyl Alamethicin: Evidence for a Channel Forming Peptide with Controllable Ion Selectivity. *Manuscript in preparation.*

Schmitt, J.D., Sansom, M.S.P., Taki, J. and Dempsy, C.E. (1998) Biophysical Characterization of Glutamine and Cysteine Mutants of Melittin. *Manuscript in preparation.*

QUOTATIONS

A POETS ADVICE

A poet is someone who feels, and who expresses his feelings through words. This may sound easy. It isn't.
A lot of people think or believe or know they feel - but that's thinking or believing or knowing; not feeling. And poetry is feeling - not knowing or believing or thinking.
Almost anybody can learn to think or believe or know, but not a single human being can be taught to feel. Why? Because whenever you think or you believe or you know, you're a lot of other people: but the moment you feel you are nobody-but-yourself.
To be nobody-but-yourself - in a world which is doing its best, night and day, to make you everybody else - means to fight the hardest battle which any human being an fight; and never stop fighting.
As for expressing nobody-but-yourself in words, that means working just a little bit harder than anybody who isn't a poet can possibly imagine. Why? Because nothing is quite as easy as using words like somebody else. We, all of us, do exactly this nearly all of the time - and whenever we do it, we are not poets.
If, at the end of your first ten or fifteen years fighting and working and feeling, you find that you have written one line of one poem, you'll be very lucky indeed.
And so my advice to young people who wish to become poets is: do something easy, like learning how to blow-up the world - unless you're not only willing, but glad, to feel and work and fight till you die.
Does this sound dismal?
Its the most wonderful life on earth.
Or so I feel.

- e.e. cummings

CONTENTS

FIGURES

TABLES

ABBREVIATIONS

Å	- Ångstrom, 10^{-10} meter
Ac	- acetyl
AIB	- α-aminoisobutyric acid
Ac_2O	- acetic anhydride
ALM	- alamethicin R_f = 50
AMBER	- molecular mechanics Forcefield
BES	- N,N-bis(2-hydroxyethyl)-2-aminoethanesulphonic acid
BLM	- black lipid membrane
BP	- boiling point
Bz	- benzene
CAN	- cerium (IV) ammonium nitrate
CFP	- channel forming peptide
CHARMm	- molecular mechanics Forcefield
cxFc-ALM	- C-terminus 1'-carboxyferrocenoyl alamethicin
cxALM-Fc	- C-terminus carboxy N-terminus ferroceneacetamidoyl alamethicin
cxALM-Ac	- alamethicin, C-terminus carboxy
DDBQ	- 2,3-dichloro-5,6-dicyanobenzoquinone
DFT	- density functional theory
DIPA	- diisopropylamine
DPhPC	- diphytanoylphosphatidylcholine
DMAP, 4-DMAP	- 4- (N,N-dimethyl)aminopyridine
DMF	- dimethylformamide
DMPC	- dimyristoylphosphatidylcholine
DMSO	- dimethylsulphoxide
DTT	- 1,4-dithiothreitol
ε	- dielectric constant
ESP	- electrostatic potential fit (least squares)

EtOH	- ethyl alcohol
F	- Faraday's constant
F'	- phenolalaninol
FAB	- fast atom bombardment (mass spectrometry)
Fc	- ferrocene
Fc-ALM	- C-terminus ferrocenoyl-alamethicin
$FcCH_2$-ALM	- C-terminus ferrocenacetoyl-alamethicin
Fm	- formyl
Fmoc	- 9-fluorenylmethoxy carbonyl
F_{oct}	- free energy in octane (calculated)
ftc-ALM	- alamethicin fluorecenylthiocarbamate
g	- conductance, 1/resistance
GHK	- the Goldman-Hodgkin-Katz equation
HOAc	- acetic acid
HPLC	- high pressure liquid chromatography
I-V	- current-voltage relationship
IVA	- isovaline
LDMS	- laser desorption mass spectrometry
MD	- molecular dynamics
MeCN	- acetonitrile
MEL	- melittin
MEL-K7Q	- melittin analog, glutamine at position 7
MEL-K23C	- melittin analog, cysteine at position 23
$(MEL\text{-}K23C)_2$	- melittin analog, cysteine at position 23, disulfide dimer
MEL-K23Q,K25C	- melittin analog, glutamine at position 23 and cysteine at position 25
$(MEL\text{-}K23Q,K25C)_2$	- melittin analog, glutamine at position 23 and cysteine at position 25, disulfide dimer
MeOH	- methyl alcohol
MP	- melting point
MS	- mass spectrometry

NMR	- nuclear magnetic resonance spectrometry
nA	- nanoamperes (10^{-9} Amperes), measure of current
PEG-PS	- polyethylene glycol - polystyrene resin for solid-phase synthesis
P_{M+}/P_{X-}	- conductance permeability ration (cation/anion)
pA	- picoamperes (10^{-12} Amperes), measure of current
pm-ALM	- pyromelitoyl alamethicin
pS	- picoSiemens (10^{-12}, Siemens), conductance $\propto \Omega^{-1}$
PLB	- planar lipid bilayer
R_f	- retentivity factor, thin layer chromatography
TASP	- template assembled protein
TEA	- triethylamine
TFA	- trifluoroacetic acid
TFB	- tetrafluoroboric acid
TFFH	- tetramethylfluoroformamidium hexafluorophosphate
TLC	- thin-layer chromatography
U	- α-aminoisobutyric acid
UFF	- universal Forcefield for molecular mechanics calculations
UHBD	- University of Houston Brownian Dynamics software package
UV_{max}	- spectrophotometric ultraviolet absorbence maximun
V_E	- electronically imposed transbilayer potential
V_{rev}	- macroscopic reversal potential
V_t	- potential required to elicit a 100 pA current during the positive (dV/dt > 0)sweep in macroscopic current- voltage measurements
V_{t+}	- potential required to elicit a 100 pA current during the positive (dV/dt > 0) sweep in macroscopic current- voltage measurements
V_{t-}	- potential required to elicit a 100 pA current during

the negative (dV/dt < 0) sweep in macroscopic current- voltage measurement

V_{25+} - potential required to elicit a 25 pA current during the positive (dV/dt > 0) sweep in macroscopic current-voltage measurements

V_{25-} - potential required to elicit a 25 pA current during the negative (dV/dt < 0) sweep in macroscopic current-voltage measurements

THE BIOPHYSICS OF ION-CHANNEL FORMING PEPTIDES

INTRODUCTION

1.1. BACKGROUND AND SIGNIFICANCE

The controlled flow of materials and information across barriers is of paramount importance in the organization of living systems. On the cellular level these processes are largely mediated through membrane bound protein assemblies, many of which form channels that selectively arbitrate the passage of particles ranging in size from protons to small polymers (Hille, 1992). The mechanisms controlling and inducing the flow of materials through such channels are ultimately associated with many biological functions. Ligand-gated or voltage-gated ion channels, found most frequently in neuronal tissue are the biochemical equivalent of transistors. They support the neuronal Hebbian network through the regulation of ionic current.

Given the significance of channel forming assemblies, a wide range of tactics has been devised to probe their structure and function (Latorre & Alvarez, 1981; Guy & Conti, 1990; Woolley & Wallace, 1992; Sansom, 1993a; Sansom, 1993b). Unfortunately, structural elucidation of most of these proteins has remained ellusive. Notable exceptions are the recent crystallographic solution to the structure of cytochrome C oxidase reconstituted in oriented multilamellar bilayer arrays (Scott, 1995), and the topological mapping of the nicotinic acetylcholine receptor using cryoelectron microscopy (Toyoshima & Unwin, 1988; Unwin, 1993). In addition, a number of β-barrel channel proteins have recently been solved by X-ray crystallography, these include: staphylococcal α-toxin, anthrax protective antigen pro-toxin and the CytB pro-toxin (for a review see: Lesieur *et al.*, 1997).

Another line of investigation, and indeed the one adopted in this Thesis, is the study of small helical peptides that appear to self-assemble in lipid bilayers forming channels through which ions, and in some cases small molecules, can pass. It has been conjectured that these channel forming peptides (CFPs) posses many of the same functional and structural characteristics as the larger and more complex channels and transporters (Latorre & Alvarez, 1981; Sansom, 1991; Sansom, 1993a; Sansom, 1993b). Indeed, some years ago Hall suggested that alamethicin could serve as a model for more complex voltage-gated channels (Hall, 1984). Recently, this hypothesis has been supported by studies conducted on the putative pore lining fragments of the nicotinic acetylcholine receptor (nAChR; Montal *et al.*, 1990), sodium (Oiki et al., 1988) and calcium channels (Ananthanarayanan & Zhorov, 1997). The nAChR is a pentameric ion channel whose cation permeability is governed by acetylcholine or other neuromodulators (for a review see: Karlin, 1993; Galzi *et al.*, 1991). Evidence suggests that the nAChR channel is lined with one transmembrane helix from each of its five constituent monomers (Stroud *et al.*, 1990; Unwin, 1989). It has been demonstrated that these helical fragments, in isolation, self-assemble in lipid bilayers to form voltage-sensitive ion channels with conductance and ion selectivity similar to the native receptor (Montal, 1989). A wide variety of biophysical and spectroscopic investigations indicate that, like CFPs, the pore lining regions of larger channel forming assemblies are composed of amphiapathic helices (Sansom, 1993a) -- giving us perhaps the single most significant justification for correlating the behavior of these simple peptides to more complex systems.

1.2. DIVERSITY OF CHANNEL FORMING PEPTIDES

Since the original observation by Mueller and Rudin (1968) that alamethicin, induces conductance (excitability) in lipid membranes, a great number of similar peptides have been isolated and characterized.

It is now known that alamethicin, an icosapeptide from *Trichoderma viride*, is representative of a class of fungal peptide antibiotics known as peptaibols (Sansom, 1992). Peptaibols are rich in the exceedingly helicogenic amino acid α-aminoisobutyric acid and are most often between 16 and 20 residues in length. The smallest are the zervamicins (Karle *et al.*, 1987), antiameobins and emericins (Kumazawa *et al.*, 1994), the harzianines (Rebuffat *et al.*, 1993) and a host of other peptides isolated from *Trichoderma* such as the trichorzins, trichodecenins, trichovins and tricocellins (Iida, 1995; Fugita *et al.*, 1994) which are 11-16 residues in length. The fungus Hypocrea has recently been shown to contain two new classes of peptaibols, the hypomurocins, which contain either 11 or 18 amino acids and are rich in isovaline (Becker *et al.*, 1997). Longer peptaibols include the saturnisporins (Rebuffat *et al.*, 1993), trichorzianines (Le Bars *et al.*, 1988), suzukacillins (Jung *et al.*, 1976), chrysospermins (Grigoriev *et al.*, 1995), polysporins (New, 1996), paracelsin-A (Brukner & Graf, 1983) and aibellin (Kumazawa *et al.*, 1994). Recently a family of N-terminal acylated peptaibols have been isolated from *Tolypocladium geodes* which also contain the novel amino acid α-ethylnorvaline (Tsantrizos *et al.*, 1996). The majority of peptaibols contain amino alcohol (phenylalinol, valinol, leucinol or isolucinol) residues at their C-terminus as well as one or more central proline or hydroxyproline residues.

A number of higher organisms produce antibiotic or defense related peptides These include melittin from the bee *Apis millefera* (Toteson & Toteson, 1981), mammalian seminalplasmin (Sitaram & Nagaraj, 1993) and magainins from *xenopus* frog (Ludtke *et al.*, 1995). Table 1.1 shows sequences of a number of characterized CFPs aligned to the central proline. Many organisms posses CFPs that are intermediate in size between the peptaibols and gated ion-channels--one might conjecture that these form an evolutionary link between the two. Diverse examples include the cardiac phospholambans (Adams,

1995), spiralins (Brenner *et al.*, 1995), cecropin from silkworm (McHourab *et al.*, 1994), dermaseptins (Strahilevitz *et al.*, 1994), the peptide shark repellent pardaxin (Shai *et al.*, 1993), human perforin (Liu *et al.*, 1995) and the bacterial protein toxins such as delta-toxin from *Staphylococcus aureus* (Mellor *et al.*, 1988).

Peptide	N	Sequence
alamethicin-Rf30	20	Ac-U-P-U-A-U-A-Q-U-V-U-G-L-U-P-V-U-U-E-Q-F-OH
alamethicin-Rf50	20	Ac-U-P-U-A-U-A-Q-U-V-U-G-L-U-P-V-U-U-Q-Q-F-OH
hypelcin-AI	20	Ac-U-P-U-A-U-U-Q-U-L-U-G-U-U-P-V-U-U-Q-Q-L-OH
suzukacillin	20	Ac-U-A-U-A-U-A-Q-U-U-U-G-L-U-P-V-U-U-Q-Q-F-OH
paracelsin-A	20	Ac-U-A-U-A-U-A-Q-U-V-U-G-U-U-P-V-U-U-Q-Q-F-OH
saturnisporin-SAII	20	Ac-U-A-U-A-U-A-Q-U-L-U-G-U-U-P-V-U-J-Q-Q-F-OH
trichorzianine-AIIIC	19	Ac-U-A-A-U-U-Q-U-U-U-S-L-U-P-V-U-I-Q-Q-W-OH
trichorzianine-BIIIC	19	Ac-U-A-A-U-U-Q-U-U-U-S-L-U-P-V-U-I-Q-E-W-OH
tricholongin-BI	19	Ac-U-G-F-U-U-Q-U-U-U-S-L-U-P-V-U-U-Q-Q-L-OH
trichotoxin-A40	18	Ac-U-G-U-L-U-Q-U-U-U-A-U-U-P-L-U-J-E-V-OH
zervamicin-IC	16	Ac-W-I-E-J-I-T-U-L-U-O-Q-U-O-U-P-F-OH
zervamicin-AI-16	16	boc-W-I-A-U-I-V-U-L-U-P-A-U-P-U-P-F-Ome
antiamoebin-I	16	Ac-F-U-U-U-J-G-L-U-U-O-Q-J-O-U-P-F-OH
harzianine-HCIII	14	Ac-U-N-L-U-P-S-V-U-P-J-L-U-P-L-OH
melittin	26	f-G-I-G-A-V-L-K-V-L-T-T-G-L-P-A-I-L-S-W-I-K-R-K-R-Q-Q-NH2

key: U, α-aminoisobutyric acid; boc, t-butoxycarbonyl; J, D-isovaline; O, hydroxyproline; me, methylester
taken, in part from: Sansom, 1993b

TABLE 1.1 CFP SEQUENCES.

Recently, the predominate proteolytic fragment of the "BSE" prion protein was shown to form ion channels with discrete conductance levels in lipid membranes (Lin *et al.*, 1997). This finding may explain much of the neurocytotoxic effects that accompany Creutzfeldt-Jacobs Disease (Budka *et al.*, 1995). The HIV-1 virus protein Vpu has also recently been shown to form voltage dependent ion channels and may be responsible for some of the dementia related symptomologies seen at latter stages of the disease (Shubert *et al.*, 1995). It is increasingly apparent that CFPs and ion-channels -- from prions to plants -- play a significant role in the homeostasis and competition of living systems.

1.3. STRUCTURAL STUDIES: CRYSTALLINE, AQUEOUS & LIPID ENVIRONMENTS

This discussion will focus primarily on alamethicin and related peptides, for these are the most intensely studied CFPs. The salient feature of these peptides is their high α-aminoisobutyric acid content. This amino acid is conformationally hindered with respect to the α-carbon and thus its (ϕ, ψ)-map is constrained to a narrow range of values ((ϕ, ψ)= ± 57°,47°), ultimately resulting in marked helicogenicity , see Figure 1.1 (Burgess & Leach, 1973; Karle & Balaram, 1990). This is reflected in the crystal structures of alamethicin-R_f=30 (Fox & Richards, 1982), zervamicin A1-16 (Karle *et al.*, 1991), zervamicin-leu (Karle *et al.*, 1991; Karle *et al.*, 1992) and trichorazine-AIIIC (Le Bars *et al.*, 1988).

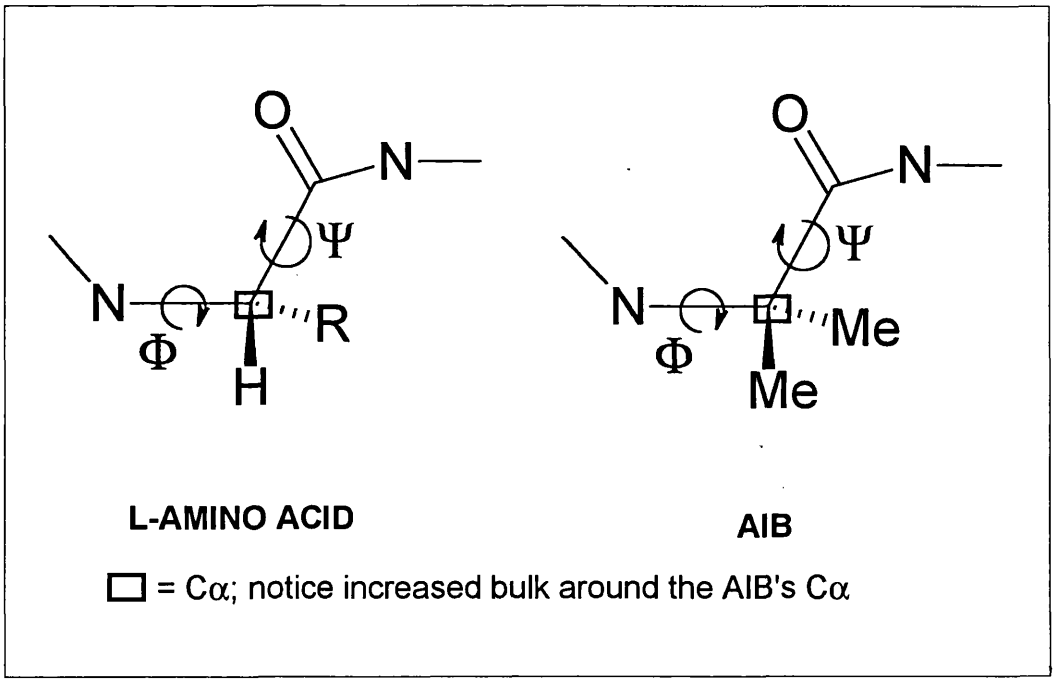

FIGURE 1.1. CONFORMATIONAL HINDRANCE OF AIB.

In addition to the structural resolution of these naturally occurring CFPs, some forty synthetic peptaibols have been studied crystallographically (Karle & Balaram, 1990; Karle, 1992).

The consistent attribute in all of these structures is the predominant α- and 3_{10}-helical content as well as the presence of a central kink in the helical rods. The crystal structure of melittin has been solved and it has a largely helical form, although much of it's helicity may be induced through intermolecular interactions – melittin forms a dimer of dimers in the solid-state and in concentrated solutions (Terwilliger & Eisenberg, 1982; Terwilliger *et al.*, 1982).

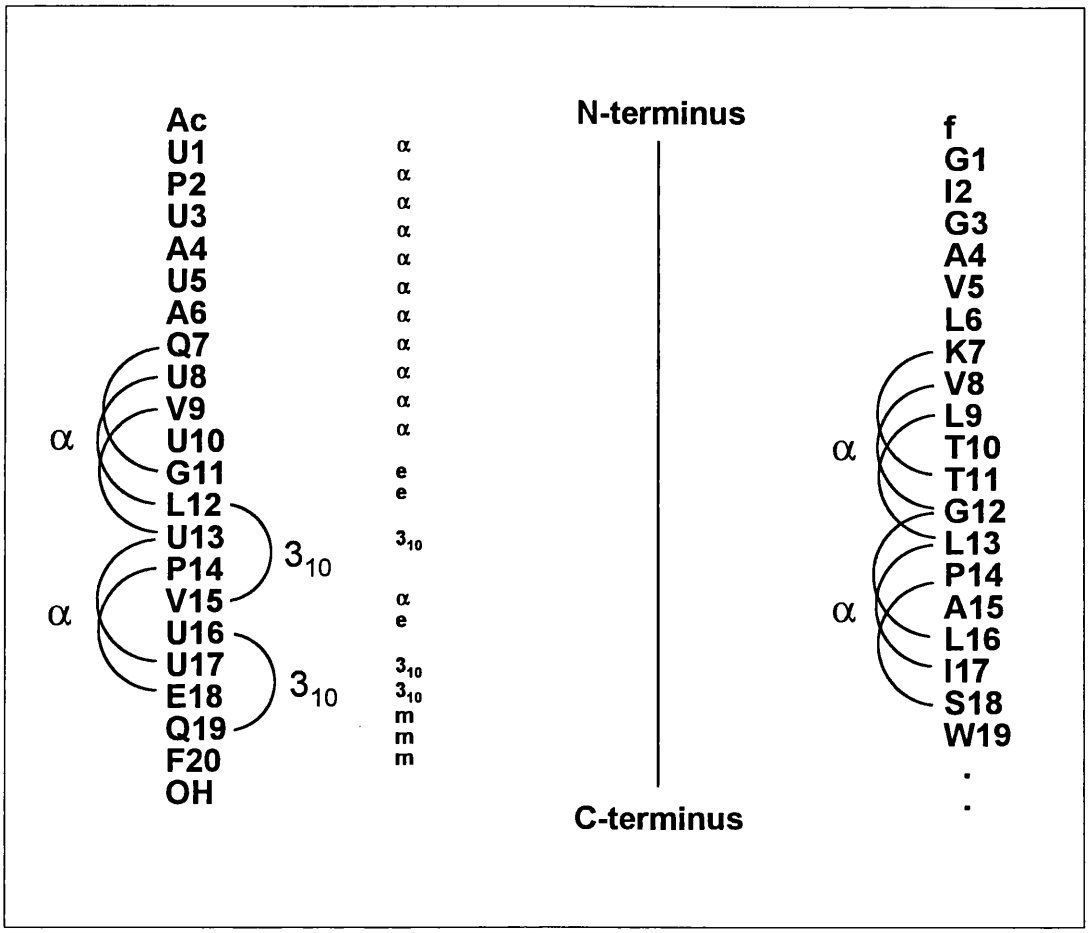

FIGURE 1.2. H-BONDING IN ALAMETHICIN AND MELITTIN. The left panel shows the sequence of alamethicin-R_f =50, the right panel shows the N-terminus of melittin. The semi-circles and adjoining resedues show the H-bonding patterns seen in these peptides: α exhibits 1→5 bonding while 3_{10} exhibits 1→4 bonding. In the left panel the specific crystallographic structure is given for alamethicin: e, extended helix; m, mixed structure.

As a result of AIB, many peptaibols exhibit considerable α-helical content in methanolic or aqueous solutions (Yee & O'Neil, 1992; Kelsh *et*

al., 1992). In general, helicity appears to be a significant factor contributing to the ease with which CFPs form channels. Molle and coworkers synthesized a less helicogenic R_f=30 alamethicin derivative where all α-aminoisobutyric acid residues were replaced by leucine, this peptide, *des*-AIB-alamethicin, was shown to form ion-channels only at peptide concentrations significantly higher than required for alamethicin (Molle *et al.*, 1988). The related CFP melittin, which is free of AIB, has been shown by NMR and other methods to adopt a random conformation in dilute solution, highlighting the structural impact of AIB (Bazzo et al., 1988).

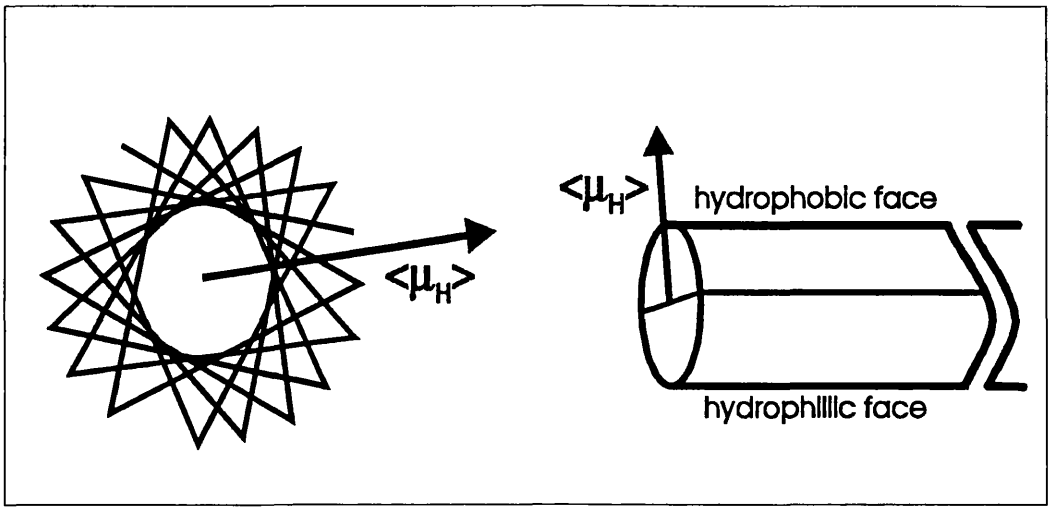

FIGURE 1.3. REPRESENTATION OF THE HYDROPHOBIC MOMENT DESCRIBED BY EISENBERG & MCLACHLAN (1986). The left figure shows the helical wheel looking down the screw-axis of the helix, while the right figure shows a side view of the helix. Individual amino acids are given a scalar value, μ_i, according to their relative hydrophobicities; hydrophilic amino acids are assigned negative μ_i and hydrophobic residues take on positive values. For a given amino acid H_i in a helix H, a vector μ_i is defined as originating at the center of the helical wheel and extending to $C_{\alpha,i}$ the alpha carbon of residue H_i. The mean scalar value of the hydrophobic moment for H is defined as:

$$\langle\mu_H\rangle = 1/N \{[\Sigma_{n,i=1} \mu_i \sin(d_i)]^2 + \{[\Sigma_{n,i=1} \mu_i \cos(d_i)]^2$$

where N is the total number of residues in the helix and d_i is the angle between successive vectors in the wheel.

The specific helical form adopted by CFPs appears to depend on physical environment as well as on peptide length (Sansom, 1993a; Sansom 1993b). ^{1}H-NMR studies on alamethicin in water and methanol

indicate that the N-terminus is α-helical and that the C-terminus is a disordered mixture of α and 3_{10} helical forms, see Figure 1.2 (Banerjee, 1983; Esposito, 1987). More recent studies using ^{1}H, ^{13}C and ^{15}N-NMR substantiate these observations and give additional evidence for a disruption in hydrogen bonding at the central proline (Yee and O'Neil, 1992; Yee *et al.*, 1995).

CFPs posses a considerable hydrophobic moment, $<\mu_h>$ (a quantitative measure of ampipathicity, Figure 1.3) perpendicular to their helical axis (Eisenberg *et al.*, 1982) and thus easily partition into lipid phases (Hall *et al.*, 1982). The nature of lipid association has been the subject of intense interest because it is an obligatory step in channel formation and also because association appears to increase structural order as determined by a host of methods. Organic solvents induce order in a similar manner. Studies of alamethicin in dioxane/octanol mixtures indicate that helicity increases with percent octanol, as measured by circular dichroism spectroscopy (Schwartz *et al.*, 1983). Triflouroethanol appears to induce helicity in most peptides even those which adopt non-helical folds in their native environments. One could imagine conducting NMR studies on alamethicin and its des-AIB analog in solvents containing varying ratios of dioxane/triflouroethanol. Such experiments would serve to differentiate the structural attributes of the peptide which lead to helicogenicity and those contributed by the solvent.

Circular dichroism spectroscopy has provided some of the clearest evidence for the induction of secondary structure by lipid environments. Vogel and coworkers in a combined circular dichroism and resonance-Raman study convincingly demonstrate that the order and helicity of alamethicin increases upon association with lipid vesicles (Vogel, 1987). More recently, circular dichroism studies in DMPC vesicles indicate that alamethicin adopts a helical content near to that of the crystal structure (Casico & Wallace, 1988). IR spectroscopy has also provided evidence

for lipid induced helicity in alamethicin (Harris & Chapman, 1988). In an elegant series of experiments DeGrado and coworkers sequentially mutated each residue of the leucine-serine CFP ($[LSSLLSL]_3$) to tryptophan. The fluorescence of these peptides was then measured in the presence of lipid membranes. They observed a periodic variation in fluorescence quenching as a function of residue number, corresponding to that of a helix lying perpendicular to the bilayer normal (Chung *et al.*, 1992). Dempsy and coworkers determined H-bond stability in alamethicin/lipid mixtures using ^{1}H-NMR derived amide hydrogen exchange rates, their results indicate that alamethicin associates with lipid vesicles in a concentration dependent manner and that amide exchange protection followed helical periodicity, indicating that the hydrophilic face of the peptide is solvent exposed (Dempsey & Handcock, 1996). It must be noted that the structural consequences of lipid association are markedly sensitive to lipid:peptide ratio (Huang & Wu, 1991; Sansom, 1993a; Sansom, 1993b). For many CFPs there is a concentration threshold below which the peptides appear to lie parallel to the plane of the bilayer and above which the peptides reorient in a transbilayer orientation. The phase-state of the bilayer also appears to have marked effect on the orientation of the membrane associated peptaibols.

One of the most pressing and difficult to probe questions is the effect of transbilayer potential on CFP structure. A particularly elegant experiment designed to address this issue was published by Brumfield and Miller (Brumfield & Miller, 1990). These investigators made lipid vesicles and imposed a Donnan potential across their bilayers by the use of polyelectrolytes. When alamethicin was added to the bulk solution circular dichroism measurements indicated an increase in helicity when the outside of the vesicles was made positive relative to the inside and a decrease in helicity when the potential was reversed. These experiments indicate that transbilayer potentials may have significant effects on CPF structure.

The induction persistent ion-channel structure by lipid association *and* the subsequent modulation of function by changes in lipid environment are increasingly important themes. It might be argued that transduction, be it material or information, occurring at boundaries posses the greatest potential for complex and subtle modulation (Kaufmann, 1993; Rayner, 1997). The nAChR is perhaps the penultimate example, considering its ability to transduce its interaction with a vast group of molecular ligands and environmental variants (e.g., changes in lipid environment) into specific physiological outcomes.

1.4. PROLINE: A MOLECULAR HINGE IN CFPs ?

It has been hypothesized that frequently found proline residues act as a molecular 'hinge' on the NMR time-scale and that these hinges contribute to the functional behavior of ion-channels (Sansom, 1993a; Dempsey *et al.*, 1991) as well as globular proteins (Creighton, 1994). However, recent investigations demonstrate that alamethicin derivatives devoid of the central proline form fully functional channels (Brachais *et al.*, 1995) albeit at higher activation potentials. Thus, the precise role of the nearly ubiquitous central proline is still a matter of debate, although they are thought to create a funneling toward the C-terminus of assembled channels, see below (Hall et al., 1982; Sansom 1993b). A recent study was undertaken to illuminate this problem by synthesizing a series of alamethicin analogs possessing proline substitutions at positions 11, 12, 13, 15 and 17 (Kaduk, *et al.*). Unfortunately, the results are somewhat difficult to interpret, although it is clear that any changes in proline position relative to native alamethicin has deleterious effects on ion channel formation. Normal-mode simulations recently published by Dauber-Osguthorpe and coworkers indicate that proline possesses preferential and limited modes of bending compared with acyclic amino acids, giving proline the overall effect of a molecular hinge; this effect has

also been observed on the NMR time-scale (Dauber-Osguthorpe & Osguthorpe, 1993). One might conjecture that such hinge regions allow the transition from a parallel to trans-bilayer orientation to occur with less disruption of favorable peptide-bilayer interactions.

1.5. CONDUCTANCE PROPERTIES OF CHANNEL FORMING PEPTIDES

Electrical conductance measurements constitute the single most important mode of investigating CFPs and ion-channels. Although experimental details of the so-called planar lipid bilayer technique is described in Chapter 2, an background introduction will be given here.

Conductance measurements on CFPs fall into two main categories: macroscopic and single-channel. In both types of experiment a lipid bilayer is exposed to a given CFP, followed by the imposition of an electrical potential across the bilayer. Macroscopic experiments are characterized by the application of a periodically varied transbilayer potential (20-40 mV/sec). Averaging the net current as a function of transbilayer potential yields a current-voltage (I-V) relationship, revealing much about the energetics of ion-channel activation. Most often, only one side of the bilayer is exposed to the CFP so that the asymmetry of channel activation may be assessed. In 1984 Hall established that the mean number of monomers, <N>, constituting the ensemble of conducting channels could be determined from such experiments. The macroscopic conductance G of a bilayer exposed to a given CFP can be described in the following manner:

$$G = \Gamma C^{<N>} \exp(V/V_e) \qquad \{1.1\}$$

$$V_e = kT/e < N > \alpha \qquad \{1.2\}$$

where Γ is a constant, C is the CFP concentration, V_e is the voltage required to induce an e-fold increase in bilayer conductance, k is the Boltzmann constant, T is the temperature and α is the effective gating charge per monomer. Thus, it is possible to calculate $<N>$ and α from a series of I-V curves obtained at different CFP concentrations.

Single-channel measurements, by contrast, focus on characterizing singe *or* small numbers of channels rather than large ensembles. Here, a constant potential is applied across the bilayer whilst data acquisition takes place. Channel openings are frequently seen as discreet and transient jumps in bilayer conductance. Quantitation of conductance level lifetimes and probabilities as well as transition probabilities serve to elucidate underlying kinetic mechanisms. Details of single-channel analysis using various kinetic theories are given elsewhere (Ball & Sansom, 1989; Hille, 1992; Balaram *et al.*, 1992; Mak & Webb, 1993; Opsahl & Webb, 1993).

In an early attempt to obtain a physical picture of single channel conductance Hille (Hille, 1984) proposed that an ion-channel could be considered an electrolyte filled cylinder embedded in a bilayer of infinite resistivity. The pore conductivity, g is the inverse of two resistance terms:

$$g = 1/(R_c + R_a) \qquad \{1.3\}$$

the terms R_c and R_a denote Ohmic resistance of the cylinder and access resistance, respectively. R_c follows a simple volumetric relationship, given L as the length of the cylinder and r as its radius:

$$R_c = \frac{\rho L}{2\pi r^2} \qquad \{1.4\}$$

where ρ is the resistivity of the electrolyte. The access resistance is given by the simple relationship:

$$R_a = \rho / 2r \qquad \{1.5\}$$

thus:

$$g = \pi r^2 / \{\rho(1 + 0.5\pi r)\} \qquad \{1.6\}$$

This treatment works to a first approximation, but more recently Smart and coworkers have developed more elegant conductance prediction methods based on a Monte Carlo simulated annealing algorithm to fit various sized spheres into ion channel models (Smart *et al.*, 1996). This procedure has been used to accurately predict the conductance levels of large number of α-helical and β-barrel CFPs.

1.6. MODELS OF CHANNEL FORMATION BY CFPs

It has long been conjectured that the obligatory step in ion-channel formation is the aggregation of membrane-bound peptides (for a review see: Woolley & Wallace, 1992). Many models have been proposed to rationalize the channel forming behavior of CFPs, some of these were conceived without the wealth of biophysical and spectrometric that exists today. These models include the membrane flip-flop model (Boheim, 1983) and the barrel-stave model (Baumann & Mueller, 1974) among others (for a review see: Woolley & Wallace, 1992; Sansom 1993a; Sansom 1993b). Since that time a great wealth of evidence has accumulated that supports the so-called helix-bundle model of ion-channel formation. In this model, α-helical monomers of the peptide

insert into the bilayer and aggregate to form bundles-- much like the barrel-stave model-- creating a pore through which ions can pass (Sansom, 1993b).

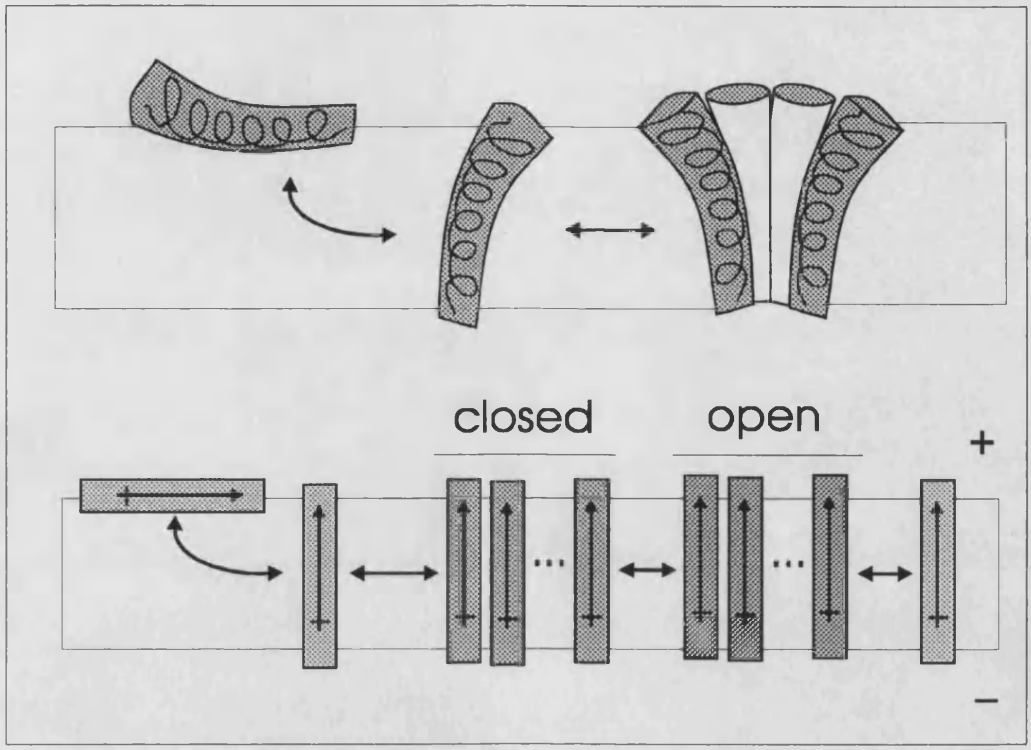

FIGURE 1.4. CHANNEL FORMATION BY CFP HELICES ACCORDING TO THE HELIX-BUNDLE MODEL. The top panel schematizes an α-helical CFP in three different membrane-associated states: left, parallel to the bilayer plane with hydrophobic side of the helix buried; center, a transbilayer orientation; and right in a parallel bundle of helices, forming a bundle. The bottom panel shows the orientation and equilibrium of membrane associated states with respect to a transbilayer potential, denoted by + and - signs. The 'open' and 'closed' designations highlight the fact that it is not known if there exist non-conducting helix-bundle states.

This structural theme, bundles of α-helices packed in various arrangements, is thought to be a key feature in numerous membrane-bound channels, transporters and receptors (Oiki *et al.*, 1990). Indeed, the first proposition of this type was put forward in 1974 by Inouye , who proposed a transmembrane α-helical bundle structure for the *Escherichia coli* outer membrane lipoprotein (Inouye, 1974).

Neutron in-plane scattering is an experimental approach that has provided a wealth of information about the structure of alamethicin (He *et al.*, 1995; He *et al.*, 1996) and magainin (Ludtke *et al.*, 1996) ion channels. These studies provide validating evidence for helix-bundle model of alamethicin ion channel formation, their measurements of both the radius of the water-filled pore and the bundle radius agree with those predicted. However, the magainin pore dimensions were twice as large as predicted by the helix-bundle model. A detailed analysis of scattering data led Ludtke and coworkers to hypothesize that magainin forms pores in such a way that the inner and outer leaflet of the bilayer bends back on itself-- like the inside of a torus. Their findings indicate that a spectrum of channel architectures are possible -depending on the CFP.

1.7. DIPOLAR EFFECTS AND CHANNEL FORMATION (AND BEYOND)

A number of factors are thought to contribute to the formation and stability of ion channels, such as: the orientation of the hydrophilic faces of the peptides so that they line the channel pore; and an orientation of the hydrophobic sidechains that maximizes lipid interaction (Sansom 1993a; Sansom 1993b). These conditions are satisfied by the experimentally observed orientation of the amphiapathic helices parallel to the bilayer plane, as mentioned in the previous section, so additional forces must contribute to the formation of these assemblies. Most CFPs are activated (observed) in the presence of a transbilayer electrostatic potential (induced by a holding potential or by different ion concentrations on either side of the bilayer, the so-called Donnan potential) indicating that an intrinsic property of the helices respond to this potential *via* reorientation. Peptide helices have molecular dipole moments due to the orientation of the amido carbonyl bonds along the helical screw axis (Wada,1976; Hol *et al.*, 1978). This observation has been extended by dipole measurements on alamethicin (Yantorno *et al.*, 1982). It is indeed

this molecular dipole that appears to orient against an imposed transbilayer electrostatic field (Sansom, 1993b; Schmitt *et al.,* 1997).

The forces that seemingly govern the formation of ion-channels can be divided into four distinct categories: 1- *lipid-peptide* interactions; 2- *peptide-peptide* interactions; 3- *peptide-electrostatic field* interaction; and 4- *peptide-water* interaction (Sansom 1993a). The nature of the latter interaction is perhaps the least well understood, but some interesting recent developments on this front have been made by Sansom and coworkers (Breed *et al.,* 1996). They conducted molecular dynamics simulations of water filled channels and subsequently calculated diffusion coefficients and rotational re-orientation rates in the bound water. There is both a striking decrease in diffusion and it appears that the bound water is oriented such that the water dipoles line up against the peptide helical dipoles. A further ordering is observed: these simulations indicate that the bound water is participating in extended H-bonding phenomena. These studies indicate that both peptide-field and peptide-water dipolar correlation effects may play a significant role in ion channel properties.

DeGrado's group introduced a mathematical formalism to describe the dipolar contributions to ion channel formation and current rectification (Kienker *et al.,* 1994). They hypothesize that a non-symmetric I-V relationships must arise from asymmetric component in the conducting pore. This model is essentially an extension of electrodiffusion theory (for an introduction to electrodiffusion theory see: Schultz, 1980; Hille, 1992) that takes into account the asymmetric element – the dipole potential. They consider the potential $\Psi(x,V)$ on a given ion in the channel is the sum of three components:

$$\Psi(x, V) = \Psi_c(x, V) + \Psi_{ec}(x) + \Psi_{img}(x) \qquad \{1.7\}$$

where $\Psi(x,V)$ is the constant field potential due to the transmembrane potential V, $\Psi_{ec}(x)$ is the helix dipole component and $\Psi_{img}(x)$ is the interfacial polarization (image) potential. Unfortunately, they simplify the dipole potential by extrapolating the sum of atomic dipoles to net partial charges located at the helix termini. Then potential function $\Psi(x,V)$ is imbedded into the Nernst-Planck electrodiffusion equation to obtain the following:

$$I(V) = \frac{F\beta DAC(e^{\{VF/RT\}} - 1)}{\int e^{\{\Psi(x,V)F/RT\}} dx} \qquad \{1.8\}$$

where F is the Faraday constant, β and D are the ion's partition coefficient and diffusion coefficients, respectively. The channels cross-sectional area is A, and R and T are the gas constant and temperature. By varying three parameters (not given here) that are embedded in the 3-term expression given for $\Psi(x,V)$, they were able to fit the above Nernst-Planck equation to I-V curves for the Leucine-Serine (LS) channel forming peptide, Ac-(LSSLLSL)$_3$. Although the physical significance of the varied parameters is a matter of question, this work signifies a 'first-step' in rigorously treating dipole effects in ion channel conductivity.

More recently Woolley and coworkers further developed this approach by replacing the potential function $\Psi(x,V)$ with an explicit polynomial expression, $f_c(x)$, for the potential of an ion as it travels down the pore axis, thus minimizing approximations (Woolley *et al.*, 1997). The linearized form of the Poisson-Boltzmann equation was used to calculate $f_c(x)$ according to Davis and coworkers (1991). The following integral was then used to describe the variation of potential as a function of position in a channel of length l:

$$\int_0^l e^{\{Z_c F \Psi_{xc}/RT\}} dx \qquad \{1.9\}$$

This term was split into two further terms, the first describing the ion's potential due to the applied field and the second due to the Poisson-Boltzmann polynomial, where z_c is the ion valence:

$$\int_0^l e^{\left\{z_c F\left(\frac{\Psi_c x}{l}+kf_c(x)\right)/RT\right\}} dx \qquad \{1.10\}$$

Now, the above equation fits into the denominator of the Nernst-Planck equation to yield:

$$I(V) = \frac{F\beta DAC(e^{\{VF/RT\}} - 1)}{\int_0^l e^{\left\{z_c F\left((\Psi_c x/l)+kf_c(x)\right)/RT\right\}} dx} \qquad \{1.11\}$$

Numerical integration of the above equation was shown to reproduce accurately the current-voltage curves measured for the tethered alamethicin dimer, ALM-BAHPDA.

1.8. ION SELECTIVITY: A CURRENT SYNOPSIS

From the equations above {eqs. 1.8 & 1.11} it should be possible to calculate the permeability of various ions and hence the selectivity ratio of a given channel ensemble (note: macroscopic I-V experiments measure characteristics of ensembles rather than on individual channels. Thus, in macroscopic experiments, permeability is a conductance-weighted average over different oligomeric states). Ion permeability also depends on the nature of the ion; variables such as charge, shape, ionic radius and water coordination properties all play a role. The Born energy and the related desolvation free energy also contribute to ionic permeability in small pores (for a review, see: Hille, 1992).

1.9. BIOPHYSICAL STRUCTURE-FUNCTION STUDIES

The biophysical study of synthetic CFP analogs has conceivably provided the greatest wealth of information about the nature of CFPs, largely supporting the helix-bundle model of ion-channel formation. A number of particularly insightful recent studies are briefly highlighted below.

The first study utilizes so-called TASP templating techniques to construct bundles of CFPs held together at their C-termini by cyclic peptide rings (Matsubara *et al.*, 1996). The technique, initially pioneered by Montal and coworkers (Montal *et al.*, 1990), restricts the variation of structures that might be driven to form in the presence of a transbilayer electrostatic potential and reduces entropic forces hindering the assembly process. Matsubara and colleagues synthesized TASP assemblies that contained 3,4 or 5 truncated alamethicin derivatives and found that all but the 5-mer showed conductance properties predicted by the helix-bundle model. Channels formed by the 5-mer appeared to be

unstable and erratic, which may be due to irregularities in the shape of the TASP template or to aggregation of multiple molecules.

The helix-bundle model describes that CFPs are in constant equilibrium between the aqueous and lipid phases, and additionally, between a complex range of monomeric and aggregate forms. At any given time, exceedingly few peptide aggregates lead to the formation of channels-- indicating that the process of channel formation is thermodynamically disfavored. You and coworkers, considering the ever-present randomization and diffusion forces present in lipid membranes, constructed alamethicin dimers held together at their C-termini by flexible linkages (You *et al.*, 1996). Knowing that diffusion is, to a first approximation, proportional to the reciprocal of the molecular weight, they conjectured that these constructs would form channels with greater stability (i.e., longer lifetimes) and more defined conductance states (i.e., less conformational entropy) which indeed appears to be the case. Molecular models of their tethered dimers, constructed using the helix-bundle paradigm, are also consistent with the model.

In another study, Molle and coworkers synthesized alamethicin analogs devoid of hydrogen bonding residues in the C-terminus of the peptide (Molle *et al.*, 1996). These analogs were shown to be far less effective at forming channels and the channels that *did* form had very short lifetimes and erratic conductance properties. They hypothesize that rings of intermolecular hydrogen bonds form between alamethicin monomers once assembled into channels, leading to the stabilization of the supra-molecular structure. Despite the fact that one may be able to envision other structural models that are consistent with these observations, it does appear that the helix-bundle model is strongly supported by the results discussed so far.

1.10. COMPUTATIONAL STUDIES

Computational modeling of CFP assemblies is of mounting interest not only because they may be prototypical of biologically important ligand gated ion-channels, such as the nicotinic acetylcholine receptor (Karlin & Akabas, 1995; Unwin, 1993), but also because of the need to establish principles of *de novo* peptide design-- And although the helix-bundle model provides a molecular rationalization for the behavior of CFPs, the model is crude, as it is not an atomistic representation.

Efforts to model channels at an atomistic level were initiated more than a decade ago (Hall *et al.*, 1982; Fox & Richards, 1984). The premise of most molecular modeling studies has been that structural data from NMR and X-ray crystallography is a valid starting point for simulations and electrostatics calculations (Sansom, 1993a). Although well founded, this assumption is indicative of the fields infancy. Here, I will briefly describe a number of works of particular relevance to this Thesis.

The first series of papers describe simulations of CFP monomers in the presence of a functional bilayer description, rather then an atomistic bilayer representation. Milik and coworkers simulated the insertion of melittin, magainin and the Pf1-bacterophage coat protein into a low-dielectric slab (Milik *et al.*, 1993). The theoretical basis of this work is of particular significance, because they describe a lipophilicity derived free energy scale that is very comprehensive. With all three peptides, they were able to reproduce the orientation of the peptide insertion into bilayers. More recently, Biggin and coworkers used a similar approach to simulate the insertion of alamethicin into a low-dielectric slab with the inclusion of a potential function designed to emulate a transbilayer potential (Biggin *et al.*, 1997). Their results were in agreement with experiment on two counts: (1) the imposition of a 'transbilayer potential' caused insertion of the peptide into the slab; and (2) that the imposed

potential accentuated the central helix kink at proline-14 seen in NMR and crystal derived structures. It should be noted that a few studies with explicit bilayer descriptions are starting to emerge, but this approach is hampered by its excessive computational cost. One notable example is the work of Shen and coworkers who conducted all-atom MD simulations of poly(32)alanine in a solvated DMPC bilayer (Shen *et al.*, 1997) . Their multi-nanosecond simulations show a marked correlation between peptide motion and an 'annulus' of lipid surrounding the peptide. Persistent lipid-peptide hydrogen bonding interactions were also observed as were marked changes in lipid acyl-chain order parameters.

Helix bundles have been modeled by Breed and coworkers using molecular dynamics simulated annealing approaches (Breed *et al.*, 1997; Breed & Sansom, 1994; You *et al.*, 1996; Kerr *et al.*, 1994). Here, parallel bundles of kinked CFP helices are minimized, constrained with regard to helical H-bonds and simulated *in vacuo* for extended periods. These simulations yield channels with conductance and conformational properties consistent with experiment.

1.11. ION-CHANNELS AS NONLINEAR DYNAMICAL SYSTEMS

It is very interesting to note that CFPs are evidenced to be the first molecules to exhibit stochastic resonance. Complex biological systems, electronic and neural networks often show increased predictability and fitness in the presence of noise (Amit, 1993), the so-called stochastic resonance effect. Recently Bezrukov and Vodyanoy described, for the first time, this effect in a molecular system (Bezrukov & Vodyanoy, 1993). In their definitive experiment, these investigators conducted single-channel measurments on alamethicin with or without a small amount of background noise (pink-noise modulation of the transbilayer potential). The conductance levels, lifetimes and transitions showed greater definition and less noise then the noiseless recordings. The channels

formed in the presence of pink-noise also exhibited a lower baseline level of random conductance fluctuations. The significance of this finding cannot be overestimated as it points to many possibilities for understanding complexity-related phenomena in neural and biological systems.

1.12. AIMS OF THIS STUDY

As outlined above, unraveling the relationship between structure and function in CFPs is of paramount importance. The characterization of a large number of CFPs, from simple peptide antibiotics to ligand-gated ion channels has undoubtedly contributed to our understanding, but many ambiguities remain. The physical determinants of self-assembly and channel formation have yet to be resolved and barring crystallographic techniques, elucidating the physics of CFP assembly is the only means of unambiguously determining CFP structure.

To this end, I have undertaken three distinct but related experimental approaches: (1) The synthesis and biophysical characterization of redox-active analogs of alamethicin. Alamethicin with ferrocene on the C- or N-terminus gives one the opportunity to probe a number of forces that are thought to be important in ion-channel formation; the introduction of a redox-active moiety allows one to alter the charge of a given peptide in a pH independent manner. Thus, electrostatic, hydrophobic and molecular dipole effects can be probed; (2) Synthesis and characterization of dimerized or tethered analogs of alamethicin and melittin with the aim of forming ion channels with enhanced stability-- thus facilitating biophysical characterization to an extent not possible with the monomeric CFPs; and (3) Structure-function studies of melittin and alamethicin analogs having distinct charge and hydrogen-bonding characteristics. A modeling study was also undertaken

in an effort to augment the conclusions and the findings from which they are drawn.

A related goal of this investigation has been to lay groundwork for the future use of ion channels as nanodevices. To this end we have sought to establish the ability of redox active CFPs to respond to changes in the chemical environment. Success in this arena will not only serve to enlighten the mechanisms behind molecular self-organization but also provide new avenues for the design and construction of molecular devices.

1.13. REFERENCES: INTRODUCTION

Acton, E. M., &. Silverstein, R.M. (1959) *J. Org. Chem. 24*, 1487-1490.

Adams, P. D., Arkin, I.T., Engelman, D.M., & Brunger, A.T. (1995) *Nature Str. Biol. 2*, 154-162.

Akerfeldt, K. S., Lear, J.D., Wasserman, Z.R., Chung, L.A., & DeGrado, W.F. (1993) *Acc. Chem. Res. 26*, 191-197.

Ananthanarayanan, V.S., & Zhorov, B.S. (1997) *Biophys. J. 72,* 1143-1152.

Balaram, P. (1992) *Curr. Opin. Struct. Biol. 2*, 845-851.

Ball, F.G., & Sansom, M.S.P. (1989) *Proc. Roy. Soc. Lond. B. 236,* 385-416.

Banerjee, U., Zidovetski, R. , Birge, S.I., & Chan, S.I. (1985) *Biochemistry 24*, 7621-7627.

Baumann, G., & Mueller, P. (1974) *J. Supramol. Str. 2*, 538-557.

Bazzo, R., Tappin, M.J. , Pastore, A. , Harvey, T.S. , Carver, J.A., & Campbell, I.D. (1988) *Eur. Biochem. J. 173*, 139-146.

Bezrukov, S.M., & Vodyanoy, I. (1995) *Nature 378,* 362-368.

Biggin, P.C., Breed., J., Son, H.S., & Sansom, M.S.P. (1997) *Biophys. J. 72,* 627-636.

Boheim, G. (1974) *J. Membr. Biol. 19*, 277-303.

Boheim, G., Hanke, W., & Jung, G. (1983) *Biophys. Struct. Mech. 9*, 181-191.

Brachais, L., Duclohier, H., Mayer, C., & Davoust, D. (1995) *Biopolymers 36*, 547-558.

Breed, J., Sankararamakrishnan, R., Kerr, I.D. & Sansom, M.S.P. (1996) *Biophys. J. 70*, 1643-1661.

Breed, J., & Sansom, M.S.P. (1996) *Biochem. Soc. Trans. 22*, 157S.

Breed, J., Biggin, P.C., Kerr, I.D., Smart, O.S., & Sansom, M.S.P. (1997) *Biochim. Biophys. Acta 1325,* 235-249.

Brenner, C., Duclohier, H., Krchnak, V., & Wroblewski, H. (1995) *Biochim. Biophys. Acta - Biomembranes 1235*, 161-168.

Brumfield, V., & Miller, I.R. (1990) *Biochim. Biophys. Acta.* 1024, 49-53.

Bruckner, H., & Graf, H. (1983) *Experientia 39*, 528-530.

Budka, H., Aguzzi, A., Brown, P., & Weller, R.O. (1995) *Brain Path. 4,* 459-466.

Burgess, A. W., & Leach, S.J. (1973) *Biopolymers 12*, 2599-2605.

Casico, M., & Wallace, B.A. (1988) *Proteins: Struc. Func. Genet. 4*, 89-98.

Chung, L. A., Lear, J.D., & DeGrado, W.F. (1992) *Biochemistry 31*, 6608-6618.

Cornut, I., Buttner, K., Dasseux, J.-L., & Dufourcq, J. (1994) *FEBS lett. 349*, 29-33.

Creighton, T.E. (1994) *Proteins,* 2nd. ed., W.H. Freeman and Co., Boston, Mass.

DeGrado, W. F., & Lear, J.D. (1990) *Biopolymers 29*, 205-213.

Dempsy, C.E., Bazzo, R, Harvey, T.S., Syperek, I., Boheim, G. & Campbell, I.D. (1991) *FEBS Lett. 281*, 240-244.

Dempsy, C. E. & Hall, L. J. (1996) *Biophys. J. 70*, 1777-1788.

Dougherty, D. A., & Stauffer, D.A. (1990) *Science*, 1558-1560.

Eisenberg, D., Weiss, R.M., & Terwilliger, H. (1982) *Nature 299*, 371-374.

Eisenberg, D., & McLachlan, A.D. (1986) *Nature 319,* 199-201

Esposito, G., Carver, J.A., Boyd, J. and Campbell, I.D. (1987) *Biochemistry 26*, 1043-1050.

Fox, R. O., & Richards, F.M. (1982) *Nature 350*, 325-330.

Fugita, T., Wada, S., Iida, A., Nishimura, T., Kanai, M., & Toyama, N. (1994) *Chem. Pharm. Bull. 42*, 489-494.

Galzi, J.-L., Revah, F., Bessis, A., & Changeaux, J.-P. (1991) *Ann. Rev. Pharm. 31*, 37-72.

Ghadiri, M. R., Granja, J.R., Milligan, R.A., McRee, D.E., & Kazanovich, N. (1993) *Nature 366*, 324-327.

Ghadiri, M. R., Granja, J.R., & Buehler, L.K. (1994) *Nature 369*, 301-304.

Grigoriev, P., Schlegel, R., Dornberger, K., & Grafe, U. (1995) *Biochim. Biophys. Acta- Biomembranes 1237*, 1-5.

Guy, H. R., & Conti, F. (1990) *Trends in Neurosci. 13*, 201-206.

Hall, J. E., Vodaynoy, I., Balasubramanian, T.M. & Marshall, G. M. (1984) *Biophys. J. 45*, 233-247.

Harris, I.L., & Chapman, D. (1988) *Biochim. Biophys. Acta 943*, 375-380.

He, K., Ludtke, S.J., Worchester, D.L., & Huang, H.W. (1995) *Biochemistry 34,* 15614-15618.

He, K., Ludtke, S.J., Worchester, D.L., & Huang, H.W. (1996) *Biophys J. 70,* 2659-2666.

Hille, B. (1992) Ionic Channels of Excitible Membranes, 2nd. ed., Sinauer Assoc., Sutherland, Mass.

Hol, W.G., von Duigen, P.T., & Berendsen, H.J.C. (1978) *Nature 273*, 443-446.

Huang, H.W., & Wu, Y. (1991) *Biophys J. 60,* 1079-1087.

Iida, A., Sanekata, M., Wada, S., Fugita, T., Tanaka, H., Enoki, A., Fuse, G., Kanai, M., & Asami, K. (1995) *Chem. Pharm. Bull. 43*, 392-397.

Inouye, M. (1974) *PNAS USA 71,* 2396-2400.

Jung, G., Konig, W.A. , Leibfritz, D. , Ooka, T. , Janko, K., & Boheim, G. (1976) *Biochim. Biophys. Acta 433*, 164-181.

Kaduk, C., Duclohier, H., Dathe, M., Wehschuh, H., Byermann, M., & Molle, G. (1997) *Biophys. J. 72,* 2151-2159.

Karle, I. L., Flippen-Anderson, J., Sukumar, M., & Balaram, P. (1987) *Proc. Natl. Acad. Sci. USA 84*, 5087-5091.

Karle, I. L., & Balaram, P. (1990) *Biochemistry 29*, 6747-6756.

Karle, I.L., Flippen-Andersen, J., Agarwalla, S., & Balaram, P. (1991) *PNAS USA 88,* 5307-5311.

Karle, I.L., Flippen-Andersen, J., Agarwalla, S., & Balaram, P. (1992) *in Structure and Function Vol. II, Proteins* (ed. R.H. Sarma & M.H. Sarma) Adenine Press, New York.

Karlin, A. (1993) *Curr. Op. Biol. 3*, 299-309.

Karlin, A., & Akabas, M.H. (1995) *Neuron 15*, 1231-1244.

Kauffman, S. A. (1993) *The Origins of Order*, Oxford University Press, New York.

Kerr, I.D., Sankararamakrishnan, R., Smart, O.S., & Sansom, M.S.P. (1994) *Biophys. J. 67,* 1501-1515.

Kienker, P.K., DeGrado, W.F., & Lear, J.D. (1994) *PNAS USA 91*, 4859-4863.

Kelsh, L.P., Ellena, J.F., & Cafiso, D.S. (1992) *Biochemistry 31,* 5136-5144.

Kumazawa, S., Kanada, M., Aoyama, H., Utgawa, M., Kondo, J., Sakamoto, S., Ohtani, H., Mikawa, T., Chiga, I., & Hayase, T. (1994) *J. Antibiot. 47*, 1136-1144.

Latorre, R., & Alverez, O. (1981) *Physiol. Rev. 61*, 77-150.

Lau, H. H., & Hart, H. (1959) *J. Org. Chem. 24*, 280-281.

Lauger, P. (1976) *Biochim. Biophys. Acta 455*, 493-509.

LeBars, M., Bachet, B., & Mornon, J.P. (1988) *Zeit. Kristallogr. 185*, 588 (abst.).

Lesieur, C., Vecsey-Semjen, B., Abrami, L., Fivaz, M., & Van Der Goot (1997) *Mol. Memb. Biol. 14,* 45-64.

Lin, M.-C. Mirzabekov, T., & Kagan, B.L. (1997) *Nature 272*, 44-47.

Liu, C.C., Walsh, C.M., & Young, J.D.E. (1995) *Immun. Today 16,* 194-201

Ludtke, S., He, K. & Huang, H. (1995) *Biochemistry 34*, 16764-16769.

Ludtke, S., He, K., Heller, W.T., Harroun, T.A., Yang, L., & Huang, H. (1996) *Biochemistry 35,* 13723-13728.

Mak, D., & Webb, W.W. (1993) *Biophys. J. 64* A95.

Matsubara, A., Asami, K., Akagi, A., & Nishiono, N. (1996) *Chem. Commun. 46,* 1156-1163.

McHaourab, H. S., Hyde, H.S., & Feix, J.B. (1994) *Biochemistry 33*, 6691-6699.

Mellor, I. R., Thomas, D.H., & Sansom, M.S.P. (1988) *Biochim. Biophys. Acta 942*, 280-294.

Milik, M., & Skolnick, J. (1993) *Proteins: Str. Fun. Genet. 15,* 10-25.

Molle, G., Dugast, J.Y. , Duclohier, H., & Spach, G. (1988) *Biochim. Biophys. Acta 938*, 310-314.

Molle, G., Dugast, J.-Y., Spach, G., & Duclohier, H. (1996) *Biophys. J. 70*, 1669-1675.

Montal, M., & Mueller, P. (1972) *Proc. Natl. Acad. Sci. USA 69*, 3561-3566.

Montal, M. O., Montal, M., & Tomich, J.M. (1990) *Proc. Natl. Acad. Sci. USA 87*, 6929-6931.

Montal, M. O., Iwamoto, T., Tomich, J.M., & Montal, M. (1993) *FEBS lett. 320*, 261-266.

Mueller, P., & Rudin, D.O. (1963) *J. Theor. Biol. 4*, 268-280.

Nesmeyanov, N., & Reutov, O.A. (1957) *Proc. Doc. Chem. 115*, 763-765.

New, A. P., Eckers, C., Haskins, N.J., Neville, W.A., Elson, S., Huesorodriguez, J.A., & Riverasagredo, A. (1996) *Tett. Lett. 37*, 3039-3042.

Oiki, S., Danho, W., Madison, V., & Montal, M. (1988) *PNAS USA 85,* 8703-8707.

Oiki, S., Madison, V., & Montal, M. (1990) *Proteins: Str. Func. Genet. 8*, 226-236.

Opsahl, L.R., & Webb, W.W. (1993) *Biophys J. 64,* A95.

Rebuffat, S., Conraux, L., Massias, M., Auvinguette, C., & Bodo, B. (1993) *Intl. J. Pept. Prot. Res. 41*, 74-84.

Sansom, M. S. P. (1991) *Biophys. Mol. Biol.*, 139-236.

Sansom, M. S. P. (1992) *Eur. Biophys. J. 21*, 281-298.

Sansom, M. S. P. (1993a) *Quart. Rev. Biophys. 26*, 365-421.

Sansom, M. S. P. (1993b) *Eur. Biophys. J. 22*, 105-124.

Schmitt, J. D., Sansom, M.S.P., Kerr, I.D., Lunt, G.G., & Eisentlal, R. (1996) *Biochemistry 36,* 1112-1115.

Shubert, U., Henklein, P., Bour, S., Ferrermonteil, A.V., Oblattmontal, M., Montal, M., & Strebel, K. (1995) *AIDS Res. Human. Retrovir. 11,* 5114-5121.

Schnur, J. M., Peckerar, M. (1992) , Plenum Press, New York.

Schule, H., & Hanke, M. (1993) *BLM Handbook.* VCH, Berlin.

Schwartz, G., Savko, P., & Jung, G. (1983) *Biochim. Biophys. Acta*, 419-428.

Schwartz, G. (1987) *Biophys. Chem. 26*, 163-169.

Scott, R. A. (1995) *Structure 3*, 981-986.

Shai, Y., Doll, L., & Miller, I.R. (1993) *Biochem. 29*, 315-326.

Shen, L., Bassolino, D., & Stouch, T. (1997) *Biophys. J. 73,* 3-20.

Sitaram, N. & Nataraj, J. (1993) *Biochemistrry 32*, 3124-3130.

Smart, O.S., Neduvelil, J.G., Wang, X., Wallace, B.A., & Sansom, M.S.P. (1996) *J. Mol. Graphics. 14,* 354-360.

Stankowski, S., & Schwartz, G. (1989) *FEBS Lett. 250*, 556-560.

Strahilevitz, J., Mor, A., Nicolas, P., & Shai, Y. (1994) *Biochem. 33*, 10951-10960.

Stroud, R. M., McCarthy, M.P., & Shuster, M. (1990) *Biochemistry 50*, 11009-11023.

Terwilliger, T.C., & Eisenberg, D. (1982) *J. Biol. Chem. 257,* 6016-6022.

Terwilliger, T.C., Weissman, L., & Eisenberg, D. (1982) *Biophys. J. 257,* 6016-6022.

Toteson, M. T., &. Toteson, D.C. (1981) *Biophys. J. 37,* 353-361.

Toyoshima, C., & Unwin, N. (1988) *Nature 336*, 247-250.

Tsantrizos, Y. S., Pischos, S., Sauriol, F., & Widden, P. (1996) *Can. J. Chem. 74*, 165-172.

Unwin, N. (1989) *Neuron 3*, 665-676.

Unwin, N. (1993) *Neuron 10 (suppl.)*, 31-41.

Vogel, H. (1987) *Biochemistry 26*, 4562-4572.

Wada, A. (1976) *Adv. Biophys. 9*, 1-63.

Woolley, G. A., & Wallace, B.A. (1993) *Biochemistry 32*, 9819-9825.

Woolley, G. A., Epand, R.M., Kerr, I.D., Sansom, M.S.P., & Wallace, B.A. (1994) *Biochemistry 33*, 6850-6858.

Woolley, G. A., & Wallace, B.A. (1992) *J. Membr. Biol. 129*, 109-136.

Woolley, G.A., Biggin, P.C., Schultz, A., Lien, L., Jaikaran, D.C.J., Breed, J., Crowhurst, K., & Sansom, M.S.P. (1997) *Biophys. J. 73,* 770-778.

Yantorno, R. E. (1982) *PhD Dissertation,* U. Pennsylvania, Philidelphia.

Yee, A. A., Babuik, R. & O'Neil. (1995) *Biopolymers 36*, 7881-792.

Yee, A. A. & O'Neil., J.D.J. (1992) *Biochemistry 31*, 3135-3143.

You, S., Peng, S., Lien, L., Breed, J. & Woolley, G.A. (1996) *Biochemistry 35,* 6225-6232.

2. SYNTHESIS

2.1. Synthetic Strategies and Targets

Here, the synthetic strategies used to synthesize all relevant alamethicin and melittin analogs are outlined. The C-terminus ferrocenoyl analogs were synthesized by modification of alamethicin from *Trichoderma viride*, using activated ferrocenecarboxyates as shown in figure 2.1.

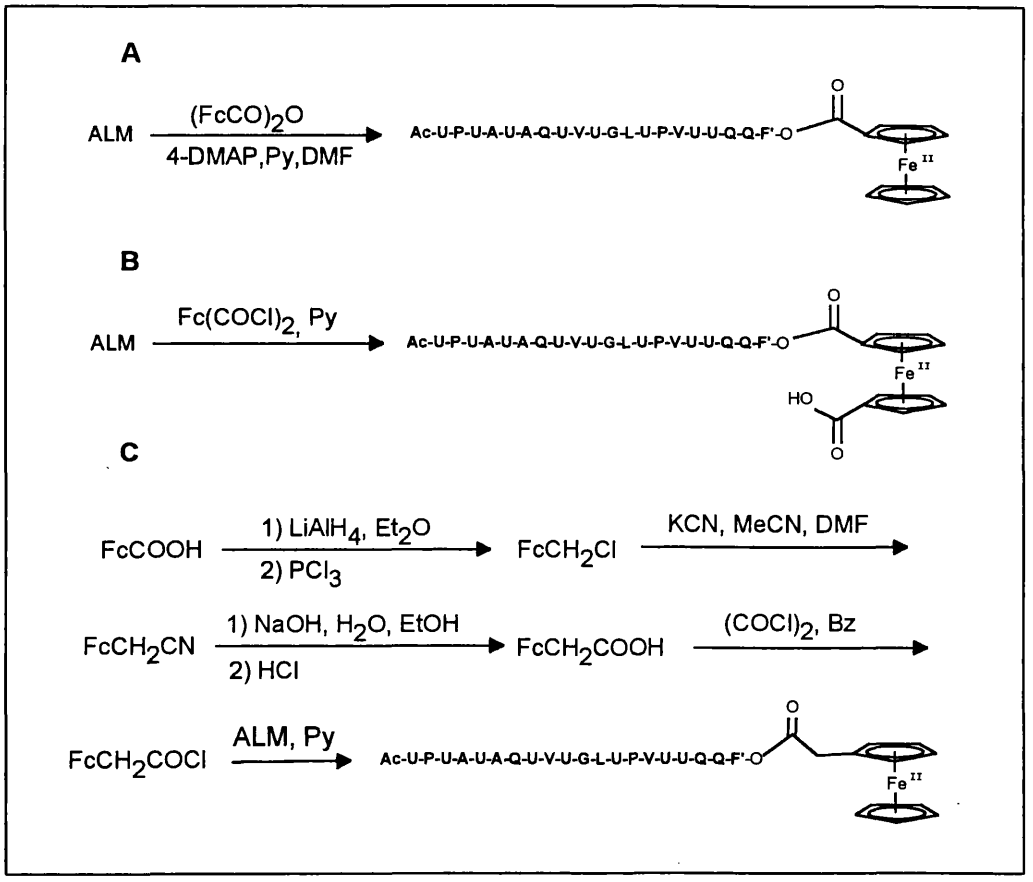

FIGURE 2.1. SOLUTION-PHASE SYNTHESIS OF C-TERMINUS ALAMETHICIN DERIVATIVES. A, Fc-ALM; B, cxFc-ALM; $FcCH_2$-ALM.

FcALM was synthesized by modification of the method of Woolley and coworkers (Woolley *et al.*, 1994), by allowing alamethicin to react with ferrocenoic anhydride using pyridine and 4-dimethylaminopyridine as

catalysts, Figure 2.1, panel A. cxFcALM was synthesized using the more reactive acid chloride under basic conditions, Figure 2.1, panel B. The synthesis of $FcCH_2$-ALM is shown in Figure 2.1, panel C; briefly, ferrocenecarboxylic acid was reduced with lithium aluminum hydride to give ferrocenemethyl alcohol which was reacted with phosphorus trichloride to give chloromethyl ferrocene. Addition of one carbon was accomplished by nucleophilic displacement of the chlorine with cyanide ion; the resulting ferroceneacetonitrile was hydrolyzed followed by acidic work-up to yield ferroceneacetic acid. Finally the ferrocene acetic acid chloride was formed by treatment of ferroceneacetic acid with oxalyl chloride. This acid chloride reacted in excess with alamethicin to give the desired product in high yield.

In a related, but unsuccessful effort a number of attempts were made at synthesis of alamethicin dimers linked at the C-terminus.

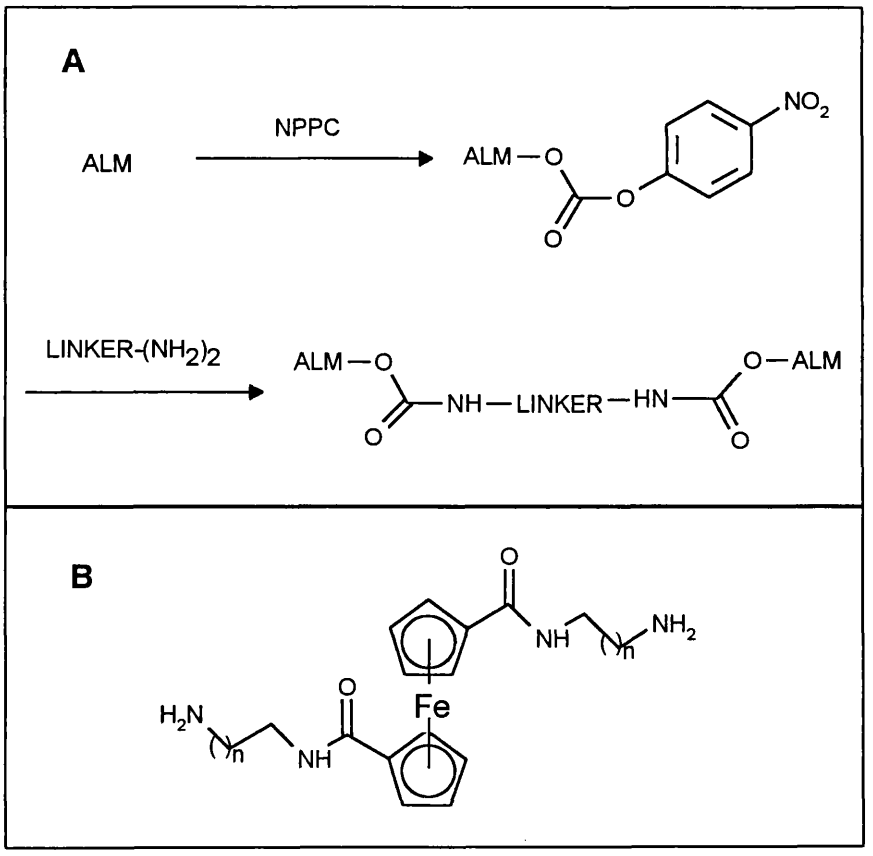

FIGURE 2.2. ALAMETHICIN DIMER SYNTHESIS STRATEGIES. A, method according to You *et al.* (1996); B, novel diamine tethers.

Figure 2.2 panel A, shows an outline of the methodology, originally described by You and coworkers (You *et al.*, 1996). This synthesis exploits an O→N transesterfication of a carbonate ester to create a very stable carbamate linkage between an amine and an alcohol. To this end two ferrocene diamide linkers were synthesized for the purposes of exploiting this methodology, these are shown in panel B of Figure 2.2; full accounts are given in Results section 4.1.

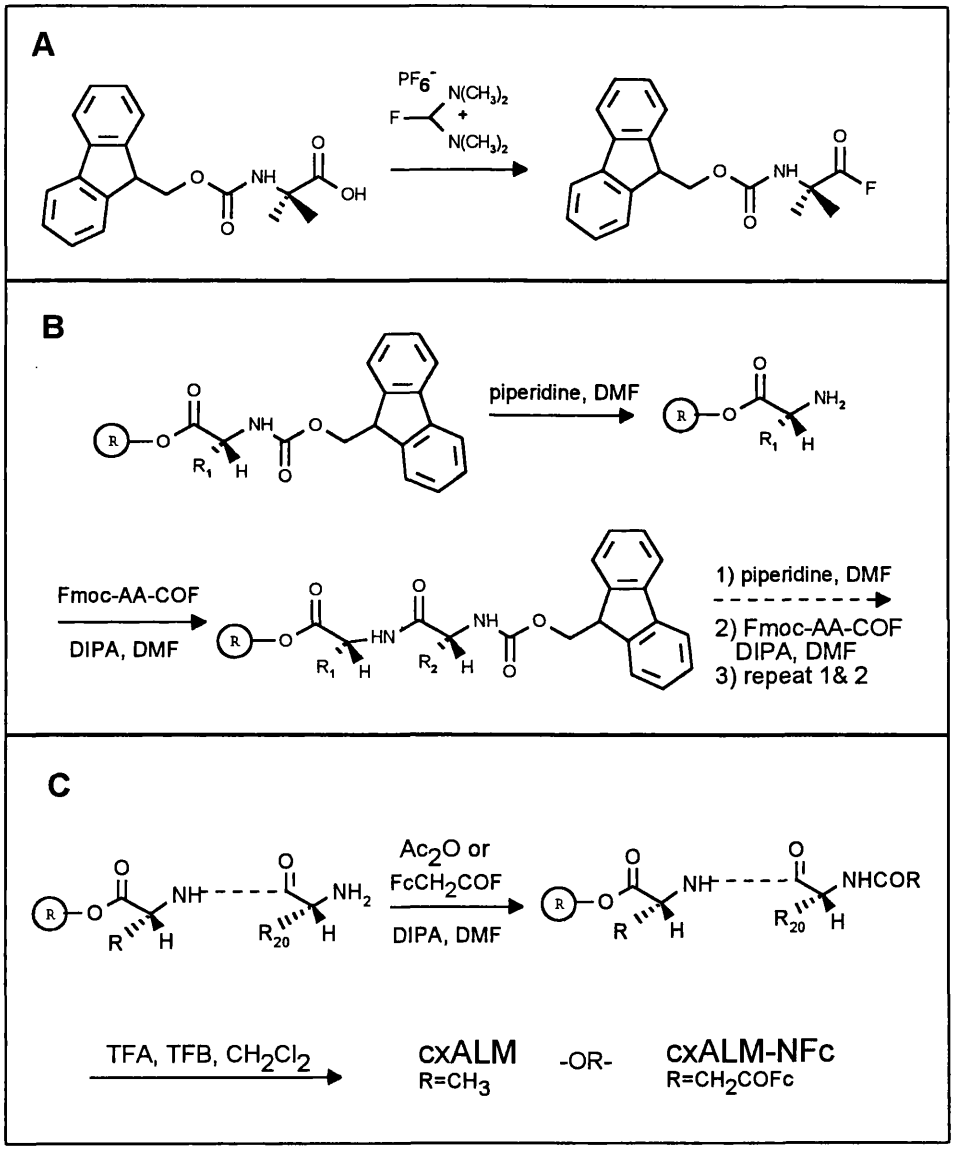

FIGURE 2.3. SOLID-PHASE SYNTHESIS OF ALAMETHICIN DERIVATIVES. Fmoc-amino acid fluoride generation; B, elongation methodology; C, N-terminus derivitization and cleavage from resin.

Alamethicin analogs cxALM-Ac and cxALM-Fc were synthesized using solid-phase synthesis methodology. Until recently, the solid-phase synthesis of hydrophobic peptides was difficult at best, requiring liquid-phase pre-assembly of 3- or 4-mers. Figure 2.3 shows the solid-phase synthetic methodology that has made the synthesis of alamethicin and its derivatives possible. The '®' symbol indicates the solid phase synthesis support. The extremely reactive Fmoc-amino acid fluorides are generated *in situ* using the fluorinating agent TFFH hexafluorophosphate. All couplings are carried out in DMF containing a high concentration of diisopropylamine which may help to expose the maximum number of reactive sites on the resin-bound peptide, as shown in 2.3B. Once elongation is complete, the N-terminus amine is reacted with either acetic anhydride or ferroceneacetic acid fluoride followed by cleavage from the resin by TFA and tetrafluoroboric acid to give cxALM and cxALM-Fc, respectively. The synthesis of three cysteine mutants of ALM was also attempted, see below.

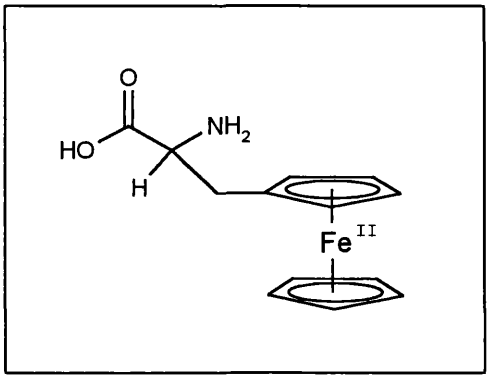

FIGURE 2.4. FERROCENYLALANINE, THE FERROCENE ANALOG OF PHENYLALANINE.

In a related, but unrealized, effort the ferrocene analog of phenylalanine was synthesized according to slight variation of the method reported by Osgerby and Pauson (1957). The compound, (±)-ferrocenylalanine, shown in figure 2.4 was to be converted into its Fmoc derivative and then used in solid-phase synthesis.

In a final attempt to make C-terminus linked dimers of alamethicin we synthesized three novel dicarboxylate analogs shown in figure 2.5. Panel A shows a redox-active compound made *via* a Friedel-Crafts acylation of ferrocene with succinic anhydride, followed by reductive work-up; Panel B shows a disuccinoylamide analog of 4,4'-diaminoazobenzene, a *cis-trans* photoisomerizable compound; the bottom panel shows a dicarboxylate analog of diaza-18-crown-6 made with the aim of bridging CFP monomers with a moiety that would itself dimerize in the presence of certain divalent ions.

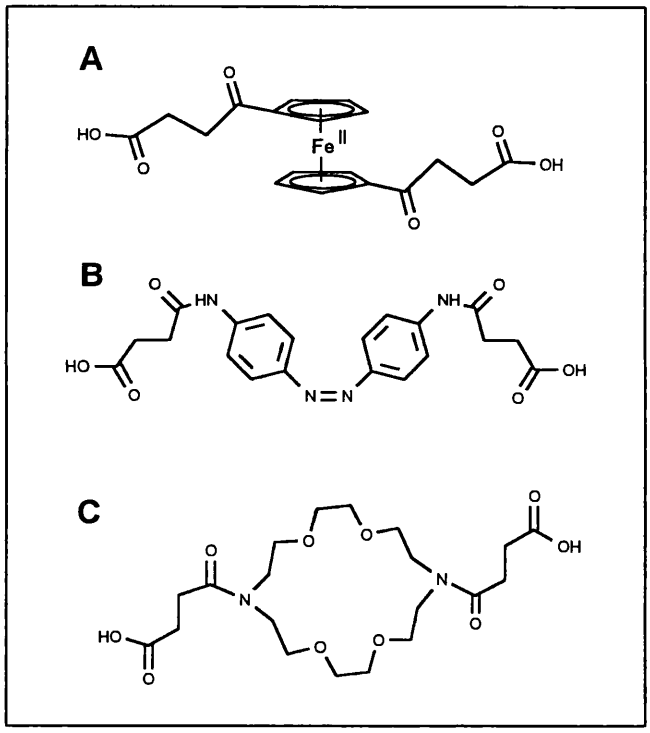

FIGURE 2.5. DICARBOXYLATE LINKERS FOR THE SYNTHESIS OF ALAMETHICIN DIMERS. A, ferrocene-1,1'-bis(1-oxobytyricacid); B, 3-(N-(4-((4-(3-carboxypropanoylamino)phenyl)diazenyl)phenyl)carbamoyl)propanoic acid; C, 4-(1,10-diaza-10(3-carboxypropanoyl)-4,7,13,16-tetraoxacyclooctadecyl)-4-oxobutanoic acid.

Melittin analogs were synthesized in collaboration with Dr. Chris Dempsy and coworkers at the University of Bristol, see below.

2.2. Suppliers, Preparation of Reagents and Chemical Analysis

Reagents for synthesis were purchased from Aldrich (Poole, UK), Lancaster Synthesis (Lancachire, UK) or Fluka (Poole, UK) and were the highest grade appropriate. Neutral alumna and silicic acid were purchased from Aldrich and oven dried (150° C) for 24 hours prior to use. Alamethicin (mixture of peptides, principally R_f = 50) from *Trichoderma veride* and high purity N,N-bis(2-hydroxyethyl)-2-aminoethanesulphonic acid were purchased from Sigma (Poole, UK). Diphytanoylphosphatidylcholine was purchased from Avanti Polar Lipids (Alabaster, Al, USA) and stored at -70° C prior to use. All Fmoc amino acids and reagents for solid-phase peptide synthesis were purchased from Calbiochem-Nova Biochemicals (Nottingham, UK). PEG-PS-Fmoc-phenylalanine resin and solvents used in solid-phase peptide synthesis were purchased from Perceptive Biosystems (Cambridge, UK). Dichloromethane, chloroform and dichloroethane were distilled from P_2O_5 under an inert atmosphere. Ethyl ether and tetrahydrofuran were distilled from sodium/benzophenone under argon. Benzene was distilled over sodium. Pyridine was distilled from calcium hydride after refluxing for 2 hours. Triethylamine was distilled from dry 4Å molecular sieves. Dimethylformamide was also distilled over dried 4Å molecular sieves prior to use. Anhydrous methanol and ethanol were each prepared by distillation from fresh magnesium turnings with a trace of iodine; care was taken to keep the apparatus and solvents under argon. Water used in bilayer experiments was distilled, Millpore-Q deionized and filtered through a 0.5 micron Teflon™ filter. Sephadex LH-20 was purchased from Pharmacia Biotech (Uppsala, Sweden). Sep-Pak C_{18} reverse-phase chromatography cartridges were purchased from Waters Ltd. (Watford, UK). Glass thin-layer chromatography plates were purchased from Whatman Inc. (Maidstone, UK). TLC plates were developed in various solvent systems, as indicated below . After development, spots were visualized by exposure to iodine vapor or, in the case of peptides,

chlorine-tolidine reagent which is based on the conversion of amines to chloramides (Stahl, 1965). Briefly, developed TLC plates were dried and exposed to a concentrated chlorine gas atmosphere for 10 minutes, then allowed to rest until no trace of chlorine remained on the plates. Plates were than sprayed with a solution of *o*-tolidine in dilute acetic acid; after a few minutes peptide containing spots turned purple to brown, depending on peptide concentration.

^{1}H and ^{13}C NMR analysis was conducted on a Bruker 200MHz nuclear magnetic resonance spectrometer using tetramethylsilane as an internal reference, see below for specific solvent mixtures used in analysis. Mass spectral samples were dissolved in 200 μl MeOH and a small portion (<1μl) applied to a sample slide, dried and then overlaid with 1μl of matrix solution (10 mg/ml α-cyano-4-hydroxycinnamic acid or 10 mg/ml sinapinic acid in 50% MeCN / 0.1% aqueous TFA). The dried sample spot was then washed with high grade water (2x 5μl) and then dried again before placing the slide in the mass spectrometer. Spectra were recorded on a Kratos MALDI III mass spectrometer in linear mode with negative ionization at threshold laser power and 20kV accelerating voltage. Calibration was internal with 1pmol/μl oxidized insulin B chain. If necessary, serial dilutions of the original sample in methanol were examined to obtain the best signal to noise response. Mass Spectroscopic analysis on small molecules was conducted using fast atom bombardment in either positive or negative ion mode on a VG Quadrapole Mass Spectrometer.

2.3. Synthesis of Ferrocene Derivatives

2.3.1. (N,N-Diphenyl)ferrocene Carboxamide. (N,N-Diphenyl)ferrocene Carboxamide was synthesized by Friedel-Crafts acylation according to the method of Little and Eisenthal (1960). Briefly, 23.1 grams (100 mmol) of [N,N-diphenyl]carbamyl chloride and 100 ml of dry, alcohol-free dichloroethane (distilled over P_2O_5) were rapidly stirred in a 3-neck flask

equipped with dropper funnel and nitrogen inlet. Then, 13.3 grams (100 mmol) of finely powdered aluminum chloride in 100 ml dichloroethane was slowly added, maintaining a nitrogen atmosphere. Once the aluminum chloride was completely added, a solution of 18.6 grams (100 mmol) ferrocene in 100 ml of dichloroethane was added over a 30 minute period. The solution was stirred under reflux for 18 hours, cooled and then quenched with 150 ml of distilled water. The resulting slurry was diluted with 300 ml dichloroethane followed by separation of the solvent layer. The aqueous phase was extracted with an equal volume of chloroform, solvent phases were combined and washed with equal volumes of 5% aqueous NaCl (w/v) until the pH of the aqueous phase increased to around 7.0. The solvent phase was dried over anhydrous sodium chloride. The resulting solution was rotary evaporated and dissolved in a small volume of chloroform then eluted from an alumna flash-chromatography column using chloroform/acetone 3:1 (v/v). The product eluted as a single orange band. Recrystallization from petroleum ether gave 36 grams of pure [N,N- Diphenyl]carbamyloxy ferrocene. 94% yield, based on ferrocene. TLC: R_f = 0.65 ($CHCl_3$, acetone 6:1 v/v).

2.3.2. <u>1'-Acetyl-1-(N,N-diphenyl)ferrocene Carboxamide</u>. 1'-Acetyl-1-(N,N-diphenyl)ferrocene carboxamide was synthesized by Friedel-Crafts acylation by slight modification of the method published by Little and Eisenthal (1960). Nineteen grams (50 mmol) of [N,N-Diphenyl]carbamyloxy ferrocene and 400 ml of dry, alcohol-free dichloroethane (distilled over P_2O_5) were rapidly stirred in a 3-neck flask equipped with dropper funnel and nitrogen inlet. Then, 7.3 grams (55 mmol) of finely powdered aluminum chloride was slowly added, maintaining a nitrogen atmosphere. Once the aluminum chloride completely dissolved, the mixture was cooled to 0° C and solution of 3.9 grams (50 mmol) acetyl chloride in 50 ml dichloroethane was added over a one hour period. The stirred solution was brought to room temperature over 30 minutes and stirred for an additional 2 hours, at which time the

reaction appeared complete by TLC ($CHCl_3$, acetone 6:1 v/v). The reaction was then quenched with 250 ml of distilled water. The resulting slurry was diluted with 100 ml each distilled water and CH_2Cl_2 followed by separation of the solvent layer. The aqueous phase was extracted with an equal volume of CH_2Cl_2, solvent phases were combined and dried over sodium chloride. The resulting solution was rotary evaporated and dissolved in a small volume of CH_2Cl_2 then eluted from an alumna flash-chromatography column using the same solvent. The product eluted as a single red-orange band. Recrystallization from CH_2Cl_2/hexane to gave 20.5 grams of pure 1'-acetyl-[N,N- diphenyl]carbamyloxy ferrocene. Yield 96 %, based on ferrocene. TLC: R_f = 0.58 ($CHCl_3$, acetone 6:1 v/v). IR: Amide-I band 1640υ; carbonyl stretch ketone 1740υ. MP 140° C. Positive ion FAB MS: 424.1 ($[M]^+$), 381.1 ($[M\text{-}COCH_3]^+$).

2.3.3. Ferrocene Acetic Acid *via* the Thiomorpholide. 1.3 Grams acetylferrocene (5.7 mmol) was dissolved in 4.0 ml dry dioxane (distilled over molecular sieves) and 10.0 ml morpholine (114 mmol). To this stirred solution 0.46 grams (14.4 mmol) elemental sulfur was added and the mixture refluxed under a nitrogen atmosphere for 18 hours. After cooling the solvents were removed *in vacuo*, leaving a black tar. The tar was suspended in a small amount of benzene and applied to a flash alumna chromatography column in the same solvent. Products were eluted with 2.0% (v/v) methanol in benzene to give eight fractions. After a failed attempt at crystallization from diethyl ether, fractions containing the putative product were dried *in vacuo* and each suspended in 50.0 ml 2N aqueous NaOH and refluxed for 4hr. The fractions were extracted with diethyl ether to remove non-carboxylic acid components then acidified with 6N HCl (to pH 5). A brown precipitate started to form in the solution soon after acidification and was collected by vacuum filtration. A number of attempts at recrystallization were made without success. The product was shown by IR to contain COOH but the yield (0.2 grams) was negligible. This approach was aborted.

2.3.4. Ferrocenecarboxylic Acid Methyl Ester from Ferrocenecarboxylic Acid. Ferrocenecarboxylic acid methyl ester was synthesized by methylation of ferrocenecarboxylic acid according to the method of Sonoda and Moritani (1971). 5 Grams (21.7 mmol) of ferrocenecarboxylic acid was dissolved in 50 ml of anhydrous methanol (distilled over I_2 and magnesium metal) and refluxed under a nitrogen atmosphere after adding 0.75 ml (14.7 mmol) concentrated sulfuric acid. After twenty four hours the reaction mixture was reduced to half of the original volume by rotary evaporation. Upon cooling, fine deep-red crystals of ferrocenecarboxylic Acid methyl ester formed. TLC analysis indicated a nearly quantitative yield in the methylation. TLC: R_f = 0.3, carboxylic acid R_f = 0 ($CHCl_3$). This material was used without further purification. Yield, 5 grams (94%).

2.3.5. Ferrocenecarboxylic Acid Methyl Ester from Acetyl Ferrocene. A reported adaptation of the Willegerodt-Kindler reaction (Myrboh *et al.*, 1981) was employed in attempts to convert acetylferrocene directly to ferrocenearboxylic acid methyl ester. 2.15 Grams acetylferrrocene (94 mmol) was dissolved in 10 ml MeOH along with 10 ml boron trifluoride etherate (79 mmol) in an addition funnel, the solution was added over 5 minutes to a vigorously stirred suspension of 4 grams (90 mmol) anhydrous lead (IV) tetraacetate in 50 ml benzene. The reaction quickly went from bright red to dark brown, presumably due to oxidation. After five hours stirring at room temperature the suspension was poured into 150 ml aqueous sodium bicarbonate (5% w/v) and diluted further with 100 ml benzene. The solvent phase was then washed with equal volumes of saturated aqueous sodium chloride and 5% w/v sodium dithionite followed by drying with anhydrous sodium sulfate. TLC analysis ($CHCl_3$:acetone 9:1 v/v) indicated that only a small amount (app. 10%) of the desired product was formed as compared to authentic standard; it

also appears that little starting remains after the reaction, but rather a number of more polar side products.

2.3.6. Ferrocenecarboxylic Acid Chloride. **METHOD A**: The original reported method for the formation of ferrocenecarboxylic acids (Lau & Hart, 1959) here employed. Briefly, 5 grams (22 mmol) ferrocene carboxylic acid was dried *in vacuo* over P_2O_5 overnight and then dissolved in 50 ml dry toluene in a flame dried flask equipped with magnetic stirrer, condenser, nitrogen inlet and addition funnel. To this solution was added 5 grams of phosphorus pentachloride (24 mmol) dissolved in 10 ml dry toluene over 10 minutes. After one hour stirring at room temperature the solution was transferred to a round bottom flask and solvents rotary evaporated (a column of Drierite was placed between the aspirator and the main chamber of the rotary evaporator to minimize exposure of the product to water vapor). The red oil was repeatedly evaporated with small quantities of benzene until no toluene or $PCl_5/POCl_3$ remained. The product was recrystallized from petroleum ether (BP 60-80°C) as dark red crystals. Yield, 4.6 grams (82 %), MP 50°C. **METHOD B**: Ferrocene carboxylic acid, 5 grams (22 mmol) was dried *in vacuo* over P_2O_5 overnight and then dissolved in 100 ml dry benzene in a flame dried flask equipped with magnetic stirrer, condenser, nitrogen inlet and addition funnel. A solution of 3.3 grams (28 mmol) of thionyl chloride dissolved in 20 ml dry benzene was then added followed by refluxing for 1 hour. The solution was transferred to a round bottom flask and work-up and crystallization proceeded as described in method A. Yield, 4.9 grams (93%), MP 49°C.

2.3.7. Hydroxymethylferrocene. Hydroxymethylferrocene was synthesized by metal hydride reduction of ferrocenecarboxylic acid methyl ester according to the method of Sonoda and Moritani (1971) with stiochometric modification. Lithium aluminum hydride (0.76 grams, 20 mmol) was cautiously added to 50 ml dry tetrahydrofuran in a three-neck

flask equipped with a condenser, drying tube and addition funnel. Then, 3.65 grams (14.9 mmol) ferrocenecarboxylic acid methyl ester dissolved in 25 ml dry benzene was added over 30 minutes with rapid stirring. The solution was then stirred under reflux until no starting material remained (usually 2 hours) as monitored by TLC ($CHCl_3$, acetone 6:1 v/v). The mixture was cooled to room temperature then an additional 100 ml of benzene was added followed by the cautious addition of 50 ml distilled water. The solvent phase was collected and washed twice again with distilled water, dried over anhydrous sodium chloride and used without purification. Yield, 3.1 grams (97%) of a bright yellow solid. TLC: R_f = 0.4 ($CHCl_3$, acetone 6:1 v/v). IR: alcohol C-O stretch 1045υ.

2.3.8. **Chloromethylferrocene**. Five grams (23 mmol) of hydroxymethylferrocene, dried *in vacuo* over P_2O_5 was dissolved in 120 ml dry THF and 2.6 ml dry pyridine (32 mmol) in a 3-neck flask equipped with a dropper funnel condenser and nitrogen inlet. To this stirred solution was added 3.4 grams (25 mmol) of phosphorus trichloride over 20 minutes; the reaction was slightly exothermic. The reaction was stirred for three hours after addition of the chlorinating agent, leaving a clear orange solution with a whitish brown residue. The solvent was poured into a round bottom flask and the residue washed with THF. The combined solutions were rotary evaporated, leaving a yellow solid. Recrystallization from hexane gave 4.2 grams product (79 %). TLC: R_f = 0.8 ($CHCl_3$, acetone 6:1 v/v). IR: C-Cl stretch 725υ. MP 77°C.

2.3.9. **Cyanomethylferrocene**. Fifteen grams of potassium cyanide was dissolved in 35 ml distilled water in an argon flushed 2-neck flask equipped with a dropper funnel and ice bath. chloromethylferrocene (4.0 grams, 17.2 mmol) was dissolved in 125 ml THF and 45 ml DMSO was slowly added with rapid stirring. After the addition the solution was brought to room temperature and stirred vigorously for 1.5 hours. The mixture was diluted with 200 ml each of THF and saturated aqueous

NaCl. The THF layer was collected and extracted three times with equal volumes of saturated aqueous NaCl and finally dried over sodium sulfate. After rotary evaporation the material was recrystallized twice from hexane to give 3.8 grams yellowish powder (97 %). TLC: R_f = 0.76 ($CHCl_3$, acetone 6:1 v/v). IR: CN stretch 2260υ. ^{1}H-NMR δ ($CDCl_3$): 3.56 (s, 2H, CH_2).

2.3.10. **Ferrocene Acetic Acid**. Cyanomethylferrocene (3.5 grams, 15.5 mmol) was suspended in 80 ml EtOH and 40 ml water, then 1.8 grams of dry powdered sodium hydroxide was then added under a blanket of argon. The suspension was refluxed until the evolution of NH_3 ceased (monitored with a mineral oil bubble meter) which took approximately 40 minutes both times this reaction was conducted. After cooling the mixture to room temperature the mixture was poured into 500 ml of 3N HCl, after cooling in ice for 30 minutes fine red crystals precipitated. The crude crystals were dissolved in 200 ml of saturated sodium bicarbonate followed by acidification with 6N HCl; soon after fine plate-like orange crystals precipitated from the solution- these were collected and dried in vacuo over P_2O_5 to give 3.2 grams (73 %) of the desired product. TLC: R_f = 0.1 ($CHCl_3$, MeOH 10:1 v/v). IR: C=O stretch 1740υ. MP 161°C. ^{1}H-NMR δ ($CDCl_3$, CD_3OD 6:1 v/v): 3.98 (2 peaks, 9H, Fc), 3.97 (s, 2H, $C\underline{H_2}$).

2.3.11. **Ferroceneacetic Acid Chloride**. Ferroceneacetic acid (0.5 grams, 1.97 mmol) was dried overnight in vacuo over P_2O_5 and then dissolved in 10 ml dry benzene. The solution was cooled to 4°C and 1.1 grams (8 mmol) oxalyl chloride was added dropwise and the solution was slowly brought to room temperature. After 1 hour stirring under nitrogen the solution was transferred to a round bottom flask and rotary evaporated (a column of Drierite was placed between the aspirator and the main chamber of the rotary evaporator to minimize exposure of the product to water vapor). The red-brown semi-solid was then recrystallized from petroleum ether (80-100°C BP) as thick plates, yielding 0.42 grams

(78 %) of the desired product. IR: C=O stretch acyl chloride 1810υ. MP 116°C.

2.3.12. Ferroceneacetic Acid Fluoride. This acid fluoride was generated and used, without isolation for the N-terminus derivitization of resin-bound alamethicin analogs. Ferroceneacetic acid (0.15 grams, 0.59 mmol) was dissolved in 5 ml dry DMF and 2ml freshly distilled DIPA, to the stirred solution was added 1.05 equivalents of TFFH with continued stirring under nitrogen. TLC analysis (R_f = 0.45 $CHCl_3$, acetone 6:1 v/v) indicates that complete conversion occurs within 2-3 minutes. The entirety of the above solution is then added to a container containing 200-250 milligrams of peptide-bound resin pre-swollen with a minimum quantity (≈ 0.5 ml) of DMF, see solid-phase synthesis methodology for more details.

2.3.13. Ferrocene-1,1'-dicarboxylic Acid Dimethyl Ester. Ferrocene-1,1'-dicarboxylic acid dimethyl ester was synthesized by methylation of 1,1'-bis(carboxy)ferrocene according to the method of Sonoda and Moritani (1971) with minor modification. 5 grams (18.25 mmol) of 1,1'-bis(methylcarboxy) ferrocene was dissolved in 50 ml of anhydrous methanol and refluxed under a nitrogen atmosphere after adding 0.75 ml (14.7 mmol) concentrated sulfuric acid. After 22 hours, the reaction mixture was concentrated to half of the original volume by rotary evaporation. Upon cooling fine deep-red crystals of 1,1'-bis(methylcarboxy)ferrocene formed. TLC analysis indicated a nearly quantitative yield in the methylation. TLC: R_f = 0.3 (monomethyl ester R_f = 0.1, dicarboxylic acid R_f = 0) ($CHCl_3$ two consecutive developments). This material (5.05 grams, (96%)) was used without further purification. IR: C=O ester stretch 1700υ. MP 114°C.

2.3.14. Ferrocene-1,1'-dicarboxylic Acid dichloride. **METHOD A**: As with ferrocenecarboxylic acid chloride, the original reported method for

the formation of ferrocenecarboxylic acids (Lau & Hart, 1959) was used. Briefly, 1 gram (4.35 mmol) ferrocene-1,1'-dicarboxylic acid was dried *in vacuo* over P_2O_5 overnight and then dissolved in 15 ml dry toluene in a flame dried flask equipped with magnetic stirrer, condenser, nitrogen inlet and addition funnel. To this solution was added 2.5 grams of phosphorus pentachloride (12 mmol) dissolved in 2 ml dry toluene over 10 minutes. After three hours stirring at room temperature the solution was transferred to a round bottom flask and solvents rotary evaporated (a column of Drierite was placed between the aspirator and the main chamber of the rotary evaporator to minimize exposure of the product to water vapor). The red oil was repeatedly evaporated with small quantities of benzene until no toluene or $PCl_5/POCl_3$ remained. The product was recrystallized from petroleum ether (BP 60-80° C) as dark red crystals. Yield, 0.72 grams (68 %). IR: C=O stretch acid chloride 1795υ. **METHOD B**: Here the bis-acid chloride was prepared using phosphorus trichloride according to the method of Nesmeyanov and Reutov (1958). Ferrocene-1,1'-dicarboxylic acid (2 grams, 8.7 mmol) was dried *in vacuo* over P_2O_5 overnight and then dissolved in 30 ml dry toluene in a flame dried flask equipped with magnetic stirrer, condenser, nitrogen inlet and addition funnel. To this solution was cautiously added 2.2 grams of phosphorus trichloride (16.1 mmol) dissolved in 5 ml dry toluene over 10 minutes. After gently heating the solution to 60° C for two hours the solution was transferred to a round bottom flask and processed as with method A. Yield 0.88 grams (86 %). IR: C=O stretch acid chloride 1795υ.

2.3.15. <u>Ferrocene-1,1'-dicarboxylic Acid Anhydride</u>. The method of Nesmeyanov and Reutov (1958) was used to make the anhydride of Ferrocene-1,1'-dicarboxylic acid. Although these conditions yield one anhydride product it is not clear if it is the *intra*molecular anhydride or the anhydride formed from 2 molecules of the ferrocene-1,1'-dicarboxylic Acid reacting to form a bis(anhydride). The evidence cited in the original manuscript gives a cryoscopically determined MW of 556 and 528 (two

different trials) and states that 3 reaction products are obtained when one reacts the product with aqueous ammonia, the *intra*molecular anhydride would give only one product. Based on the analysis given, one might surmise that the majority of the product is the bis(anhydride) with varied but minor contamination by the *intra*molecular anhydride. Ferrocene-1,1'-dicarboxylic acid dichloride (1.4 Grams 5 mmol) was dissolved in 8 ml of dry chloroform and added dropwise to a stirred solution of 1.9 grams distilled pyridine (25 mmol). Water, 0.6 ml was then added dropwise to the solution with very vigorous stirring. Ten minutes after the addition the solution was allowed to stand for 12 hours. The reaction mixture was then poured into 100 ml of 2% v/v (relative to concentrated (12M) HCl), the solvent was then collected and washed with a 5% w/v solution of sodium bicarbonate. Finally, solvents were removed by rotary evaporation, the yellowish residue was then washed with dry Et_2O, dissolved in a minimum amount of warm ethylene dichloride and recrystallized from nitromethane. Yield, 1.15 grams (82 %), MP 234° C. IR: C=O stretch anhydride 1825υ, C-O-C bend 1220υ.

2.3.16. **1,1'-Bis(hydroxymethyl)ferrocene**. 1,1'-Bis(hydroxymethyl) ferrocene was synthesized by metal hydride reduction of 1,1'-bis(carboxymethyl) ferrocene according to the method of Sonoda and Moritani with minor modification. Lithium aluminum hydride (0.75 Grams, 9.8 mmol) was added to 50 ml dry tetrahydrofuran in a three-neck flask equipped with a condenser, drying tube and addition funnel. Then, 4.5 grams (14.9 mmol) 1,1'-bis(carboxymethyl) ferrocene dissolved in 30 ml dry benzene was added over 30 minutes, with rapid stirring. The solution was then stirred under reflux until no starting material remained (usually 2 hours) as monitored by TLC ($CHCl_3$, acetone 6:1 v/v). The mixture was cooled to room temperature then diluted with an additional 100 ml of benzene followed by the cautious addition of 50 ml ice-cold distilled water. The solvent phase was collected and washed twice again with distilled water, dried over anhydrous sodium chloride and used without

purification. TLC: R_f = 0.2 (monomethyl ester R_f = 0.4-0.45, dicarboxylic ester R_f = 0.8) ($CHCl_3$, acetone 6:1 v/v). IR: alcohol C-O stretch 1040υ. MP 107°C.

2.3.17. 1,1'-Bis(chloromethyl)ferrocene. Three grams (12.3 mmol) of 1,1-bis(hydroxymethyl)ferrocene, dried *in vacuo* over P_2O_5 was dissolved in 75 ml dry THF and 0.6 ml dry pyridine (7.7 mmol) in a 3-neck flask equipped with a dropper funnel condenser and nitrogen inlet. To this stirred solution was added 1.5 grams (10.9 mmol) of phosphorus trichloride over 20 minutes, the reaction was slightly exothermic. The reaction was stirred for five hours after addition of the chlorinating agent, leaving a clear orange solution with a whitish brown residue. The solvent was poured into a round bottom flask and the residue washed with THF. The combined solutions were rotary evaporated, leaving a yellow semi-crystalline residue. Recrystallization from hexane gave 2.4 g product (68 %). TLC: R_f = 0.74 ($CHCl_3$, Acetone 6:1 v/v). IR: C-Cl stretch 725υ. MP 97°C. The product decomposes completely after one month stored dry at 4°C.

2.3.18. 1,1'-Bis(cyanomethyl)ferrocene . Ten grams of potassium cyanide was dissolved in 20 ml distilled water in an argon flushed 2-neck flask equipped with a dropper funnel and ice bath. 1,1'-Bis(chloromethyl)ferrocene (2.0 grams, 7.1 mmol) was dissolved in 70 ml THF and 20 ml DMSO was slowly added with rapid stirring. The solution was stirred vigorously for 1.5 hours after the addition was complete. The mixture was diluted with 100 ml each of THF and saturated aqueous NaCl. The THF layer was collected and extracted three times with equal volumes of saturated aqueous NaCl and finally dried over sodium sulfate. After rotary evaporation the material was recrystallized twice from hexane to give 1.4 grams of yellow crystalline product (74 %). TLC: R_f = 0.65 ($CHCl_3$, acetone 6:1 v/v). IR: C≡N stretch 2260υ. MP 97°C.

2.3.19. 1,1'-Bis(cyanomethyl)ferrocene from 1,1-bis(hydroxymethyl) ferrocene. Direct conversion of the diol to the bis-nitrile was accomplished by modification of the method of Davis and Untch (1981), albeit with inconsistent results. 1,1-Bis(hydroxymethyl)ferrocene (0.25 grams, 1.0 mmol) was dissolved in 10 ml dry THF in a flame dried flask equipped with a dropper funnel an nitrogen inlet. To this solution was added 0.66 grams (4 mmol) finely powdered anhydrous potassium iodide followed by the dropwise addition of 0.44 grams (4 mmol) trimethylsilyl chloride in 2 ml dry THF. After stirring at room temperature for 4 hours the reaction mixture was added dropwise to another reaction vessel containing 20 ml each of dry acetonitrile and DMF and 0.7grams of potassium cyanide. After three hours stirring under nitrogen the reaction mixture was diluted with 50 ml THF and poured into 100 ml aqueous saturated NaCl. The solvent phase was collected and extracted again with an equal volume of aqueous saturated NaCl. After rotary evaporation the brownish-yellow material was recrystallized from hexane to give 0.12 grams and 0.14 grams (on a second attempt) yellow powder (52 & 56%, respectively). TLC: R_f = 0.65 and 0.54 (possibly the OH/CN intermediate) ($CHCl_3$, acetone 6:1 v/v).

2.3.20. Ferrocene-1,1'-bis(acetic Acid). 1,1'-Bis(cyanomethyl)ferrocene (1.6 grams, 6.1 mmol) was dissolved in 10 ml EtOH and 10 ml water, 1.6 grams of dry, powdered sodium hydroxide was then added under a blanket of argon. The crimson colored mixture was refluxed until the evolution of NH_3 ceased (monitored with a mineral oil bubble meter) which took 20 minutes both times this reaction was conducted. After cooling the mixture to room temperature the mixture was poured into 20 ml of 3N HCl, after standing for 30 minutes fine brown-red crystals precipitated along with a small amount of black tar which proved impossible to separate from the product. Thus, the crude crystals were dissolved in 30 ml of saturated sodium bicarbonate followed by acidification with 6N HCl, soon after fine plate-like orange crystals

precipitated from the solution, these were collected and dried in vacuo over P_2O_5 to give 1.2 grams (66%) of the desired product. TLC: R_f = 0.05 ($CHCl_3$, Acetone 6:1 v/v, with trace of HOAc). IR: carboxylic acid carbonyl 1740υ. MP 145°C. Positive ion FAB MS: 302.1 ($[M]^+$), 257.1 ($[M-COOH]^+$), 244 ($[M-CH_2COOH]^+$).

2.3.21. **Ferrocene-1,1'-bis(acetic Acid Chloride)**. Ferroceneacetic acid (0.26 grams, 0.87 mmol) was dried overnight in vacuo over P_2O_5 and then dissolved in 5 ml dry benzene. The solution was cooled to 4°C and 1.14 grams (9 mmol) oxalyl chloride was added dropwise and the solution was slowly brought to room temperature. After 1 hour stirring under nitrogen, the solution was transferred to a round bottom flask and rotary evaporated (a column of Drierite was placed between the aspirator and the main chamber of the rotary evaporator to minimize exposure of the product to water vapor). Recrystallization from hexane/Et_2O gave 0.21 grams (69 %) of the desired product. IR: C=O stretch acid chloride 1790υ.

2.3.22. **Ferrocene-1,1'-bis(Acetic Acid) Anhydride**. Ferrocene-1,1'-bis(acetic acid) (0.3 grams, 1.1 mmol) was dissolved in 50 ml dry $CHCl_3$ along with 0.01 grams of 4-DMAP (0.08 mmol). The solution was stirred under nitrogen while 0.23 grams (1.4 mmol) of 1,1-carbonyldiimidazole in 3 ml $CHCl_3$ was added dropwise to the solution over a 30 minute period. TLC analysis ($CHCl_3$, Acetone 6:1) indicates the formation of 3 to 4 products in addition to the imidazoline byproduct. IR analysis of the crude product, a red semi-solid, shows very strong absorbence in the anhydride fingerprint region (1810-1790, 1300-1050υ). This methodology was abandoned because of difficulties in characterization and purification, as the crude product failed to crystallize from a number of solvents.

2.3.23. Ferrocene(α-keto)butyric Acid and Ferrocene-1,1'-bis((α-keto)butyric Acid). These compounds were synthesized by Friedel-Crafts acylation modifying the method of Little and Eisenthal (1959). Vacuum dried ferrocene (21 grams, 113 mmol) and 500 ml dry, alcohol-free dichloroethane were rapidly stirred in a 3-neck flask equipped with dropper funnel, nitrogen inlet and mechanical propeller stirrer. Then, 29.3 grams (220 mmol) of finely powdered aluminum chloride was slowly added, maintaining a nitrogen atmosphere. Once the aluminum chloride completely dissolved, the mixture was cooled to 0°C and solution of 22 grams (220 mmol) succinic anhydride in 150 ml of dichloroethane was added over a one hour period. The stirred solution was brought to room temperature over 30 minutes and stirred for an additional 6 hours. During this time the ferrocenic compounds formed a black tarry mass on the propeller, leaving a nearly clear yellowish solution. The reaction was quenched with 800 ml saturated aqueous sodium dithionite. After 10 minutes of vigorous stirring the tar dissolved, leaving a thick orange suspension which was diluted with 500 ml of CH_2Cl_2. The solvent layer was collected and the aqueous layer was back-extracted with an equal volume of CH_2Cl_2 , the combined solvents were combined and dried over sodium sulfate and dried by rotary evaporation. The orange solid was dissolved in a small volume of CH_2Cl_2:MeOH 20:1 (v/v) then eluted from an alumna flash-chromatography column using the same solvent. The products eluted as two separate red-orange bands. The band to elute first corresponds to the monoacylated product, ferrocene(α-keto)butyric acid; the second, more polar band, corresponds to ferrocene-1,1'-bis(α-keto)butyric acid. Recrystallization of ferrocene(α-keto)butyric acid from EtOH/Et_2O gave 4.0 grams (12 %) of product. IR: C=O stretch ketone 1666υ. ^{1}H-NMR δ ($CDCl_3$, CD_3OD 2:1 v/v): 3.98 (2 peaks, 9H, Fc), 2.95 $CH_2C\underline{H}_2COOH$ (t, 2H), 2.60 $ArCO\text{-}C\underline{H}_2CH_2COOH$ (t, 2H).. Positive ion FAB MS: 286.1 ($[M]^+$), 257.1 ($[M\text{-}COOH]^+$), 244 ($[M\text{-}CH_2COOH]^+$). Recrystallization of ferrocene-1,1'-bis(α-keto)butyric acid from EtOH/Et_2O gave 15.4 grams (57 %) of product. IR: C=O stretch ketone 1660υ. ^{1}H-

NMR δ ($CDCl_3$, CD_3OD 1:1 v/v): 3.98 (2 peaks, 9H, Fc), 3.05 $CH_2C\underline{H}_2COOH$ (t, 4H), 2.61 $ArCO\text{-}C\underline{H}_2CH_2COOH$ (t, 4H). Positive ion FAB MS: 386.0 ($[M]^+$), 369.1 ($[M\text{-}H_2O]^+$), 329.1 ($[M\text{-}CH_2COOH]^+$). Negative ion FAB MS: 385.1 ($[M\text{-}1]^-$).

2.3.24. (N,N-Dimethyl)aminomethylferrocene. Ferrocene (20.0 grams, 107 mmol) was dissolved in 175 ml glacial acetic acid and 16 grams concentrated phosphoric acid in a three neck flask equipped with condenser, addition funnel and nitrogen inlet. 16 Grams (160 mmol) of methylenebis(dimethyl)amine was added in one portion, followed by heating of the reaction flask in a boiling water bath for 12 hours. After cooling the mixture was poured into 250 ml distilled water and extracted twice with 100 ml portions of Et_2O to remove any trace of unreacted ferrocene. The aqueous phase was then brought to pH = 8 with aqueous NaOH and extracted three times with equal volumes of Et_2O. The solvents were pooled, dried over NaCl and evaporated to give 22.5 grams (92 %) of the desired product which was quarternized without further purification. IR: methyl C-H stretch 1375υ. MP 115°C.

2.3.25. (Ferrocenylmethyl)trimethylammonium Iodide. (N,N-Dimethyl)aminomethylferrocene (22 Grams, from 2.3.24) was dried *in vacuo* over P_2O_5 overnight then dissolved in 500 ml dry benzene, the solution was stirred under argon while methyl iodide (≈ 35 grams, 250 mmol) was added dropwise. After the first third of the methyl iodide was added the desired product began precipitating as yellow-orange crystals, these were collected after 15 min, dried *in vacuo* giving 23.1 grams of the desired product. IR: methyl C-H stretch 1360υ. MP 225°C, decomposes. ^{1}H-NMR δ (D_2O): 2.8 (s, $(C\underline{H}_3)_3N$, 9H).

2.3.26. Diethyl(ferrocenylmethyl)formamidomalonate. Sixty-six mmoles of diethylformamidomalonate anion was generated as the sodium salt by dissolving 10.6 grams (66 mmol) diethylformamidomalonate in 150

ml anhydrous EtOH in which 0.6 grams sodium metal had been dissolved, taking care to maintain an anhydrous argon atmosphere. The salt, (ferrocenylmethyl)trimethylammonium iodide (11 grams, 26 mmol) dissolved in 60 ml anhydrous EtOH was added dropwise to the malonate ion followed by refluxing for 22 hours. The reaction mixture was cooled to room temperature and poured into 300 ml water; the resulting slurry was extracted three times with 150 ml potions of Et_2O. The pooled solvents were dried over NaCl and rotary evaporated to give a red oil. Recrystallization from ethanol gave 6.4 grams (62 %, based on the ferrocenemethylamine) of the desired product as a yellow-orange powder. MP 90°C. ^{1}H-NMR δ ($CDCl_3$): 3.7 (s, $COOC\underline{H}_3$, 6H), 8.1 (s, $N\underline{H}CO$, 1H), 2.9 (m, $ArC\underline{H}_2$- ,2H). ^{13}C-NMR δ ($CDCl_3$): 172 ($R\underline{C}OOMe$), 55 ($CH_2\underline{C}(COOMe)_2NHCOH$). Positive ion FAB MS: 397.0 ($[M]^+$), 373.1 ($[M-COH]^+$), 258.1 ($[Fc-CH_2]^+$).

2.3.27. [+/-]-(Ferrocenyl)alanine {α-Amino-β-Ferrocenylpropionic Acid}. Diethyl-(ferrocenylmethyl)formamidomalonate (3 grams, 7.5 mmol) was refluxed in 160 ml of 6N aqueous HCl for 45 minutes. The cooled solution was evaporated under reduced pressure to give yield the crude product as the hydrochloride salt. Titration with 0.1M NaOH to pH≈7 led to the precipitation of the amino acid as a yellow-orange powder. Yield, 1.1 grams (52 %). TLC: R_f = 0.42 (*n*-BuOH, AcOH, H_2O 7:1:1 (v/v)). MP 290°C ^{1}H-NMR δ (CD_3OD): 2.65 (m, $FcCH_2C\underline{H}R_2$, 1H), 2.85 (m, $FcC\underline{H}_2CHR_2$,2H). Positive ion FAB MS: 272.0 ($[M]^+$).

2.3.28. 1,1'-Bis(4-amino)propanoyl)ferrocene Amide. Ferrocene-1,1'-dicarboxylic acid dichloride (0.62 grams, 2 mmol) was dissolved in 25 ml anhydrous THF and 3 ml TEA in a flask equipped with a nitrogen inlet and addition funnel. Propane-1,3-diamine (0.88 Grams,14 mmol) was added in one portion with rapid stirring. After one hour the solvents were removed by rotary evaporation followed by repeated rotary evaporation of small aliquots (≈20ml) of toluene. Vacuum desiccation of the red oil over

P_2O_5 for 72 hours proved sufficient to remove traces of unreacted diamine. The putative diamine was purified by flash chromatography on basic alumna using CH_2Cl_2 as a solvent. A single red-orange band was collected and dried to give 0.71 grams an oil which failed to solidify or crystallize under a number of different conditions. TLC: R_f = 0.8 (acetone, TEA 20:1 v/v) NMR analysis indicates the presence of [-C<u>H</u>$_2$NH$_2$] at 2.85δ and [FcCONHC<u>H</u>$_2$-] at 3.4δ. IR analysis also indicates the presence of amide (amide I and II) as well as amine. Attempted isolation of product as a free base as well as a solid (di)hydrochloride salt failed. Positive ion FAB MS: 387.1 ($[M]^+$), 330 ($[M-(CH_2)_3NH_2]^+$).

2.3.29. <u>1,1'-Bis((6-amino)hexanoyl)ferrocene Amide</u>. The method used for the synthesis of 1,1'-bis(4-amino)propanoyl)ferrocene amide was employed, substituting a stiochometric quantity of hexane-1,6-diamine for propane-1,3-amine. Similar inconclusive results were obtained with this reaction. Positive ion FAB MS: 429.6 ($[M]^+$).

2.3.30. <u>1,1'-Bis(piperazineoyl)ferrocene Amide</u>. The method used for the synthesis of 1,1'-bis(4-amino)propanoyl)ferrocene amide was used, substituting piperazine for propane-1,3-amine. Inconclusive results were obtained with this reaction, as product(s) were also difficult to purify and characterize. ^{1}H-NMR δ (CD_3OD): 2.95 (m, CONC<u>H</u>$_2$CH$_2$). Positive ion FAB MS: 411.2 ($[M]^+$), 391.5 ($[M-H_2O]^+$?) 240.2 ($[Fc(CO)_2]^+$).

2.4. Solution-Phase Synthesis of Ferrocenoyl Peptides

2.4.1. <u>C-terminus Ferrocenoyl Alamethicin</u>. The following synthesis is based on an adaptation of the published method of Woolley *et al.* (1994). Alamethicin (7.5 mg, 3.6 μmol), 4-DMAP (10 mg, 82 μmol) and ferrocenoic anhydride (125 mg, 264 μmol) were dissolved in 1.2 ml dry DMF and 0.5 ml pyridine. The mixture was stirred overnight under a

nitrogen atmosphere. The reaction was quenched by the addition of 1.8 ml distilled water in small portions. After stirring for a short period a precipitate formed which was removed by centrifugation. The entire reaction mixture was applied to an LH-20 gel filtration column (2 x 30 cm), eluted with methanol at a flow rate of 10 ml/min and monitored for absorbance at 260 ηm. The first peak to elute was collected and solvents removed by rotary evaporation. The residue was dissolved in MeCN and loaded onto a Sep-Pak cartridge. The cartridge was then washed with 5 ml water followed by elution of peptide with 15 ml MeCN. The eluent was dried and the above process repeated. The resulting residue was dissolved in acetonitrile and purified by reverse phase HPLC (Zorbax C_{18}, using a linear gradient of H_2O/MeCN, starting at 91:9 H_2O/MeCN (v/v) and ending at 10:90 H_2O/MeCN (v/v)). Using a flow rate of 2.0 ml/min, the desired product eluted at 95 min. The product migrates as one spot on TLC, R_f = 0.7 compared to Alamethicin R_f = 0.4 ($CHCl_3$, MeOH, H_2O 65:25:2 v/v/v); Negative ion LDMS: 2187.4 ($[M-H]^-$) , 2173.1 ($[M-H_2O]^-$), 2070.9 ($[M - FeC_5H_5]^-$).

2.4.2. <u>C-terminus (1'-Carboxy)ferrocenoyl Alamethicin</u>. During the course of our investigations a simpler method for the synthesis and purification of the peptides was developed and used to make the following compound. Ferrocene-1,1'-dicarboxylic acid dichloride (100 mg, 321.7 μmol) and alamethicin (10 mg, 4.8 μmol, stored *in vacuo* over P_2O_5) were combined in a flame-dried screw-capped tube (with Teflon™ septum) with a stirring bar, followed by the addition of 1 ml dry pyridine. The reaction mixture was vigorously stirred under argon for 36 hours, at which time only a trace of starting material remained. The reaction was quenched with 0.5 ml water and stirred for an additional 4 hours. To reduce any ferrocenic compounds that may have oxidized during the course of the reaction 0.2 ml of concentrated aqueous sodium dithionite was added. The solvents were removed under a stream of nitrogen followed by *in vacuo* removal any remaining volatiles. The mixture was

suspended in 1-2 ml methanol and applied to a Sephadex LH-20 column (2 x 30 cm) equilibrated in methanol. Products were eluted with methanol (acidified with 1% HOAc, gravity flow, ~ 5 ml/min) taking 2 ml fractions. The peptide containing fractions were pooled, concentrated and reapplied to an LH-20 column (1.5 x 20 cm) and eluted with the same solvent (gravity flow, ~ 4 ml/min) collecting 1ml fractions. The desired product eluted as a single band having an R_f = 0.3, compared to alamethicin R_f = 0.45 ($CHCl_3$, MeOH, H_2O, HOAc 70:30:3:2 v/v/v/v). Negative ion LDMS: 2219.7 ([M-H] $^-$), 2059.2 ([M -FeC_5H_4COOH]$^-$). Pyridine was found to have a deleterious effect on chromatographic separation of the peptides using LH-20.

2.4.3. C-terminus (Ferrocene)acetyl Alamethicin. Ferroceneacetic acid chloride (100 mg, 394 μmol) and alamethicin (10 mg, 4.8 μmol, stored *in vacuo* over P_2O_5) were combined in a flame-dried screw-capped tube (with Teflon™ septum) with a stirring bar, followed by the addition of 1 ml dry pyridine. The reaction mixture was vigorously stirred under argon for 36 hours, at which time only a trace of starting material remained, as evidenced by TLC. The reaction was quenched with 0.5 ml water and stirred for an additional 2 hours. Concentrated aqueous sodium dithionite (0.2 ml) was added and the solvents were removed under a stream of nitrogen followed by *in vacuo* removal of remaining volatile materials. The mixture was suspended in 1-2 ml methanol and applied to a Sephadex LH-20 column (2 x 30 cm) equilibrated in methanol. Products were eluted with methanol (gravity flow, ~ 5 ml/min) taking 2 ml fractions. The peptide containing fractions were pooled, concentrated and reapplied to an LH-20 column (1.5 x 20 cm) and eluted with the same solvent (gravity flow, ~ 4 ml/min) collecting 1ml fractions. The desired product eluted as a single band having an R_f = 0.4, compared to alamethicin R_f = 0.45 ($CHCl_3$, MeOH, H_2O, HOAc 70:30:3:2 v/v/v/v). Negative ion LDMS: 2201.6 ([M-H]$^-$).

2.5. Solid-Phase Synthesis of Alamethicin and Melittin Derivatives

2.5.1 HOOC-Alamethicin. The methodology described by Wenschuh *et al.* (1995) for the synthesis of ALM was adapted for the synthesis of C-terminus carboxyl alamethicin derivatives. Here, the standard carboxyl activation methodology is replaced by the in situ generation of the highly reactive acid fluorides. An automated peptide synthesizer from Perceptive Biosystems with version 1.12 Software was employed in all alamethicin analog synthesis.

The first target peptide has the following amino acid sequence:

AcNH-U-P-U-A-U-A-Q-U-V-U-G-L-U-P-V-U-U-Q-Q-F-COOH

Briefly, 0.525 grams (0.10 milliequivalents) of PEG-PS resin pre-loaded with Fmoc-phenylalanine was swollen for 1 hour in DMF and placed in the peptide synthesis apparatus. The following protocol was employed, all flow rates set at 3 ml/min:

1- **Deprotect** for 11 minutes with 25% v/v piperidine in DMF. Loop volume 5 ml.
2- **Wash** resin with 20 ml DMF.
3- **Pre-activate** Fmoc amino acid with fluorinating agent TFFH for 3 minutes.
4- **Couple** Fmoc-amino acid fluoride with resin-linked peptide. A total volume of 5 ml of 0.3 molar acid fluoride and 0.6 M DIPA in DMF was reacted with resin for 30 minutes or 1 hour for couplings with Fmoc-U-COF.
5- **Wash** resin with 20 ml DMF.
6- **Go to step 1** until end of sequence, then
7- **Deprotect**, as above.
8- **Wash** resin with 20 ml DMF.

9- **Acetylate** N-terminus with 10 ml Ac_2O/DIEA/DMF 1:2:7 v/v/v.

10- **Wash** resin with 20 ml DMF.

The resin is then collected from the peptide synthesizer and desolvated by washing with the following sequence of solvents using a peristaltic pump: MeOH then Et_2O followed by petroleum ether (60°C BP). Dry resins were stored under P_2O_5 desiccation at 4°C. Decoupling the peptides from the resin proved to be exceedingly difficult. Treatment of the resin with 1M tetrafluoroboric acid in TFA:CH_2Cl_2 (3:2 v/v) at 4°C for one hour is the only deprotection condition that proved successful for this peptide as well as the N-Terminus (Ferrocene)acetamido-HOOC-alamethicin. Tetrafluoroboric acid was first described for the purpose of peptide-resin decoupling by Kiso *et al.* (1989). The peptide containing reagent was separated from the PEG-PS resin by filtration and washing with CH_2Cl_2, the solvents were then rotary evaporated to leave a yellow oil. The entirety of the crude peptide containing oil was placed in a minimum amount of HPLC solvent mixture B (MeCN/H_2O 8:2 (v/v) acidified with 0.1% TFA). HPLC purification was conducted on a reverse phase Zobax-C_{18} preparative column, using a linear gradient of 40% to 100% B relative to solvent system A (0.1% TFA in H_2O). Using a flow rate of 2.0 ml/min, the desired product, cxALM, eluted at 38 minutes as one peak, giving 0.01 grams. Negative ion LDMS: 1975.4 ($[M-H]^-$).

2.5.2. **N-Terminus (Ferrocene)acetamido-HOOC-Alamethicin**. A minor variation of the procedure used for the synthesis of HOOC-ALM was used to synthesize the following peptide:

$FcCH_2CONH$-U-P-U-A-U-A-Q-U-V-U-G-L-U-P-V-U-U-Q-Q-F-COOH

Step 9 of the solid phase synthesis scheme, described above, was substituted with reaction of the peptidic resin with the ferrocene acetic

acid fluoride/DIPA/DMF mixture prepared as described in section 2.3.12. Identical HPLC purification strategy is used with this peptide except for a brief pretreatment of the crude peptide with an equal quantity of sodium dithionite in 200-300 μl of water. The desired product eluted at 81.5 minutes, giving 8 milligrams. Negative ion LDMS: 2158 ($[M-H]^-$), 2174.5 ([M+16(O)]).

2.5.3. **Melittin analogs**. The melittin analogs shown below were synthesized by Dr. Chris Dempsy and Colleagues at the University of Bristol:

MEL ≡

Fm-G-I-G-A-V-L-K-V-L-T-T-G-L-P-A-L-I-S-W-I-K-R-K-R-Q-Q-NH_2

MEL-K7Q ≡

Fm-G-I-G-A-V-L-Q-V-L-T-T-G-L-P-A-L-I-S-W-I-K-R-K-R-Q-Q-NH_2

MEL-K23C ≡

Fm-G-I-G-A-V-L-K-V-L-T-T-G-L-P-A-L-I-S-W-I-K-R-K-C-Q-Q-NH_2

$(MEL-K23C)_2$ ≡

Fm-G-I-G-A-V-L-K-V-L-T-T-G-L-P-A-L-I-S-W-I-K-R-K-C-Q-Q-NH_2
|
Fm-G-I-G-A-V-L-K-V-L-T-T-G-L-P-A-L-I-S-W-I-K-R-K-C-Q-Q-NH_2

MEL-K23Q,Q25C ≡

Fm-G-I-G-A-V-L-K-V-L-T-T-G-L-P-A-L-I-S-W-I-K-R-K-Q-Q-C-NH_2

$(MEL-K23Q,Q25C)_2$ ≡

Fm-G-I-G-A-V-L-K-V-L-T-T-G-L-P-A-L-I-S-W-I-K-R-K-Q-Q-C-NH_2
|
Fm-G-I-G-A-V-L-K-V-L-T-T-G-L-P-A-L-I-S-W-I-K-R-K-Q-Q-C-NH_2

Briefly, MEL, MEL-K7Q, MEL-K23C and MEL-K23Q,Q25C were synthesized by an AMGEN 9050 solid phase peptide synthesizer, using standard Fmoc and HOBT chemistry. The peptides were purified by HPLC as follows: a solution of crude peptide in water was loaded on a preparative C-4 reverse phase column, and eluted with an acetonitrile gradient from 20-70% in water containing 0.1% TFA. Peptide was detected at 280 ηm (UVmax of W19) and fractions containing the desired peptide were collected and freeze dried. Purity was confirmed by HPLC, mass spectrometry and 2D-NMR.

Cysteine containing melittin analogues were dimerized by mild alkaline oxidation, dissolving each in water and stirring at room temperature at pH 8-9. The progress of disulfide formation was checked by HPLC. The resulting dimers elute about 2 minutes later than the respective monomer. The pH of the reaction mixture was kept above 8 by addition of dilute aqueous NaOH. The dimerization was complete within 24 hours. Dimers were isolated from residual monomers by HPLC, as described above. The purity was confirmed by HPLC, mass spectrometry and 2D-NMR.

2.6. Synthesis of Other Synthetic Intermediates and Reagents

2.6.1. <u>Alamethicin p-Nitrophenylcarbonate Ester</u>. Slight modification of the method of You *et al.* (1996) was employed to make the following compound. In a flame-dried screw-capped tube (Teflon™ septum) p-nitrophenyl chloroformate (54 mg, 269 μmol) was dissolved in 1 ml THF containing 1.8 ul distilled H_2O (100 μmol). After 15 minutes stirring in an ice bath, 0.11 grams TEA (109 μmol) was added with continued stirring. Alamethicin (8 mg, 4 μmol, stored *in vacuo* over P_2O_5) dissolved in THF was then added over 5 minutes to the stirred solution. The reaction mixture was vigorously stirred under argon for 24 hours, at which time

only a trace of starting material remained. The reaction was quenched with 0.5 ml water and stirred for an additional 4 hours. The solvents were removed under a stream of nitrogen followed by *in vacuo* removal any remaining volatiles. The mixture was suspended in 1-2 ml methanol and applied to a Sephadex LH-20 column (2 x 30 cm) equilibrated in methanol. Products were eluted with methanol (gravity flow, ~ 5 ml/min) taking 2 ml fractions. The desired product eluted as a single band having an R_f = 0.55, compared to alamethicin R_f = 0.45 ($CHCl_3$, MeOH, H_2O, HOAc 70:30:3:2 v/v/v/v). Negative ion LDMS: 2076.4 ($[M-H]^-$).

2.6.2. Fmoc-aminoisobutyric Acid. Aminoisobutyric acid (5 grams, 48.5 mmol) was dissolved in 15 ml dry THF and 4 grams TEA (62 mmol) in a flame-dried reaction vessel equipped with an addition funnel and nitrogen inlet. A solution of 14.2 grams (55 mmol) fluorenylmethylchloroformate in 20 ml THF was then added dropwise to the stirred solution. After 2 hours stirring at room temperature solvents were removed by rotary evaporation the desired product was crystallized from THF/hexane to give 11.9 grams (96 %) of the desired product as an off white waxy solid. TLC: R_f = 0.3 (MeCN, $CHCl_3$, AcOH 8:1:1 v/v/v). Positive ion FAB MS: 325.4 ($[M]^+$).

2.6.3. Tetramethylchloroformamidium oxalate. The methodology for the synthesis of TFFH described by Carpino and El-Faham (1995) was used in the following three reactions (2.5.3, 2.5.4 and 2.5.5). Tetramethyl urea (11.6 grams, 100 mmol) was dissolved in 125 ml of dry toluene in a two neck flask equipped with addition funnel and nitrogen inlet. A solution of 26 grams (205 mmol) oxalyl chloride in 100 ml toluene was added dropwise over a 30 minute period. After the evolution of CO_2 had ceased (≈20 minutes) 350 ml of dry Et_2O was added with rapid stirring. The precipitated product, a crystalline and exceedingly hygroscopic salt was filtered under a blanket of argon and washed with additional dry Et_2O. The product was immediately used in reaction 2.6.4.

2.6.4. Tetramethylchloroformamidium pentaflourophosphate. The entire crop of tetramethylchloroformamidium oxalate, generated above, was dissolved in 500 ml CH_2Cl_2 in a 2 L Erlenmeyer flask. The solution was vigorously stirred while a saturated solution of potassium hexaluorophosphate (30 grams in 35 ml H_2O) was added. After 15 minutes of stirring, the organic phase was collected and washed three times with 50 ml portions of distilled water then dried over magnesium sulfate. Rotary evaporation gave 25.1 grams (91%) of a white semi-crystalline solid. MP 92°C.

2.6.5. Tetramethylfluoroformamidium pentaflourophosphate {TFFH}. The chloro- formamidium compound synthesized above (22.4 grams, 85 mmol) was dissolved in 120 ml of dry MeCN along with 4.5 grams (770 mmol) potassium fluoride (Aldrich anhydrous grade) that had been finely ground and oven dried (100° C) overnight. After stirring for 3 hours the KCl/KF was removed by filtration and the filtrate freed of solvents on a rotary evaporator to give a white semi-crystalline residue. The solution was crystallized from MeCN/Et_2O to give 9 grams (41%) of the desired product as a white crystalline semisolid. We attempted recrystallizing the reaction mixtures using a number of methods with little success at improving yields. MP 111°C, decomposes.

2.6.6. 4-(1,10-diaza-10(3-carboxypropanoyl)-4,7,13,16-tetraoxa-cyclo-octadecyl)-4-oxobutanoic acid. 4,13-Diaza-18-crown-6 (0.150 grams, 0.572 mmol) was dissolved in 8 ml dry THF and 0.5 ml TEA in a 2 neck flask equipped with a nitrogen inlet and addition funnel. A solution of 0.14 grams (1.4 mmol) succinic anhydride in 3 ml THF was added dropwise with stirring. After 18 hours the reaction mixture was freed of solvents by rotary evaporation, small quantities of $CHCl_3$ were added to the flask with repeated evaporation until no trace of amine remained. TLC analysis (MeCN, MeOH, HOAc 10:1:0.05 v/v) of the crude reaction mixture indicated the presence of starting material [R_f = 0.2], the monosuccinate

[R_f = 0.35] and the desired product [R_f =0.47]. The crude yellow semisolid was dissolved in a small volume of CH_2Cl_2 containing 5% (v/v) HOAc, applied to small silica chromatography column, and eluted using the same solvent. Under these conditions only the desired product 4,13-diaza-18-crown-6 disuccinoylamide eluted from the column. Rotary evaporation gave 0.06 grams (23 %) of the desired product. IR: amide I 1690υ.

2.6.7. **3-(N-(4-((4-(3-carboxypropanoylamino)phenyl)diazenyl)phenyl) carbamoyl)propanoic acid**. 4,4-Diaminoazobenzene (0.15 grams, 0.61 mmol) was dissolved in 8 ml dry THF and 0.5 ml TEA in a three neck flask equipped with a condenser, nitrogen inlet and addition funnel. A solution of 0.13 grams (1.3 mmol) succinic anhydride in 3 ml THF was added dropwise with stirring. After 24 hours of heating (45°C sand bath) the reaction mixture was freed of solvents by rotary evaporation, small quantities of $CHCl_3$ were then added to the flask with repeated evaporation until no trace of amine remained. The purification strategy employed in 2.5.7 was employed to give 0.04 grams (15 %) of the desired product. IR: amide I & II 1700 & 1610υ.

2.7. A Quantitative Assay for Ferrocenoyl Peptides

2.7.1. **Overview**. An assay was developed to quantitate ferrocenoyl peptides based on their iron content. Colormetric determination of the iron is accomplished by formation of deep red iron-thiocyanate complexes ($Fe(CNS)_3$, $Fe(Fe(CNS)_6$ and $FeCNS^{+2}$) once the ion is freed from the peptide by acidic digestion.

2.7.2. **The Assay**. Solution for standardization curve: 0.2 mg/ml (1.07 ηmol/μl) ferrocene carboxylic acid in MeOH. In duplicate place 1, 3, 10, 50 and 100μl of ferrocene standard in digestion tubes (corresponding to 1.07, 3.23, 10.7, 53.5 and 107 ηmol) bring the volume of each to a total

of 250μl with MeOH. In a similar manner, 3 different concentrations of peptide sample were aliquoted into digestion tubes using a best guess based on mass. Add 0.7 ml of concentrated nitric acid to each tube and place glass marbles on top. Place samples (and blanks) in a boiling water bath for 20 minutes and after cooling, correct for any volume change that may have occurred. Finally, add 0.5 ml of 500 mM aqueous potassium thiocyanate (use deionized water), vortex, wait for 10 minutes and then measure absorbence at 476 ηm.

2.8. BIOPHYSICAL STUDIES USING PLANAR LIPID BILAYERS

2.8.1. PLB Methodology

Modern PLB methodology is an adaptation of the so called Black Lipid Membrane (BLM) technique described by Mueller *et al.* (1962). BLM techniques are based on the deposition of a small quantity of lipid dissolved in organic solvent as smear across a small hole in a thin plastic film separating two electrolyte buffer containing vessels. After a short time, most solvent diffuses into the surrounding medium leaving a solvent-rich bilayer. The membranes formed by this technique suffer from low capacitance, mechanical instability and variable composition due to the presence of solvent. Montal and Mueller (1972) made significant improvements to this technique by first spreading the phospholipid as a monolayer on the electrolyte surface in each of the two vessels. The level of the electrolyte is raised from below the hole and (with a bit of luck and good timing) the monolayers fold together in apposition as they pass the hole, due to the surface tension of the buffer, to form a stable bilayer. The Montal and Mueller technique produces bilayers with higher capacitance, resistivity, stability and less solvent than the BLM counterparts.

2.8.1.1. <u>The PLB Apparatus</u>. Two identical Teflon™ chambers form the heart of the apparatus. Each chamber has a 2 ml capacity circular well, syringe inlet ports drilled into the bottom of the chambers and a perpendicular opening in the well face that forms the bridge between the two chambers. Figure 2.6 shows schematic views of the assembly.

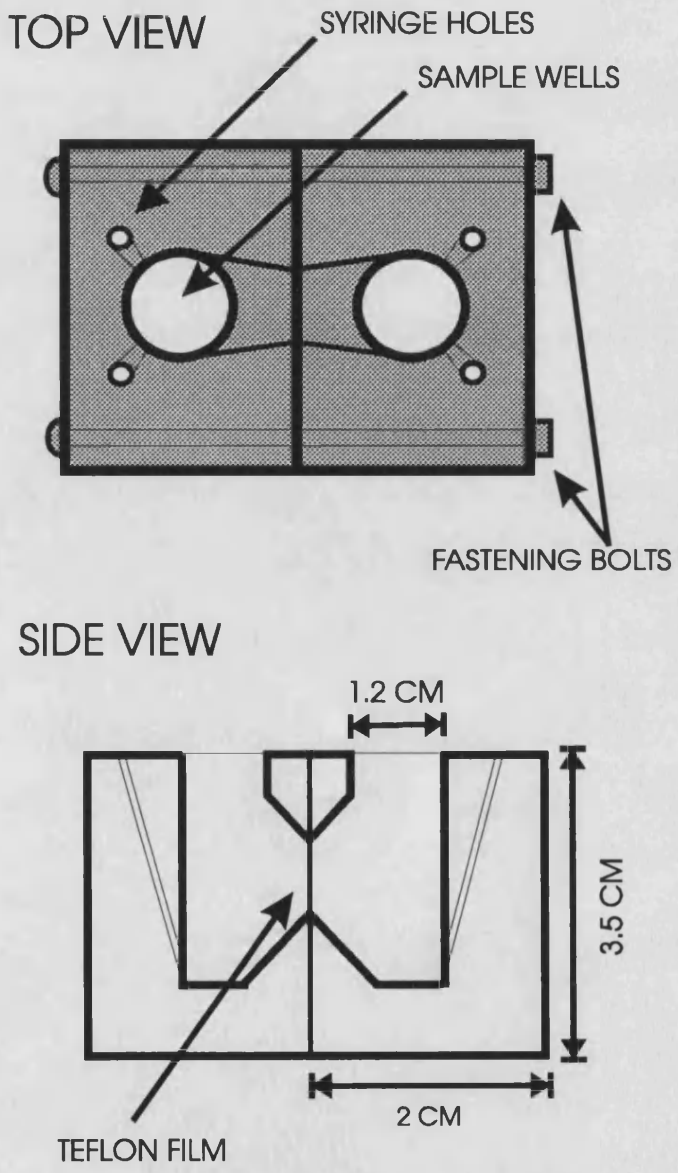

FIGURE 2.6. TOP AND SIDE VIEWS OF THE PLB ASSAMBLY.

Before use the chambers are cleaned by boiling in alkaline decontaminating solution (Decon-90) for 30 minutes then in distilled

water. After washing the chambers with deionized water the chambers are stored in EtOH and washed in hexane just prior to use. This sequence ensures that the chambers are freed of both hydrophilic and hydrophobic contaminants.

The Teflon™ film (25 μm thickness, oxygen electrode grade, Yellow Springs Instruments, Oh, USA) is tightly sandwiched between the two chambers by means of screw clamps that hold the apparatus together. A high resistance seal is insured using a small amount of petroleum wax applied to each of the blocks near the Teflon™ film junction. The aperture is formed in the Teflon™ film, prior to assembly, by means of piercing by a glass micropipette (made on a home-made pipette puller) the edges of the aperture are then polished by passing through it a spark generated by an automotive capacitor (10 kV) . The circular-to-oval holes formed by this technique have very smooth edges and range between 80 to 150 μm in diameter.

2.8.1.2. Formation of DPhPC Bilayers. The top panel of Figure 2.7 shows an enlarged view of the Teflon™ film and aperture. DPhPC monolayers are first formed on the surface of the two electrolyte-filled chambers by the careful addition of 40 μg lipid to each buffer surface in a small amount of pentane. DPhPC was used because it does not posses a gel to liquid crystal phase transition (Redwood, 1971), thus significantly reducing the effect of temperature variation. After the pentane evaporates from the chambers, the electrolyte level is simultaneously raised from below in such a way that the monolayers fold together at the aperture and form a stable bilayer separating the two chambers. Since Teflon™ is not lipophillic the process of apposition is greatly facilitated by brushing a small amount of hexadecane on the surface around the aperture. The bottom panel of Figure 2.7 shows the process of apposition leading to bilayer formation. It is important to note that the bilayers formed with this technique are not 'solvent free' in the strict sense due to the unavoidable inclusion of hexadecane into the bilayer.

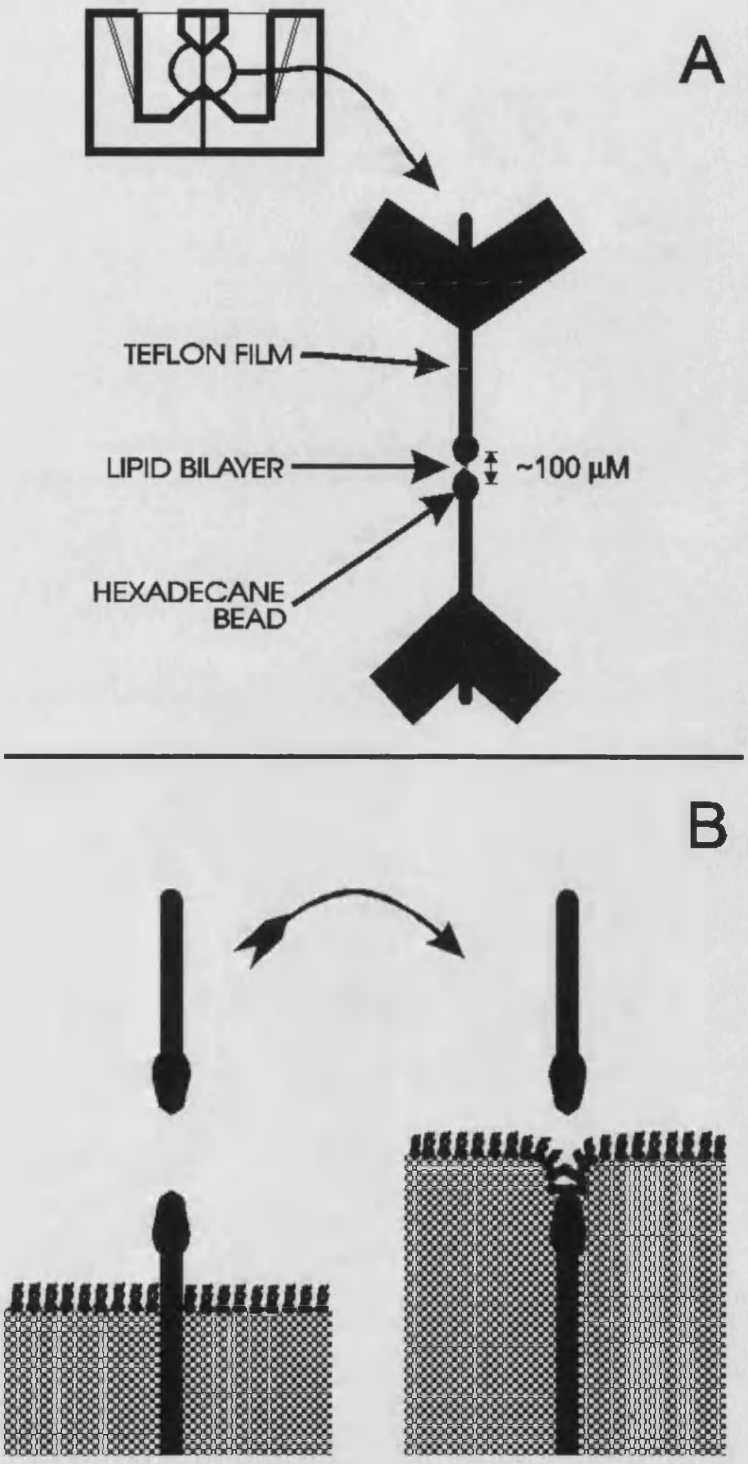

FIGURE 2.7. FORMATION OF LIPID BILAYERS IN THE PLB APPARATUS. A, close-up of Teflon film; B, formation of bilayer by apposition of monolayers.

Bilayer formation is followed by an increase in capacitance of the system from background levels, noting that an ideal DPhPC bilayer should have

a capacitance of 0.7 $\mu F/cm^2$ (Montal and Mueller, 1972). Bilayer capacitance is lipid specific and is dependent on factors such as acyl-chain length, degree of unsaturation, headgroup polarity and phase-state contribute (Montal and Mueller, 1972).

2.8.1.3. PLB Circuitry and Electronics. The electronics associated with the PLB apparatus is similar to the classic patch-clamp electrophysiology apparatus developed at the Max Planck Institute. Measurements are performed using silver / silver chloride electrodes submerged in each of the electrolyte wells.

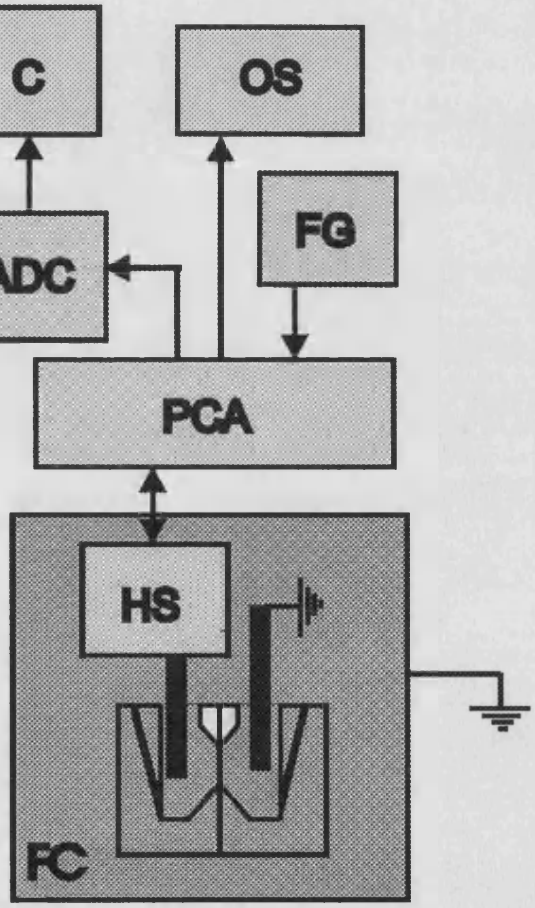

FIGURE 2.8. PLB ELECTRONICS. Key: FC, Faraday cage; HS, head-stage amplifier; PCA, patch-clamp amplifier; ADC, analog to digital converter; FG, function generator; OS, oscilloscope; C, computer. Arrows indicate direction of signal flow.

The electrode connected to the Axopatch (CV-9B) head-stage amplifier is designated the 'cis' side well. The CV-9B amplifier is designed for PLB work. The experimental convention is to denote imposed bilayer potentials relative to the 'cis' side of the apparatus. The other electrode, in the well labeled 'trans', is grounded to earth. An Axopatch Patch-Clamp 1-D amplifier, oscilloscope, Digidata AD converter, function generator and computer running Axoscope data acquisition software (Axon Instruments, Foster City, Ca) form rest of the apparatus. The 1-D amplifier also contains the current to voltage converter, 9-pole Bessel filter and capacitance correcting circuitry. A schematic of the PLB apparatus electronics is shown above in figure 2.8. Great care is taken both mechanically and electrically to isolate the BLM apparatus, as signal amplification on the order of 10^8 is required. It is possible to reduce the background noise to ≈2 pA in a typical PLB experiment by electrical and mechanical isolation.

2.8.1.4. **Single-channel Conductance Measurements**. The first family of PLB experiments described in this Thesis are the so called single-channel measurements. Here the opening and closing of single or small numbers of ion-channels is recorded. These openings are measured as integral jumps of current flow between the *cis* and *trans* side of the BLM apparatus.

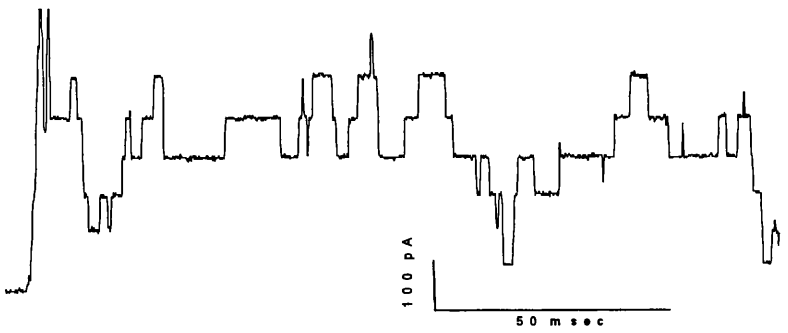

FIGURE 2.9. A TYPICAL SINGLE-CHANNEL RECORDING OF A CHANNEL FORMING PEPTIDE.

For alamethicin, these current jumps are on the order of 10 -1500 pA and last on the order of ten to hundreds of milliseconds. Figure 2.9 shows a typical single-channel recording of cxALM-Ac. For the sake of ease and accuracy in signal processing and amplification, the current is converted to voltage in the patch-clamp amplifier. The above trace was recorded at a sampling rate of 5KHz, after filtering through a 9-pole Bessel filter at the same frequency. Typically five minutes or more worth of sampling is conducted in order to insure adequate representation. Analysis of recordings, like the one above, takes two forms in this thesis: 1) conductance level histograms, which yield mean conductances of the channel openings and also the relative probabilities of the openings; and 2) dwell-time histograms which describe the mean opening times for each of the conductance levels.

2.8.1.5. Macroscopic Current-Voltage Measurements. The second family of PLB experiments conducted in this Thesis deals with the ensemble behavior of ion-channels, hence the term macroscopic. Here, after peptide is added to the *cis* side of the apparatus, the transbilayer potential is repeatedly swept between two *exterma* sampling at a lower rate (-200 to 200 mV, λ = 40 seconds, 20 sweeps, for example), then the resulting ion-channel current from the sweeps is averaged together. A plot of ion-channel current flow (I) versus applied transbilayer potential (V) gives an estimation of a peptide's channel formation propensity. The macroscopic experiment also gives a quantitative estimate of conductance asymmetry.

2.8.1.6. Macroscopic Voltage-Step Measurements. The final type of experiment employed in this Thesis is the so called voltage-step experiment. Here, the equilibrium macroscopic conductances are recorded while discreetly stepping between a variety of transbilayer potentials. These experiments help to establish reversal potentials,

ultimately affording relative ion permabilities, by application of the Goldman-Hodgkin-Katz (Hille, 1992) adaptation of the Nernst equation:

$$V_{rev} = \left(\frac{RT}{zF}\right)\ln\left(\frac{P_K[K]_t + P_{Cl}[Cl]_c}{P_k[K]_c + P_{Cl}[Cl]_t}\right) \qquad \{m1\}$$

Where P_K and P_{Cl} are the permeabilities of potassium and chloride ions, respectively. $[X]_t$ and $[X]_c$ denote the *trans* and *cis* concentrations of the given ions and z is the charge of the given ions. This equation can be conveniently rearranged to give the ratio of permeabilities:

$$\frac{P_k}{P_{Cl}} = \frac{\alpha[K]_t - [Cl]_c}{[K]_c - \alpha[Cl]_t} \qquad \{m2\}$$

where α equals:

$$\alpha = e\frac{FV_{rev}}{RT} \qquad \{m3\}$$

Voltage-step experiments are also useful in distinguishing between conductance induced by ion-channels and those induced by nonspecific membrane perturbation effects.

2.9. PLB DATA PROCESSING AND MANIPULATION.

PLB data acquisition, filtering and sample-rate conversion was conducted using AxoScope (v1.1, Axon Instruments, Foster City, Ca. USA), this software also converts channel recordings to columnar ASCII data for processing in other programs. Data from macroscopic I-V experiments was processed using custom written code in Matlab (v4.2c.1, Math

Works, Natic, Mass. USA). Single-channel data processing, plotting and related tasks were conducted using Origin Software (v4.0, Northampton, Mass). Dwell time histograms and probabilities were calculated using Strathclyde Electrophysiology Software program Pat (v7.0, University of Strathclyde, Glasgow, Scotland).

2.10. MOLECULAR MODELING

Although computational modeling was not the focus of this study, some preliminary studies were undertaken in attempt to rationalize some of the findings discussed herein. Most of the ion-channel modeling is in the spirit of Sansom and co-workers (Kerr *et al.*, 1994) who used a combination of molecular mechanics minimization and molecular dynamics. One of the principal challenges was incorporating ferrocene into the mechanics forcefield treatments. Atomic partial charges and inter-atomic distances for oxidized and reduced ferrocene were calculated using Density Functional Theory (for a review, see: Parr and Yang, 1989).

2.10.1. Background to the Modeling Techniques Used in this Study.

2.10.1.1. <u>Molecular Mechanics</u>. Molecular mechanics is a computational method whose basic formulation lies in the fundamental equations of vibrational spectroscopy. The idea is to create an additive potential energy function that relates molecular geometry to energy in a meaningful way, and in turn predict molecular properties (for a review, see: Reviews in Computational Chemistry, Volume 2, 1991). These potential energy equations are elaborations of the following basic form, which taken with the necessary empirical parameters, is called the *Forcefield*:

{m4}

$$U = \sum E_{bonds} + \sum E_{angles} + \sum E_{torsion} + \sum E_{Coulomb} + \sum E_{VdW} + \sum E_{Hbond}$$

here, the first three energy summation terms define the extent to which individual bonds, angles and torsion angles contribute to the overall empirical potential energy U; the last three terms define the so-called non-bonding terms, describing the Coulombic, Van der Waals and Hydrogen bond contributions to the overall energy of the molecule. These energy terms are most often harmonic potential functions that describe the deviation of the terms from an equilibrium value. Many currently used forcefields absorb the H-bonding term into the electrostatics term, thus increasing computational efficiency.

Three forcefields are used in the current study; the Tripos forcefield (Clark *et al.*, 1989) is used in the initial model building while the more highly parameterized Amber forcefield (Weiner *et al.*, 1984) is used in refinement and molecular dynamics treatments. Forcefield treatments on ferrocene containing peptides utilize the so-called Universal Forcefield, UFF (Rappe *et al.*, 1992). As an example, the potential energy function employed in the Tripos forcefield takes the following form:

$$U = \sum_{i=1}^{Nbonds} \frac{1}{2} k^{di} (d_i - d_i^o)^2 + \sum_{i=1}^{Nangles} \frac{1}{2} k^{\theta i} (\theta_i - \theta_i^o)^2 + \sum_{i=1}^{Ntor} \frac{1}{2} V_i^{\omega} [1 + S_i \cos(|n_i| \cdot \varpi_i)] +$$
$$332.17 \left[\sum_{i=1}^{Natoms} \sum_{j>1} \frac{Q_i Q_j}{r_{ij} \varepsilon} \right] + \sum_{i=1}^{Natoms} \sum_{j>1} E_{ij} \left[\frac{1}{a_{ij}^{12}} - \frac{2}{a_{ij}^{6}} \right] \qquad \{M5\}$$

This equation is an elaboration of {M4}; d_i is bond distance of the ith bond, d^o_i is the equilibrium bond length for that bond type and K^{di} is the force constant for that bond type. Likewise, for the angle (θ) term. The torsion term, being periodic, takes the form of a cosine function, V_i^{ϖ} is the torsion barrier height, S_i is a switch function taking on the value of +1 for a staggered conformation and -1 for an eclipsed conformation, n_i is the periodicity and ϖ_i is the torsion angle. The next term is the classic energy of Coulombic interaction of atoms i and j with respective charges Q_i and Q_j at distance r_{ij} apart, and finally ε is the value of the dielectric screening function. Finally the Van der Waals term is a classic '12-6'

function where E_{ij} is the VdW constant and a_{ij} is the interatomic distance between atoms i and j weighted to correct for VdW radii.

The amber forcefield includes an explicit H-bond term and a different torsion term:

$$U = \sum_{i=1}^{Nbonds} k^{di}(d_i - d_i^o)^2 + \sum_{i=1}^{Nangles} k^{\theta i}(\theta_i - \theta_i^o)^2 + \sum_{i=1}^{Ntor} \frac{1}{2} V_i^{\omega}[1 + \cos(n_i \varpi_i - \gamma_i)] +$$
$$\left[\sum_{i=1}^{Natoms}\sum_{j>1} \frac{Q_i Q_j}{r_{ij}\varepsilon}\right] + \sum_{i=1}^{Natoms}\sum_{j>1}\left[\frac{A_{ij}}{R_{ij}^{12}} - \frac{B_{ij}}{R_{ij}^{6}}\right] + \sum_{H-bonds}\left[\frac{C_{ij}}{R_{ij}^{12}} - \frac{D_{ij}}{R_{ij}^{10}}\right]$$

{M6}

Here, the first two terms are identical; in the torsion term γ_i is the phase angle of the system, replacing the switch function in {M5}. The Coulomb function takes the same functional form as in the Tripos forcefield. The next term is a classic Lennard-Jones term where A_{ij} and B_{ij} are the nonbonding repulsion and attraction coefficients, respectively. Likewise C_{ij} and D_{ij} are the hydrogen bonding repulsion and attraction terms. In searching for equilibrium conformations the potential function is minimized with respect to Cartesian coordinates using any of a number of first and second derivative minimization techniques, specified in Chapter seven.

2.10.1.2. Charge Calculation. Atomic partial charges are either taken from the Kollman parameter set for use in Tripos and AMBER forcefield calculations. Goddard's charge equilibration charges are also used in certain calculations (Rappe and Goddard, 1991). This methodology takes into account the effect of nonbonding interactions and atomic polarizabilities on atomic charge, allowing for robust conformation sensitive charge calculations to be used with forcefield treatments.

2.10.1.3. Quantum Mechanical Methods: Density Functional Theory.

In an attempt to obtain accurate forcefield parameters for ferrocene the method of density functional theory was employed, because, unlike *ab initio* molecular orbital methods, diffuse orbitals such as **d** and **f** are easily treated. In DFT the time dependent Schrödinger {M7} equation is solved for electron density:

$$\hat{H}\Psi = E\Psi \qquad \{m7\}$$

Where, the Born-Oppenheimer Hamiltonian operator is:

$$\hat{H} = -\frac{1}{2}\sum_{i=1}^{N}\nabla_i^2 + \sum_{i.j}^{N} 1/\vec{r}_{ij} - \sum_{\alpha=1}^{M}\sum_{i=1}^{N}\frac{Z_\alpha}{\vec{r}_{i\alpha}} + \sum_{\alpha<\beta}\frac{Z_\alpha Z_\beta}{R_{\alpha\beta}} \qquad \{M8\}$$

The central approximation here is that electrons move freely in a field of static nuclei, thus allowing the kinetic energy of the electrons (the first term), the electrostatic repulsion of the electrons (second term), the electrostatic attraction between the electrons and nuclei to (third term) and nuclear repulsion (fourth term) to be partitioned. Each of the terms in {M8} are converted to a density functional equivalent recalling that the electron density is given by:

$$\rho(\vec{r}) = \sum_{i=1}^{N}\Psi_i^*(\vec{r})\Psi_i(\vec{r}) \qquad \{M9\}$$

according to the Kohn-Sham equations ground state energy E as a function of density distribution:

$$E[\rho, v] = T[\rho] + J[\rho] - K[\rho] + V_{ne}[\rho] \qquad \{M10\}$$

Where $T(\rho)$ is the kinetic component, $J(\rho)$ is the electron-electron repulsion component, $K(\rho)$ is the exchange correlation term and $V(\rho)$ is the nuclear-electron attraction component. Thus, the solutions of $\partial(E[\rho, v])/\partial\rho = 0$ gives stable conformations, molecular geometries and the electron density.

2.10.1.4. **Molecular Dynamics**. Allows for the time-dependent evolution of molecular systems by numerical integration of Newtonian or Lagrangian equations of motion. Thus the force F at time t on a given atom i with respect to Cartesian coordinate is given by:

$$F_i(t) = -\frac{\partial}{\partial r_i} U(\vec{r}_1, \vec{r}_2, \vec{r}_3, \ldots, \vec{r}_{3N}) \qquad \{M11\}$$

Where U corresponds to a additive potential function described in section 2.10.1.1. At $t = 0$ atoms are assigned velocities by any number of means but most frequently by Boltzmann distribution corresponding to a given temperature T. Then the above equation is re-evaluated at small (usually fs) time steps and then the following equation is solved for the new atomic coordinates:

$$\frac{\partial^2 r_i}{\partial t^2}(t) = \frac{F_i(t)}{m_i} \qquad \{M12\}$$

where m_i is the mass of atom i. Thus, the acceleration of atom i is given by adding up all of the force vectors resulting from interactions with all other atoms j, recalling the fundamental equation $F = ma$:

$$\sum_j F_i(t) = m_i a_i \qquad \{M13\}$$

So, the above equation needs to be solved for the position of each atom i so the time dependent evolution of the system can be evaluated. This is accomplished by a number of different methods. The Sybyl MD tools suite uses the so called Leap-Frog algorithm (Verlet, 1967) to solve the above equation.

2.10.1.5. Dipole Calculations Using Semiempirical Molecular Orbital Methodology. The program MOPAC (version 6.0; Stewart, 1990) was used to calculate the molecular dipole and the z-vectorial component for alamethicin derivatives, as described in Chapter 7. In the case of ferrocene containing peptides, dipole calculations were calculated in Cerius^2. Briefly, MOPAC charges of the amino acids was used in combination with charges calculated for the ferrocenoyl moiety using DFT.

2.10.1.6. Poisson-Boltzmann Electrostatics Calculations on Alamethicin Bundles. In electrostatics theory, the potential Φ at a given point r away from a uniformly charged body is given by the following equation:

$$\Phi = \frac{ze}{\varepsilon r} \qquad \{M14\}$$

where z is the body's charge and e is the dielectric constant. Unfortunately, this simple relationship breaks down in electrolytic media. Poisson and Boltzmann showed that the screening effects of the media could be accounted for by the addition of a screening parameter k and by taking into account the radius a of the body:

$$\Phi_{P-B} = \frac{ze}{\varepsilon r} e\{[\kappa(a-r)]/[1+\kappa a]\} \qquad \{M16\}$$

where κ is a root function of the ionic strength. A number of different schemes have been developed for the numerical solution of this equation. In these investigations we use a finite-difference approximation to the integral describing a surface at radius r from the body's center of mass. This is implemented in the UHBD software program (Madura *et al.*, 1995).

2.10.1.7. Assembly of CFP Bundles. Parallel bundles of alamethicin and melittin analogs were assembled using a highly minimized hexameric alamethicin (R_f = 50) bundle generated by Jason Breed (Breed *et al.*, 1996). The bundle had been generated as a united-atom model, minimized and subjected to 100 psec molecular dynamics using the CHARMm forcefield.

For the purposes of this Thesis the model was converted to an all-atom model in the Tripos and AMBER forcefields and minimized using the following protocol: constrained minimization without electrostatics, constrained minimization with electrostatics (slowly reducing from ε = 80 $\rightarrow$ 1) and then unconstrained minimization with electrostatics.

2.10.1.8. Molecular Dynamics Simulated Annealing of Melittin Bundles. The MD simulated annealing technique explores conformational space by virtual 'heating' of a structure in molecular dynamics, allowing it to escape basins of local minima and (hopefully)

find better (or global minima). The simulated annealing tools in the SYBYL modeling and simulation program (v6.0, Tripos Associates, St. Louis, Mo., USA) were used for all of the simulations with melittin. A standard protocol was developed whereby a pre-minimized bundle was annealed for 10 cycles by heating to 2000K and exponentially cooled to 300K over 500 fsec. Between each heating the structure was equilibrated for 2000 fsec. The lowest energy structure form the ensemble was further minimized and visualized in Chapter 7-- additional details are given in the Figure Legends of this Chapter.

2.10.1.9. Hardware and Software. All computational modeling described in this Thesis was conducted on a Silicon Graphics R4400 and R5000 UNIX workstations. The bulk of the protein modeling was done using SYBYL (v6.0, Tripos Associates, St. Louis, Mo., USA). DFT calculations and some protein modeling was conducted using Cerius2 software (v.2.6 and 3.0, Molecular Simulations Inc., San Diego Ca., USA).

2.11. REFERENCES: MATERIALS AND METHODS

Acton, E. M., & Silverstein, R.M. (1959) *J. Org. Chem. 24*, 1487-1490.

Breed, J., Sankararamakrishnan, R., Kerr, I.D., & Sansom, M.S.P. (1996) *Biophys. J. 70*, 1643-1661.

Carpino, L. A. & El-Faham, A. (1995) *J. Am. Chem. Soc. 117*, 5401-5402.

Clark, M., Cramer, R.D., & Van Opdenbosch, N. (1989) *J. Comp. Chem. 10*, 982-1012.

Davis, R., & Untch, K.G. (1981) *J. Org. Chem. 46*, 2987-2988.

Little, W.F., & Eisenthal, R.E. (1960) *J. Am. Chem. Soc. 82,* 1577-1580.

Hille, B. (1991) Ionic Channels of Excitable Membranes, Sinauer Assoc., Sunderland Mass.

Kerr, I. D., Sankararamakrishnan, R., Smart, O., & Sansom, M.S.P. (1994) *Biophys. J. 67*, 1501-1515.

Kiso, Y., Yoshida, M., Tatsumi, T., Kimura, T., Fujiwara, Y., & Akaji, K. (1989) *Chem. Pharm. Bull. 37*, 3432-3434.

Lau, H. H., & Hart, H. (1959) *J. Org. Chem. 24*, 280-281.

Lipkowitz, K. B., & Boyd, D.B. *ed.* (1991) Reviews in Computational Chemistry, Volume II, VCH, New York.

Little, W. F., & Eisenthal, R. (1960) *J. Am. Chem. Soc. 82*, 1577-1583.

Madura, J.D., Briggs, J.M., Wade, R.C., Davis, M.E., Luty, B.A., Llin, A., Antosciewicz, A., Gilson, M.K., Bagheri, B., Scott, L.R., & McCammon, J.A. (1995) *Comp. Phys. Commun. 91*, 57-95.

Montal, M., & Mueller, P. (1972) *Proc. Natl. Acad. Sci. USA 69*, 3561-3566.

Mueller, P., Rudin, D., Tien, H.T., & Westcott, W.C. (1962) *Circulation 26,* 1167-1171.

Mueller, P., & Rudin, D.O. (1963) *J. Theor. Biol. 4*, 268-280.

Myrboh, B., Ilia, H., & Junjappa, H. (1981) *Synthesis 39*, 126-127.

Nesmeyanov, N. A., & Reutov, O.A. (1958) *Doklady Acad. Nauk. S.S.S.R. 120*, 1267-1270.

Osgerby, J. M., & Pauson, P.L. (1958) *J. Org. Chem 22*, 656-660.

Parr, R. G., & Yang, W. (1989) *Density-Functional Theory*, Oxford University Press, Oxford.

Rappe, A. K., Casewit, C.J., Colwell, K.S., Goddard, W.A, & Skiff, W.M. (1992) *JACS 114,* 10024-10032.

Rappe, A. K., & Goddard, W.A. (1991) *J. Phys. Chem. 95*, 3358-3363.

Redwood, W.R., Pfeiffer, F.R., Weisbach, J.A., & Thompson, T.E. (1971) *Biochim. Biophys. Acta. 233,* 1-6.

Sonoda, A., & Moritani, I. (1971) *J. Organometal. Chem. 26,* 133-140.

Stewart, J.J.P. (1990) MOPAC Sixth Edition, *QCPE, Release 455.*

Verlet, L. (1967) *Phys. Rev. 159*, 98-101.

Weiner, S. J., Kollman, P.A., Case, D.A., Singh, U.C., Ghio, C., Alogona, G., Profeta, S., & Weiner, P. (1984) *JACS 106*, 765-778.

Wenschuh, H., Beyermann, M., Haber, H., Seydel, S., Krayuse, E., & Bienert, M. (1995) *60*, 405-410.

Woolley, G. A., Epand, R.M. , Kerr, I.D. , Sansom, M.S.P., & Wallace, B.A. (1994) *Biochemistry 33*, 6850-6858.

You, S., Peng, S., Lien, L., Breed, J., & Woolley, G.A. (1996) *Biochemistry 35,* 6225-6232.

RESULTS

3. SYNTHESIS AND CHEMISTRY

The principal objective of the organic synthesis described herein was to provide a diversity of CFP analogs for our biophysical investigations. The specific aims of the synthetic effort were to: 1) incorporate ferrocene into both the N- and C-termini of alamethicin; 2) synthesize stabilized dimeric forms of alamethicin and mellitin; and 3) synthesize mutants of mellitin with reduced cationic character. During the course of these investigations a total of 39 compounds was synthesized- these can be grouped in a number of categories:

- **24** Ferrocene derivatives.
- **3** Ferrocene derivatives that eluded purification but for which strong spectroscopic evidence exists.
- **4** Ferrocenoyl alamethicin analogs.
- **2** Non-ferrocenoyl alamethicin analogs.
- **6** Ligands and reagents.

3.1. SOLUTION-PHASE SYNTHESIS

3.1.1. Ferrocene Analogs. The work described in this Thesis has turned out to be an exploration of modern metallocene chemistry as much as an investigation probing the biophysics of channel forming peptides. As mentioned above, a number of ferrocene analogs were made, including: (N,N-diphenyl)ferrocene carboxamide, 1'-acetyl-1-(N,N-diphenyl) ferrocene carboxamide, ferrocenecarboxylic acid methyl ester, ferrocenecarboxylic acid chloride, hydroxymethylferrocene, chloromethylferrocene, cyanomethylferrocene, ferroceneacetic acid, ferrocene acetyl chloride, ferrocene acetyl fluoride, ferrocene-1,1'-dicarboxylic acid dimethyl ester, ferrocene-1,1'-dicarboxylic acid

anhydride, 1,1'-bis(hydroxymethyl)ferrocene, 1,1'-bis(chloromethyl) ferrocene, 1,1'-bis(cyanomethyl)ferrocene, ferrocene-1,1'-bis(acetic acid), ferrocene-1,1'-bis(acetic acid) anhydride, ferrocene(α-keto)butyric acid, ferrocene-1,1'-bis(α-keto)butyric acid, (N,N-Dimethyl)amino-methylferrocene, (Ferrocenylmethyl)trimethylammonium Iodide and Diethyl- (ferrocenylmethyl)formamidomalonate. These compounds were all made in yields varying from acceptable to excellent. The spectroscopic and chromatographic characterization of these compounds is given in Chapter 2, Section 2.2.

3.1.2. Diamine Linkers. Efforts to make a diamide ferrocene linker for the Pillilar type synthesis, mentioned above, does warrant some discussion. Synthesis of the following compounds: 1,1'-bis(4-amino)propanoyl) ferrocene amide, 1,1'-bis(6-amino)-piperazinoyl)ferrocene amide and 1,1'-bis(4-amino)propanoyl)ferrocene amide, was attempted by reaction of ferrocenedicarboxylic acid dichloride with an excess of the appropriate diamine in the presence of triethylamine. Following each of the reactions by TLC, conversion of the starting material to products with amine-like properties was observed; indeed, mass spectrometric and infrared analysis does indicate the presence of the desired products. The caveat in this effort was the isolation of the putative products. The free base forms of these compounds, especially the dihexanoyl amine proved exceedingly difficult to purify using a number of different chromatographic conditions. The dipiperazinoyl and dipropanoyl amines were converted to the dihydrochloride salts, these (surprisingly) also eluded crystallization and chromatographic purification.

3.1.3. Dicarboxylate Linkers. In a final effort to make 'linkers' for C-terminus coupling pairs of alamethicin molecules, we made the novel compounds shown in Chapter 2, Figure M5. Each of these compounds was made with the aim of using conventional anhydride/carbodiimide or

similar activation chemistry to couple two alamethicin molecules with the linker *via* ester functions. Ferrocene-1,1'-bis(α-keto)butyric acid was synthesized in moderate yield from the Fridel-Crafts type acylation of ferrocene using succinic anhydride. 4,13-Diaza-18-crown-6 disuccinoylamide and 4,4'-diaminoazobenzene disuccinoylamide were both synthesized in acceptable yield by the trivial reaction of the parent diamides with succinic anhydride. Unfortunately, the coupling of alamethicin to these compounds was not perused.

3.1.4. [+/-]-(Ferrocenyl)alanine. This compound, shown in Chapter 2 Figure M4, was made by slight variation of the published method of Osgerby and Pauson (1954). This compound was synthesized with the aim of making its Fmoc derivative so it could then be used in solid-phase peptide synthesis.

3.1.5. Monomeric Alamethicin Derivatives. Four alamethicin derivatives were synthesized by acylation of the C-terminus hydroxyl moiety, using activated carboxyl reagents. Synthesis and purification of C-terminus ferrocenoyl-alamethicin (Fc-ALM) were achieved by adaptation of the published method for alamethicin pyromellitate (Woolley *et al.*, 1994). Reaction of alamethicin with ferrocenoic anhydride proceeded acceptably to give the desired product; mass spectroscopic evidence of the HPLC purified material gave the molecular ion and expected fragmentation patterns. Additional analysis of the purified peptide using thin-layer chromatography showed the presence of a single amide-containing product migrating faster than alamethicin. Synthesis of 1'-carboxyferrocenoyl-alamethicin (cxFc-ALM) proceeded smoothly by reaction of the anhydrous alamethicin with ferrocene-1,1'-dicarboxylic acid dichloride in pyridine followed by hydrolysis of remaining acid chloride (N-acylpyridinium salts) with water. C-terminus ferrocenacetoyl-alamethicin ($FcCH_2$-ALM) was synthesized in high yield by the reaction of alamethicin with ferroceneacetic acid chloride which itself was

synthesized by an adaptation of the method of Sonoda and Moritani (1971). Care was taken to not expose the alamethicin directly to the acid chloride reagents Thus acid chlorides were converted to their N-acylpyridinium derivatives prior to reaction with peptide. This is due to the fact that alamethicin's glutamine sidechains are easily dehydrated by acyl chlorides and similar reagents. C-terminus alamethicin p-nitrophenyl carbonate was also synthesized in high yield for use in O→N Pillilar type transacylation coupling with nucleophillic amines. The results of this work are discussed below (section 3.1.6.).

Finally, during the course of the investigations, a significantly simpler purification method was devised: double purification using lipophillic Sephadex LH-20. Both the HPLC purification and the Sephadex LH-20 based purification methods yielded one product in the purification of Fc-ALM, as evidenced by TLC and mass spectrometry. We found no evidence for contamination of any of the purified peptides with unmodified alamethicin.

3.1.6. Dimeric Alamethicin Derivatives: Solution-Phase. Three tactics were devised to accomplish the synthesis of alamethicin dimers:1) Pillilar coupling of p-nitrophenyl carbonate esters with diamines; 2) coupling of alamethicin to dicarboxylate 'linkers'; and 3) solid-phase synthesis of cysteine-disulfide containing alamethicin derivatives. For a number of practical reasons, discussed below, I was unable to realize any of these objectives. Our first approach was to make dimers by variation of the method of You and coworkers described above (You *et al.*, 1996). Although the synthesis of the critical p-nitrophenyl carbonate intermediate was successful, we found it impossible to reproduce the results of the O→N coupling reaction reported by You. Displacement of the p-nitrophenyl carbonate ester was attempted with propane-1,3-diamine, hexane-1,6-diamine as well as the highly reactive diamine piperazine. In every case there was no evidence for the formation of dimeric products, but it did appear that base catalyzed hydrolysis of the

ester was competing with the desired reaction. A number of different conditions were attempted, including variation in temperature, solvent and amine concentration. Thus, the O→N Pillilar type transacylation coupling based approach was abandoned.

3.2. SOLID-PHASE SYNTHESIS

3.2.1. Momomeric Alamethicin Derivatives. C-terminus carboxy alamethicin (cxALM-NAc) and C-terminus carboxy alamethicin containing an N-terminus ferrocencacetamide (cxALM-NFc) were successfully synthesized using a variation of the solid-phase synthesis method for alamethicin described by Wenschuh and coworkers (Wenschuh *et al.*, 1995). Elongation of the peptide on PEG-PS resin proceeded smoothly using Fmoc-amino acid fluorides in the presence of diisopropylamine. After elongation the free N-terminus amine was carboxylated with either acetic anhydride (to give cxALM-NAc) or ferroceneacetic acid fluoride (to give cxALM-NFc). Cleavage from the resin was accomplished by a mixture of trifluoroacetic acid and boron tetrafluoride made more hydrophobic by the inclusion of dichloromethane. Despite the fact that yields were around ten percent, we were able to obtain enough of each of the peptides for hundreds of PLB experiments. Detailed mass spectroscopic analysis was conducted on these peptides, both giving strong molecular ion and the expected fragmentation patterns.

3.2.2. Dimeric Alamethicin Derivatives: Solid-Phase. Next, solid-phase synthesis methodology, as described in Chapter 2 (2.5 and Figure M3) was employed in attempt to synthesize dimers of alamethicin mutants containing cysteine, hence linking the peptides *via* cysteine disulfide bridges. We attempted making the following peptides: ALM-U3C, ALM-P14C and ALM-Q18C. These mutations were chosen based on how well the dimerized mutants conform to the hexameric channel model proposed by Sansom, see modeling Chapter 7. There is compelling evidence that

the solid phase synthesis for all but one of these peptides was successful. The failed synthesis was due to electrical power to the peptide synthesizer being accidentally shut off. Problems arose in cleavage of the peptide from the solid-phase resin. Conditions that successfully cleaved cxALM-NAc and cxALM-NFc from the resin failed with the cysteine variants. The numerous decoupling conditions either left the peptide uncleaved or adversely degraded. The hydrophobicity, acidity and free-radical-scavenger content of the decoupling mixtures were varied, as was temperature and reaction length. Exacting care was also taken in the analysis to uncover evidence for t-butyl-S-cysteine fragments (as, Fmoc-(t-butyl-S-)cysteine was used in the synthesis) or peptides containing oxidized forms (sulfonic or sulfinic acids) of the cysteinyl peptides. With considerable quantities of the resin-bound peptides still in-hand, perhaps a more chemistry minded investigator will have success in obtaining these peptides.

3.2.3. Mellitin Derivatives. Mellitin derivatives, MEL-K7Q, MEL-K23C and MEL-K23Q,K25C were synthesized by Dempsy and co-workers at the University of Bristol. Standard solid-phase chemistry using standard Fmoc-PFB amino acids was employed to give the desired amino acids in high yield. Dimers of the two cysteine mutants [$(MEL\text{-}K23Q,K25C)_2$ and $(MEL\text{-}K23C)_2$] were formed by the spontaneous oxygen catalyzed oxidation of the respective monomers. All of the melittin derivatives described were isolated using HPLC to a high level of purity. Mass spectroscopic, spectrophotometric and NMR techniques were used in the assessment of peptide purity. Biophysical studies of $(MEL\text{-}K23C)_2$ were conducted using two separate batches of peptide, both producing similar results.

3.3. QUANTITATION OF FERROCENE CONTAINING PEPTIDES

As these peptides were to be used in biophysical studies, we sought an accurate method of quantitating the ferrocenoyl peptides described above. Inspired by the accuracy of phosphorus based quantitation methods for phospholipids, a method for measuring nanogram quantities of iron containing peptides was sought. Acidic digestion of ferrocenoyl peptides in methanolic nitric acid at elevated temperatures affords free iron (presumably Fe^{3+}) which was complexed with thiocyanate to form highly colored Fe-thiocyanate complexes. Increasing quantities of iron lead to increased absorption of visible light following a Beer-Lambert relationship, thus making this an ideal spectrophotometric assay, Figure 3.1.

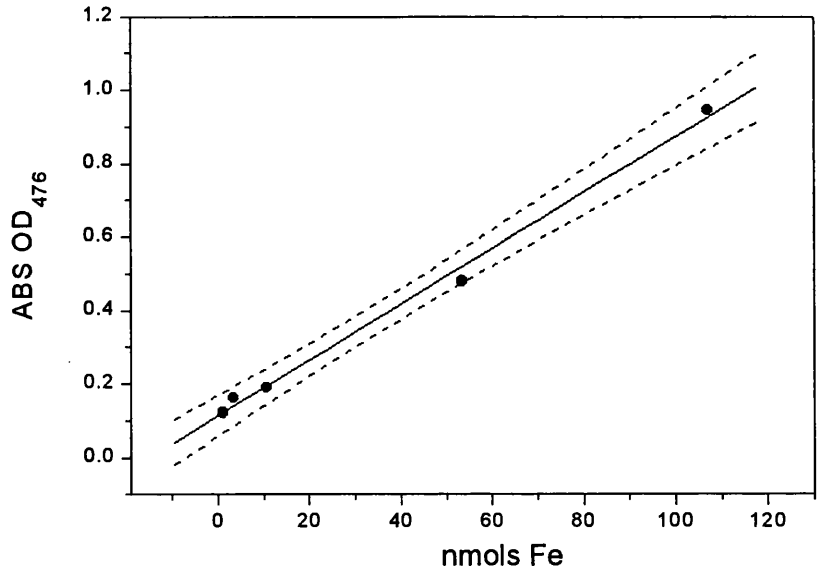

FIGURE 3.1. STANDARD CURVE FROM PEPTIDIC IRON ASSAY. Above is a plot of a typical standard curve obtained with the thiocyanate-based iron assay. The solid line indicates the equation of linear regression and the dashed lines show the 95% confidence interval.

4. PLB STUDIES ON C-TERMINUS FERROCENOYL ALAMETHICIN

To evaluate the channel-forming behavior of Fc-ALM and cxFc-ALM both macroscopic current-voltage and single channel measurements using planar lipid bilayers were conducted. Conductance level histograms were also calculated. When Fc-ALM and cxFc-ALM are incorporated into diphytanoylphosphatidylcholine PLBs they form voltage sensitive channels similar to alamethicin. In the last series of experiments we exposed the ferrocenoyl peptides to cerium ammonium nitrate to explore the putative redox behavior of these peptides

4.1 Macroscopic Studies. Figure 4.1 demonstrates that higher potentials are required to activate equivalent concentrations of the ferrocene containing peptides compared to ALM. Current-voltage (I-V) measurements were conducted by adding peptides to the *cis* chamber of the PLB apparatus.

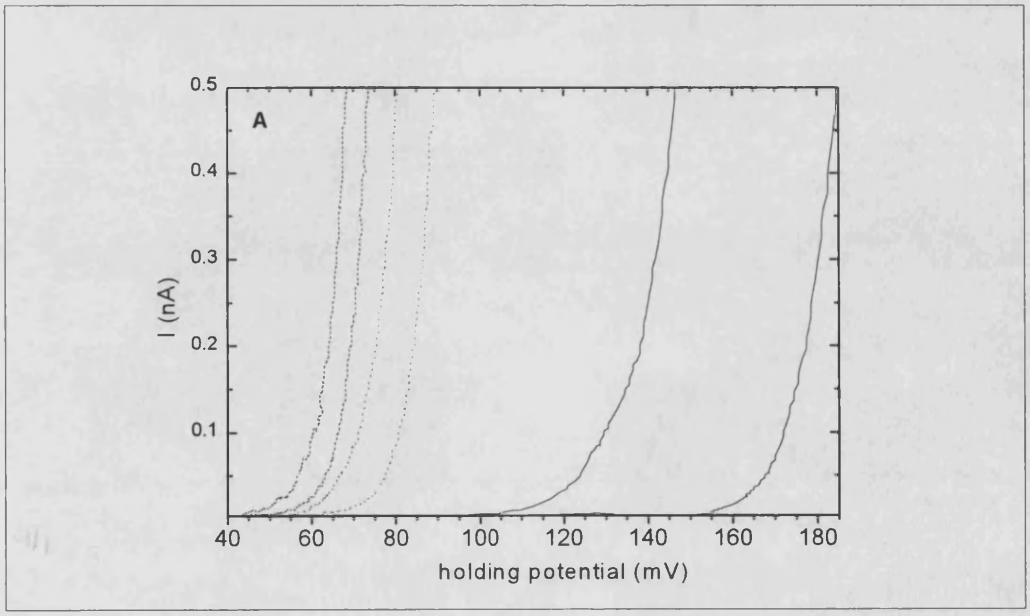

FIGURE 4.1. I-V ANALYSIS OF C-TERMINUS FERROCENOYL PEPTIDES. Legend on next page.

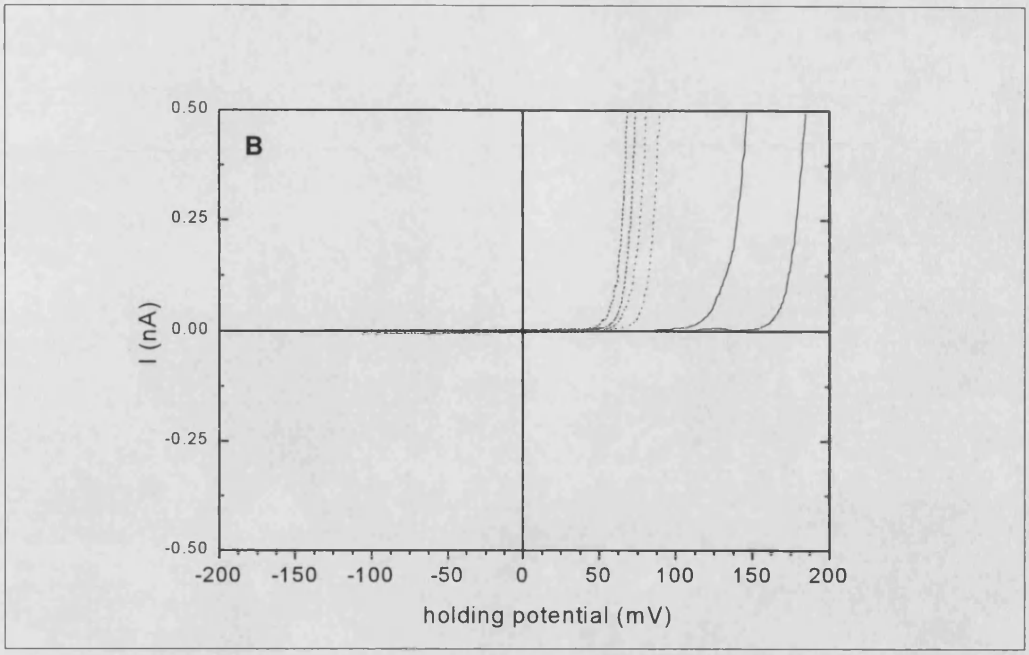

FIGURE 4.1. I-V ANALYSIS OF C-TERMINUS FERROCENOYL PEPTIDES. Current-voltage (I-V) measurements in planar lipid bilayers were conducted by adding peptides to the *cis* (positive potential) chamber of the PLB apparatus to a final concentration of 0.25 μM in buffered electrolyte (0.5 M KCl, 10 mM BES, pH 7.0). Triangular voltage sweeps (λ = 20 sec) from -100 mV to +100 mV for ALM, -90 mV to +90 mV for Fc-ALM and -180 mV to +180 mV for cxFc-ALM were then applied. Currents from 20 such sweeps were averaged together and are plotted as follows: ALM (----------); Fc-ALM (- - - - - - - -); and cxFc-ALM (————). The right hand curve of each pair represents the induced current during the ascending portion of the voltage sweep (i.e. dV/dt > 0) and the left hand curve the descending (dV/dt < 0) portion.

The higher potentials required to activate the Ferrocenoyl peptides can be shown by measuring the voltage (V_t) required to elicit a 0.1 nA current. V_t Values for Fc-ALM and cxFc-ALM are +81 mV and +174 mV, respectively, compared to +66 mV for ALM. These peptides only form channels at *cis* positive potentials, consistent with the behavior of native alamethicin (Figure 4.1b). This Figure demonstrates a marked increase in hysteresis of the current-voltage relationship of cxFc-ALM compared to Fc-ALM or ALM. The degree of hysteresis is reflected in the difference between induced current during ascending and descending portions of the voltage sweep. The possible implications of this phenomenon are discussed in Chapter 8.

4.2. Single-Channel Studies. The single-channel properties of these peptides appear qualitatively similar to alamethicin. Figure 4.2 indicates that, despite the need for higher activation potentials, the ferrocenoyl ALM channels (Figure 4.2b) are qualitatively comparable to ALM. The cxFc-ALM channels exhibit more complex gating kinetics than do the other peptides; there appear to be two distinct populations, the first having lifetimes of approximately 500-3000 msec and an additional group having 10-50 msec lifetimes (Figure 4.2c). Note that the short lifetime openings appear more frequently when the channel is already open to the 2nd conductance level. Gaussian curves were fitted to the single-channel conductance histograms for ALM, Fc-ALM and cxFc-ALM shown in Figure 4.3. The results of the single channel subconductance levels are summarized in table 4.1.

4.3. Redox Activity of Fc-ALM. The effect of oxidative conditions on channel formation was explored using two approaches, employing the oxidizing agent cerium ammonium nitrate. In the first experiments excess CAN was added directly to the *cis* side of the PLB apparatus during single-channel recording. The quantity of CAN added to the PLB apparatus was tenfold the concentration required to oxidize the peptide, as determined by redox titrations (data not shown). In subsequent experiments, the ferrocenoyl peptides were combined with buffered CAN before addition to the PLB apparatus.

The *in situ* addition of CAN causes a time-dependent diminution of Fc-ALM channels at constant bilayer potential; in the case of cxFc-ALM, the long lifetime openings appear to be selectively eliminated. This effect was not observed when CAN was added to the *trans* side of the apparatus, indicating that the C-terminus side of the peptide does not penetrate the bilayer. CAN appears to not exhibit these effects on alamethicin channels, as shown in Figure 4.4.

FIGURE 4.2. SINGLE CHANNEL BEHAVIOR OF C-TERMINUS FERROCENOYL ALAMETHICIN DERIVATIVES. This figure shows three seconds of single channel recording from 0.375 μM ALM (panel A), 0.25 μM Fc-ALM (panel B) and 0.25 μM cxFc-ALM (panel C). Peptides were added to the *cis* chamber of the PLB apparatus; each chamber contains 2 ml of buffered electrolyte (0.5 M KCl, 10 mM BES, pH 7.0). The following potentials were applied: +140 mV, panel A; +170 mV, panel B; +136 mV, panel C.

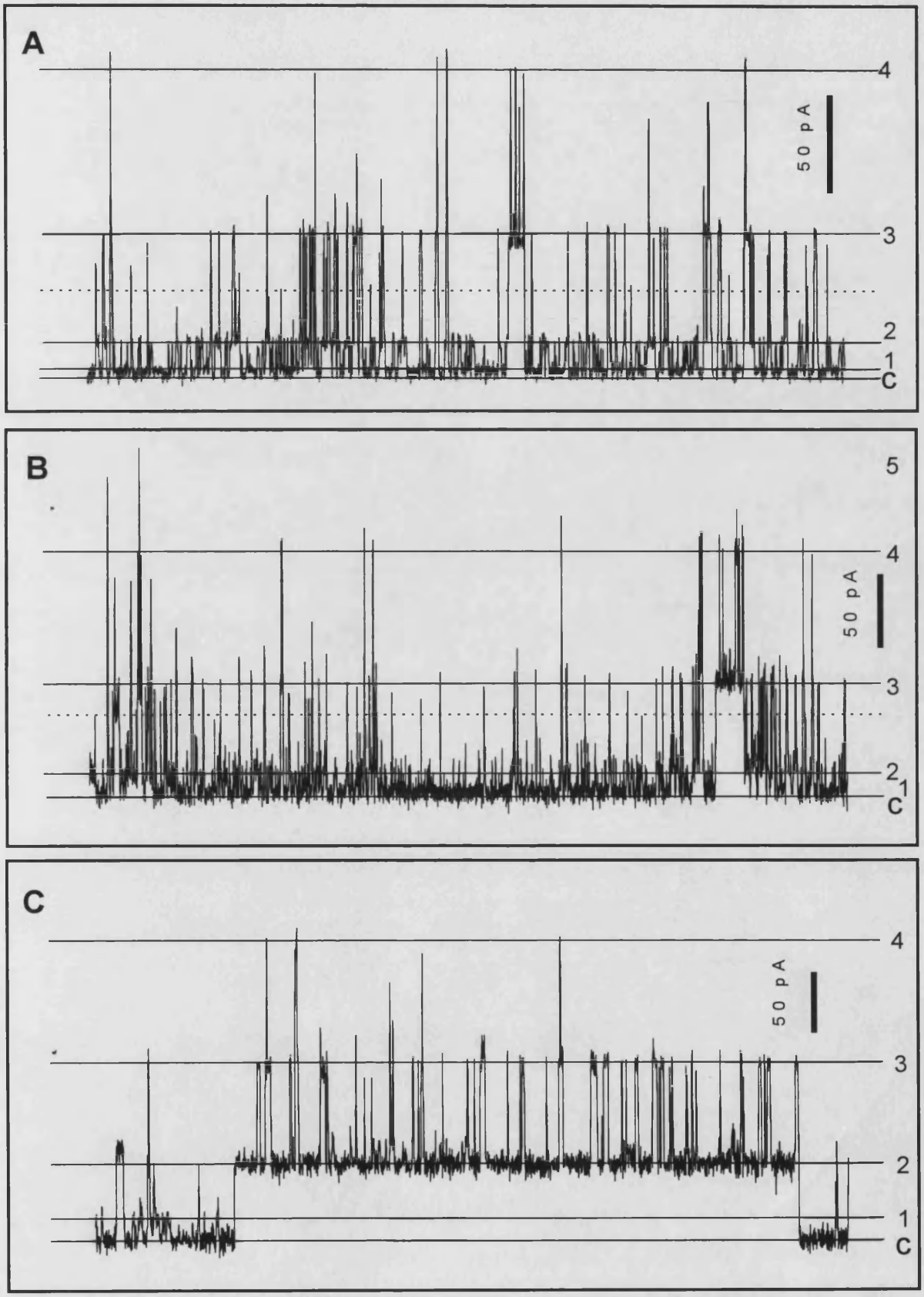

FIGURE 4.2

FIGURE 4.3. CONDUCTANCE LEVEL HISTOGRAMS FOR C-TERMINUS FERROCENOYL ALAMETHICIN DERIVATIVES. This figure shows histograms from 120 seconds of single channel recording from 0.375 μM ALM (panel A), 0.25 μM Fc-ALM (panel B) and 0.25 μM cxFc-ALM (panel C).

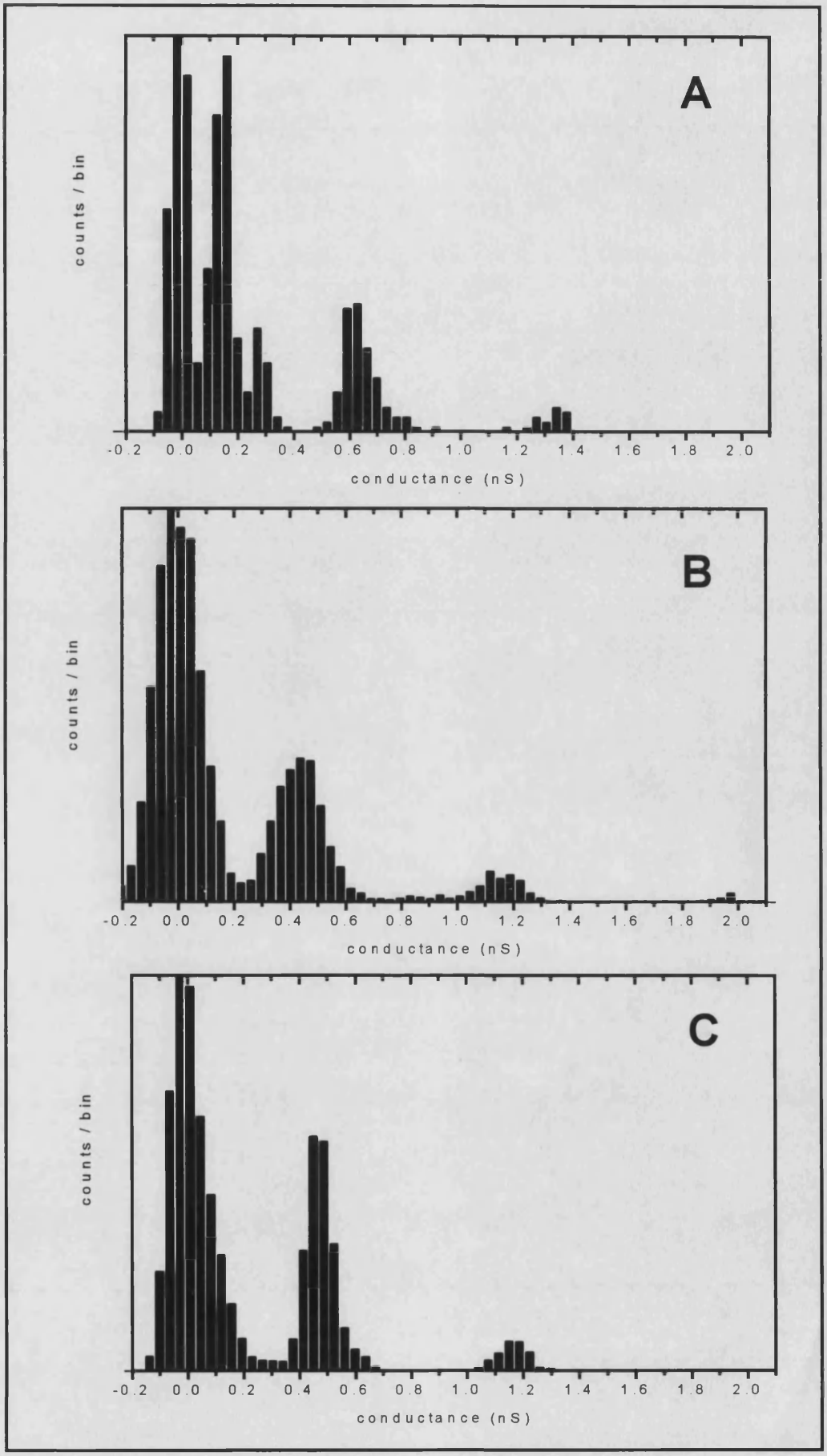
A
counts / bin
-0.2 0.0 0.2 0.4 0.6 0.8 1.0 1.2 1.4 1.6 1.8 2.0
conductance (nS)
B
counts / bin
-0.2 0.0 0.2 0.4 0.6 0.8 1.0 1.2 1.4 1.6 1.8 2.0
conductance (nS)
C
counts / bin
-0.2 0.0 0.2 0.4 0.6 0.8 1.0 1.2 1.4 1.6 1.8 2.0
conductance (nS)

FIGURE 4.3

	conductance (nS)				
level	**ALM**	**Fc-Alm**	**Fc-Alm(ox)**	**cxFc-ALM**	**cxFc-ALM(ox)**
1	0.14[b]	0.15[b]	0.10	0.11[b]	0.11[b]
2	0.28	0.24[b]			0.37
3	0.62	0.43	0.52	0.46	0.68
4	1.34	1.15		1.16	0.84
5		1.75[b]		1.70[b]	0.99
6					1.14[b]
7					2.03[b]

b: indicates manual measurement

TABLE 4.1. CONDUCTANCE LEVELS FROM SINGLE CHANNEL RECORDINGS OF REDUCED AND OXIDIZED C-TERMINUS FERROCENOYL PEPTIDES.

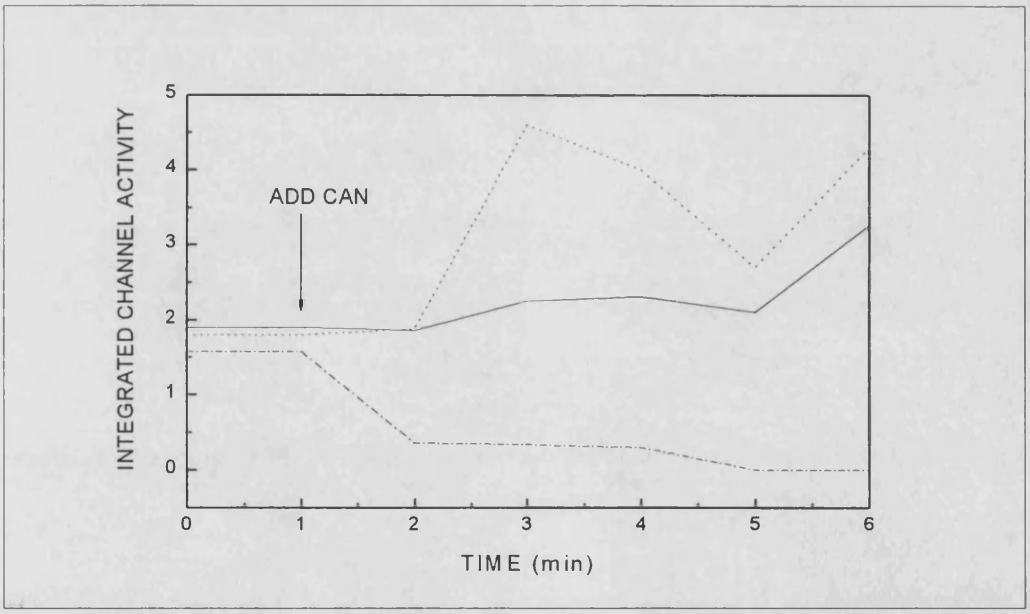

FIGURE 4.4. TEMPORAL BEHAVIOR OF C-TERMINUS REDOX ACTIVE PEPTIDES IN THE PRESENCE OF CAN. This figure shows average channel activity levels from ALM (————), Fc-ALM (·-·-·-

calculated by integration. Data-points are normalized to match the signal level of ALM before the addition of CAN. The zero time point was derived from 1 min of channel recording before the addition of CAN (indicated by arrow).

It is noteworthy that channel activity of the oxidized Fc-ALM peptides can be restored by increasing the bilayer potential by 25-35 mV (data not shown). Furthermore, the increase in net CFP channel conductance that occurs during bilayer experiments was not observed where oxidizing agent is employed. The presence of CAN diminishes the gating to such an extent that it was not possible to collect I-V data for Fc-ALM and cxFc-ALM. However, CAN had no effect on the macroscopic behavior of ALM. Thus, additional evidence has been provided that oxidative conditions elicit a specific effect on the ferrocenoyl peptides .

Premixing of peptide and CAN produced similar results. Figure 4.5 shows representative traces of Fc-ALM (panel A) and cxFc-ALM (panel B) pretreated with CAN. Note that two separate sections of a channel recording are shown side-by-side in panel A due to sparseness of Fc-ALM channel activity. In both cases the final concentration of peptide added to the PLB apparatus was about twice that required to elicit channel activity by the corresponding peptide in the absence of CAN (see Figure legend). Conductance histograms shown in (Figure 4.6) suggest that the oxidized peptides mainly open to the first one or two conductance levels, in contrast to the reduced peptides (Figure 4.3), and that the percentage of time spent in the closed state is greater for the oxidized peptides. Table 4.1 also summarizes the results of multiple Gaussian fittings to these histograms, although these results may be somewhat inaccurate due to short opening times (bandwidth limited).

FIGURE 4.5. SINGLE CHANNEL RECORDINGS OF C-TERMINUS FERROCENOYL PEPTIDES PREMIXED WITH CAN. Single channel recordings from 0.5 μM Fc-ALM (panel A) and 0.5 μM cFc-ALM (panel B) pre-mixed for 3 min with 20 μl 10 mM CAN and 20 μl. electrolyte buffer. This quantity of CAN is tenfold the molar ratio required to fully oxidize the either ferrocenecarboxylic acid or ferrocenedicarboxylic acid in 3 min (determined by spectrophotometric titration, data not shown). Peptides were added to the *cis* chamber of the PLB apparatus; each chamber contains 2 ml. of buffered electrolyte (0.5 M KCl, 10 mM BES, pH 7.0). The following potentials were applied: +185 mV, panel A; and +96 mV, panel B. Data in each case is displayed on two different time-scales.

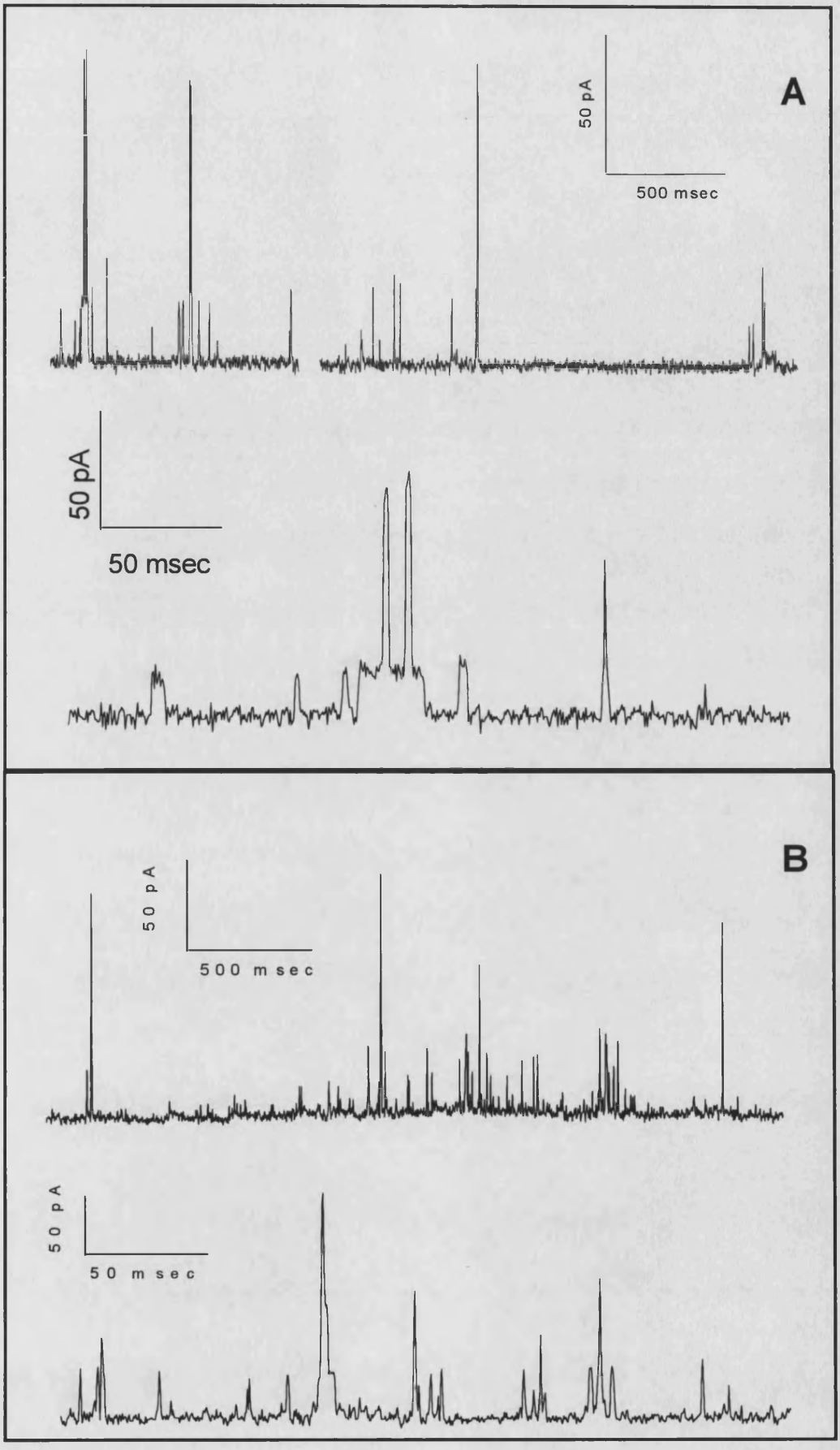

FIGURE 4.5

FIGURE 4.6. CONDUCTANCE LEVEL HISTOGRAMS FOR C-TERMINUS FERROCENOYL ALAMETHICIN DERIVATIVES PREMIXED WITH CAN. This figure shows histograms from 120 seconds of single channel recording from 0.5 μM Fc-ALM (panel A) and 0.5 μM cFc-ALM (panel B) pre-mixed for 3 min with 20 μl 10 mM CAN and 20 μl. electrolyte buffer. The following potentials were applied: +185 mV, panel A; and +96 mV, panel B.

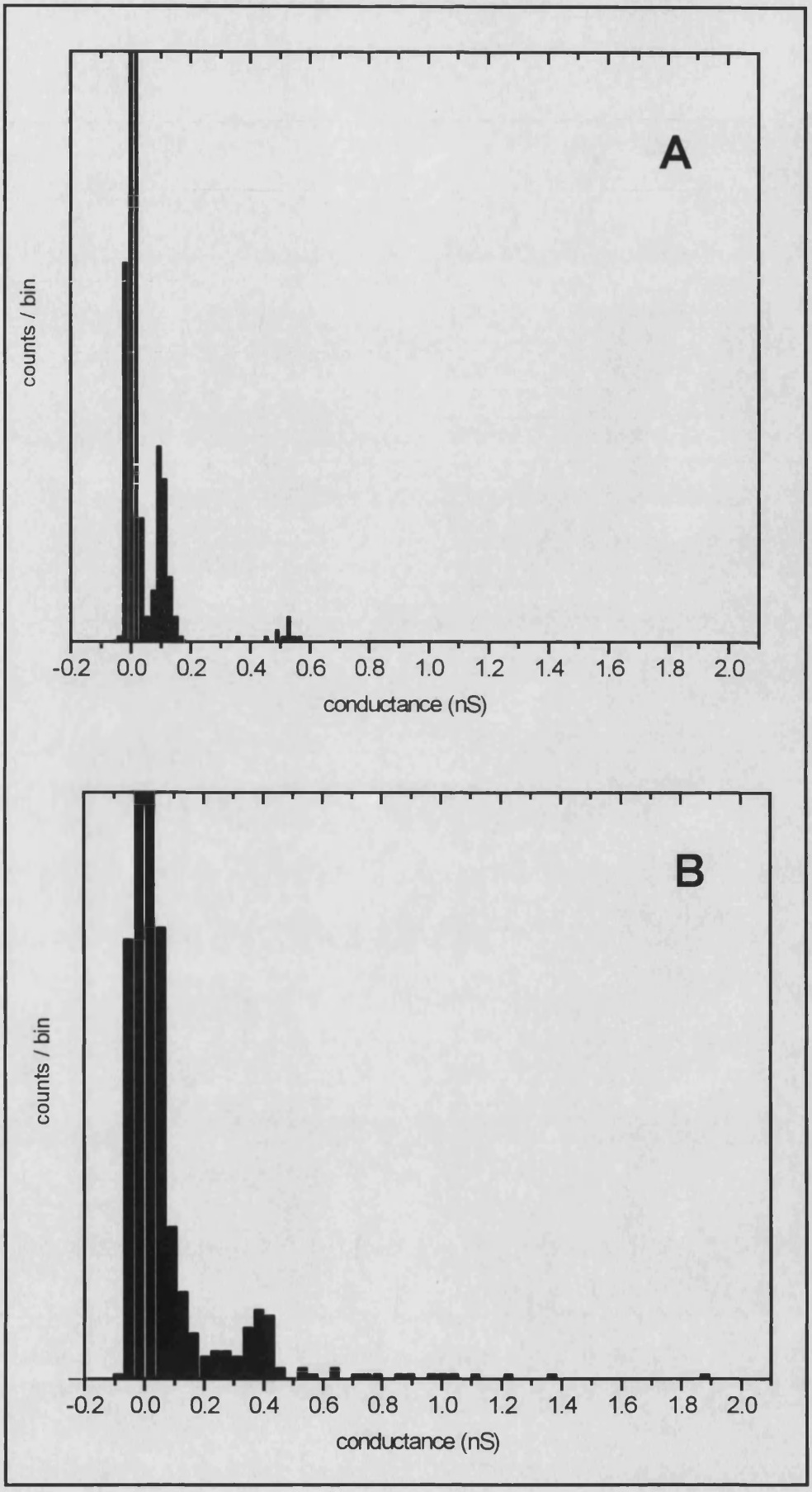
A
counts / bin
-0.2 0.0 0.2 0.4 0.6 0.8 1.0 1.2 1.4 1.6 1.8 2.0
conductance (nS)
B
counts / bin
-0.2 0.0 0.2 0.4 0.6 0.8 1.0 1.2 1.4 1.6 1.8 2.0
conductance (nS)

FIGURE 4.6

5. PLB STUDIES ON C-TERMINUS CARBOXYL AND N-TERMINUS FERROCENOYL ALAMETHICIN

In this chapter the channel-forming behavior of cxALM-Ac and cxALM-Fc is evaluated. Both macroscopic current-voltage and single channel measurements using planar lipid bilayers were conducted. When cxALM-Ac and cxALM-Fc are incorporated into diphytanoylphosphatidylcholine PLBs they form multiple conductance voltage sensitive channels similar to alamethicin. cxALM-Fc was also studied in its oxidized form by exposure to cerium ammonium nitrate or 2,3-dichloro-5,6-dicyanobenzoquinone to explore its redox behavior; Evidence for anion selectivity in the oxidized form of cxALM-Fc is also provided.

5.1. **Macroscopic Studies**. Current-voltage measurements in planar lipid bilayers were conducted by *cis* addition of the peptides to the PLB apparatus.

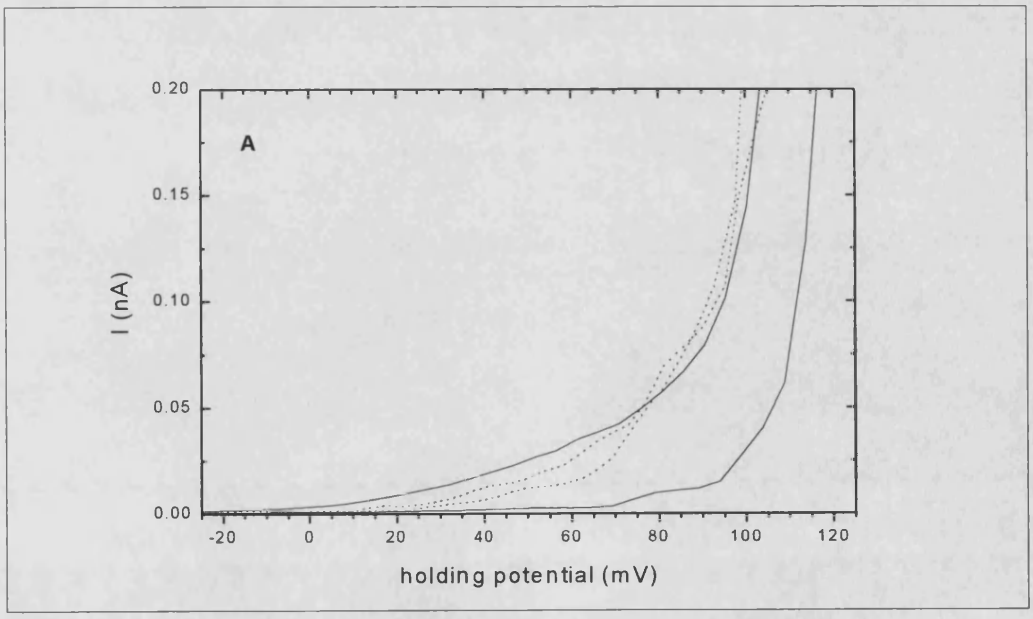

FIGURE 5.1. I-V ANALYSIS OF CARBOXY ALAMETHICIN AND N-TERMINUS FERROCENOYL ALAMETHICIN. Legend on next page.

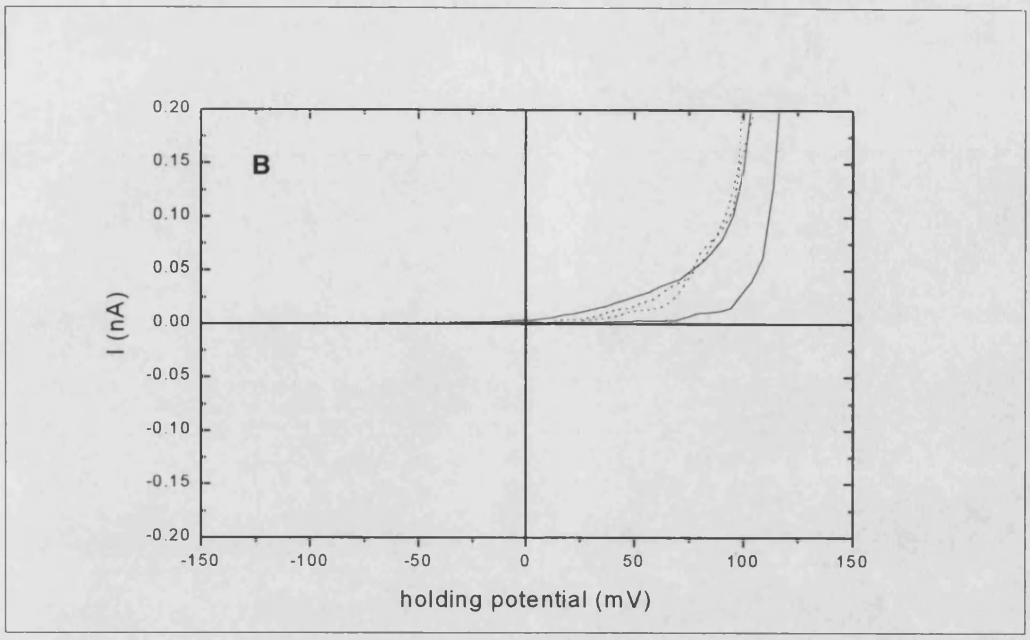

FIGURE 5.1. I-V ANALYSIS OF CARBOXY ALAMETHICIN AND N-TERMINUS FERROCENOYL ALAMETHICIN. Current-voltage (I-V) measurements in planar lipid bilayers were conducted by adding peptides to the *cis* (positive potential) chamber of the PLB apparatus to a final concentration of 2.5 μM in buffered electrolyte (0.5 M KCl, 10 mM BES, pH 7.0). In the case of cxALM-NFc, the peptide was exposed to 50 mM sodium dithionite in electrolyte buffer for 15 minutes, to insure full reduction of the ferrocene moiety, before it was added to the PLB apparatus. Triangular voltage sweeps (λ = 20 sec) from -100 mV to +100 mV for cxALM-NFc and -125 mV to +125 mV for cxALM-NAc were then applied. Currents from 20 such sweeps were averaged together and plotted as follows: cxALM-NFc (- - - - - - - -); and cxALM-NAc (————). The right hand curve of each pair represents the induced current during the ascending portion of the voltage sweep (i.e. dV/dt > 0) and the left hand curve the descending (dV/dt < 0) portion. Full scale I-V curve (panel B) shows the decreased asymmetry of channel activation of the ferrocenoyl peptide.

As a measure to ensure that all of the peptide is in the reduced state, cxALM-NFc was exposed to reducing agent prior to biophysical characterization. Figure 5.1 shows the results of macroscopic characterization. Notice the reduction in hysteresis when the N-terminus is changed from acetate to (ferrocene)acetate.

5.2. <u>Single Channel Studies</u>. As with the C-terminus ferrocenoyl analog of alamethicin, the single-channel properties of C-terminus carboxy-alamethicin and its N-terminus ferrocenoyl analog appear to form multiple

conductance level channels similar to alamethicin. Figure 5.2 shows single channel data from cxALM-NAc (5.2A), 2.5 μM cxALM-NFc (5.2B) and an expansion of the cxALM-NFc trace (5.2C). This figure indicates that, despite the need for higher peptide concentrations, the cxALM-NAc and cxALM-NFc channels are qualitatively comparable to ALM. The cxALM-NFc channels exhibit both quicker gating and lower conductance levels as compared to cxALM-NAc. Gaussian curves were fitted to the single-channel conductance histograms for ALM, Fc-ALM and cxFc-ALM shown in Figure 5.3. The single channel subconductance levels are summarized in table 5.1. These results clearly indicate that introduction of a metallocene moiety onto the N-terminus has a dramatic impact on the microscopic behavior cxALM.

HOOC-ALM-Nac			HOOC-ALM-NFc		
pS	g_n-g_{n-1}	prob	pS	g_n-g_{n-1}	prob
33(?)			14(?)		
50		9	25	11	16
90	40	4	48	23	
250	160	5	58	10	4
360	110	10	94	36	
500	140	28	102	8	
650	150	23	106	4	6
810	160	7.5	119	13	
980	170	4	136	17	5
1140	160	1	184	48	
1300	160	>1	208	24	5
			220	12	3
			256	36	1
			274	18	1

TABLE 5.1. SINGLE CHANEL SUBCONDUCTANCE LEVELS FOR CARBOXY ALAMETHICIN AND N-TERMINUS FERROCENOYL ALAMETHICIN. In cases where the Gaussian fit was unable to distinguish between two conductance levels, dashed lines indicate divisions between group conductance level probabilities. The 'g_n-g_{n-1}' column indicates the difference between neighboring conductance levels in pS.

FIGURE 5.2. SINGLE CHANNEL BEHAVIOR OF CARBOXY ALAMETHICIN AND N-TERMINUS FERROCENOYL ALAMETHICIN.
Traces from 0.5 seconds of single channel recording of 2.5 μM cxALM-NAc (panel A), 2.5 μM cxALM-NFc (panel B) and an expansion of the cxALM-NFc trace (panel C). cxALM-NFc was pretreated with reducing agent, as described in section 5.1. Peptides were added to the *cis* chamber of the PLB apparatus; each chamber containing 2 ml of KCl/BES electrolyte. The following potentials were applied: +140 mV, panel A; and +170 mV, panel B.

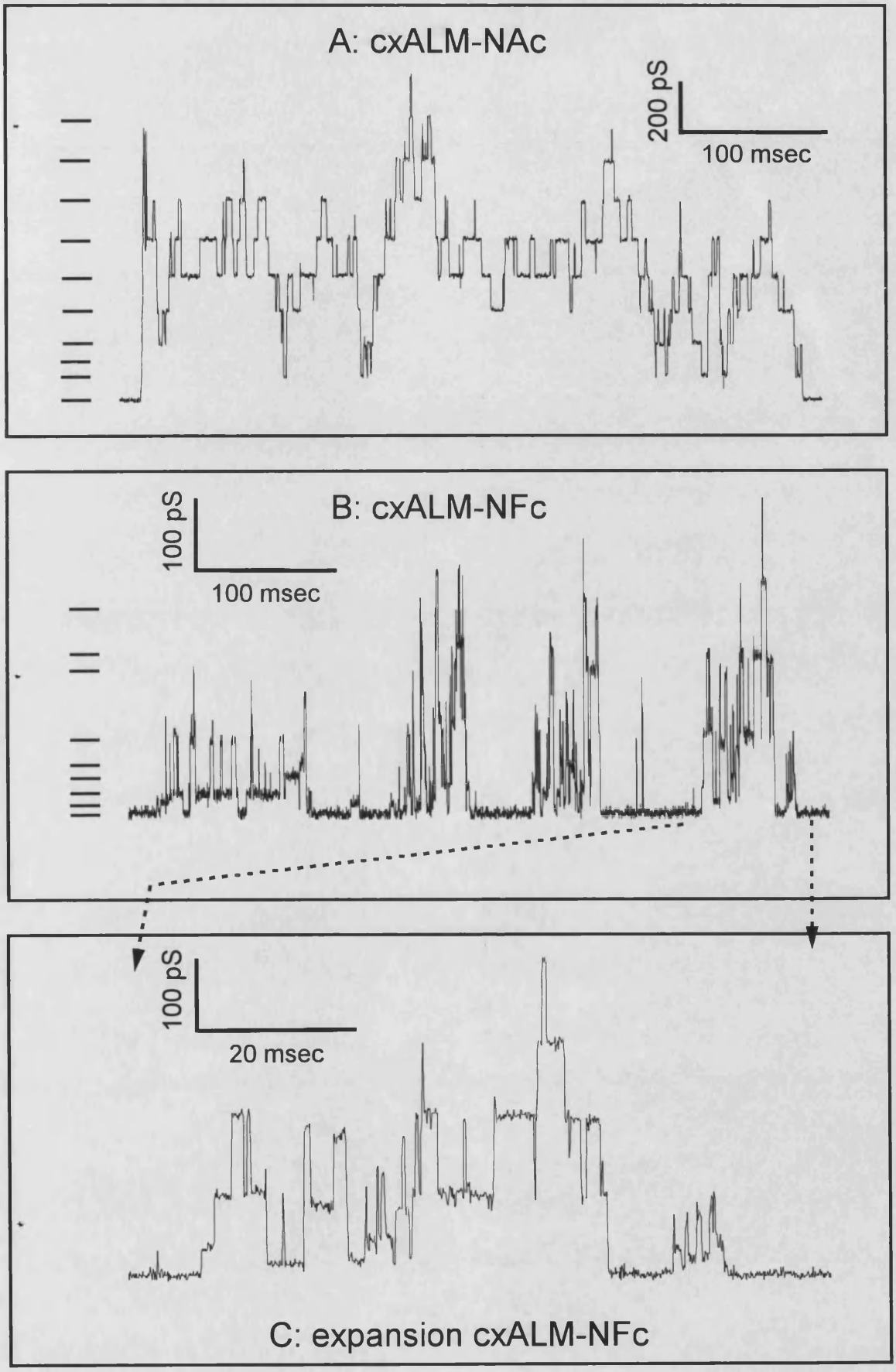
A: cxALM-NAc
200 pS
100 msec
B: cxALM-NFc
100 pS
100 msec
100 pS
20 msec
C: expansion cxALM-NFc

FIGURE 5.2

FIGURE 5.3. CONDUCTANCE LEVEL HISTOGRAMS FOR CARBOXY ALAMETHICIN AND N-TERMINUS FERROCENOYL ALAMETHICIN. This figure shows histograms from 120 seconds of single channel recording from 2.5 μM cxALM-NAc (panel A), 2.5 μM cxALM-NFc (panel B) and an expansion of the cxALM-NFc trace (panel C)

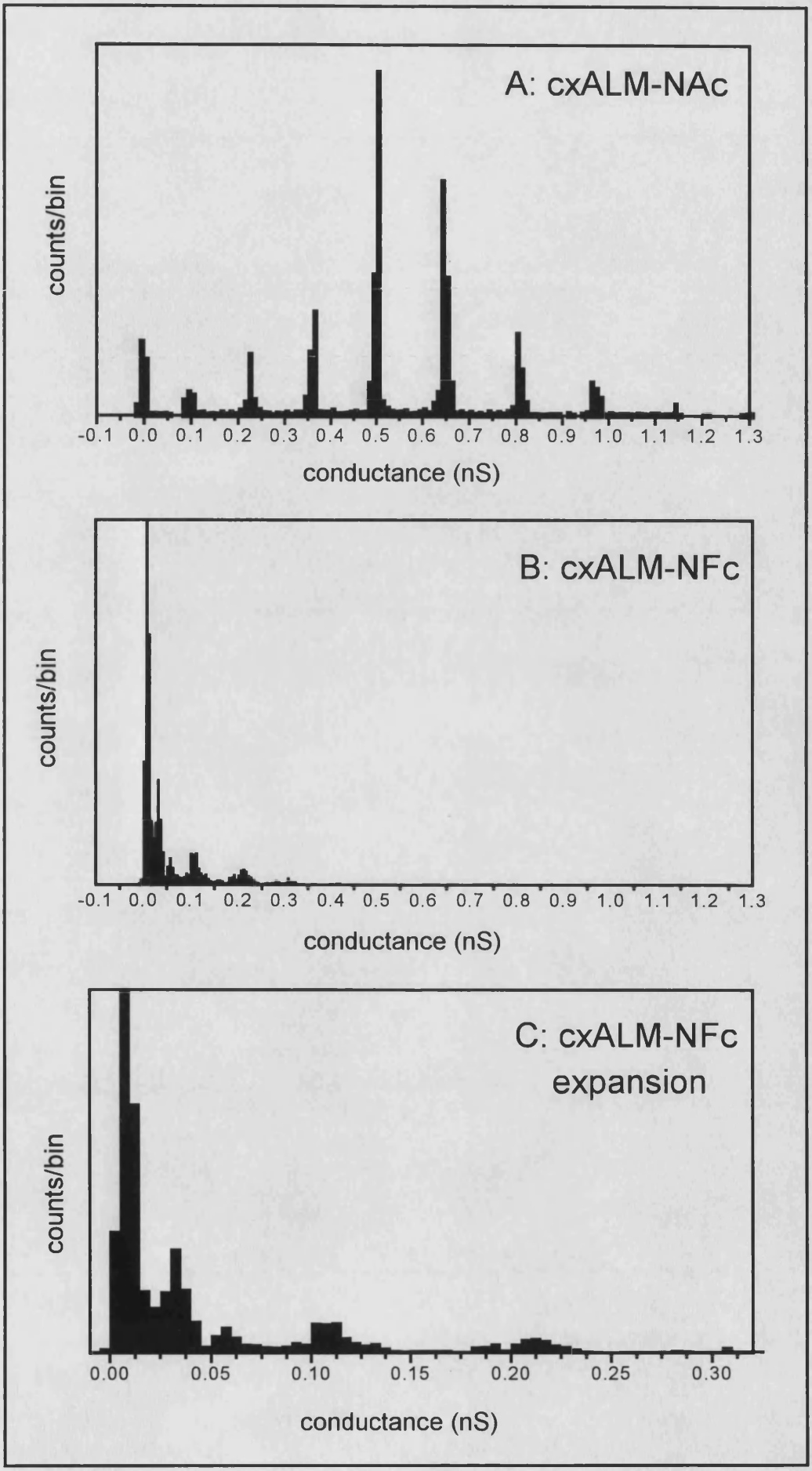
A: cxALM-NAc
counts/bin
-0.1 0.0 0.1 0.2 0.3 0.4 0.5 0.6 0.7 0.8 0.9 1.0 1.1 1.2 1.3
conductance (nS)
B: cxALM-NFc
counts/bin
-0.1 0.0 0.1 0.2 0.3 0.4 0.5 0.6 0.7 0.8 0.9 1.0 1.1 1.2 1.3
conductance (nS)
C: cxALM-NFc
expansion
counts/bin
0.00 0.05 0.10 0.15 0.20 0.25 0.30
conductance (nS)

FIGURE 5.3

5.3. <u>**DDBQ as an Alternative Oxidizing Agent**</u>. In earlier experiments we established the fact that cerium ammonium nitrate modifies channel behavior of C-terminus ferrocenoyl alamethicin *via* a specific redox-related effect, i.e. by oxidation of the ferrocene moiety from the neutral Fc[Fe(II)] to the positive Fc[Fe(III)] state. However, it has not been possible to establish if the channel-forming behavior of the oxidized peptides are further modified by the asymmetric presence of cerium (III and IV) and other ions. To address these concerns we used the oxidizing agent 2,3-dichloro-5,6-dicyanobenzoquinone in parallel single-channel experiments with cerium ammonium nitrate. The structure and putative first step redox mechanism is shown in Figure 5.4.

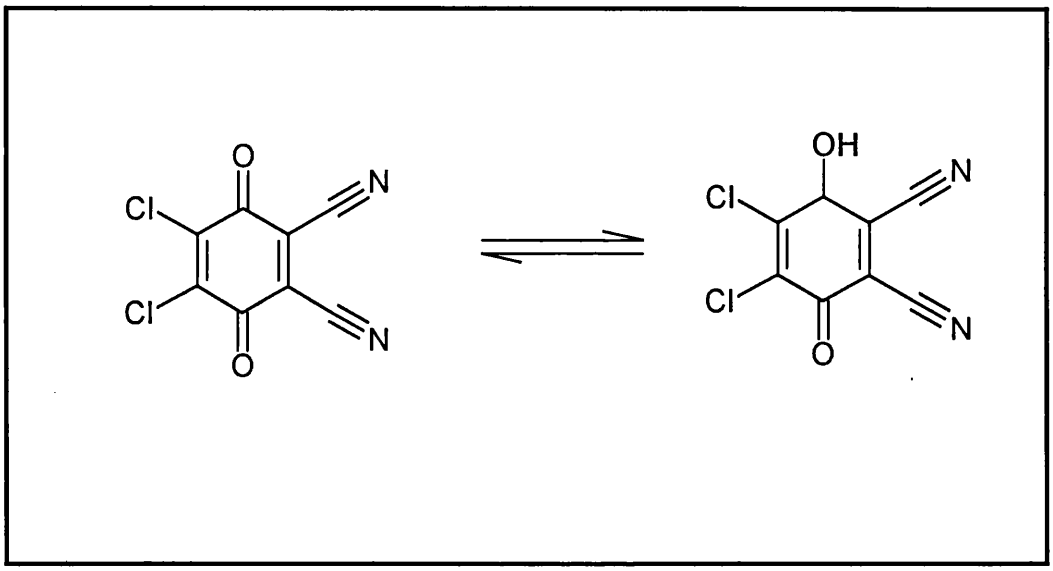

FIGURE 5.4. REDUCTION OF DDBQ TO THE SEMIQUINONE FORM. One electron oxidation in the presence of water yields the uncharged semiquinone. The anionic singlet state may be also be stabilized by resonance/induction due to the nitrile moieties.

Prior to the PLB experiments, spectrophotometric titrations were used to establish the amount of oxidant required to oxidize ferrocene completely to its Fe(III) state. In experiments where peptides are treated before addition to the PLB apparatus, a ten-fold excess of CAN or DDBQ is employed. Experiments probing the effect of *in situ* oxidation, where agent is added directly to the PLB apparatus, use a much greater excesses (~ 50-fold) to assure complete oxidation of both dissolved and

membrane-bound peptide. Related advantages of DDBQ are that it carries no counter-ion in the reduced form and its size may significantly preclude its permeation through small ion channels.

5.4. Macroscopic Studies of Oxidized cxALM-NFc. Here we compare the I-V relationships of reduced cxALM-NFc and two instances of the oxidized peptide, one where CAN is added to the *trans* side of the PLB apparatus and one where CAN is added to the *cis* side. The rationale behind comparing the macroscopic behavior of CAN added to the *cis* versus the *trans* side of the PLB relates to probing which terminus of the peptide penetrates the bilayer. If the helix bundle model of CFP formation is correct, the rectification of current by alamethicin channels is specifically due to the fact that only the N-terminus will penetrate the bilayer. Addition of oxidizing agent to the *trans* side of the apparatus would elicit an effect, relative to the control, only if the ferrocene moiety is therein exposed.

Figure 5.5 demonstrates that the reduced and oxidized N-terminus ferrocenoyl peptide channels have different ensemble properties. Additionally, it appears that there exists asymmetry with regard to the addition of oxidizing agent. Table 5.2 summarizes the results of these experiments; Here, I introduce an additional threshold index, V_{25}, that, when compared to V_t helps estimate the persistence of hysteresis. When CAN is added to the *trans* side of the BLM apparatus the ascending ($dV/dt > 0$) portion of the voltage sweep remains very similar to the I-V trace without CAN. Notice however, the marked hysteresis in the descending ($dV/dt < 0$) portion of the I-V curve, indicating that the rate at which the peptide either disassociates or comes out of bilayer is slowed relative to the reduced peptide.

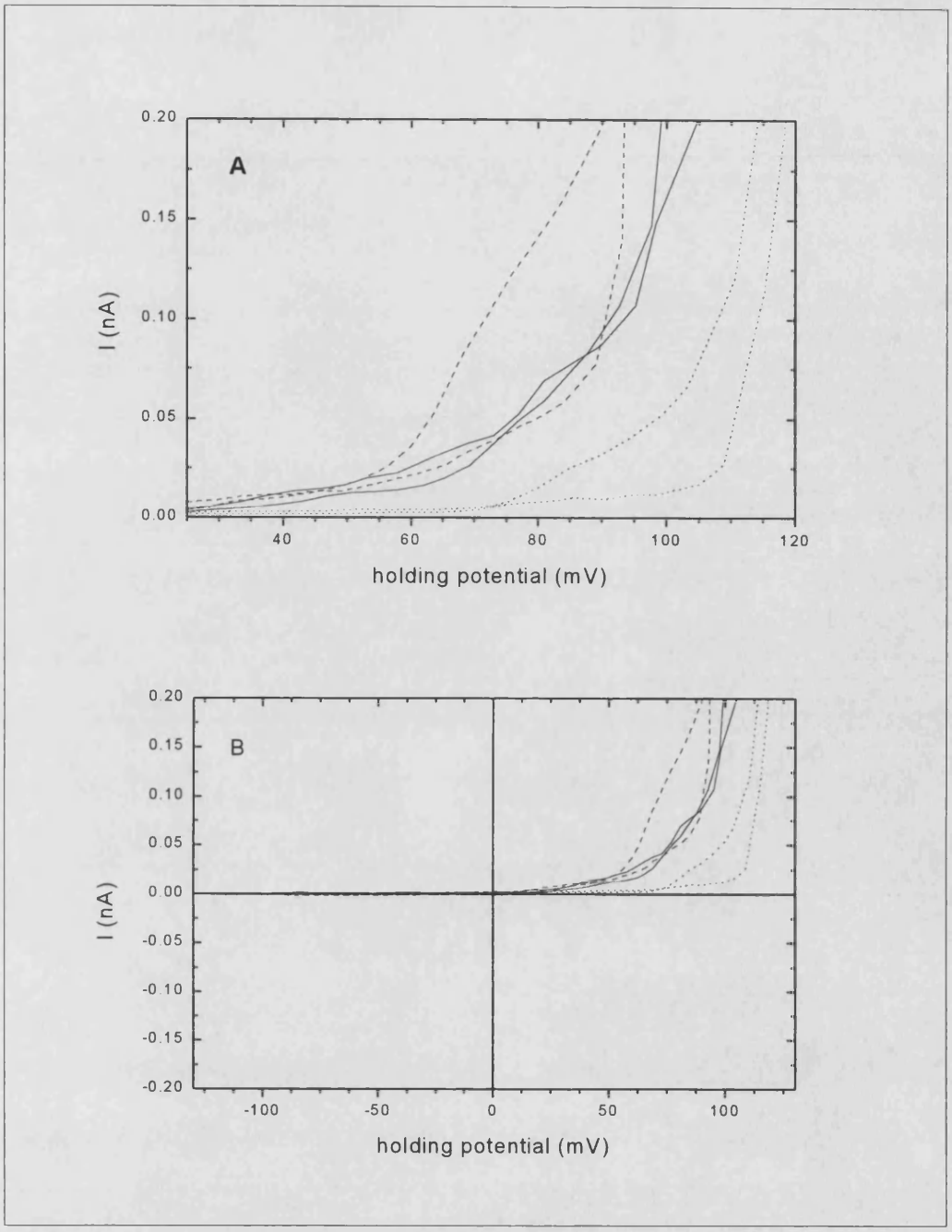

FIGURE 5.5. DIFFERENTIAL EFFECTS OF *CIS* VERSUS *TRANS* OXIDATION OF cxALM-NFc. Current-voltage measurements in planar lipid bilayers were conducted by adding peptides to the *cis* (positive potential) chamber of the PLB apparatus to a final concentration of 2.5 μM in buffered electrolyte (0.5 M KCl, 10 mM BES, pH 7.0). In the case of the *trans* CAN addition, cxALM-NFc was exposed to 50 mM sodium dithionite for 15 minutes before it was added to the PLB apparatus. CAN is added to final concentration of 2.5 mg/ml in the PLB apparatus fifteen minutes prior to I-V analysis, where appropriate. Triangular voltage sweeps (λ = 20 sec) from -100 mV to +100 mV for cxALM-NFc, -100 mV to +100 mV for cxALM-NFc [*trans* CAN]; and -115 mV to +115 mV for cxALM-NFc [*cis* CAN] were then applied. Currents from 20 such sweeps were averaged together and are plotted as follows: cxALM-NFc

(————); cxALM-NFc [*trans* CAN] (- - - - -); and cxALM-NFc [*cis* CAN] (· · · · · · ·). The right hand curve of each pair represents the induced current during the ascending portion of the voltage sweep (i.e. dV/dt > 0) and the left hand curve the descending (dV/dt < 0) portion.

	V_{t+}	V_{t-}	$V_{t+} - V_{t-}$	V_{25+}	V_{25-}	$V_{25+} - V_{25-}$
cxALM-NAc	112	94	18	98	50	48
cxALM-NFc	93	91	2	69	60	9
cxALM-NFc *cis* CAN	114	106	8	108	86	22
cxALM-NFc *trans* CAN	90	72	18	64	56	8

TABLE 5.2. DIFFERENTIAL EFFECTS OF *CIS* VERSUS *TRANS* OXIDATION OF cxALM-NFc: 25 mV AND 100 mV INDEXES.

When CAN is added to the *cis* side of the apparatus, thereby oxidizing the all of the peptide, the potential required to elicit a 25 and 100 mV ion current is markedly increased relative to reduced cxALM-NFc. Note again the substantial hysteresis seen in the *cis* CAN experiment. It is compelling to consider the hysteresis observed in the *cis* and *trans* experiments to arise from common mechanisms.

5.5. **Single Channel Studies of Oxidized cxALM-NFc**. The oxidation of cxALM-NFc by CAN or DDBQ alters its single channel properties. Figure 5.6 shows single channel recording of cxALM-NAc (5.6A), cxALM-NFc oxidized with DDBQ (5.6B) and cxALM-NFc oxidized with CAN (5.6C). To ensure equilibration oxidizing agents are to the PLB apparatus at least ten minutes prior to I-V analysis. The cxALM-NFc channels oxidized with DDBQ exhibit longer lifetime channels compared to cxALM-NFc. cxALM-NFc channels oxidized with CAN show a population of channels- long lived channels interspersed with 'spiky' short lived events. The presence of CAN also appears to diminish the presence of higher conductance levels seen with DDBQ oxidation. This effect is similar to the

one observed with the C-terminus ferrocenoyl peptides, see Chapter 4. Gaussian curves were fitted to the single-channel conductance histograms for cxALM-NFc, cxALM-NFc/DDBQ and cxALM-NFc/CAN are shown in Figure 5.7. The single channel subconductance levels are summarized in table 5.3.

HOOC-ALM-Fc/DDBQ			HOOC-ALM-Fc/CAN		
pS	g_n-g_{n-1}	prob	pS	g_n-g_{n-1}	prob
20(?)			44		nd
80	60	6	80	36	nd
			102	22	nd
			150	48	nd
180	100		180	30	nd
215	35	4	245	65	nd
305	90				
340	35	26			
460	120	41	460	215	nd
580	120	22			
725	145	2			

nd: not determined

TABLE 5.3. SINGLE CHANNEL CONDUCTANCE LEVELS FOR cxALM-NFc OXIDIZED WITH CAN AND DDBQ. Boxes indicate conductance levels similar in both oxidative conditions. As with table 5.2, dashed lines indicate divisions between conductance level probabilities. The 'g_n-g_{n-1}' column indicates the difference between neighboring conductance levels in pS.

FIGURE 5.6. DIFFERENTIAL EFFECTS OF CAN AND DDBQ: SINGLE CHANNEL BEHAVIOR OF CARBOXY ALAMETHICIN AND N-TERMINUS FERROCENOYL ALAMETHICIN. This figure shows 0.5 seconds of single channel recording from 2.5 μM cxALM-NAc (panel A), 2.5 μM cxALM-NFc oxidized with DDBQ (panel B) and 2.5 μM cxALM-NFc oxidized with CAN (panel C). Where appropriate, CAN or DDBQ is added to final concentration of 2.5 or 0.6 mg/ml, respectively, in the PLB apparatus at least ten minutes prior to I-V analysis. The peptide producing the trace in panel A was pretreated with reducing agent, as described in section 5.1. Peptides were added to the *cis* chamber of the PLB apparatus; each chamber containing 2 ml of KCl/BES electrolyte. The following potentials were applied: +140 mV, panel A; and +145 mV, panel B; and +40 mV, panel C.

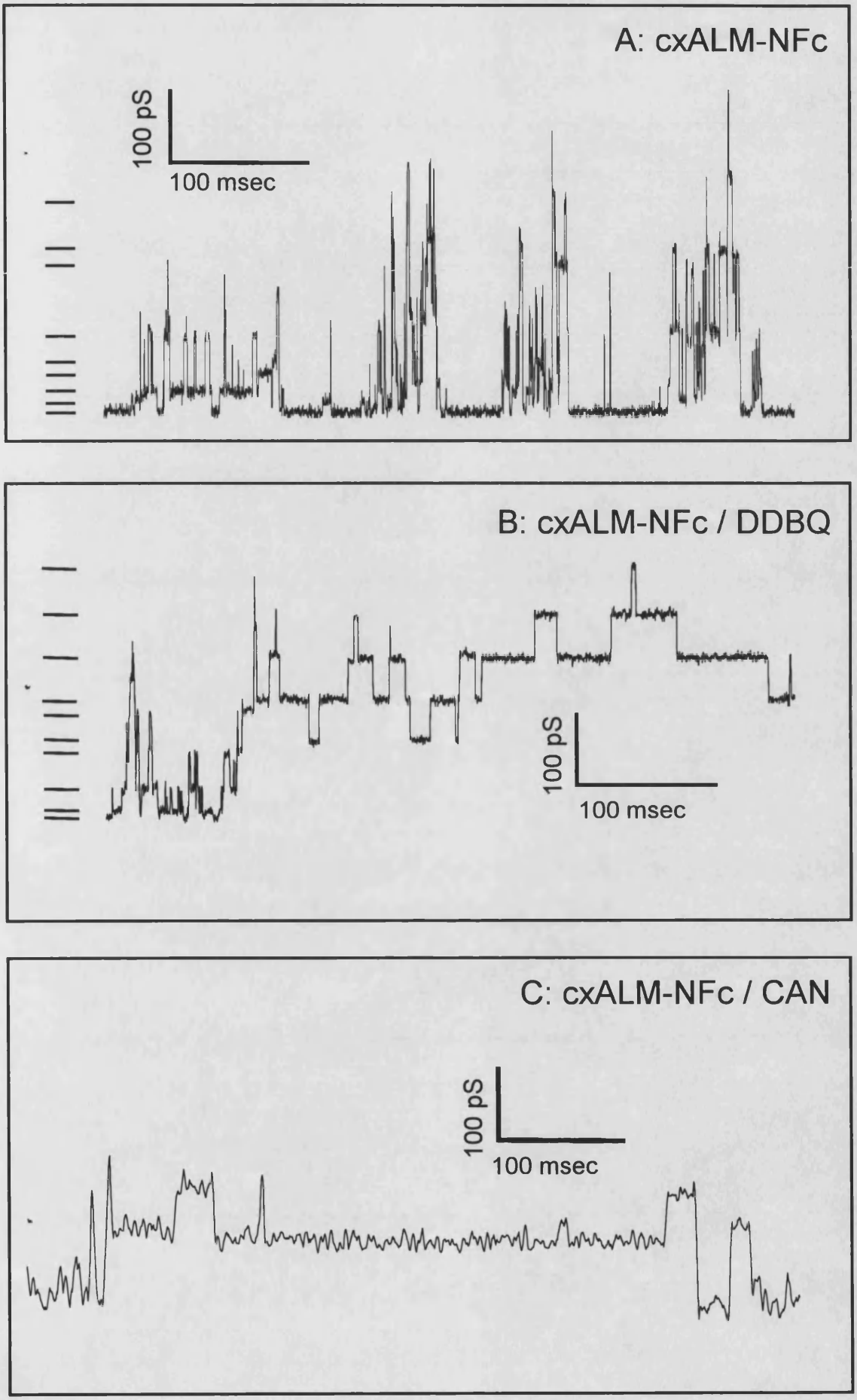
A: cxALM-NFc
100 pS
100 msec
B: cxALM-NFc / DDBQ
100 pS
100 msec
C: cxALM-NFc / CAN
100 pS
100 msec

FIGURE 5.6

FIGURE 5.7. CONDUCTANCE LEVEL HISTOGRAMS: SINGLE CHANNEL BEHAVIOR OF CARBOXY ALAMETHICIN AND N-TERMINUS FERROCENOYL ALAMETHICIN EXPOSED TO CAN AND DDBQ. This figure shows histograms from 120 seconds of single channel recording from 2.5 μM cxALM-NAc (panel A), 2.5 μM cxALM-NFc oxidized with DDBQ (panel B) and 2.5 μM cxALM-NFc oxidized with CAN (panel C).

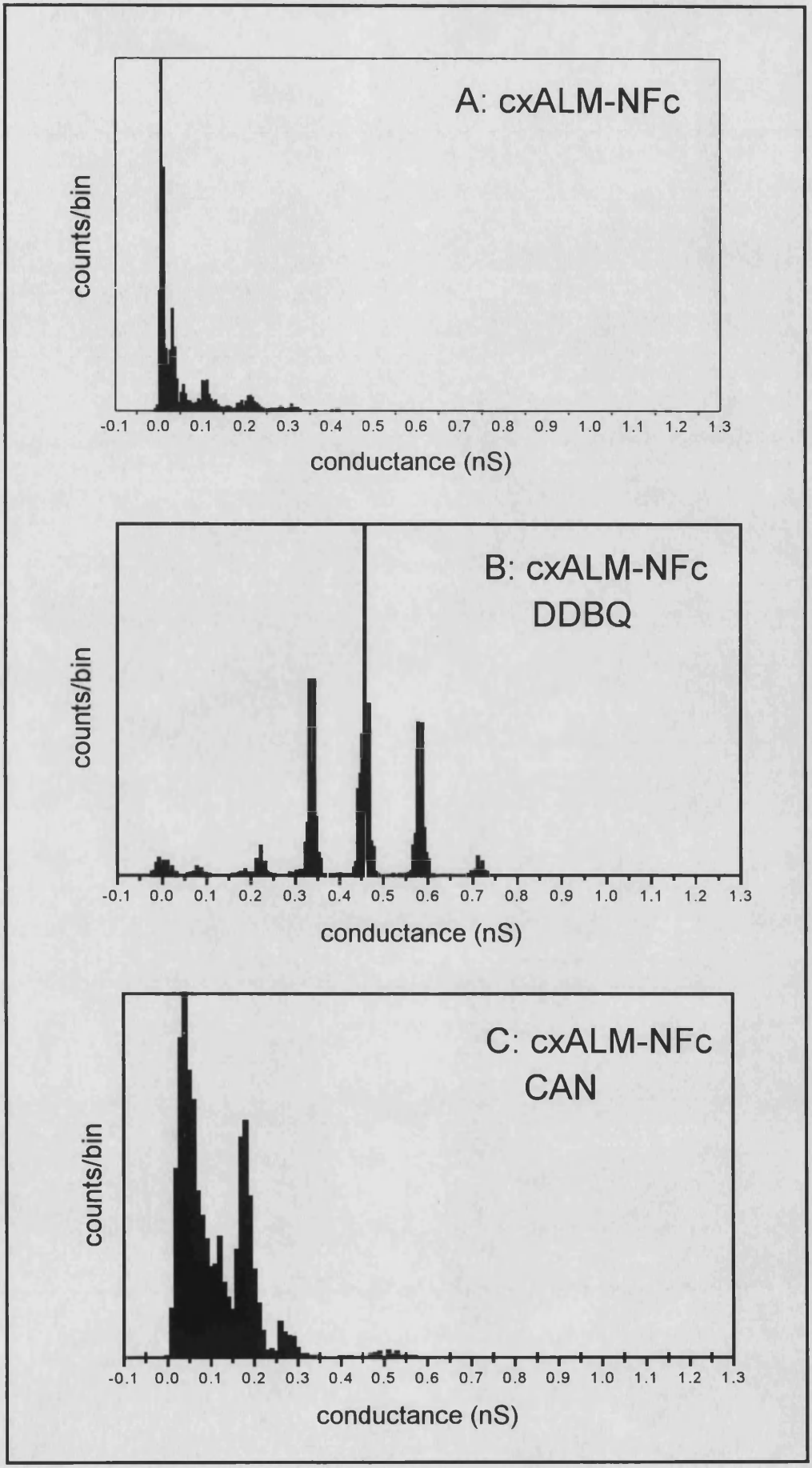
A: cxALM-NFc
counts/bin
-0.1 0.0 0.1 0.2 0.3 0.4 0.5 0.6 0.7 0.8 0.9 1.0 1.1 1.2 1.3
conductance (nS)
B: cxALM-NFc
DDBQ
counts/bin
-0.1 0.0 0.1 0.2 0.3 0.4 0.5 0.6 0.7 0.8 0.9 1.0 1.1 1.2 1.3
conductance (nS)
C: cxALM-NFc
CAN
counts/bin
-0.1 0.0 0.1 0.2 0.3 0.4 0.5 0.6 0.7 0.8 0.9 1.0 1.1 1.2 1.3
conductance (nS)

FIGURE 5.7

5.6. Evidence for Anion Selectivity in Oxidized cxALM-NFc Channels.

During the single channel characterization of *trans* CAN oxidized cxALM-NFc we observed persistent channels at very modest to zero holding potential values. Since we failed to observe this behavior with DDBQ oxidation, it was hypothesized that the ionic excess due to the *trans* CAN might be revealing anion selectivity in channels formed from oxidized cxALM-NFc. The experiments described in this section seek to verify this hypothesis. To this end, four types experiments were conducted: 1) voltage-step experiments measuring the time dependent effect of added trans CAN on macroscopic conductance; 2) voltage-step experiments conducted after equilibration of the *trans* CAN treated peptide to obtain a macroscopic value of V_{rev}; 3) voltage-step experiments using DDBQ as the oxidizing agent, after equilibration, to reproduce the ionic imbalance in the *trans* CAN experiments, potassium nitrate is added to the *trans* side and macroscopic conductance properties measured; and measurement of V_{rev} in DDBQ oxidized channels with asymmetric electrolyte concentrations. It is important to stress that although, it is possible to determine if oxidation increases anion selectivity (or more precisely, the ratio of anion to cation selectivity), it is not possible to quantitate the difference. A *sine qua non* for application of the Goldman-Hodgkins-Katz equation to determine permeability ratios is that exact concentrations of all ionic species be known. Addition of an oxidizing agent to a complex mixture of redox active peptide, lipid, electrolyte and buffering agent precludes one knowing its exact ionic makeup, it is also possible that there are electrochemical effects on ion composition as well. So the estimates of permeability ratios shown below should be considered first order approximations.

Figure 5.8A shows the results of a typical voltage-step experiment of the first category described above. Peptides were added to the *cis* chamber of the PLB apparatus. To ensure full reduction, the peptide was pretreated with the reducing agent sodium dithionite. Identical results

were obtained using ascorbic acid (data not shown). The time dependent increase in channel activity in the absence of an applied transbilayer potential (0 mV) is due to ionic potential due to the difference in ionic compositions of the *cis* and *trans* wells. In these experiments we guaranteed that the observed behavior was not due to membrane perturbation by analyzing these traces at the single channel level. Indeed, even after more than one hour cycling through the voltage-step regime well resolved channels were still observed. Finally, it is worth noting that the increase in channel activity was reversed by the addition of an equivalent quantity of CAN to the *cis* side of the PLB apparatus (data not shown).

The next figure (5.8B) shows a typical trace aimed at finding V_{rev} for the CAN experiment. Here the system was allowed to reach equilibrium before the recording—this typically requires 15-20 minutes of cycling through the voltage-step protocol. The reversal potential was determined by calculating the mean signal level at each holding potential and then averaging together these values over 5 cycles. The results are plotted in Figure 5.8C, the line represents the linear regression best-fit ($r = 0.946$), giving a function zero at V_{rev}= -65 mV.

In the third series experiments DDBQ was used as the oxidizing agent. In this case, no channel activity is observed in the absence of a transbilayer potential, even after prolonged times (more than 2 hours, data not shown). The top panel of Figure 5.8D shows a typical voltage-step trace beginning with the *trans*-side addition of KNO_3 to a concentration of 12.5 mM, the concentration of nitrate ion present in the *trans*-side CAN experiments. Here, a nearly instantaneous increase in channel activity at 0 mV potential is observed. This zero potential activity was eliminated by the addition of an equivalent quantity of KNO_3 to the *cis* side of the bilayer.

FIGURE 5.8. VOLTAGE-STEP EXPERIMENTS WITH cxALM-NFc. Panel **A**: cxALM-NFc was added to the *cis* chamber of the PLB apparatus to a final concentration of 2.5 μM, each chamber containing 2 ml of KCl/BES electrolyte. The peptide was pretreated with reducing agent, as described in section 5.1. The following potentials were applied in cyclical fashion: –50 mV, +110 mV, +35 mV, 0 mV. Data was collected for around 30 seconds at each holding potential. Data was filtered at 5 KHz. After equilibration CAN was added to a final concentration of 2.5 mg/ml in the *trans* well, then data was collected for an additional 10-12 minutes. Care was taken to not over-stir or disrupt the bilayer upon addition of the oxidizing agent. The data shown in the top panel of Figure 5.8A has been averaged over 10 data points for clarity. The bottom panel shows the holding potentials.
B: shows a typical trace aimed at finding V_{rev} for the CAN experiment. Conditions were identical to those described in 5.8A, with the exception that the system was allowed to come to equilibrium before the commencement of recording; the trace shown in the top panel represents the original data averaged over 30 points. The following voltage steps were employed in these experiments: +100 mV, -33 mV, -43 mV, -53 mV, -63 mV, -73 mV and -83 mV. The reversal potential was determined by calculating the mean signal level at each holding potential and then averaging together these values over 5 cycles.
C: The results from 5.8B are plotted, the line represents a linear regression best-fit (r=0.946), giving a V_{rev}= -65 mV.
D: DDBQ oxidized peptide followed by the *trans*-side addition of KNO_3 to a concentration of 12.5 mM, the concentration of nitrate ion present in the *trans*-side CAN experiments. DDBQ was added to the *trans* side of the apparatus as described for CAN above.

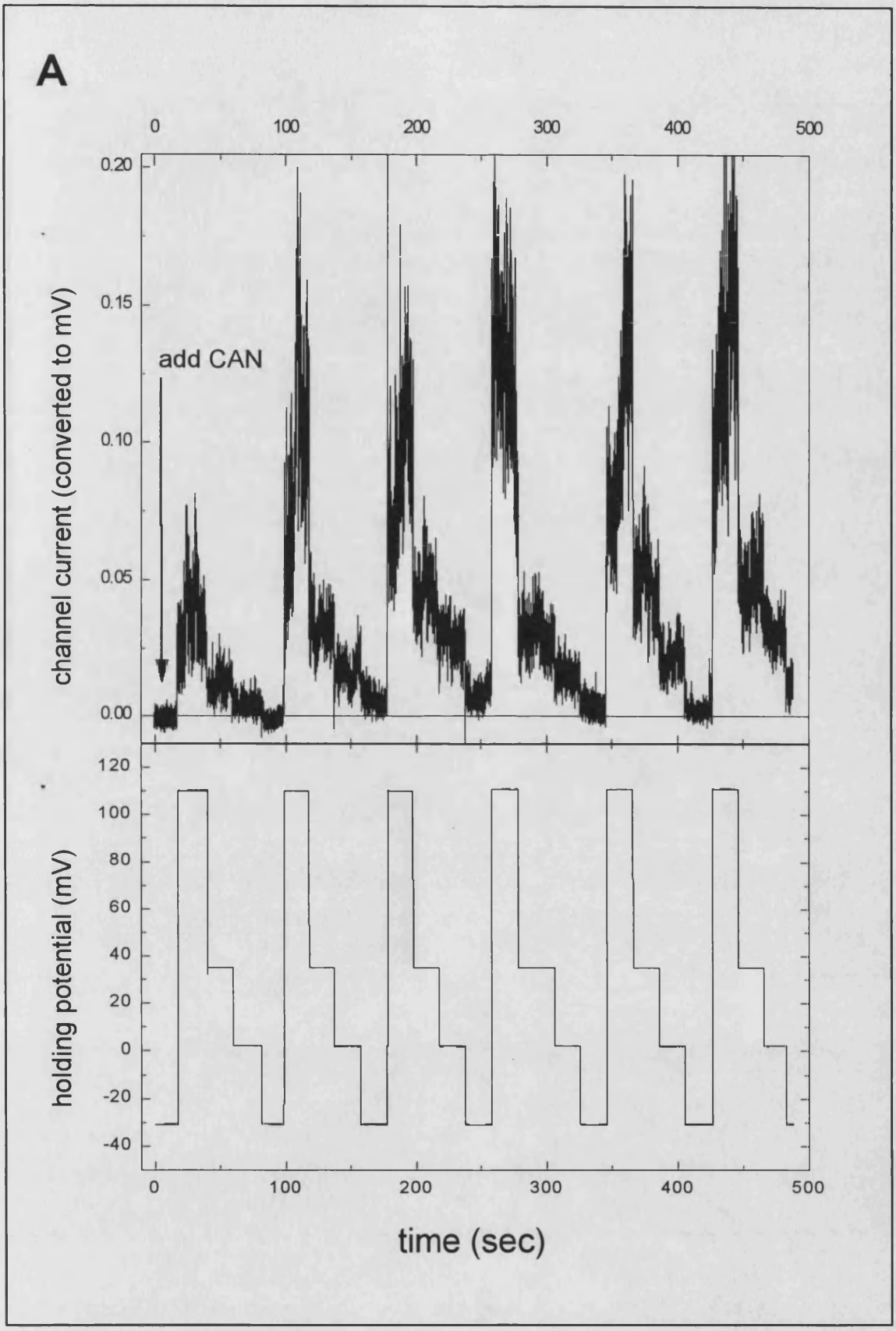

FIGURE 5.8 page 1

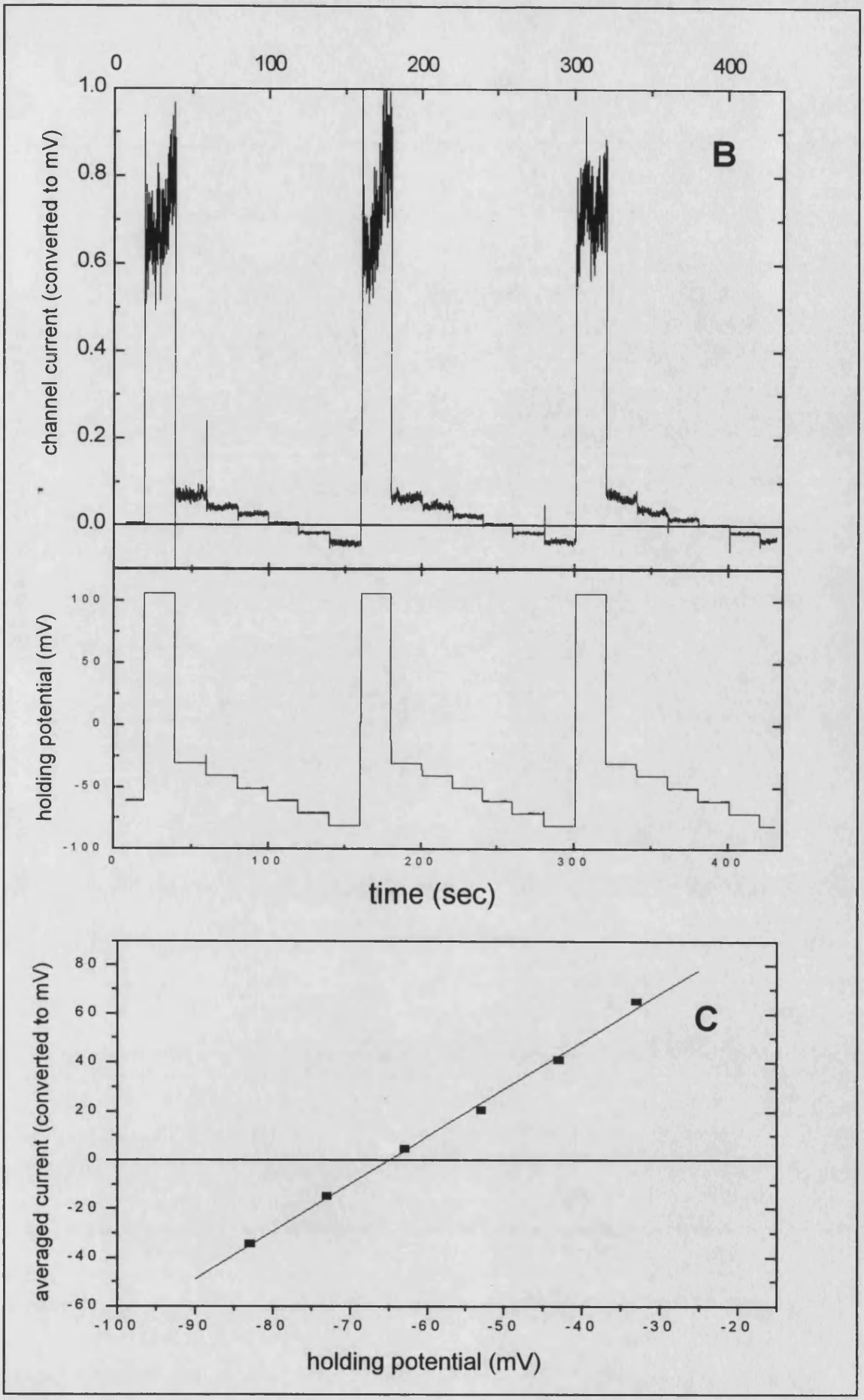

FIGURE 5.8 page 2

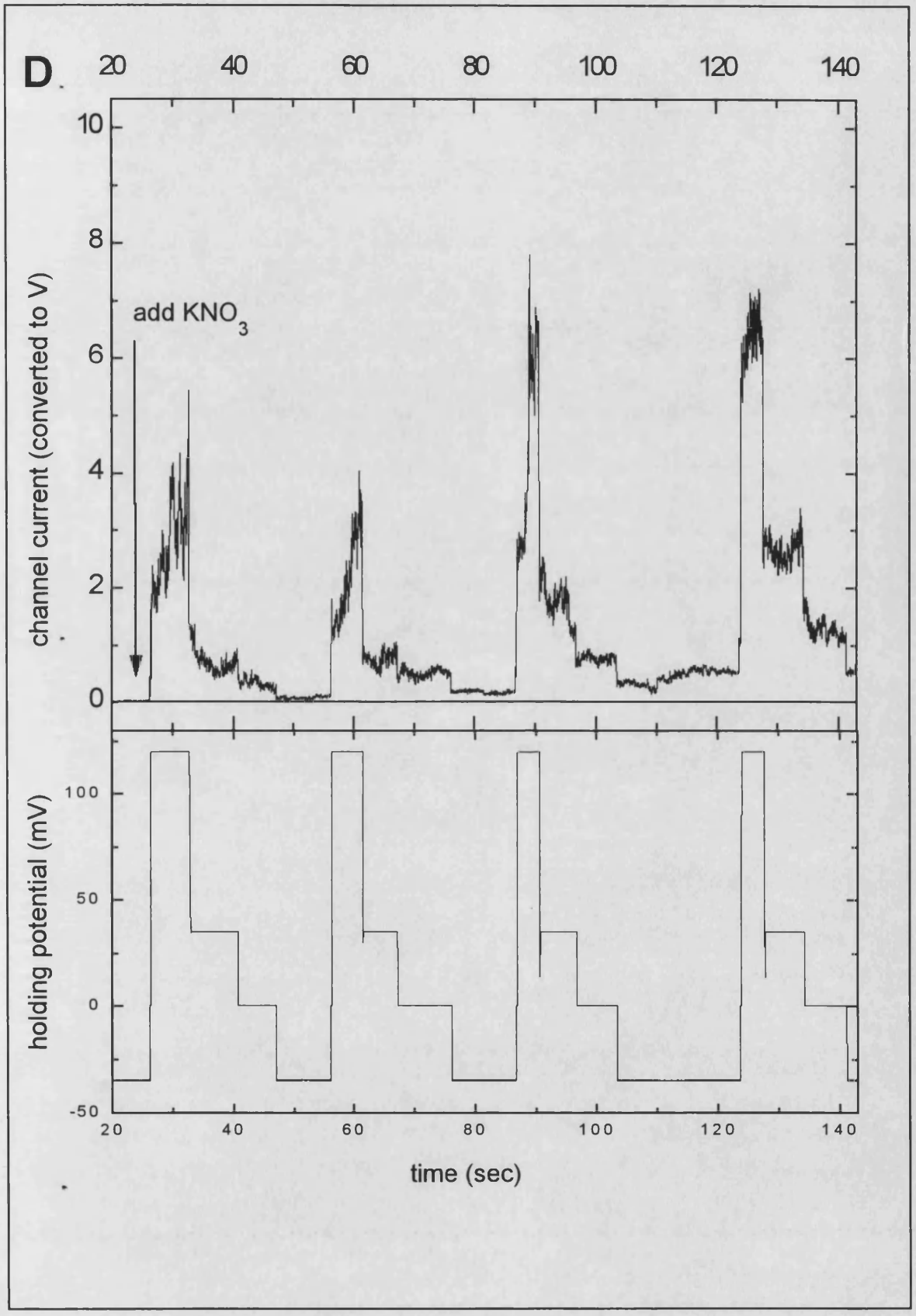

FIGURE 5.8 page3

The last series of experiments employ asymmetric buffered electrolyte concentrations: 0.5 M KCl in the *cis* side of the apparatus and 1.0 M KCl in the *trans* side. Figure 5.9 panel A shows the results of a typical voltage-step experiment with 2.5 μM reduced cxALM-NFc added to the *cis* well. A reversal potential of V_{rev}= -26 mV applied in the GHK equation yields a permeability ratio, $P_K/P_{Cl} \approx 0.9$. When the equivalent experiment was conducted, with the DDBQ oxidized peptide a marked increase in V_{rev} was observed, as shown in Figure 5.9B. A value, V_{rev}= -84.5 mV, for the reversal potential was determined as described above. If one assumes that DDBQ and its reduced forms contribute nothing to the permeable ion concentration application of the GHK equation gives $P_K/P_{Cl} \approx 0.12$.

FIGURE 5.9. CALCULATING V_{rev} FOR REDUCED AND OXIDIZED cxALM-NFc CHANNELS. **A:** The following electrolyte concentrations were used in these experiments: 0.5 M KCl in the *cis* side of the apparatus and 1.0 M KCl in the *trans* side. The results of a typical voltage-step experiment with 2.5 μM *cis* cxALM-NFc in the reduced state are shown. The following voltage steps were employed in these experiments: +10 mV, 0 mV, -10 mV, -20 mV, -30 mV and -40 mV. After equilibration of conductance levels, five cycles of data were recorded and processed as described above. The averaged channel activity at +10 mV was omitted from the calculations, as the conductance levels were exceedingly high and varied between sweeps. The reversal potential obtained from the zero value of the linear regression equation (r = 0.923) is V_{rev}= -26 mV.
B: When the equivalent experiment was conducted, with the addition of DDBQ (final concentration = 0.6 mg/ml) to the *trans* side of the apparatus, a marked increase in V_{rev} was observed. After equilibration, recordings were taken with holding potentials cyclically stepped through: -60 mV, -70 mV, -80 mV, -90 mV and -100 mV. The equation of linear regression (r = 0.952) for this data yields V_{rev}= -84.5 mV.

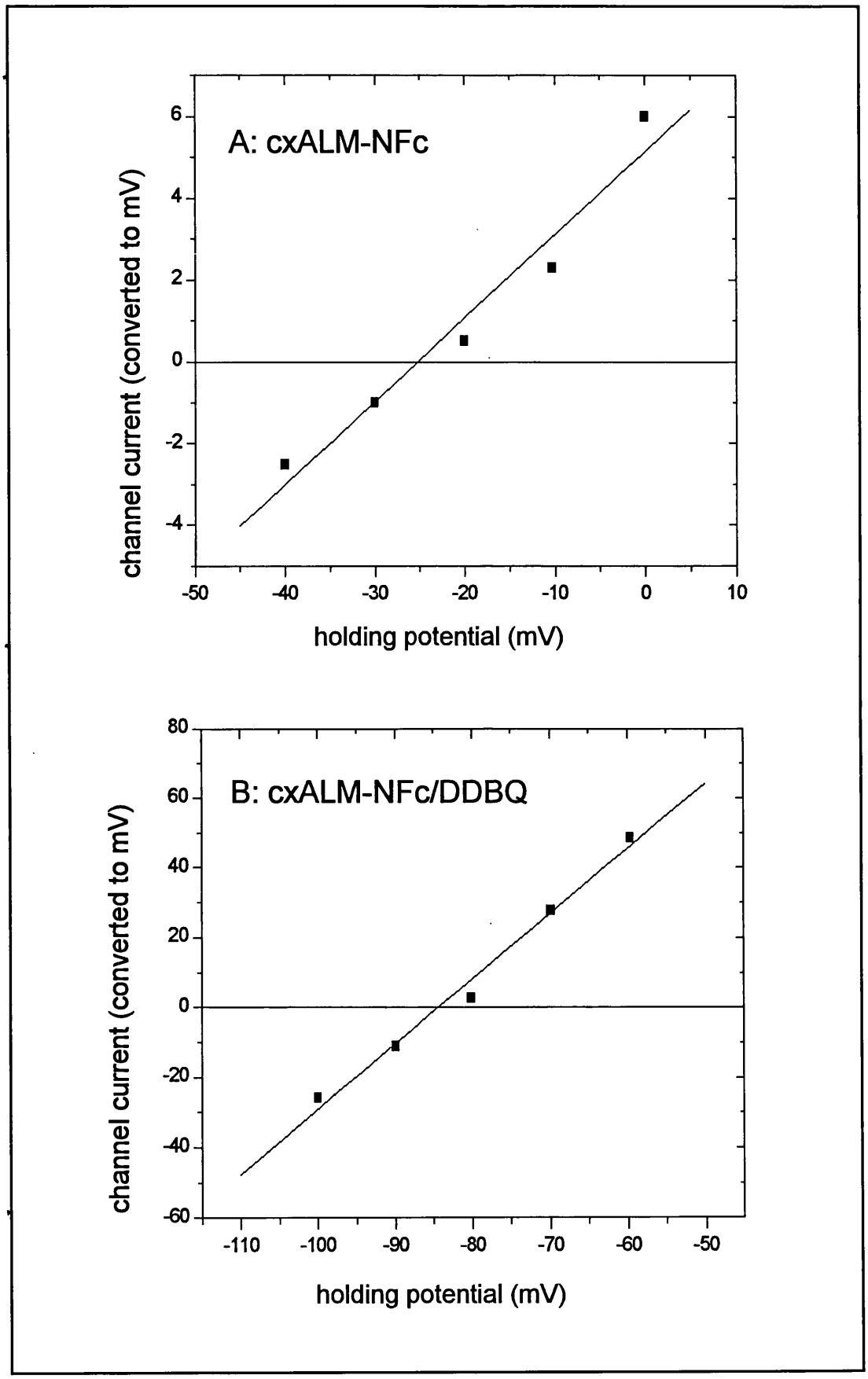
A: cxALM-NFc
channel current (converted to mV)
6
4
2
0
-2
-4
-50
-40
-30
-20
-10
0
10
holding potential (mV)
B: cxALM-NFc/DDBQ
channel current (converted to mV)
80
60
40
20
0
-20
-40
-60
-110
-100
-90
-80
-70
-60
-50
holding potential (mV)

FIGURE 5.9

RESULTS

6. PLB STUDIES ON MELITTIN ANALOGS

In this chapter the channel-forming behavior of three monomeric and two dimeric analogs of melittin is explored. The rationale for the synthesis and biophysical characterization of these analogs is twofold: (1) exploration of the relationship between peptide charge and channel formation propensity (providing structure-function information complementary to the alamethicin analog studies reported in Chapters four and five); and (2) the creation of stabilized melittin channels *via* dimerization of the parent peptides. Both macroscopic current-voltage and single channel measurements using planar lipid bilayers were conducted. The melittin analog MEL-K7Q forms channels which have longer lifetimes and more resolvable conductance levels relative to melittin. The gating kinetics of this analog are complex and, with the study conditions employed here, give rise to two families of conductance bursts. The monomeric analog, MEL-K23C, forms channels very similar to melittin with difficult to resolve conductance levels, perhaps due to bandwidth limiting. The peptide also has pronounced surfactant properties. The third monomeric analog is a double-mutant of melittin: MEL-K23Q/Q25C. This analog also has conductance properties similar to melittin with difficult to resolve conductance levels. Interestingly, its extreme surfactive properties precluded any I-V data from being generated, as even minimal concentrations of this peptide caused repeated breakage of the bilayer.

6.1. Macroscopic Studies of Monomeric Analogs. Current-voltage (I-V) measurements were conducted by adding peptides to the *cis* (positive potential) chamber of the PLB apparatus. MEL-K23C was added to a lower final concentration than the other peptides due to its lytic properties.

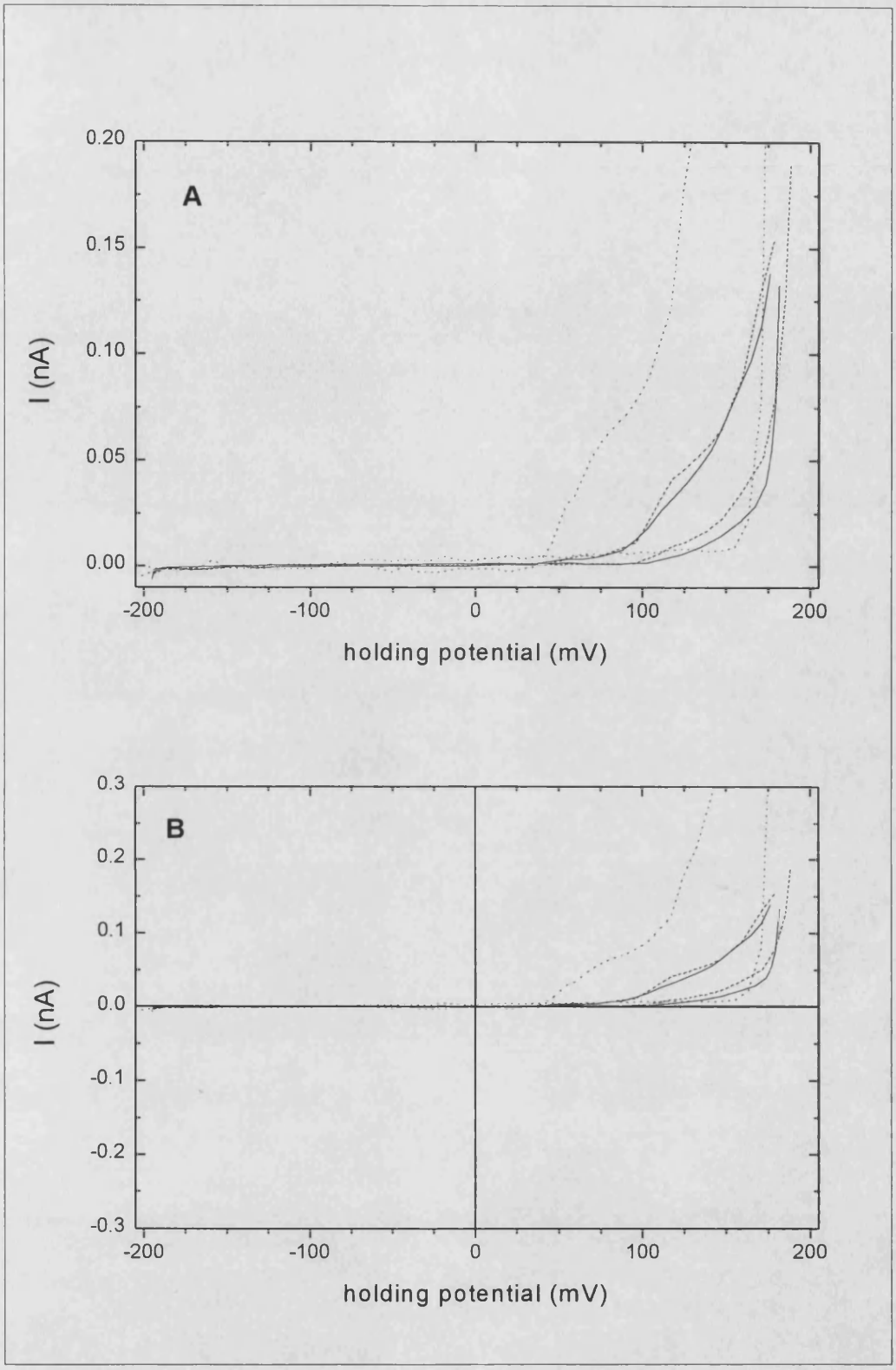

FIGURE 6.1. I-V ANALYSIS OF MELITTIN, MELITTIN-K7Q and MELITTIN-K23C. Measurements in planar DPhPC lipid bilayers were conducted by adding peptides to the *cis* (positive potential) chamber of the PLB apparatus in buffered electrolyte (0.5 M KCl, 10 mM BES, pH 7.0). MEL and MEL-K7Q were added to the PLB apparatus to a final concentration of 2.5 μg/ml, while MEL-K23C was added to a final concentration of 0.75 μg/ml. In the case of MEL-K23C and MEL-

K23Q/K25C, the respective dimer was treated with DTT for 20 minutes (10μl of a 1mg/ml solution of peptide and 10μl of 5% v/v aqueous DTT), to insure full reduction to the monomeric form, before it was added to the PLB apparatus; Electrolyte buffer used to characterize these peptides also contained 1mg/ml DTT. Triangular voltage sweeps (λ = 40 sec) from -195 mV to +195 mV for MEL-K7Q and -200 mV to +200 mV for MEL and MEL-K23C were then applied. Currents from 4-15 such sweeps were averaged together and are plotted in as follows: MEL-K7Q (- - - - -); MEL-K23C (— — —); and MEL (————). The right hand curve of each pair represents the induced current during the ascending portion of the voltage sweep (i.e. dV/dt > 0) and the left hand curve the descending (dV/dt < 0) portion.

DTT was added to the electrolyte to insure full reduction of the MEL-K23C. Notice the increased hysteresis that occurs when lysine-7 is replaced with the H-bonding amino acid glutamine (MEL-K7Q). The implications are discussed in Chapter 8. Table 6.1 summarizes the V_t and V_{25} values for these peptides.

	V_{t+}	V_{t-}	$V_{t+} - V_{t-}$	V_{25+}	V_{25-}	$V_{25+} - V_{25-}$
MEL	180	166	14	164	110	54
MEL-K7Q	171	108	63	164	52	112
MEL-K23C	182	163	19	150	106	44
MEL-K23Q/K25C	nd	nd	nd	nd	nd	nd
$(MEL-K23C)_2$	nd	nd	nd	nd	nd	nd
$(MEL-K23Q/K25C)_2$	nd	nd	nd	nd	nd	nd

nd: not determined

TABLE 6.1. MACROSCOPIC PROPERTIES OF MELITTIN ANALOGS: 25 mV AND 100 mV INDEXES. Summary of the conductance threshold indexes from the experiment described in Figure 6.1.

6.2. <u>Single Channel Studies of Monomeric Analogs</u>. The single-channel properties of the monomeric analogs have produced interesting results. Figure 6.2 shows typical single channel activity induced by melittin: mixed conductance level channels (6.2A), low conductance level

channels (6.2B), and an expansion of the low conductance-level trace (6.2C) and high conductance-level channels (6.2D). Brief bursts of activity are often accompanied by long periods of inactivity and the channel-lifetimes (or perturbation-lifetimes) are difficult to resolve due to bandwidth limiting. Conductance-level histograms for the mixed and low conductance-level melittin channels is shown in Figure 6.5, panels A and B, respectively. Extrapolation of conductance levels from such histograms is speculative at best.

The single channel activity of MEL-K7Q, like mellitin, occurs as bursts of activity accompanied by long periods of inactivity. This peptide, however forms channels with more clearly resolved conductance states than does melittin. In addition, neighboring bursts will often have different characteristics, Figure 6.3A shows the formation of alamethicin-like multiple conductance-state openings, whilst panel 6.3B shows the formation of short lived channels that share channel characteristics of both alamethicin and melittin. Panel C of Figure 6.3 shows an expanded view of the bursts from 6.3B, notice here that one can begin to see differentiated and sustained conductance levels. Conductance-level histograms for the two types of bursts are shown in Figure 6.5. Panel 6.5C shows a histogram of the type of bursts shown in Figure 6.3A; Panel 6.5D shows a histogram of the type of bursts shown in Figure 6.3B. The implication here is that the different 'burst types' result from non-equivalent bundle geometries.

The peptide MEL-K23C appears to form channels much like melittin. This highly perturbative peptide gives only transient bursts of activity with quick bandwidth-limited conductance. Figure 6.4 shows sections of recording MEL-K23C. It appears that intermittent low conductance level channels with relatively sustained openings occur, as seen in 6.4B. Conductance-level histograms for traces 6.4A and 6.4B are shown in Figure 6.6 Panels A and B, respectively.

FIGURE 6.2. SINGLE CHANNEL BEHAVIOR OF MELITTIN. Peptides were added to the *cis* chamber of the PLB apparatus, each chamber containing 2 ml of KCl/BES electrolyte as previously described. Typical single channel activity induced by 2.5 μg/ml melittin at 160 mV transbilayer potential: mixed conductance level channels (panel A), low conductance level channels (panel B), and an expansion of the low conductance-level trace (panel C) and high conductance-level channels (panel D).

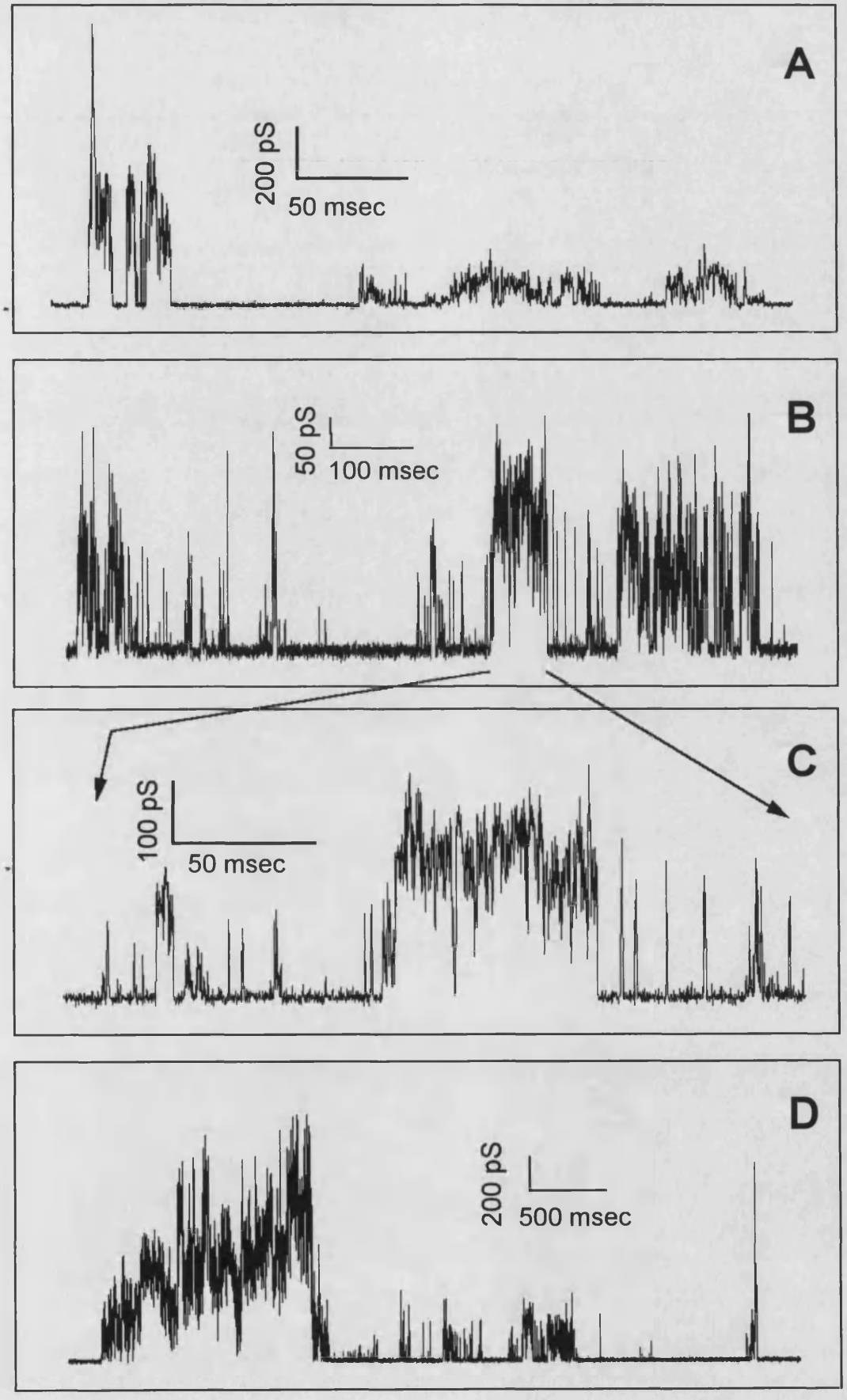

FIGURE 6.2

FIGURE 6.3. SINGLE CHANNEL BEHAVIOR OF MELITTIN-K7Q. Peptides were added to the *cis* chamber of the PLB apparatus, each chamber containing 2 ml of KCl/BES electrolyte as previously described. Panels A and B, show different sections of a single record, acquired with 1.25 μg/ml MEL-K7Q and a transbilayer potential of 170 mV.

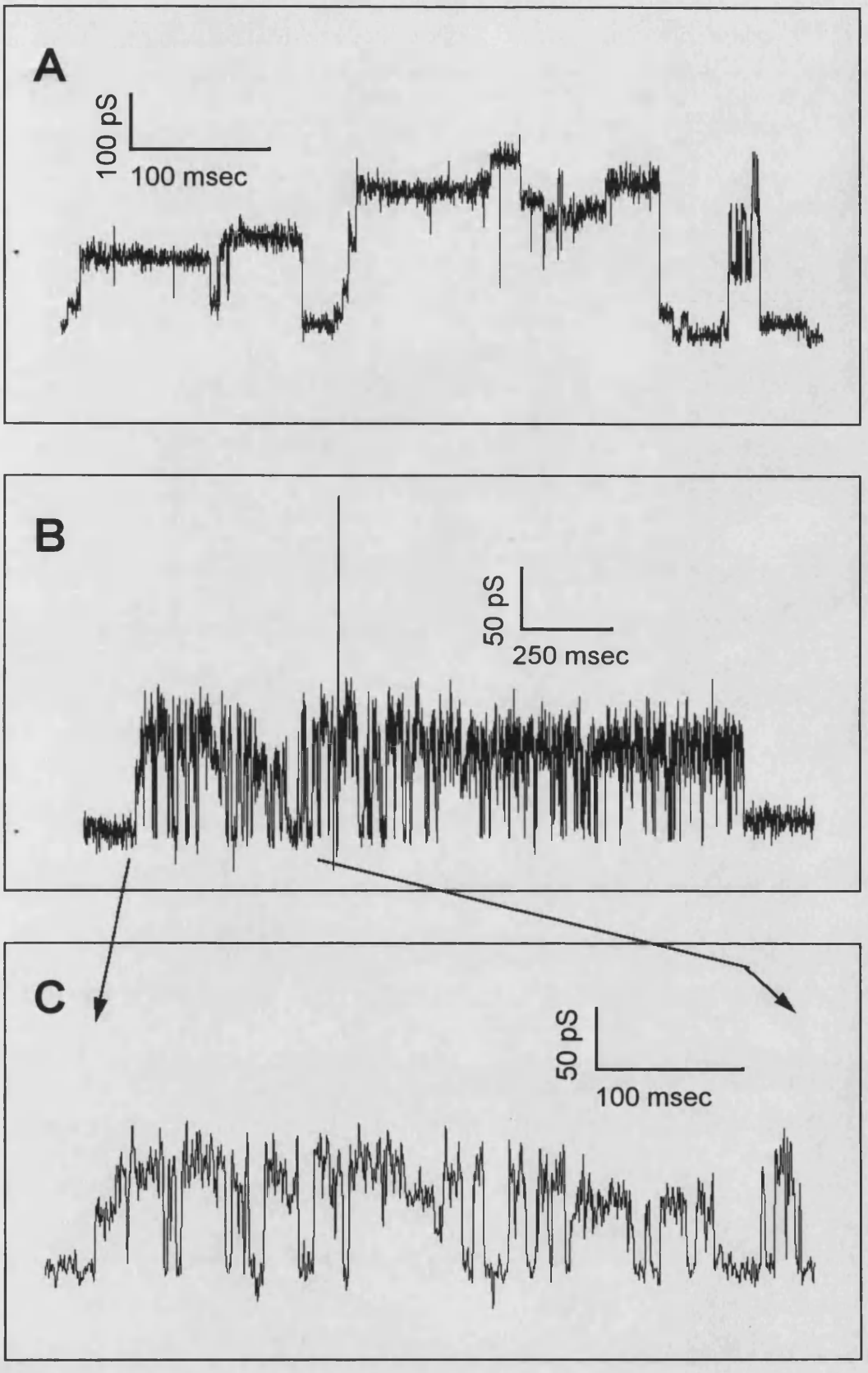

FIGURE 6.3

FIGURE 6.4. SINGLE CHANNEL BEHAVIOR OF MELITTIN-K23C AND MELITTIN-K23Q,Q25C. Peptides were added to the *cis* chamber of the PLB apparatus, each chamber containing 2 ml of KCl/BES electrolyte as previously described. Panels A and B show sections of recording from 0.75 μg/ml MEL-K23C at a potential of 140 mV. Panels C and D show representative sections of recordings taken with 1.5 μg/ml MEL-K23Q,K25C at a transbilayer potential of 75 mV.

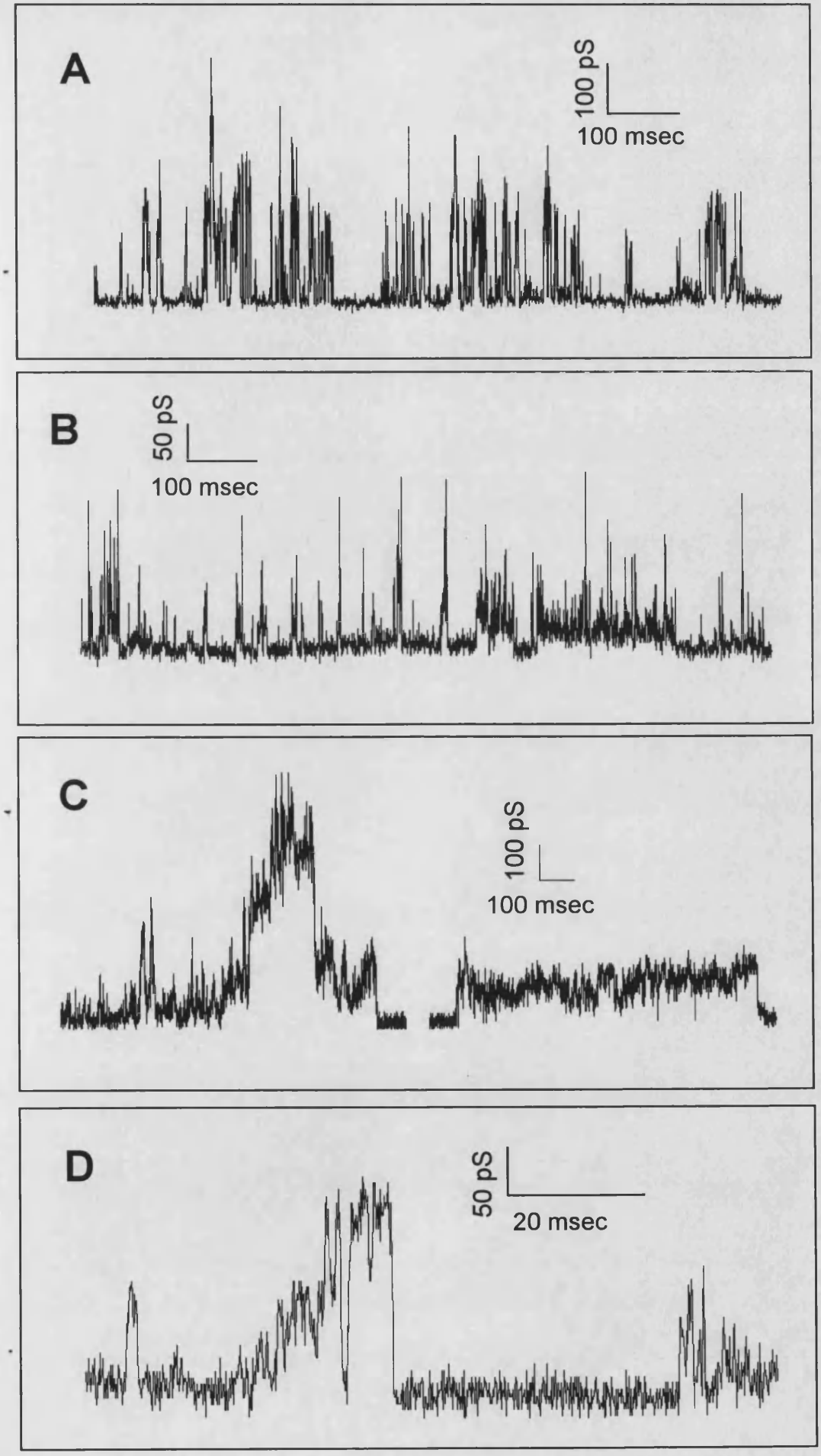

FIGURE 6.4

FIGURE 6.5. CONDUCTANCE LEVEL HISTOGRAMS FOR MELITTIN AND MELITTIN-K7Q. This figure shows histograms from 120 seconds of single channel recording from 2.5 μM MEL (panel A and B) and 1.25 μM MEL-K7Q (panel C and D). The mixed and low conductance-level melittin channels are shown in panels A and B, respectively. Panel 6.5C shows a histogram of MEL-K7Q bursts shown in Figure 6.3A; Panel 6.5D shows a histogram of MEL-K7Q bursts shown in Figure 6.3B.

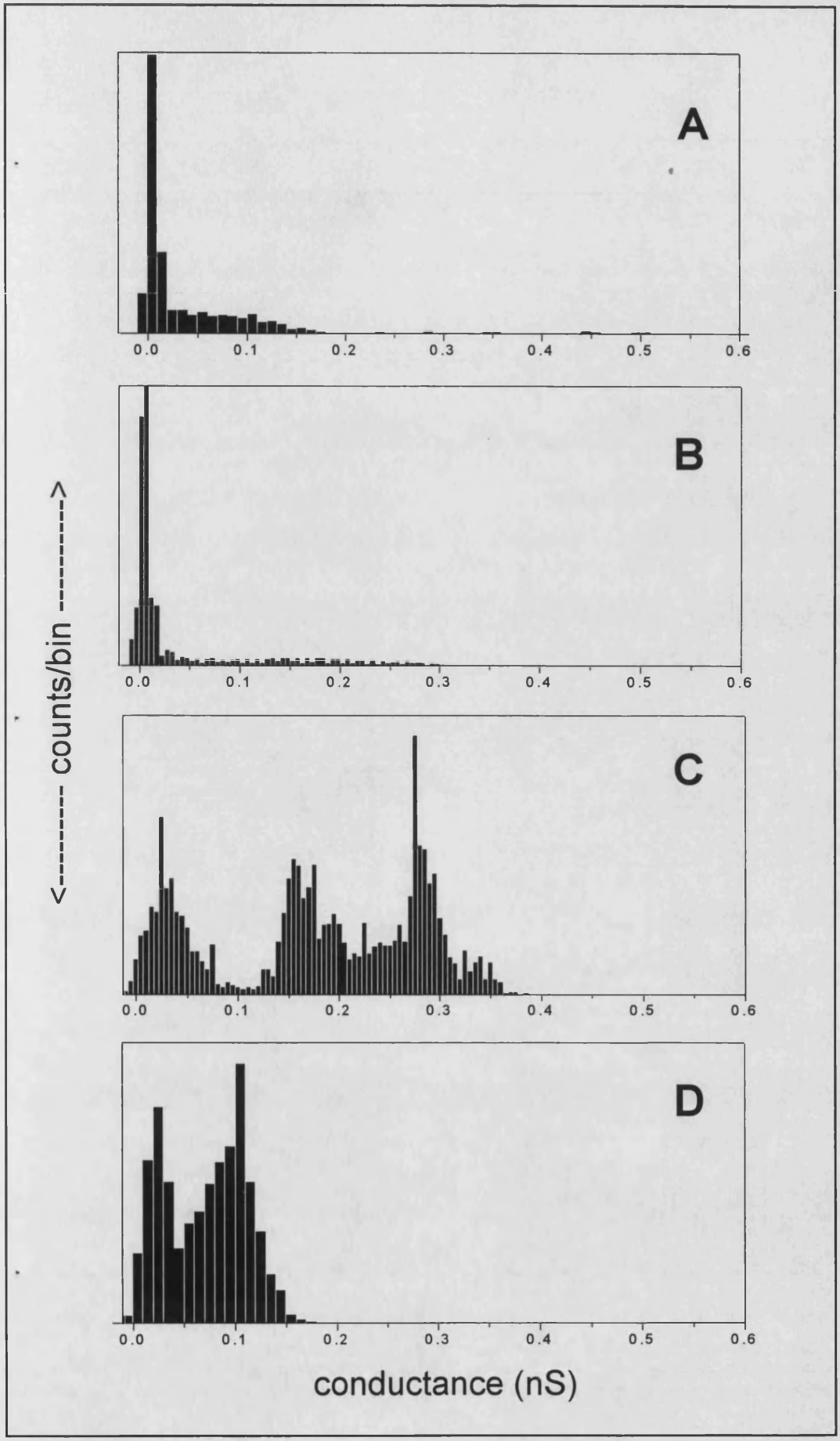

FIGURE 6.5

FIGURE 6.6. CONDUCTANCE LEVEL HISTOGRAMS FOR MELITTIN-K23C AND MELITTIN-K23Q,Q25C. This figure shows histograms from 120 seconds of single channel recording from 0.75 μM MEL-K23C (panel A and B) and 1. 5 μM MEL-K23Q,Q25C (panel C and D). Panel A shows a histogram of MEL-K23C the type of bursts shown in Figure 6.4A; Panel B shows a histogram of MEL-K23C bursts shown in Figure 6.4B. Panel C shows a histogram of MEL-K23Q,Q25C bursts shown in Figure 6.4C; Panel D shows a histogram of 1 second recording of MEL- K23Q,Q25C bursts shown in Figure 6.4D.

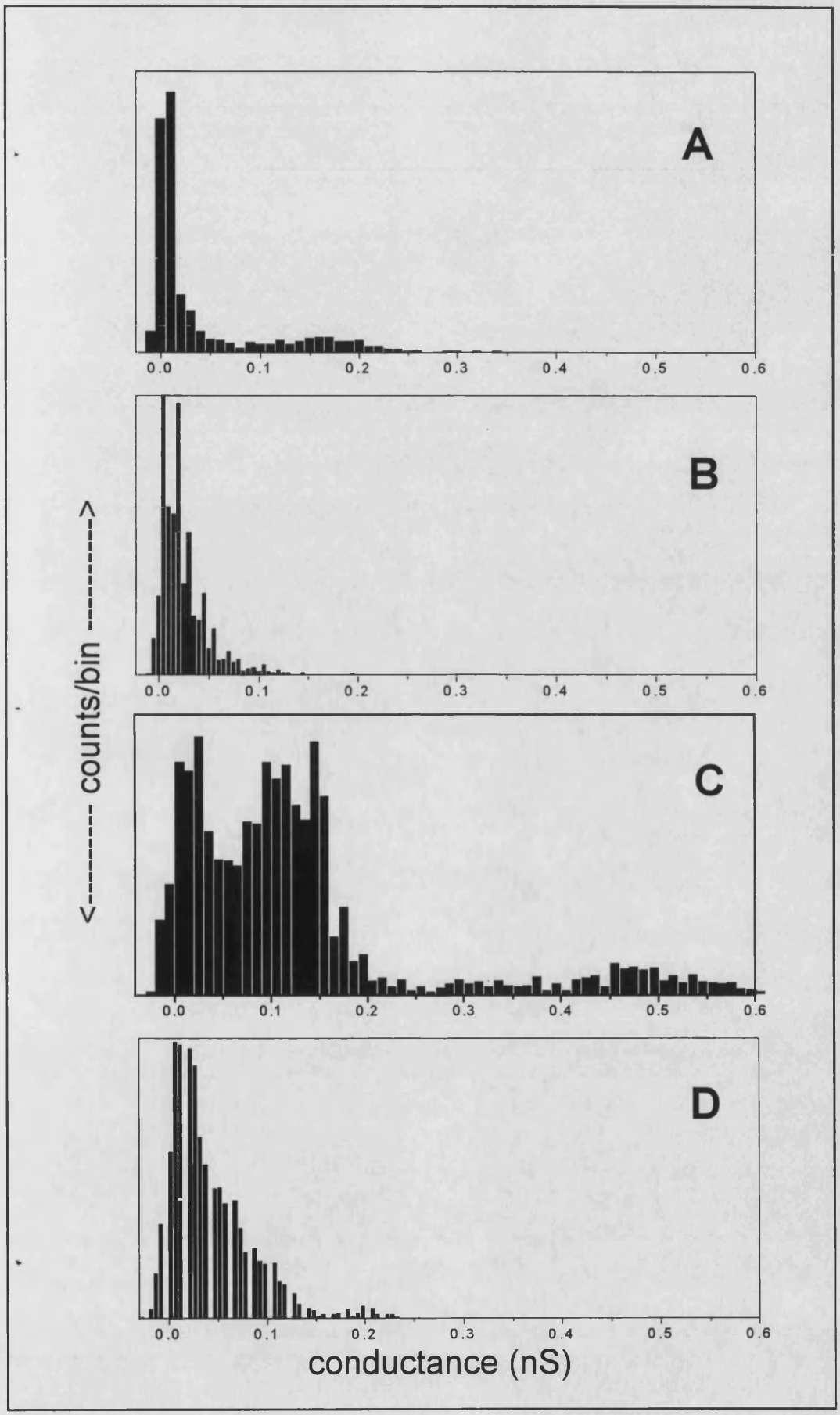

FIGURE 6.6

Single-channel characterization of the double mutant MEL-K23Q,K25C was difficult due to the extreme surfactant-like properties of this peptide. Panels C and D of Figure 6.4 show representative sections of recordings of MEL-K23Q,K25C. Concentrations higher than 1μg/ml and/or transbilayer potentials led to frequent breakage of the bilayer. Figure 6.4C shows two bursts, which like melittin are accompanied by long periods of inactivity. Since conductance levels were difficult to determine, a histogram was taken for 1 second of recording (Figure 6.6, Panel D); In an attempt to resolve conductance levels more clearly, a histogram of the combined traces from Figure 6.4C is shown in Figure 6.6C.

The single channel subconductance levels are summarized in Table 6.2. The 'g_n-g_{n-1}' column indicates the difference between neighboring conductance levels in pS. Multiplicity (i.e. $g_n = j \times g_{n-1}$) may imply the opening of more than one channel.

MEL		MEL-K7Q		MEL-K23C		MEL-K23Q/K25C	
pS	g_n-g_{n-1}	pS	g_n-g_{n-1}	pS	g_n-g_{n-1}	pS	g_n-g_{n-1}
<77>[a]	na	27		20		92	
<278>	na	<50>	na	<160>	na	131	39
<416>	na	<90>	na			315	184
<750>	na	133	106[b]			460	145
		178	45				
		211	33				
		250	39				
		311	61				

a: average conductance; b: g_n-g_{n-1} = 133-27 pS; na: not applicable

TABLE 6.2. SINGLE CHANEL CONDUCTANCE LEVELS FOR MELITTIN ANALOGS.

6.3. <u>Macroscopic Studies of Dimeric Analogs</u>. Unfortunately, it was impossible to generate I-V data with the dimeric analogs $(MEL\text{-}K23C)_2$ and $(MEL\text{-}K23Q/K25C)_2$. A great number of experimental protocols were attempted (peptide concentration, voltage-ramp and cycle time were

independently varied experiments) these peptides either failed to produce consistent channel bursts or, at higher concentrations, repeatedly broke the bilayer.

6.4. Single Channel Studies of Dimeric Analogs. The dimeric melittin analogs $(MEL\text{-}K23C)_2$ and $(MEL\text{-}K23Q/K25C)_2$ form voltage-dependent channels in DPhPC bilayers. $(MEL\text{-}K23C)_2$ forms multiple conductance level channels, with the unique property that some openings are accompanied by a dramatic increase in bilayer noise while other openings appear highly resolved. These two types of channel activity are evident with a moderate peptide concentration; notice that the both types of opening share roughly the same conductance levels. At the same peptide concentration and transbilayer potential this peptide also forms persistent low conductance level channels, as shown in Figure 6.7B. Table 6.3 summarizes the conductance levels for this peptide.

$(MEL\text{-}K23C)_2$		$(MEL\text{-}K23C/K25C)_2$	
pS	g_n-g_{n-1}	pS	g_n-g_{n-1}
16.5		<225>	
33	16.5	<485>	na
79	46		
96	17	(-) rectification:	
129	33	<-165>	
		<-293>	na

TABLE 6.3. SINGLE CHANNEL CONDUCTANCE LEVELS OF MELITTIN ANALOG DIMERS.

The final melittin analog studied was the dimer of the double mutant: $(MEL\text{-}K23Q/K25C)_2$. Figure 6.7C shows a section of record taken with this peptide. Although the channels formed by this peptide are noisy, it is possible to estimate their average conductance levels

(Table 6.3 summarizes the results). This is the only analog that showed significant propensity to form channels at negative potentials, albeit at very large potentials. Panel D of Figure 6.7 shows representative negative rectification at -260 mV.

FIGURE 6.7. SINGLE CHANNEL BEHAVIOR OF (MELITTIN-K23C)$_2$ AND (MELITTIN-K23Q,Q25C)$_2$. Peptides were added to the *cis* chamber of the PLB apparatus, each chamber containing 2 ml of KCl/BES electrolyte as previously described. Panels A and B show sections of recording from 1.25 μg/ml (MEL-K23C)$_2$ at a potential of 190 mV. Panel C shows a representative section of recordings taken with 1.5 μg/ml (MEL-K23Q,Q25C)$_2$ at a transbilayer potential of 190mV. Panel D shows a representative section of recordings taken with 1.5 μg/ml (MEL-K23Q,Q25C)$_2$ at a transbilayer potential of -260 mV.

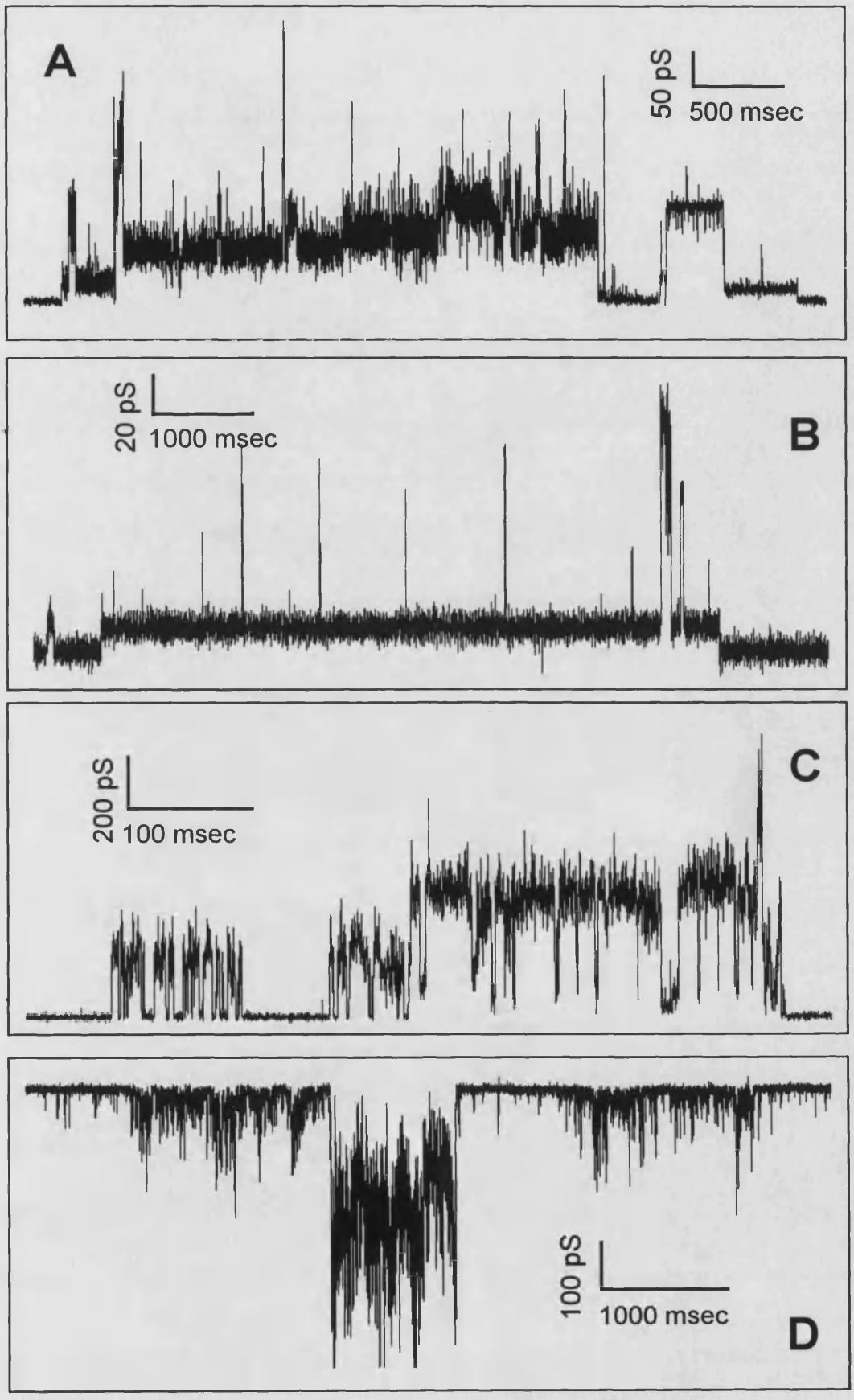
A
50 pS
500 msec
20 pS
1000 msec
B
200 pS
100 msec
C
100 pS
1000 msec
D

FIGURE 6.7

FIGURE 6.8. CONDUCTANCE LEVEL HISTOGRAMS FOR (MELITTIN-K23C)$_2$ AND (MELITTIN-K23Q,Q25C)$_2$. Histograms from the recordings described in Figure 6.7. Panel A is the histogram from recording 6.7A ect.

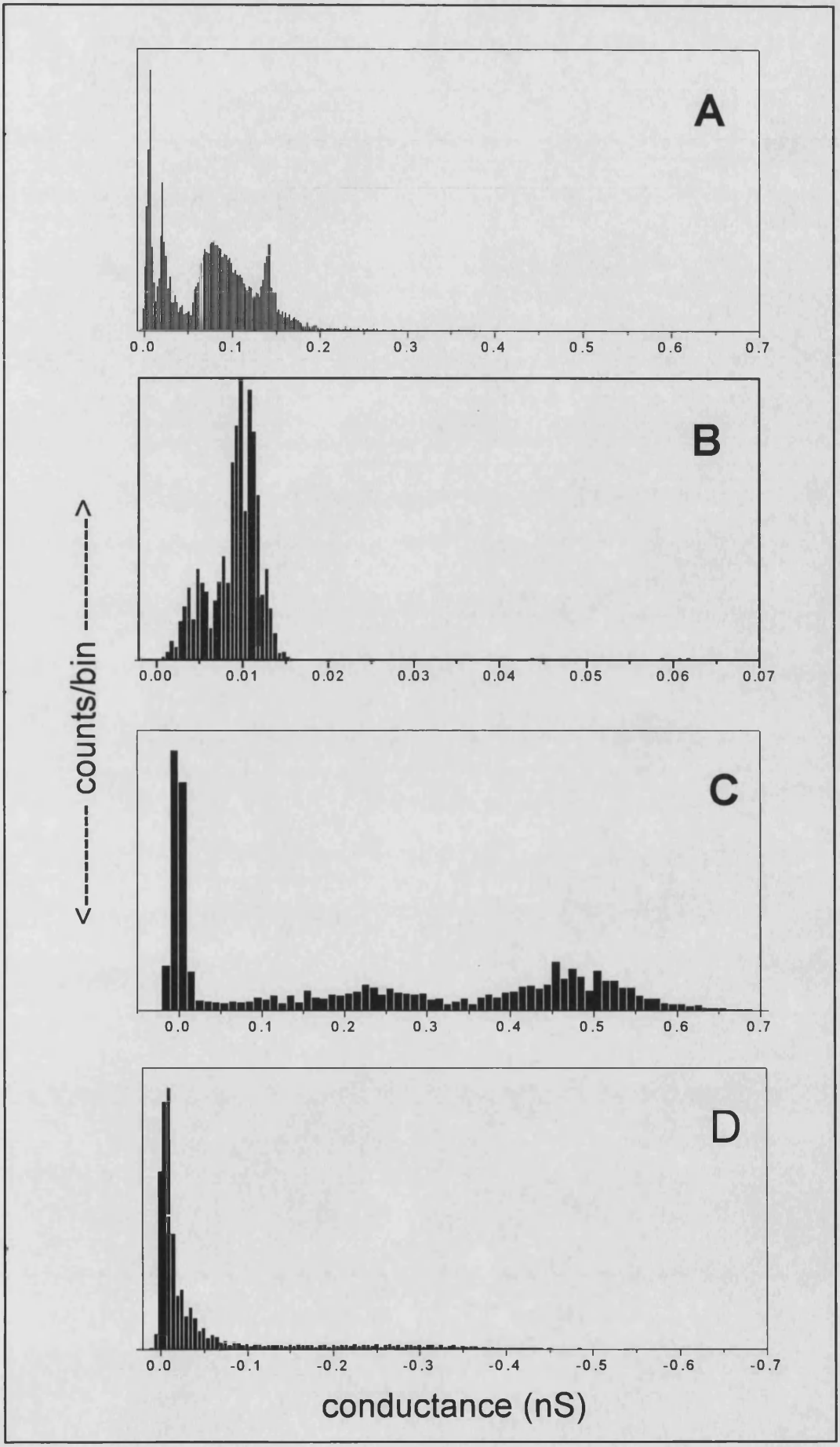
A
B
C
D
0.0
0.1
0.2
0.3
0.4
0.5
0.6
0.7
0.00
0.01
0.02
0.03
0.04
0.05
0.06
0.07
-0.1
-0.2
-0.3
-0.4
-0.5
-0.6
-0.7
<---------- counts/bin ---------->
conductance (nS)

FIGURE 6.8

RESULTS

7. COMPUTATIONAL MODELING

This chapter describes the computational modeling efforts conducted with the aim of facilitating interpretation of results described in previous chapters. Starting with X-ray crystal structures shown in Figure 7.1, bundles of redox-active alamethicin derivatives described in chapters four and five were built using methodologies described by Breed and coworkers as described in Chapter 2, see also Figure 7.2. Incorporation and paramiterization of the ferrocene moiety for use in these studies proved a formidable task. The quantum mechanical technique of density functional theory was used to generate equilibrium geometries and charges used in the calculations described below.

The technique of molecular dynamics simulated annealing has been used to develop plausible models of the melittin analogs described in chapter six. Hexameric bundles of these analogs were chosen with the aim of providing a basis for qualitative structure-property assessment. Although this choice was one of convenience, the conductance properties of many analogs fall within the regime of 'alamethicin like' channel conductance expected with hexameric bundles. Here it is important to note that some of the analogs are likely to form considerably larger assemblies.

7.1. Density Functional Theory Calculations on Ferrocene Analogs.

Atomic partial charges for Forcefield and MD calculations on ferrocenoyl peptides was generated with density functional theory. The results for calculations conducted on ferrocene acetic acid are given in Table 7.1. Despite the fact that there were minor convergence problems with the oxidized ferrocene acetic acid molecule, reached self-consistent field convergence within three days calculation on an R5000 CPU.

FIGURE 7.1. CRYSTAL STRUCTURES OF MELITTIN AND ALAMETHICIN R_f30. The X-ray structure of melittin as described by Terwilliger and Eisenberg (1982) is shown on the left, alamethicin R_f30 (Fox and Richards, 1982) is shown on the right. Hydrophobic amino acids are colored cyan and hydrophilic amino acids are colored magenta, both peptides are oriented such that the C-termini point up and a line-ribbon shows the secondary structure. Note the pronounced interruption of helical structure around proline-15 of melittin.

FIGURE 7.1. CRYSTAL STRUCTURES OF MELITTIN AND ALAMETHICIN R_f30. The X-ray structure of melittin as described by Terwilliger and Eisenberg (1982) is shown on the left, alamethicin R_f30 (Fox and Richards, 1982) is shown on the right. Hydrophobic amino acids are colored cyan and hydrophilic amino acids are colored magenta, both peptides are oriented such that the C-termini point up and a line-ribbon shows the secondary structure. Note the pronounced interruption of helical structure around proline-15 of melittin.

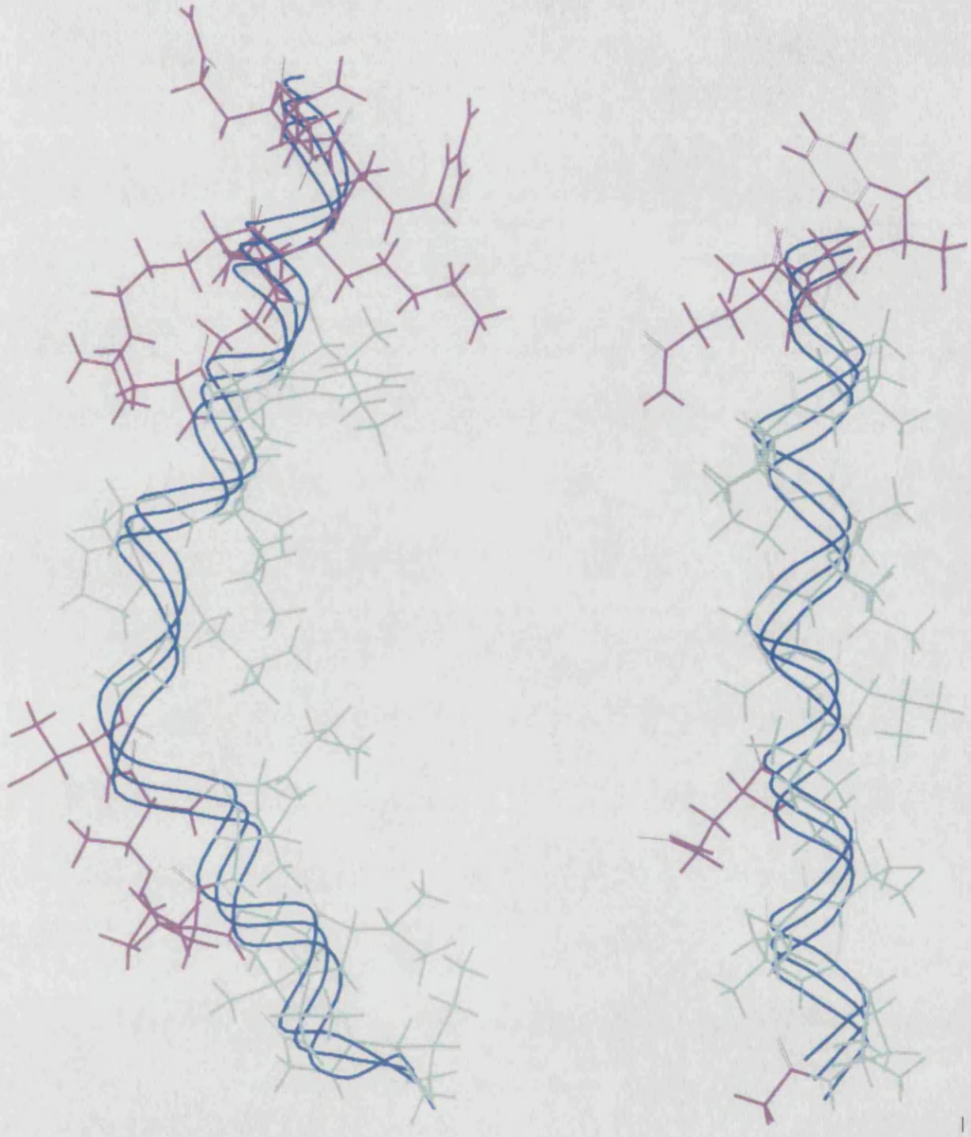

FIGURE 7.2. HEXAMERIC ALAMETHICIN R_f50 BUNDLE GENERATED BY MOLECULAR DYNAMICS SIMULATED ANNEALING. An optimized hexameric bundle of alamethicin R_f50, generated by Breed and coworkers, was changed from a CHARMm extended-atom model to a model with explicit hydrogens using CERIUS^2 (version 3.5, Molecular Simulations Inc.) and minimized using the UFF forcefield and parameter set. Partial atomic charges were derived using the charge equilibration method described by Rappe and Goddard (see Chapter 2). Conjugate gradient minimization of the bundle converged in less than 200 steps indicating that conversion of the model from CHARMm to UFF had little impact on the structure.

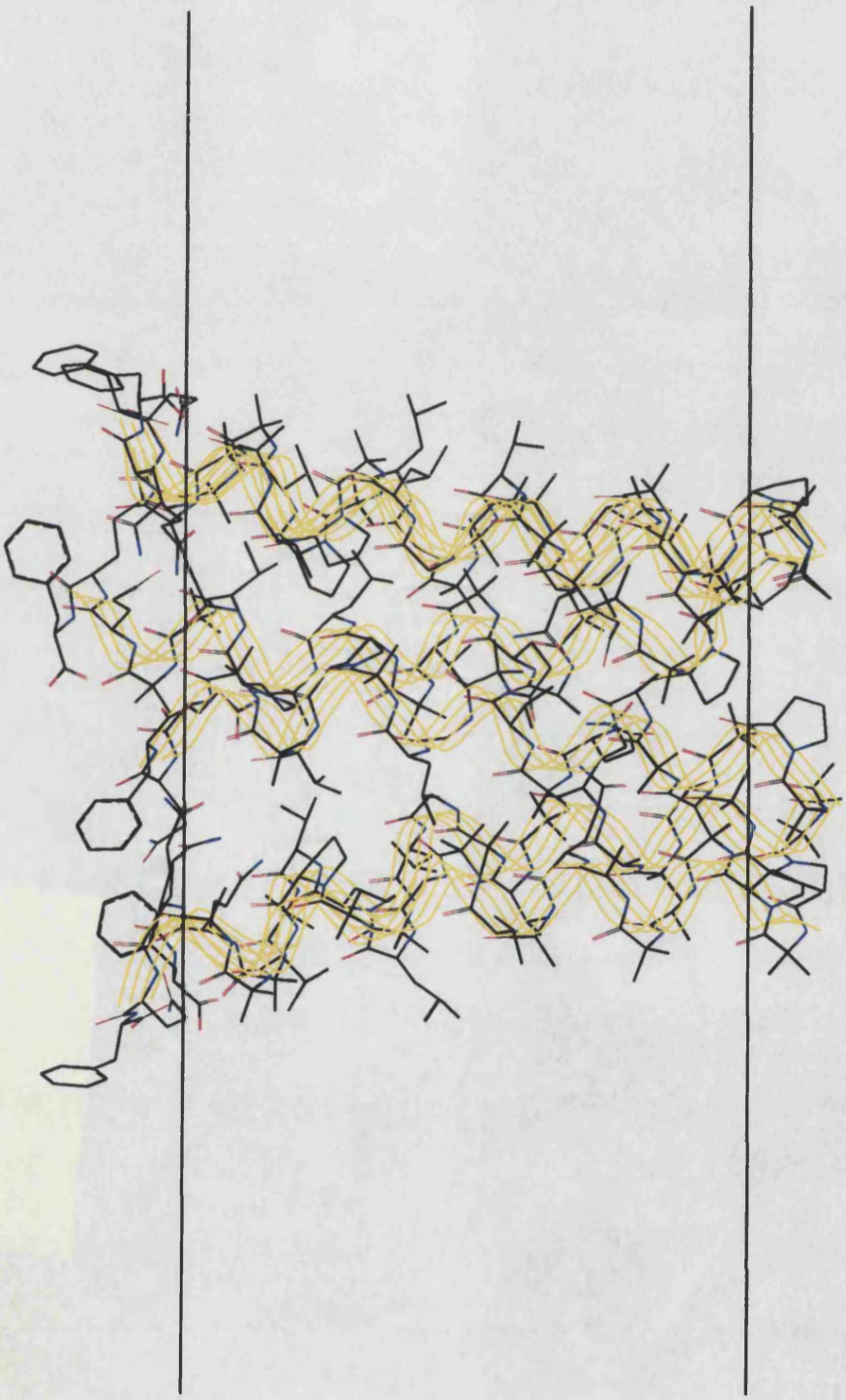

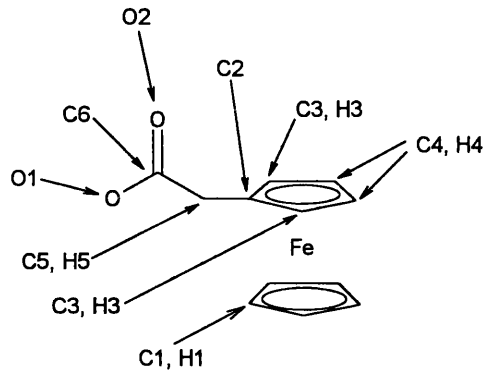

	DFT CHARGE	
ATOM	REDUCED	OXIDIZED
C1	-0.17	-0.13
H1	0.10	0.97
C2	0.03	0.06
C3	-0.14	-0.11
H3	0.13	0.14
C4	-0.18	-0.15
H4	0.10	0.11
C5	-0.21	-0.21
H5	0.08	0.07
C6	0.63	0.63
O1	-0.52	-0.53
O2	-0.46	-0.45
Fe	0.55	1.54

TABLE 7.1. DFT PARTIAL CHARGE CALCULATIONS ON FERROCENE ACETIC ACID. The Amsterdam DFT package (Molecular Simulations Inc.) was used with the following parameters for the reduced molecule: large core approximation, local density approximation, spin=0, charge=0, basis sets {II/H, II/C.1s, II/O.1s, III/Fe.3p}, spin calculation {restricted}, SCF {direct inversion of iteration subspace}, Hessian update {BFGS}, Density Functional {VWN, no exchange correlation}. Parameters for the oxidized molecule: large core approximation, local density approximation, spin=1, charge=1, basis sets {II/H, II/C.1s, II/O.1s, III/Fe.3p}, spin calculation {restricted}, SCF {direct inversion of iteration subspace}, Hessian update {BFGS and DFP}, Density Functional {VWN, no exchange correlation}. Charges assignments on designated atoms represent averages taken over equivalent atoms.

Charges calculated in this method were shown to be similar to 3-21G** *ab initio* charges generated with Møller-Plesset perturbation theory (data not shown). The advantage of DFT over *ab initio* methods relates mostly to computational efficiency-- *ab initio* calculations on ferrocene acetic acid at the stated level of theory took 22 days to converge (SGI R5000 CPU).

7.2. <u>Dipole Moment Calculations on Alamethicin Analogs</u>. One of the aims of this project has been explore the physical determinants of ion-channel formation. It is evidenced that the net molecular dipole of helical CFPs is one such determinant. Thus we sought a robust way of calculating the net dipoles of the alamethicin analogs we synthesized. Table 7.2 summarizes the dipole calculation results using MOPAC and

DFT derived charges. One of the most significant properties of the ferrocene containing peptides is the ability to change the net molecular dipole (and also the electrostatic profile of the peptide without changing molecular structure or the chemical environment.

		molecular dipole (Debye)	
peptide	charge	moment	z-component
ALM	0	81.3	76.4
cxALM-Ac	-1	163.7	155.4
Fc-ALM	0	25.5	22.5
Fc-ALM(ox)	1	32.6	-31.2
cxFc-ALM	-1	84.6	75.4
cxFc-ALM(ox)	0	43.5	27.8
cxALM-Fc	-1	154.3	151.1
cxALM-Fc(ox)	0	269.2	261.8
ALM-pm	-3	369.8	366.1

TABLE 7.2. CALCULATED DIPOLE VALUES OF ALM DERIVATIVES. The values listed above are quantitative estimates. Charges calculated using MOPAC derived charges and DFT derived charges in the case of the ferrocene moieties, peptides were modeled in helical form and aligned with the helical axis in the z-direction and the C-terminus at the coordinate origin. MOPAC charge calculations required that the peptide be split in half so to not exceed the heavy-atom limit, thus after charge calculation on the fragments the peptides were rejoined preserving the original conformation.

7.3. Hexameric Bundles of Fc-ALM. To examine the conformational and electrostatic effects of adding ferrocene to the C-terminus of alamethicin we built models of hexameric bundles of Fc-ALM using a molecular mechanics approach. The minimized bundle is shown in Figure 7.3. The ferrocene moieties are well accommodated despite the steric constraints imposed by the nascent phenyl ring and the other bundles.

7.4. Hexameric Bundles of cxALM-Ac. The approach described in Section 7.3 was used to model hexameric bundles of alamethicin derivatized at the N-terminus with ferrocene. The inclusion of ferrocene at this terminus may have a greater impact on channel structure and electrostatics, see Figure 7.4.

FIGURE 7.3. HEXAMERIC BUNDLE OF Fc-ALM. The C-terminus hydroxyl of each peptide in the alamethicin bundle (described in the legend of Figure 7.2) was converted to the ferrocenoyl ester using a DFT optimized model of reduced ferrocene carboxylic acid. Parameters for the ferrocene moiety were taken from the UFF parameter set and partial atomic charges were derived from the DFT electron densities. The model was energy minimized using a conjugate gradient algorithm. The left model shows a side view of the bundle with the C-termini pointing up and the left model is a 90° rotation showing the pore. Line ribbons are overlaid with the models to show secondary structure.

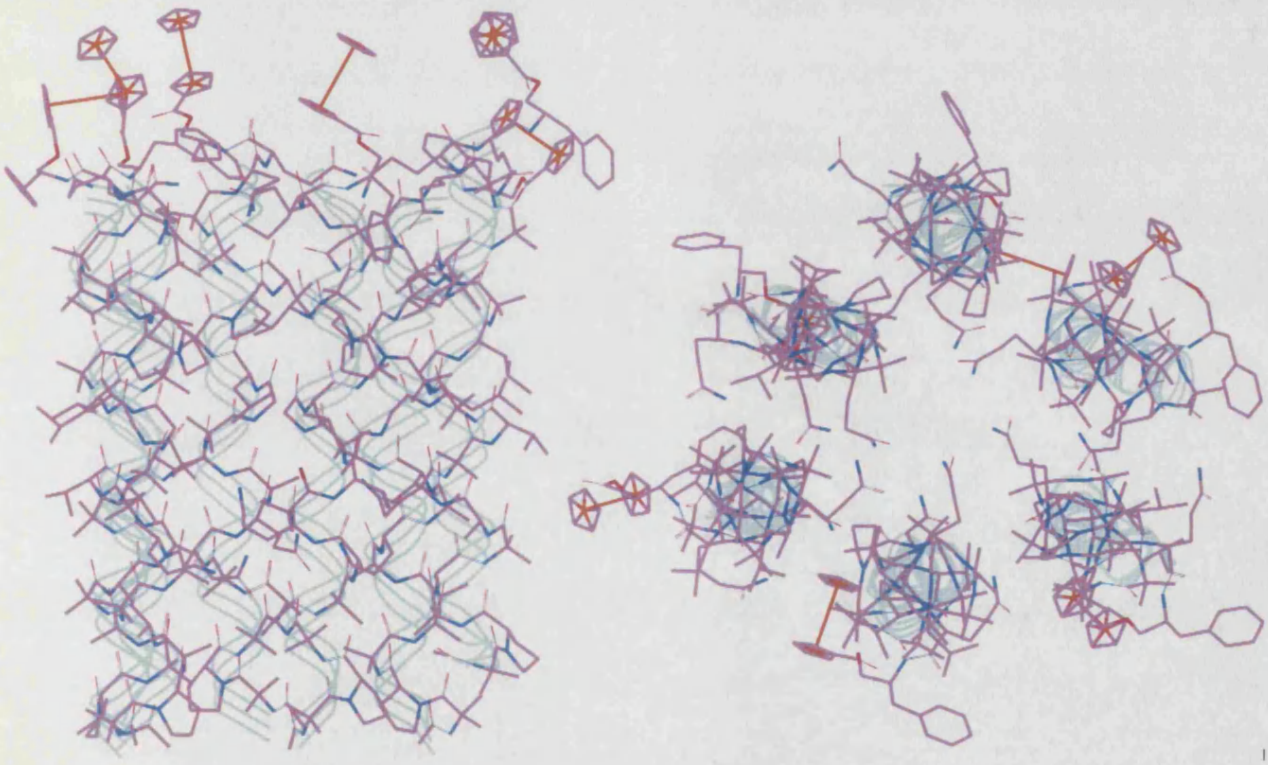

FIGURE 7.4. HEXAMERIC BUNDLE OF cxALM-NFc. The N-terminus acetyl amide of each peptide in the alamethicin bundle (described in the legend of Figure 7.2) was converted to the ferrocene acetic acid ester using a DFT optimized model of reduced or oxidized ferrocene acetic acid. Likewise, the C-terminus hydroxyl moieties were converted to carboxyls. Parameters for the ferrocene moiety were taken from the UFF parameter set and partial atomic charges were derived from the DFT electron densities. The model was energy minimized using a conjugate gradient algorithm. The left model shows a side view of the bundle with the C-termini pointing up and the left model is a 90° rotation showing the pore. Line ribbons are overlaid with the models to show secondary structure.

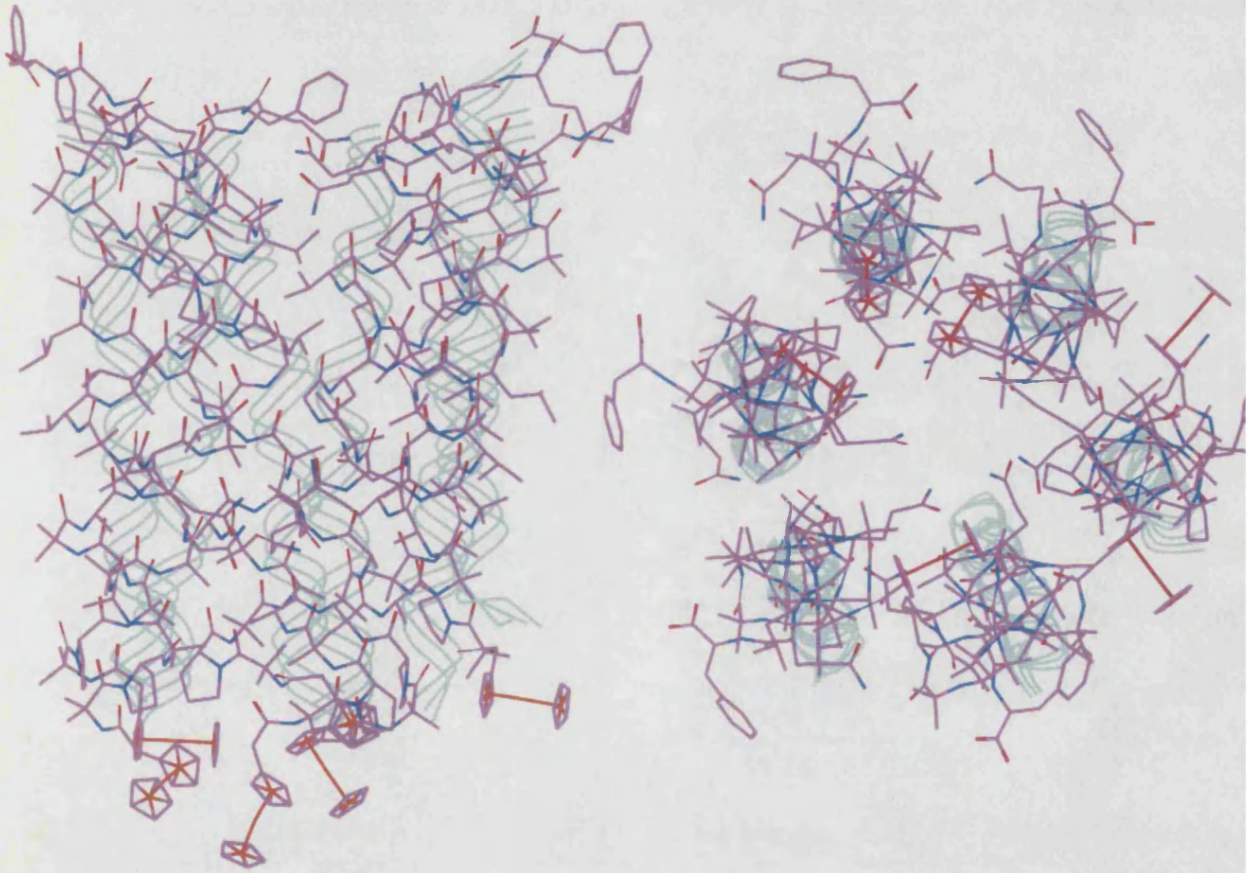

7.5. Electrostatics Calculations on cxALM-Ac and cxALM-NFc. It is well established that the electrostatic profile of the pore formed by CFP bundles largely determines the permeability of various ions (Hille, 1992)--we hypothesize that this is one explanation for the change in channel ion-selectivity that occurs when cxALM-NFc is oxidized. Calculation of the electrostatic potential using the Poisson-Boltzmann methodology described in along the channel axis in bundles of cxALM-Ac, cxALM-NFc (reduced) and cxALM-NFc (oxidized) was attempted. Unfortunately, the hexameric bundle is sufficiently narrow that at a number of points the pore radius is less then twice the low dielectric layer (Stern layer), this creates very dramatic discontinuities in the electrostatic profile. So we used the electrodiffusion model of Lear and coworkers (Lear *et al.*, 1997) to calculate a theoretical reversal potential ($V_{rev,calc}$) for the N-terminus redox peptides (see Appendix A). The results are encouraging, in that the change in ion selectivity is predicted, although the magnitude is not well approximated. I-V experiments reveal that cxALM-NFc in the reduced form has a V_{rev} = -26 mV (P_K/P_{Cl}= 0.9), the Lear model predicts $V_{rev,calc}$ = -27.3 mV (P_K/P_{Cl}= 0.84); the oxidized form of cxALM-NFc has a V_{rev}= -84.5 mV (P_K/P_{Cl}= 0.12), the Lear model predicts $V_{rev,calc}$ = -66.9 mV (P_K/P_{Cl}= 0.23).

7.6. Hexameric Bundles of Melittin Analogs. The ability of the melittin analogs described in this study to form stable helix-bundles was assessed using molecular dynamics simulated annealing. Figure 7.5 compares the structures of MEL and MEL-K7Q bundles. Both bundles appear roughly identical with the exception that the MEL-K7Q bundle is slightly more constricted near the interruption in α-helical structure at proline-15. Far more dramatic structural changes are seen with the MEL-K23C and $(MEL-K23C)_2$ bundles relative to MEL. Figure 7.6 shows a pronounced increase in the pore radius of $(MEL-K23C)_2$ relative to MEL-K23C and MEL. The kink angle between the two segments of a-helix is

reduced in $(MEL\text{-}K23C)_2$ while in MEL-K23C it is increased with respect to MEL. The effect of MEL-K23Q,K25C dimerization is quite different. In figure 7.7 the structures of MEL-K23Q,K25C and $(MEL\text{-}K23Q,K25C)_2$ are compared. The $(MEL\text{-}K23Q,K25C)_2$ bundle possesses nearly the same kink angle as MEL and the bundle of monomeric MEL-K23Q,K25C is nearly identical to MEL.

7.7. Electrostatics Calculations on Melittin Analog Bundles. The melittin bundles shown in Figures 7.5-7.7 were loaded with AMBER atomic charges and used in electrostatic potential fit calculations. Since the bundles are qualitatively similar, ESP calculations may help to reveal areas of unfavorable electrostatic interaction and thus loci of instability. Since melittin possesses an excess of basic amino acids contour plots at the +50 Kcal/mol *iso*potential contour are shown. Figure 7.8 shows the characteristic positively charged C-termini, mutation of LYS7 to GLU diminishes the pocket of positive charge at the N-terminus. The ESP profile of MEL-K23C highlighted in Figure 7.9 indicates extensive areas of unfavorable electrostatic interaction along the channel axis relative to MEL; this effect is considerably diminished upon dimerization. Bundles of the double mutants MEL-K23Q,K25C and $(MEL\text{-}K23Q,K25C)_2$ both appear to have extensive regions of disfavored electrostatic interaction along their channels, as shown in Figure 7.10.

FIGURE 7.5. HEXAMERIC BUNDLES OF MEL AND MEL-K7Q GENERATED USING MD SIMULATED ANNEALING. All modeling with melittin and its analogs was performed using the AMBER forcefield implemented in SYBYL Biopolymer (Version 6.1 and 6.2; Tripos Associates). Unless otherwise indicated, charge and atom parameters were taken from the AMBER parameter set. Six all-atom melittin momomers were taken from the crystal structure and overlaid onto the hexameric bundle described in Figure 7.5 such that the greatest steric and hydropathic overlap was achieved, this alignment results in overlap between the N-termini of melittin and alamethicin leaving the melittin C-terminus exposed to the aqueous milieu. At this point, methodology similar to that described by Kerr & Sansom (1994) was employed to optimize the bundle geometry. Briefly, backbone atoms were constrained with a 200 kcal/mol harmonic constraint and the sidechains were minimized (steepest descent algorithm) in the absence of electrostatics to relieve bad steric contacts. After convergence the constraints were reduced to include only the Cα atoms and further minimization was conducted. At this point, electrostatics were gradually introduced by decreasing ε from 80 to 1 over the course of 5 rounds of conjugate gradient minimization. In the case of the K7Q mutant, lysine 7 was converted to the glutamine prior to the initial minimization. Ten cycles of molecular dynamics simulated annealing were conducted using an exponential cooling from 2000K to 300K followed by constant temperature equilibration periods. The structure possessing the lowest energy was subjected to further energy minimization and the convergent structure for hexameric melittin is shown on the left and MEL-K7Q, on the right.

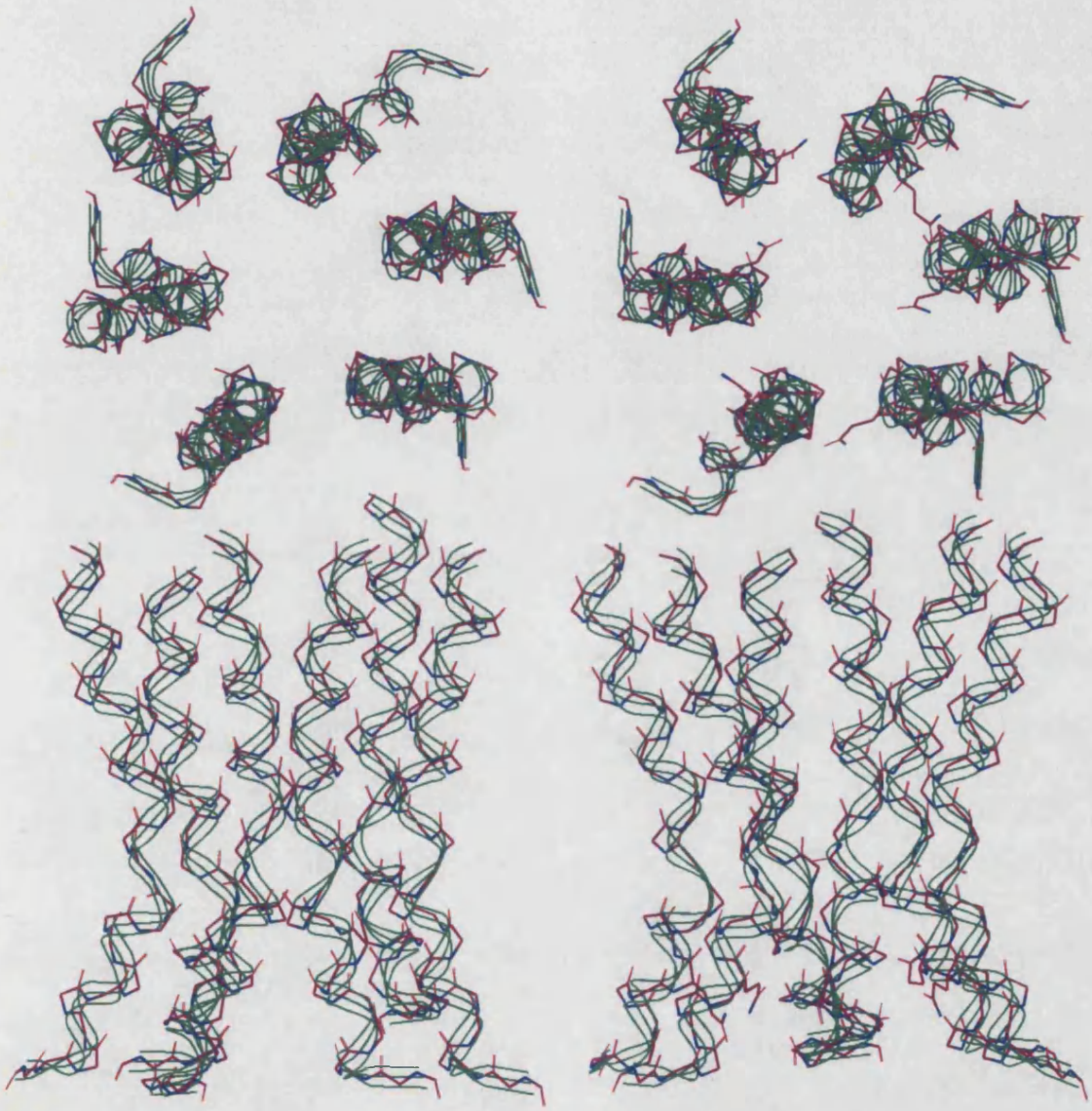

FIGURE 7.6. HEXAMERIC BUNDLES OF MEL-K23C AND $(MEL\text{-}K23C)_2$ GENERATED USING MD SIMULATED ANNEALING. The procedure outlined in the legend of Figure 7.5 was used to generate these mutants, with the exception that an additional series of constrained minimizations were needed to generate the disulfide bonds in the case of $(MEL\text{-}K23C)_2$. Before simulated annealing, cysteine sulfurs were brought into proximity by a series of minimizations using distance constraints between the said sulfurs. Disulfide bonds were then formed between neighboring peptide pairs followed by exhaustive minimization.

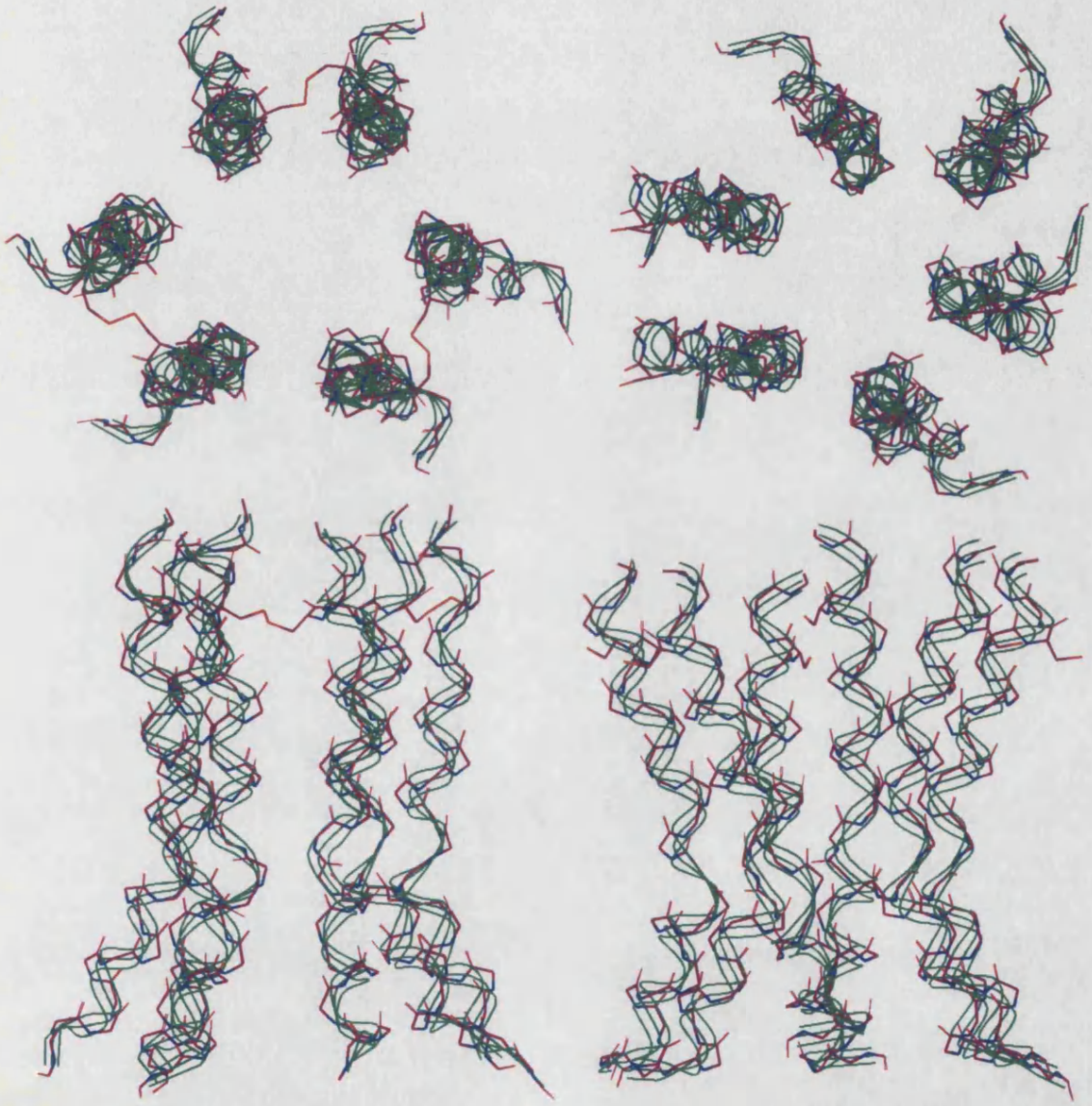

FIGURE 7.7. HEXAMERIC BUNDLES OF MEL-K23Q,Q25C AND (MEL-K23Q,Q25C)$_2$ GENERATED USING MD SIMULATED ANNEALING. The procedure outlined in the legend of Figure 7.5 was used to generate these mutants, with the exception that an additional series of constrained minimizations were needed to generate the disulfide bonds in the case of (MEL-K23Q,Q25C)$_2$. Before simulated annealing, cysteine sulfurs were brought into proximity by a series of minimizations using distance constraints. Disulfide bonds were then formed between neighboring peptide pairs followed by exhaustive minimization.

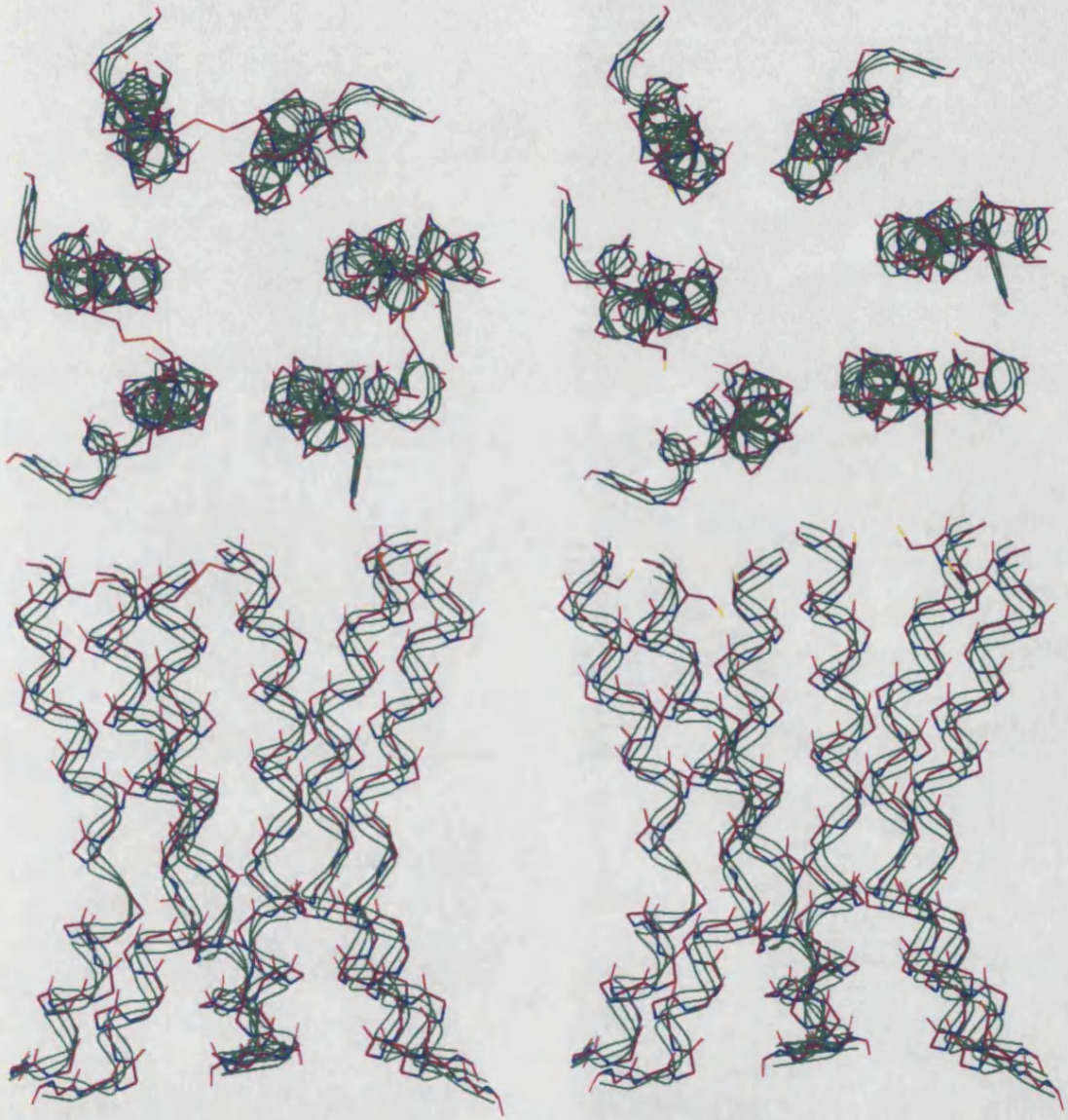

FIGURE 7.7. HEXAMERIC BUNDLES OF MEL-K23Q,Q25C AND (MEL-K23Q,Q25C)$_2$ GENERATED USING MD SIMULATED ANNEALING. The procedure outlined in the legend of Figure 7.5 was used to generate these mutants, with the exception that an additional series of constrained minimizations were needed to generate the disulfide bonds in the case of (MEL-K23Q,Q25C)$_2$. Before simulated annealing, cysteine sulfurs were brought into proximity by a series of minimizations using distance constraints. Disulfide bonds were then formed between neighboring peptide pairs followed by exhaustive minimization.

FIGURE 7.8. ELECTROSTATIC ISOPOTENTIAL CONTOUR PLOTS OF HEXAMERIC BUNDLES OF MEL AND MEL-K7Q. Hexameric bundles described in Figure 7.5 were used to generate electrostatic isopotential contour maps at the +50kcal/mol level; The top figure is MEL and the bottom is MEL-K7Q.

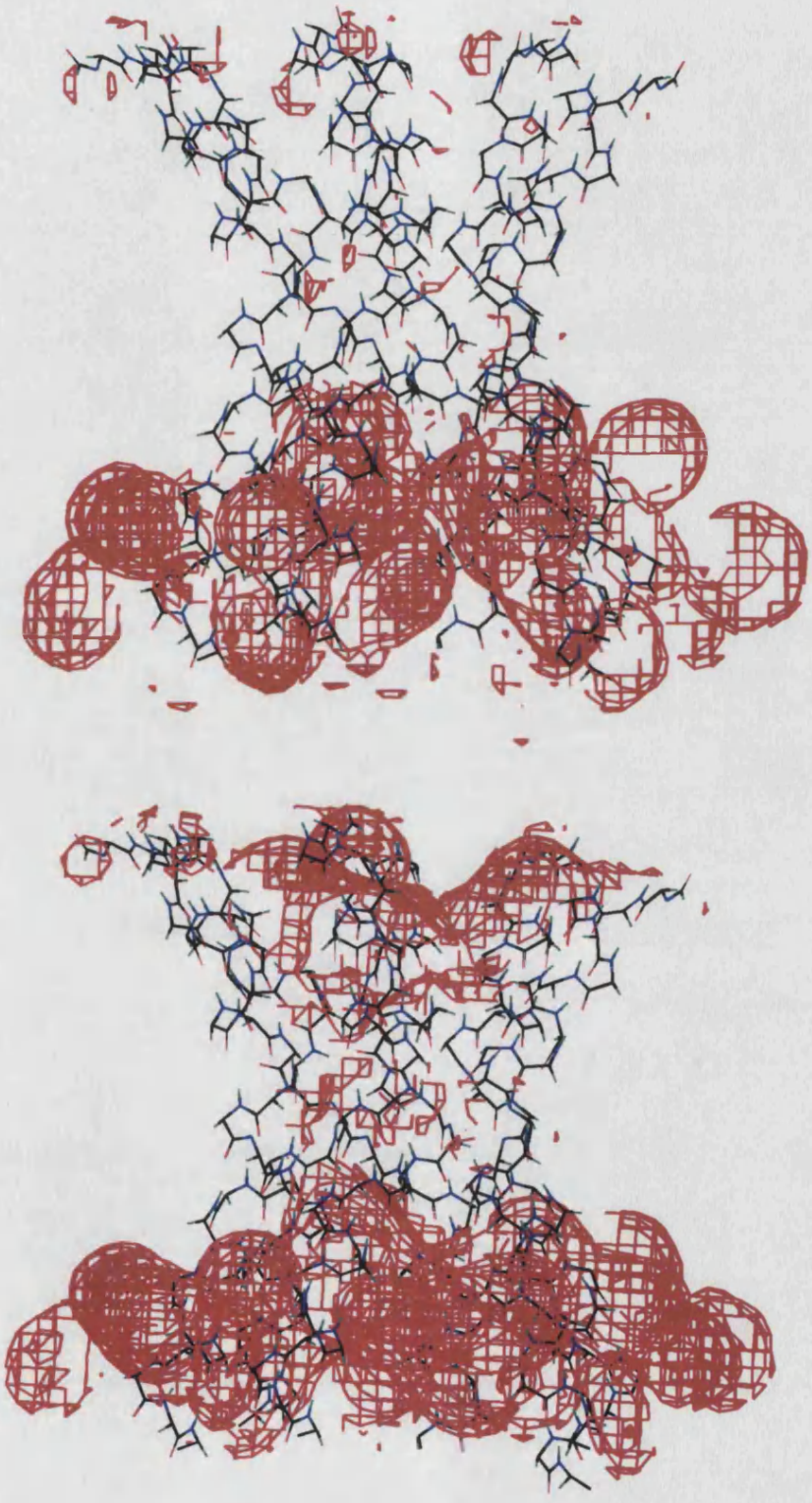

FIGURE 7.9. ELECTROSTATIC ISOPOTENTIAL CONTOUR PLOTS OF HEXAMERIC BUNDLES OF MEL-K23C AND $(MEL\text{-}K23C)_2$. Hexameric bundles described in Figure 7.6 were used to generate electrostatic isopotential contour maps at the +50kcal/mol level; The top figure is MEL-K23C and the bottom is $(MEL\text{-}K23C)_2$.

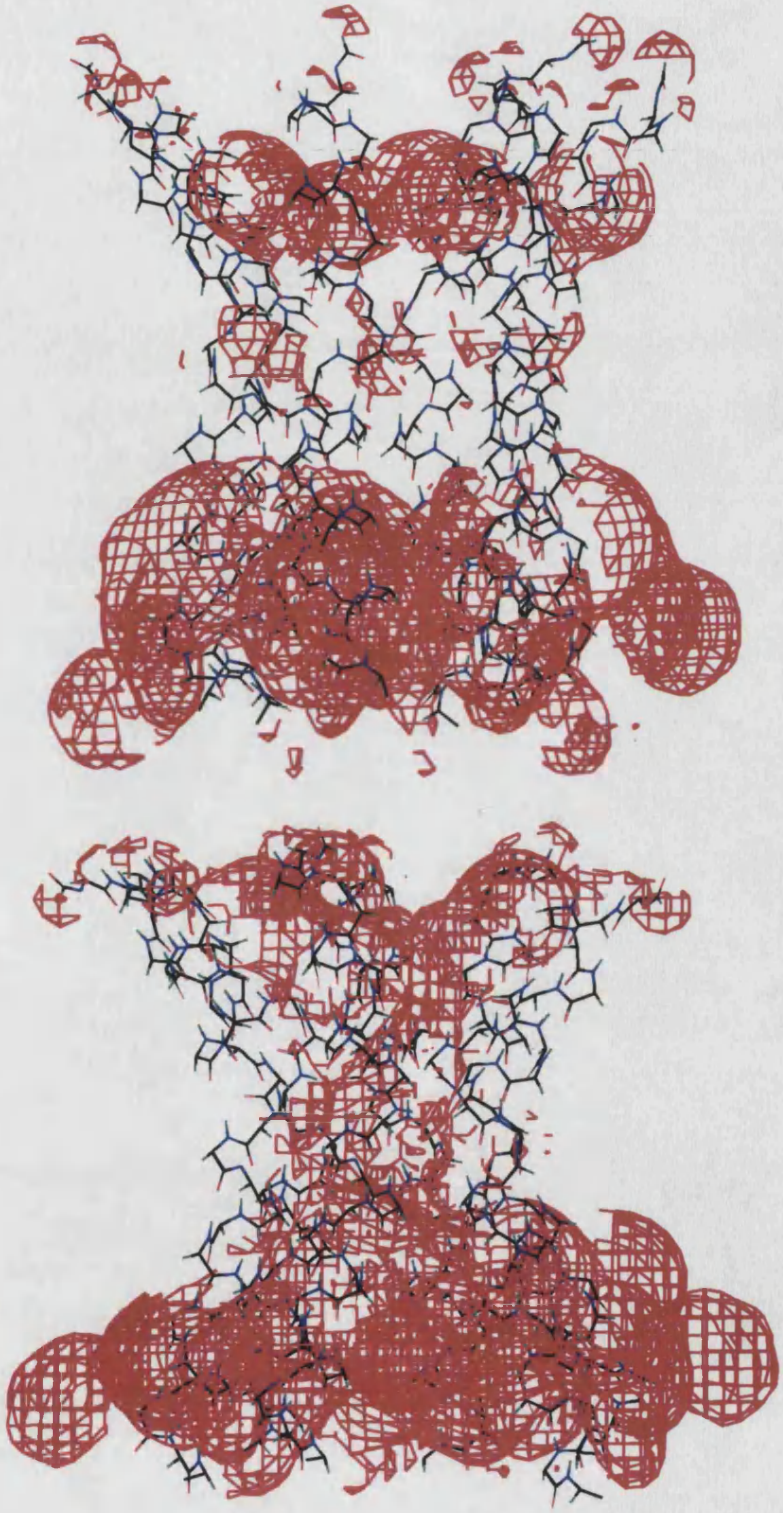

FIGURE 7.10. ELECTROSTATIC ISOPOTENTIAL CONTOUR PLOTS OF HEXAMERIC BUNDLES OF MEL-K23Q,Q25C AND (MEL-K23Q,Q25C)$_2$. Hexameric bundles described in Figure 7.7 were used to generate electrostatic isopotential contour maps at the +50kcal/mol level; The top figure is MEL-K23Q,Q25C and the bottom is (MEL-K23Q,Q25C)$_2$.

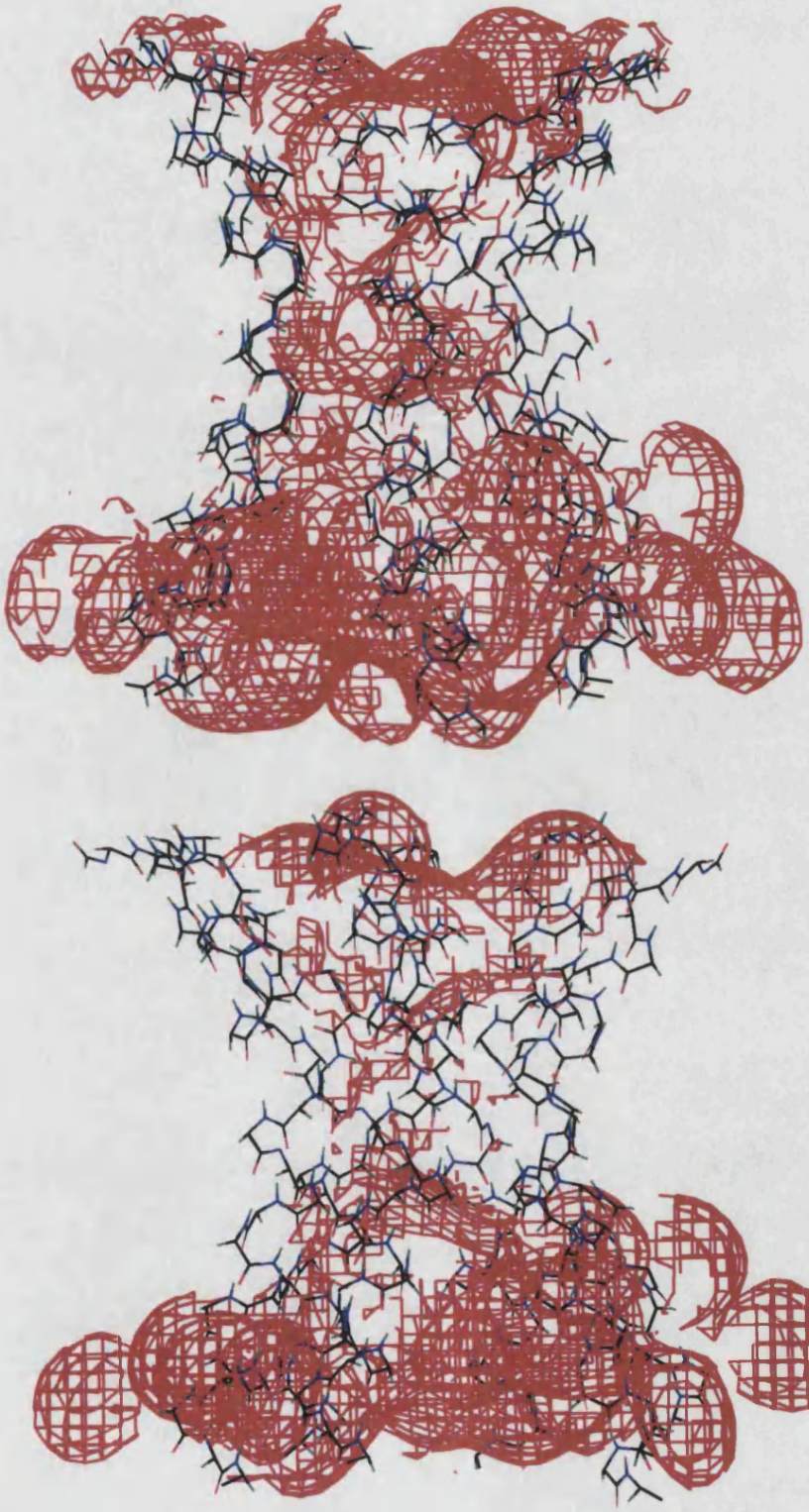

7.8. Hydrogen Bonding Patterns in Melittin Analog Bundles. Hydrogen bonding patterns are examined in the melittin and melittin mutant bundles. Since changes in hydrogen bonding patterns may correlate with channel behavior, the melittin bundles generated as described above were separated into monomer pairs are shown with the hydrophillic face of the peptides pointing out of the plane of the paper. The rationale in splitting the bundles into pairs is based on the observation that during the MDSA simulations monomers appear to pair-up. This pairing interaction is seen in the uppermost models in Figures 7.5-7.7.

Figure 7.11 shows H-bonding in MEL with the characteristic 1→4 interruption around Proline-15, characteristic intermolecular H-bonding is also seen between LYS, ARG, THR and GLN residues. MEL-K7Q appears to preserve the backbone H-bonding patterns with additional (stabilizing) intermolecular H-bonding between GLN-7 and THR-10, as shown in Figure 7.12. The next Figure (7.13) shows that the cysteine mutant MEL-K23C appears to have an extended area of H-bond disruption around GLY-12 while the intermolecular bonding patterns appear to be preserved with respect to melittin. Figure 7.14 shows respective pairs of the dimer $(MEL\text{-}K23C)_2$; the left pair is a dimer showing the diminution of H-bond disruption around PRO-15. The rightmost pair in Figure 7.14 shows the interaction between two neighboring dimers, here there appears to be a decrease in the number of intermolecular interactions. Finally, the H-bonding interactions for MEL-K23Q,Q25C and $(MEL\text{-}K23Q,Q25C)_2$ are shown in Figures 7.15 and 7.16, respectively. MEL-K23Q,Q25C appears to have far fewer intermolecular H-bonding patterns compared to MEL and MEL-K23C (Figure 7.14) while dimerization appears to cause a re-establishment of inter- and intramolecular H-bonding interactions (Figure 7.15).

FIGURE 7.11. HYDROGEN BONDING IN MEL BUNDLES. Hydrogen bonding patterns in MD simulated annealing generated melittin bundles are shown here. Two pairs of helices were taken from the bundles and shown from the hydrophilic (channel facing) side.

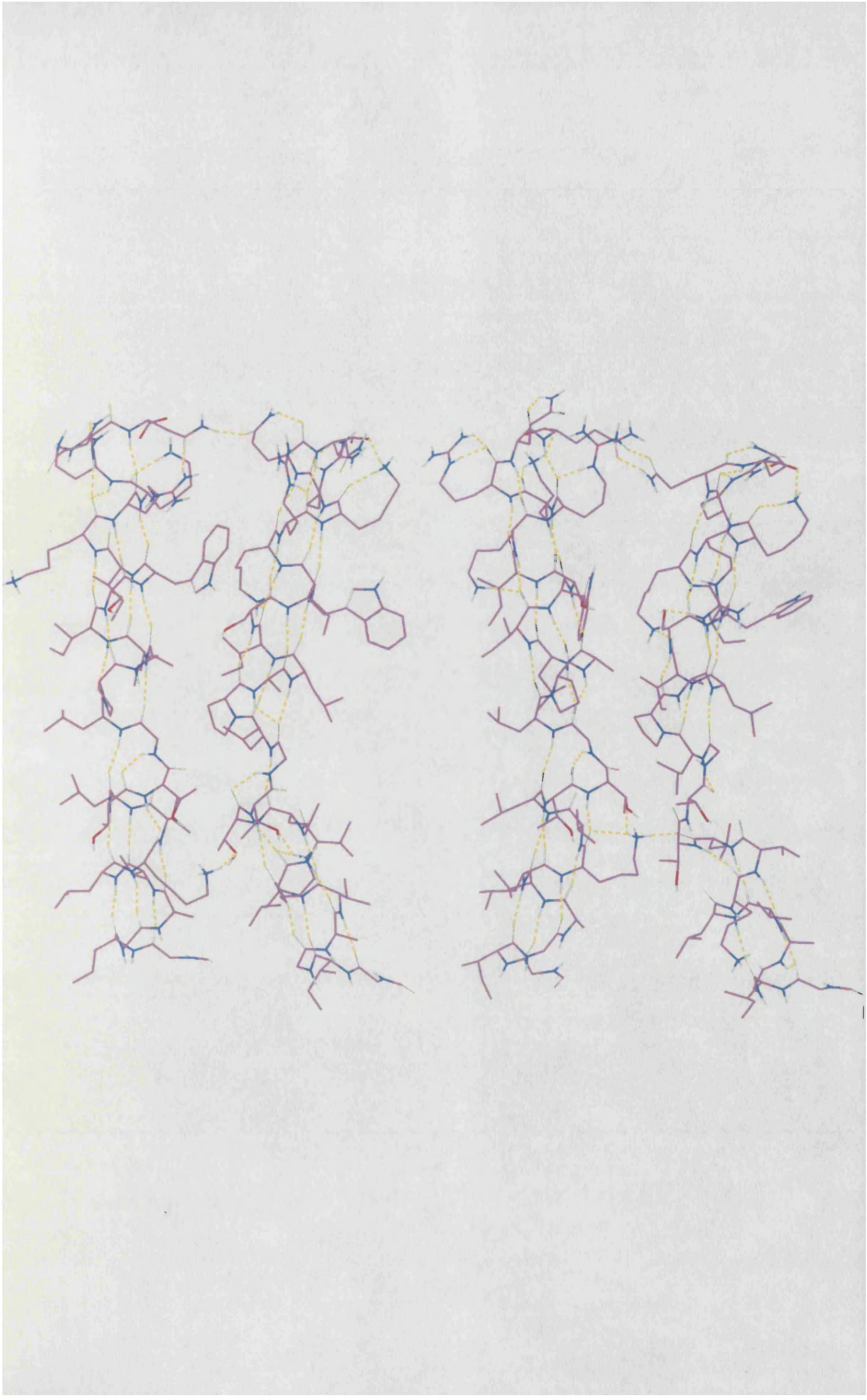

FIGURE 7.12. HYDROGEN BONDING IN MEL-K7Q BUNDLES. Hydrogen bonding patterns in MD simulated annealing generated melittin bundles are shown here. Two pairs of helices were taken from the bundles and shown from the hydrophilic (channel facing) side.

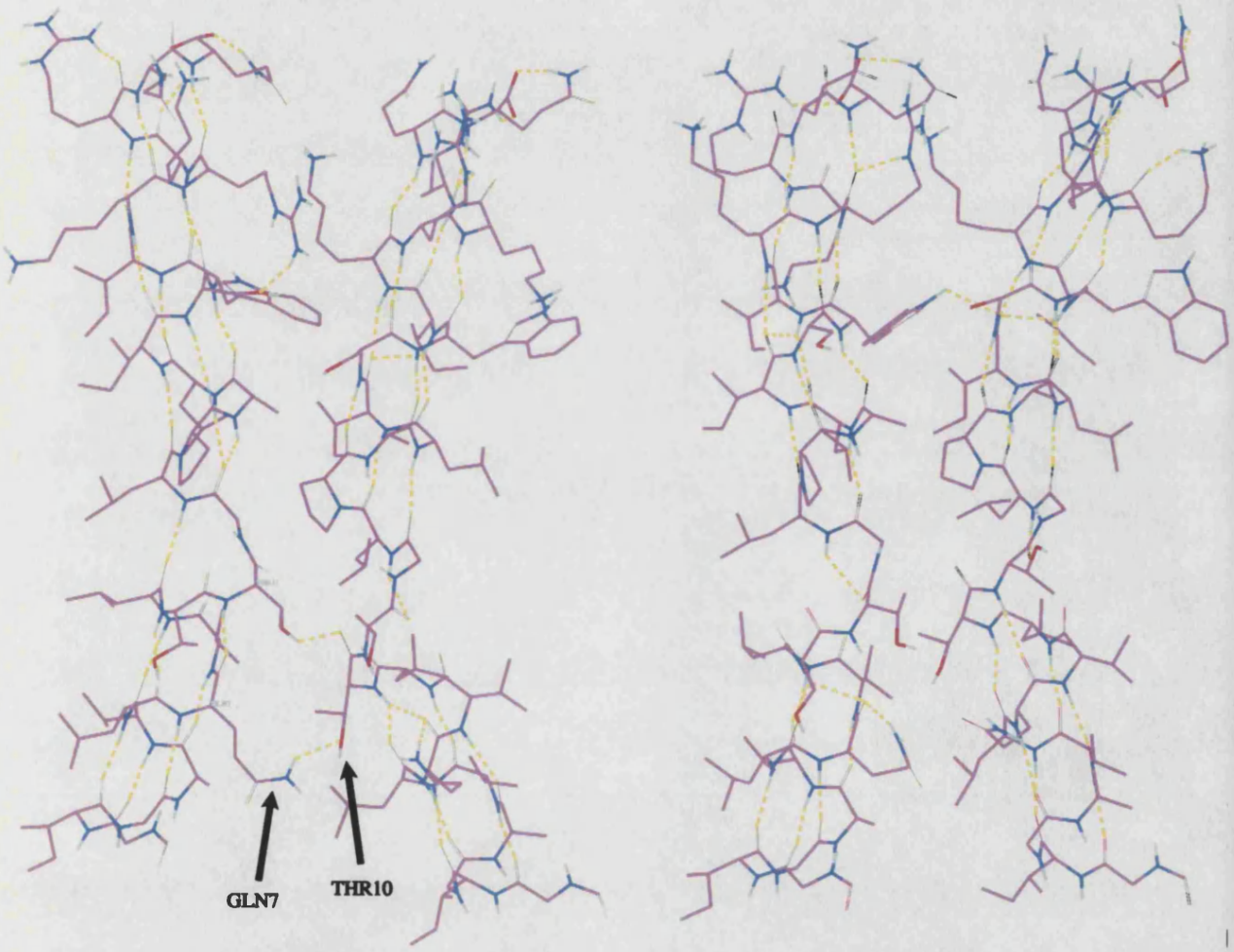
GLN7
THR10

FIGURE 7.13. HYDROGEN BONDING IN MEL-K23C BUNDLES. Hydrogen bonding patterns in MD simulated annealing generated melittin bundles are shown here. Two pairs of helices were taken from the bundles and shown from the hydrophilic (channel facing) side.

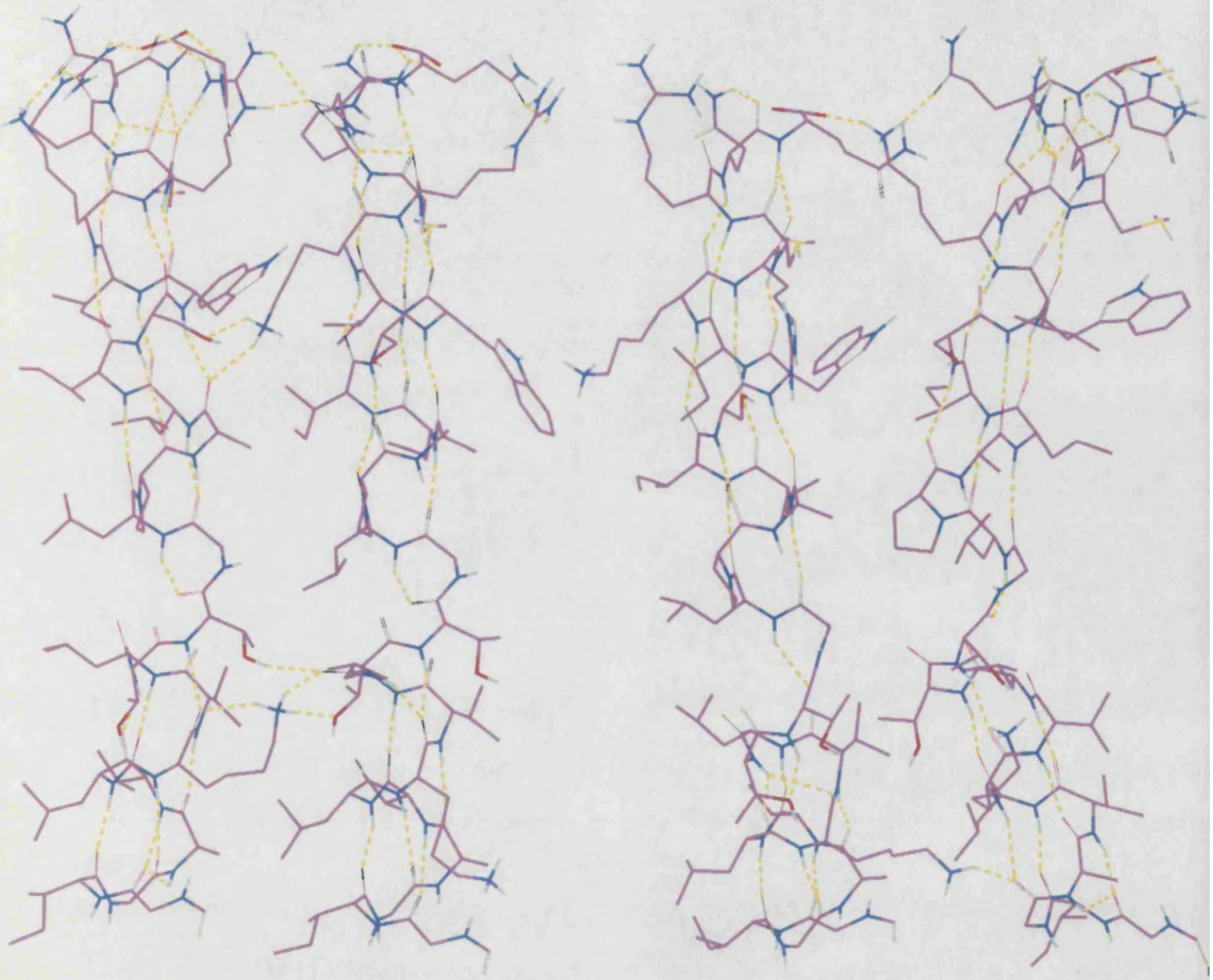

FIGURE 7.14. HYDROGEN BONDING IN $(MEL\text{-}K23C)_2$ BUNDLES. Hydrogen bonding patterns in MD simulated annealing generated melittin bundles are shown here. Two pairs of helices were taken from the bundles and shown from the hydrophilic (channel facing) side.

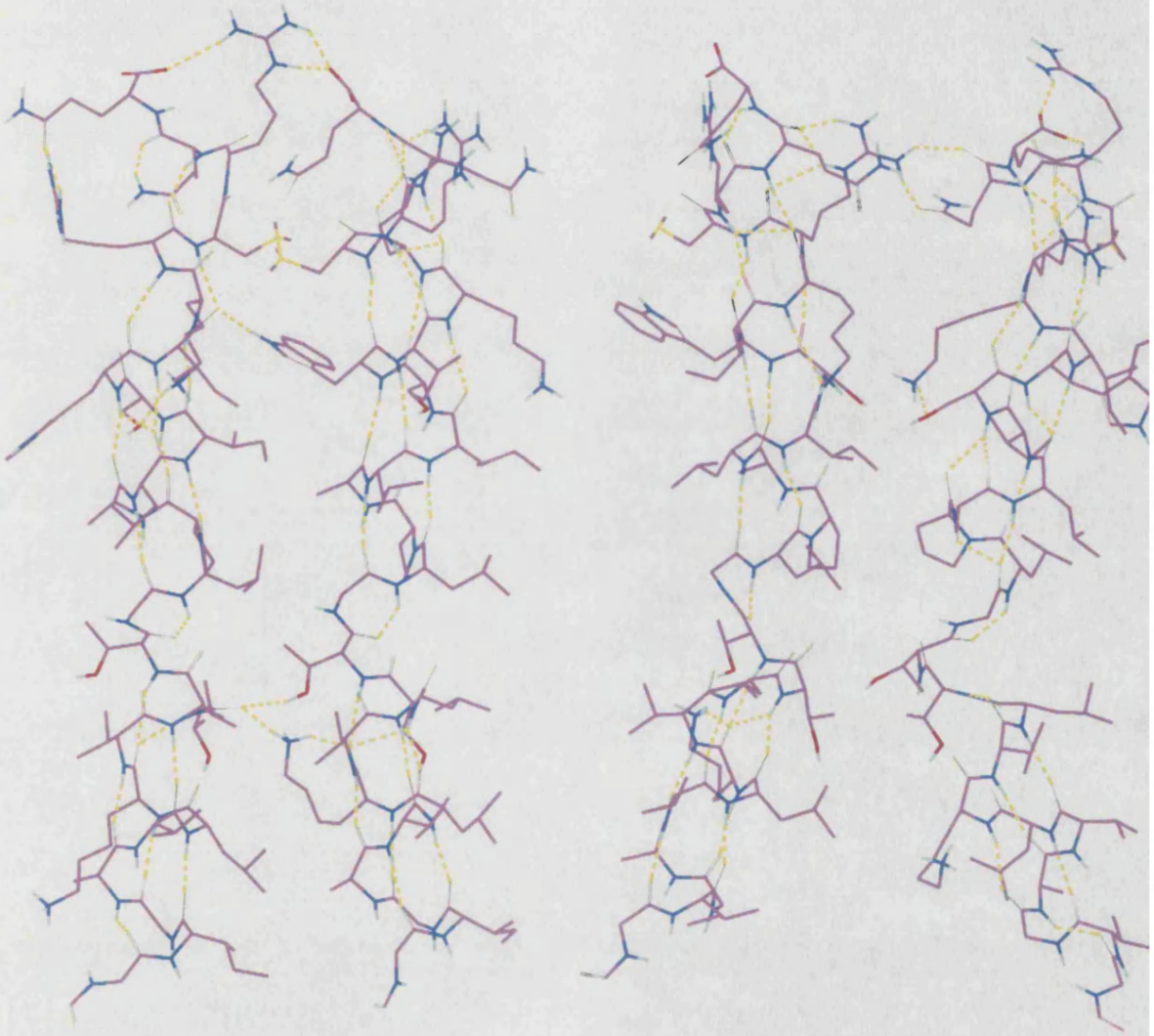

FIGURE 7.15. HYDROGEN BONDING IN MEL-K23Q,Q25C BUNDLES. Hydrogen bonding patterns in MD simulated annealing generated melittin bundles are shown here. Two pairs of helices were taken from the bundles and shown from the hydrophilic (channel facing) side.

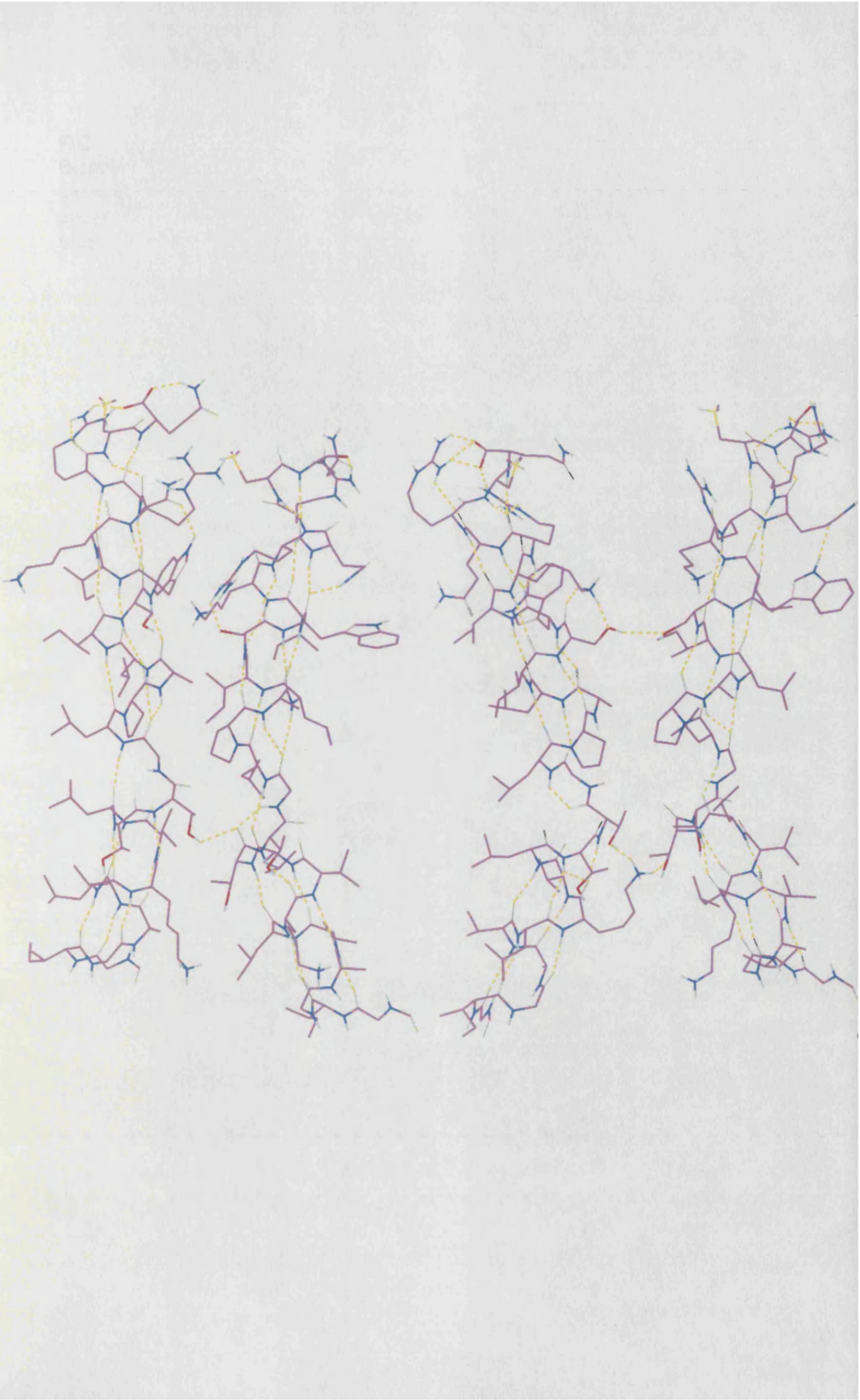

FIGURE 7.16. HYDROGEN BONDING IN (MEL-K23Q,Q25C)$_2$ BUNDLES. Hydrogen bonding patterns in MD simulated annealing generated melittin bundles are shown here. Two pairs of helices were taken from the bundles and shown from the hydrophilic (channel facing) side.

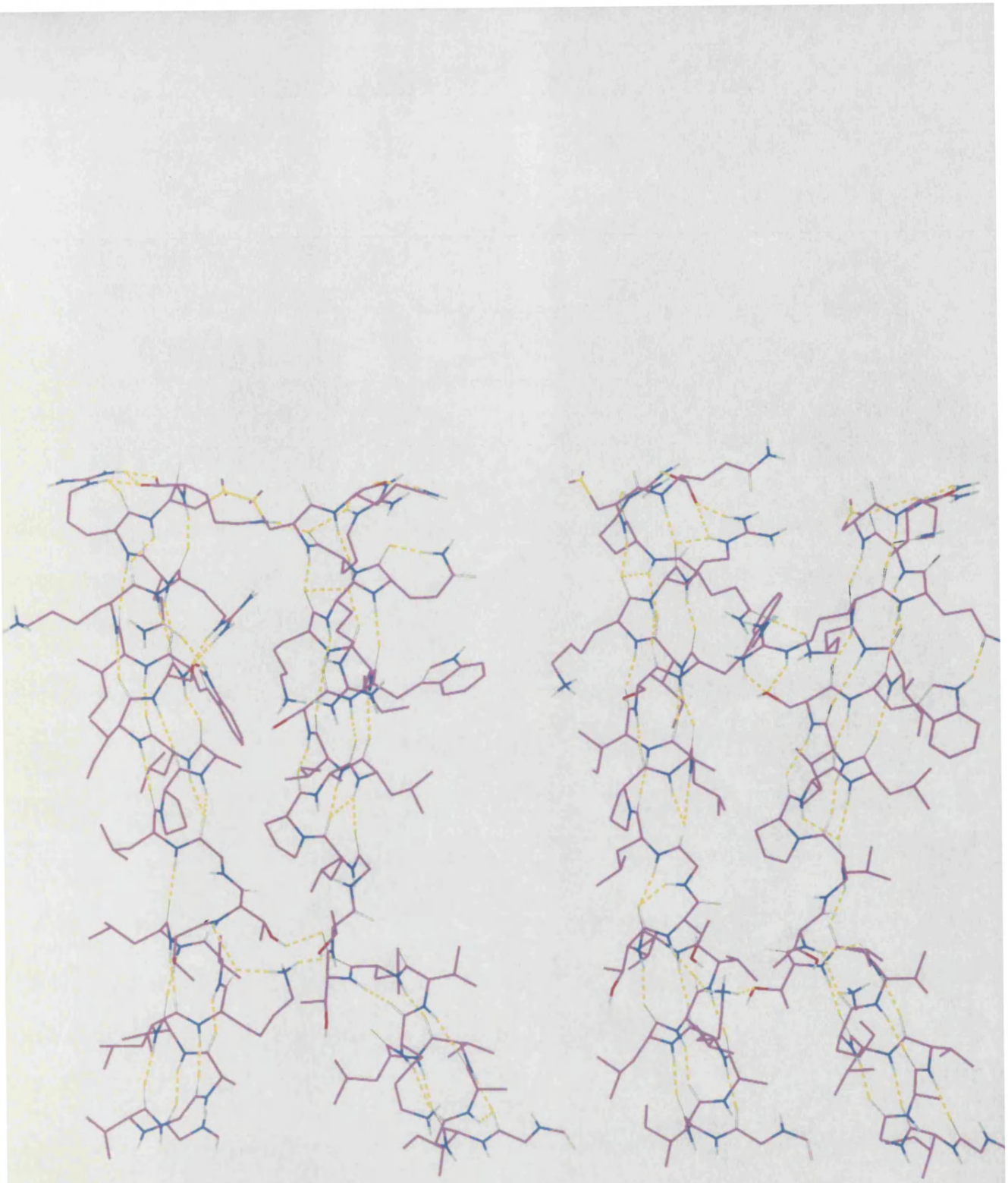

FIGURE 7.16. HYDROGEN BONDING IN (MEL-K23Q,Q25C)$_2$ BUNDLES. Hydrogen bonding patterns in MD simulated annealing generated melittin bundles are shown here. Two pairs of helices were taken from the bundles and shown from the hydrophilic (channel facing) side.

7.9. Heptameric Bundles of Melittin. The high conductance levels often seen with melittin may indicate either non-specific membrane perturbations or the assembly of channels with larger pore radii. A heptameric bundle of melittin was built and subjected to molecular dynamics simulated annealing to assess the stability of a larger bundle. Interestingly, the helical distortions due to the kink angle around PRO-15 appear to be significantly diminished in these channels, the leftmost models in Figure 7.17 show two views of the heptameric channel. Notice the markedly increased pore diameter and the lack of kink-derived constriction at the center of the channel. The rightmost model in this figure shows a hydropathy profile of the amino acids, indicating a favorable clustering of polar and non-polar moieties.

FIGURE 7.17. HEPTAMERIC BUNDLE MODEL OF MEL GENERATED USING MD SIMULATED ANNEALING. The leftmost figures show orthogonal views of heptameric bundles of melittin. The figure on the right shows the relative orientation of hydrophobic (green) and hydrophilic (purple) amino acids in the bundle.

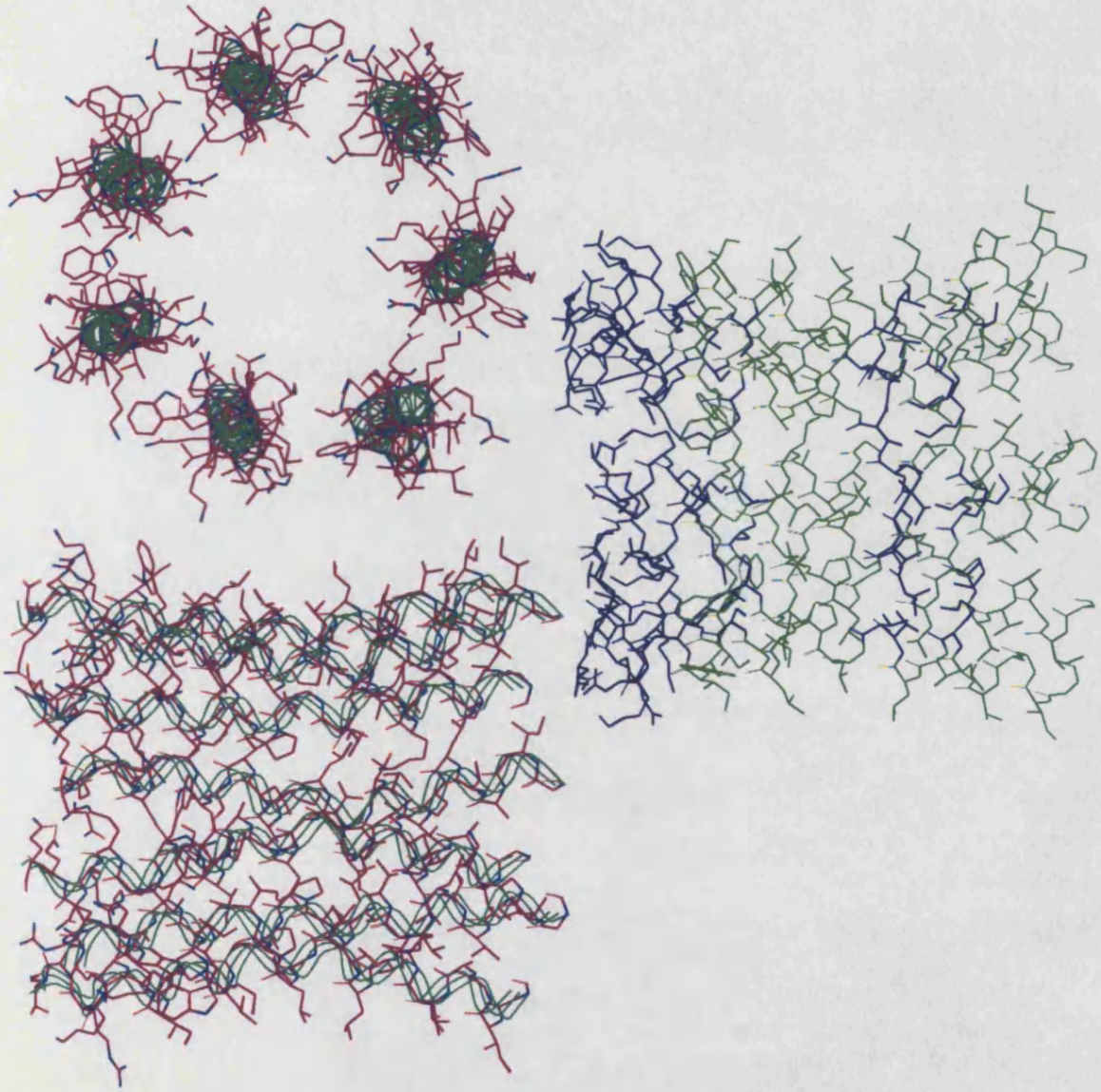

DISCUSSION AND CONCLUSIONS

8.1. CHEMISTRY AND SYNTHESIS

8.1.1. Ferrocene Derivatives. At the outset of this project a great number of ferrocene intermediates were synthesized with the aim of providing starting materials for a variety of peptide-synthetic strategies. The majority of ferrocenes described in this Thesis were made *via* modification of established chemistry and methodologies. A number of notable exceptions are discussed below.

The novel compound ferrocene-1,1'-bis((α-keto)butyric acid) {2.3.23} was synthesized from ferrocene and succinic anhydride using Friedel-Crafts electrophilic aromatic substitution. The seemingly intractable tars that often result from ferrocene/Friedel-Crafts reactions, as well as misleading results from chromatographic analysis, have prevented this methodology from being widely used. In the course of this investigation it was discovered that the desired alkylation products could easily be isolated in high yield by reduction of the crude reaction mixture with a large excess of sodium dithionite.

Another class of novel ferrocene compounds investigated are the bis((amino)alkylamido)ferrocenes. These compounds were designed with the intention of using them as cross-linking agents in Pillilar-type dipeptide synthesis, described in Chapters 2 and 3. Despite the fact that we have spectroscopic and spectrometric evidence that three such compounds were synthesized [1,1'-bis(4-amino)propanoyl)ferrocene amide {2.3.28}, 1,1'-bis((6-amino)hexanoyl)ferrocene amide {2.3.29} and 1,1'-bis(piperazineoyl) ferrocene amide {2.3.30}] they proved difficult to isolate. It is possible that conversion of the respective diamines to an alternative, less hygroscopic, salt form might allow crystallization. This is

an example of the difficulties one encounters when dealing with the purification of aromatic compounds with flexible sidechains.

8.1.2. Solution Phase Synthesis of Ferrocenoyl Peptides. The standard methodology for the synthetic modification of peptide hydroxyl moieties has traditionally precluded the use of acid chlorides due to their propensity to dehydrate amino acid sidechains containing acidic hydrogens, especially glutamine. As one might expect, the use of docile acylating reagents such as anhydrides often results in poor yields. During this investigation it was established that conversion of an acid chloride (ferrocenoyl chloride) to the equally reactive N-acylpyridinium salt prevented sidechain dehydration while affording high yields of desired peptide derivatives (Schmitt *et al.*, (1997)). Using this methodology we were able to successfully synthesize C-terminus ferrocenoyl alamethicin {2.4.1} and C-terminus (1'-carboxy)ferrocenoyl alamethicin {2.4.2}.

8.1.3. Coupling Strategies—Dimeric Alamethicin Derivatives. On a more pejorative note, we were unsuccessful using Pillilar coupling methodology for the synthesis of tethered alamethicin dimers described by You *et al.* (1996). This methodology converts the alamethicin hydroxyl to a carbonate ester followed by O→N transesterfication with a diamine tether, this results in two alamethicin molecules linked to tether *via* carbamate groups. The p-nitrophenylcarbonate ester {2.6.1} was synthesized in high yield and proved easy to purify. Unfortunately, O→N transesterfication was attempted using a large number of mono- and diamines without success. Chromatographic analysis on the reaction mixtures indicate that hydrolysis of the carbonate ester was largely responsible for the failed reactions.

8.1.4. Solid Phase Synthesis of Alamethicin Derivatives. The first successful synthesis of C-terminus carboxy alamethicin is described in Chapter 2. Until recently, the solid phase synthesis of hydrophobic

peptides has been very difficult often requiring tenuous fragment based assembly (Nagaraj & Balaram, 1981). Alamethicin brings additional challenges in that it contains exceedingly hindered α-amino-isobutyric acids and two racemizable proline resedues. Not long ago, Wenschuh and coworkers (Wenschuh *et al.*, 1995) reported a solid phase synthesis of alamethicin utilizing Fmoc-amino acid fluorides. The extreme reactivity of acid fluorides toward amine nucleophiles appears to overcome all of the problems mentioned above. The disadvantage is that it is not possible to monitor the progress of individual coupling steps. This new methodology was adapted for the synthesis of C-terminus carboxyl peptides. The rationale for making C-terminus carboxyl alamethicin was based on the literature precedent that CFP bundles containing C-terminus hydrogen bonding moieties are stabilized relative to their non-carbonyl counterparts, although the presence of a ionizable group often has a destabilizing effect, as mentioned above. The inclusion of a carboxy group also makes possible a number of robust derivitization chemistries not possible with C-terminus hydroxyl peptides. Although the synthesis of C-terminus carboxyl alamethicin {2.5.1} and C-terminus carboxyl alamethicin containing an N-terminus ferrocene amide {2.5.2} were accomplished, yields suffered due to difficulty in cleaving the peptide from the PEG-PS resin. It is reasonable to hypothesize that the hydrophobic nature of the bound peptide is preventing the highly polar cleavage reagent(s) from accessing the cleavage site.

8.1.5. <u>Synthesis of Difunctional Linkers</u>. After many unsuccessful attempts in exploiting the Pillilar O→N transesterfication reaction described above (Section 8.1.3) other routes to tethered alamethicin derivatives were explored. One well established ester/amide synthesis methodology: carbodiimide activation of carboxylic acids (Sheehan & Hess, 1955). Thus, three novel dicarboxylate linkers or tethers were synthesized for use with this chemistry. The first compound, ferrocene-1,1'-bis((α-keto)butyric acid){2.3.23} mentioned above, was made in high

yield using Friedel-Crafts acylation. The next compound was synthesized with the aim of designing photosensitive ion channels; diazobenzenes undergo *trans*-to-*cis* photoisomerization when irradiated with UV light, therefore a dicarboxylate derivative of this compound was synthesized: 3-(N-(4-((4-(3-carboxyprop- anoylamino)phenyl)diazenyl)phenyl)carbamoyl) propanoic acid {2.6.7}, see also Figure 2.5. Finally, a crown ether derivative was synthesized {4-(1,10-diaza-10-(3-carboxypropanoyl)-4,7,13,16-tetraoxa-cyclooctadecyl)-4-oxobutanoic acid; 2.6.6 ,see also Figure 2.5} with the idea of mediating the formation of higher-order alamethicin aggregates *via* ion-specific interactions. Imagine two molecules of crown ether tethered alamethicin dimerizing *via* crown ether-ion interactions, as shown in Figure 8.1.

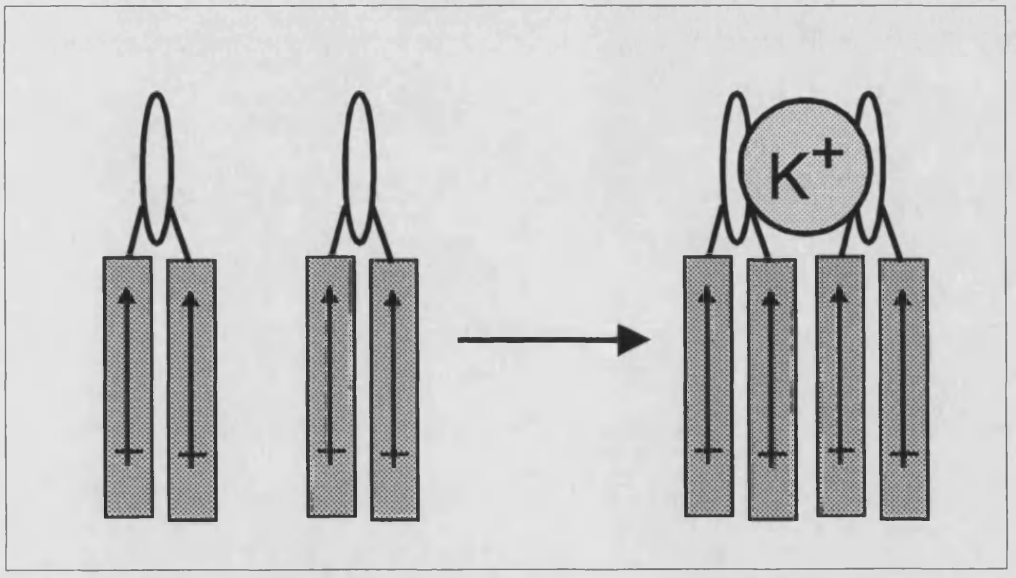

FIGURE 8.1. SCHEMATIC OF THE POSSIBLE ASSOCIATION OF TWO CROWN ETHER TETHERED ALAMETHICIN DIMERS MEDIATED THROUGH POTASSIUM ION.

Since there is a strong correlation between the number of helical peptide units in CFP molecule and channel stability (Montal, 1990; You *et al.*, 1996; Matsubara *et al.*, 1996) the structures described above may provide a means of generating channels whose stability can be modulated with metal ions. The exploitation of these novel linkers is most appropriately the subject of future investigations.

8.1.6. Analytical Methodology. One of the challenges in the synthesis of and modification of expensive natural products is the difficulty in accurate quantitation. For the purpose of quantitation of sub-milligram quantities of ferrocene containing peptides, a simple colormetric assay was developed {2.7.2; 3.3}. This assay, based on complexation of iron ion with thiocyanate is able to quantitate nanomole quantities of ferrocenoyl peptides.

8.2. BIOPHYSICAL AND MODELING STUDIES: C-TERMINUS DERIVATIVES OF ALAMETHICIN

Inspired by the finding of Woolley and coworkers (Woolley *et al.*, 1994) that the C-terminus pyromellitoyl ester of alamethicin acts as a "calcium-activated channel forming peptide", two C-terminus ferrocenoyl alamethicin esters were synthesized and their behavior evaluated under neutral and oxidative conditions. The postulate that CFPs with redox sensitivity, like calcium activation, could be designed has been validated by the experiments described in Chapters 4 and 5. These data were interpreted based on the helix-bundle model of channel formation. Thus considerations include possible effects on membrane association (dependent on hydrophobicity), orientation of the bound peptide relative to the bilayer (related to the net molecular dipole of the peptide helix) and self-association of the peptide within the bilayer.

8.2.1. Macroscopic and Single Channel Characterization. Macroscopic current-voltage measurements indicate that both the ferrocenoyl and 1'-carboxyferrocenoyl peptides require a higher transbilayer potential to induce channel formation (V_t) relative to the parent peptide (Figure 4.1). Since Fc-ALM is uncharged in the reduced state, we attribute this to steric and/or conformational effects imposed by the bulky ligand and to a decrease in the net molecular dipole. In the

case of cxFc-ALM, the introduction of a negatively charged carboxyferrocene ester (1,1'- dicarboxyferrocene monoethyl ester pK_a = 6.08 (measured in 68% MeOH (aq.) (Nesmeyanov & Reutov, 1957), this value may be as low as 5.0 if extrapolated to 100% H_2O) causes a further increase in V_t -- this finding is qualitatively consistent with the effect observed by Woolley and coworkers (Woolley *et al.*, 1994) where addition of a $(pyromellitoyl)^{3-}$ ester roughly triples V_t. On the other hand, it is likely that additional steric or conformational effects contribute to the behavior of cxFc-ALM: introduction of the carboxyferrocene, with its single negative charge, also triples its activation potential relative to ALM. The relationship between Fc-ALM and cxFc-ALM is consistent with the observation of Hall (Hall *et al.*, 1984) that (Glu19-benzoyl)-$ALM_{Rf = 30}$ has a lower V_t than R_f = 30 ALM. Recent work by Dugast (Dugast *et al.*, 1997) provides evidence that the C-terminus derivitization of alamethicin with a bulky/hydrophobic moiety (fluorescin isothiocyanate) increases its V_t. However, unlike Fc-ALM, ftc-ALM channels posses higher single-channel conductance levels, see below.

Overall, a general principal appears to be that C-terminus modification of ALM leads to higher activation potentials. It is important to note that cxFc-ALM also exhibits markedly higher hysteresis compared to ALM or Fc-ALM (Figure 4.1). One possibility discussed in detail below, is that the carboxylate ion forms stabilizing *inter*molecular interactions once the channels assemble, leading to hysteresis. However, similar effects are not seen with pyromellitoyl-alamethicin, as one would expect based on this argument (Woolley, personal communication)— but it is clear that disfavored electrostatic interactions between neighboring highly negative pyromellitoyl moieties might exceed or disallow stabilizing hydrogen bonding interactions.

The single-channel conductance levels of Fc-ALM are slightly lower than alamethicin (Table 4.1). Possible explanations include the effect of added steric bulk at the mouth of the channel or favorable

aromatic-cation interactions supported by the ferrocenoyl moieties, which in turn may hinder the free passage of ions through the channels. It also appears that the opening times are shorter (Figure 4.2). The conductance levels for cxFc-ALM are nearly identical to those of Fc-ALM, although the presence of the carboxylate ion in the former increases the conductance levels slightly (Table 4.1). However, the temporal behavior of the cxFc-ALM channels is dramatically different from either ALM or Fc-ALM (Figure 4.2), single channel traces characterized by long opening times. Unlike the other peptides, one aggregation state (the n = 2 level) of cxFc-ALM seems particularly stable, as evidenced by the population of long-lived channels at n = 2. Short-lived bursts to higher conductance levels (n = 3, 4) appear frequently during these long-opening events. It is compelling to reason that these bursts represent short sojourns to *sub*states of the long-lived channels since the short lived bursts occur less frequently in the absence of the stable population. These short n = 3 bursts lack the conductance multiplicity [$g_{n=3} \neq 2\times(g_{n=2})$] that would result from multiple openings. However, the possibility that these conductance bursts represent multiple openings cannot be ruled out.

8.2.2. <u>Redox studies on Fc-ALM and cxFc-ALM</u>. The *in situ* addition of cerium ammonium nitrate to Fc-ALM channels causes the elimination of single-channel activity at a given holding potential, an effect not seen with ALM channels (Figure 4.4). Calculations indicate that the orientation of the net molecular dipole of Fc-ALM may reverse upon oxidation (table 8.1). Channel activity can however be restored by increasing the bilayer potential 25-35 mV (data not shown). Again, this is consistent with the finding that charged groups at the termini of CFPs decreases their propensity to form channels.

Figure 4.4 compares the behavior of ALM, Fc-ALM and cxFc-ALM channels under oxidative conditions; it appears that the introduction of a positive charge counterbalances the deleterious effect of the carboxylate

ion seen in cxFc-ALM, i.e. oxidation of Fc-ALM results in a charged C-terminus but oxidation of cxFc-ALM results in a neutral C-terminus. Thus, three types of macroscopic redox behavior are evident: (1) oxidative conditions eliciting no effect [ALM], (2) decreasing channel activity [Fc-ALM] and (3) increasing channel activity [cxFc-ALM].

peptide	total charge	C-term charge	N-term charge	molecular dipole (Debye) moment	z-component	V_{t+} (mV)	F_{oct} (kcal/mol)
ALM	0	0	0	81.3	76.4	66	-117.5
cxALM-NAc	-1	-1	0	163.7	155.4	112	-113.2
Fc-ALM	0	0	0	25.5	22.5	81	-116.7
Fc-ALM(ox)	1	1	0	32.6	-31.2	>200	-113.9
cxFc-ALM	-1	-1	0	84.6	75.4	174	-115.4
cxFc-ALM(ox)	0	0	0	43.5	27.8	170	-112.6
cxALM-NFc	-1	-1	0	154.3	151.1	93	-115.6
cxALM-NFc(ox)	0	-1	1	269.2	261.8	114	-110.9
pm-ALM	-3	-3	0	369.8	366.1	198	-111.1
ftc-ALM	0	0	0	34.2	31.9	117	-122.3

TABLE 8.1. PHYSICAL PROPERTIES OF ALAMETHICIN DERIVATIVES. Dipoles were calculated using charge equilibration and DFT derived charges, as described in Chapter 7. F_{oct}: calculated free energy in octanol relative to vacuum, as described by Pearlman (1980), with added parameters for ferrocene: -0.570 for the reduced form and 0.840 oxidized form. In the case of oxidized (ox) form of the ferrocenoyl peptides V_t is reported here due to *cis* addition of CAN.

It might be argued that the large concentration of CAN present in the *in situ* experiments elicits a non-specific effect. To address this possibility, small quantities of peptides and buffered CAN were combined prior to addition to the PLB apparatus. Single-channel traces clearly indicate that these conditions alter the characteristics of both Fc-ALM and cxFc-ALM channels (Table 4.1; compare figure 4.2b to 4.5a and 4.2c to 4.5b). Opening lifetimes are considerably shorter, and in the case of Fc-ALM the highest observed conductance state is absent. This is in marked contrast to cxFc-ALM where one favored conductance state is replaced by a number of equally probable levels; indeed the long openings observed with reduced cxFc-ALM appear to be selectively

eliminated by oxidation of the ferrocenoyl moiety. The possibility that the cerium ions are participating in specific interactions such as coordination by the aromatic rich C-termini of the channels cannot be ruled out and will be further discussed below. It is also somewhat surprising that Fc-ALM does not form channels at *cis* negative potentials given the hydrophobic nature of the reduced ferrocene moiety-- but nonetheless stands as additional evidence of the primacy of dipole effects in CFP channel formation.

Another possibility is that the introduction of interfacial charge may create disfavored electrostatic interactions with the phosphocholine headgroups. This view is consistent with the observation that introduction of negative charge into C-terminus in pyromellitoyl peptide increases its conductance threshold (Woolley *et al.*, 1994). It is possible that attractive (*inter-* and *intra*molecular) cation-aromatic interactions between F'-20 and the Fe(III) center may induce conformational changes in the oxidized peptides relative to the reduced. Favorable cation-aromatic interaction has been postulated to be important in a number of systems (Dougherty & Stauffer, 1990). In addition, the *cis* lumen of the ferrocenoyl channels are very rich in aromatic character due to the presence of multiple F' sidechains and ferrocene moieties, possibly giving rise to enhanced interaction with solvated ions.

8.2.3. Modeling Studies. Cursory molecular modeling of hexameric Fc-ALM bundles indicates that the metallocene moieties impose little steric constraint on the C-terminus domain of the bundles, do not perturb peptide helicity and have diminutive effect on overall bundle architecture. Unfortunately, MD simulations needed to rigorously explore the structural effects of the ferrocene moiety were hampered by lack of Forcefield paramiterization. Preliminary molecular dynamics simulations of monomeric Fc-ALM bundles in methanol droplets, using the UFF Forcefield, indicate that inclusion of a C-terminal ferrocene moiety

decreases RMS backbone movement in the C-terminus, thus implying a stabilizing effect (data not shown). Despite the fact that these results should be regarded as speculative, their further refinement may lead to a theoretical system with great predictive potential.

8.3. BIOPHYSICAL AND MODELING STUDIES: N-TERMINUS FERROCENOYL DERIVATIVES OF ALAMETHICIN

Based on the success of these experiments we were motivated to synthesize alamethicin analogs containing N-terminus redox centers.

C-terminus carboxyl alamethicin (cxALM-Ac) and its N-terminus ferrocenoyl derivative (cxALM-NFc) were synthesized and their channel forming behavior was extensively evaluated under neutral and oxidative conditions. The usefulness of these peptides in unraveling the forces which contribute to channel formation have been demonstrated by the experiments described in Chapter 6. This data is supportive of the helix-bundle or barrel stave model of channel formation (Sansom, 1993). Experiments described herein show for the first time a CFP with changeable ion selectivity.

8.3.1. <u>Macroscopic and Single Channel Characterization</u>. Macroscopic current-voltage measurements demonstrate that both cxALM-Ac and cxALM-NFc require a higher transbilayer potential to induce channel formation (V_t) relative to ALM (Figure 5.1; Table 8.1). Since cxALM-Ac has a negatively charged C-terminus, disfavored peptide-peptide and peptide-lipid electrostatic interactions may account for this difference. It is also possible that the decreased hydrophobicity (F_{oct} = -113.2 for cxALM-Ac *vs.* -116.7 kcal/mol for ALM) contributes to the increased V_t value. Both of these inferences are consistent with results reported above for cxFc-ALM {see Chapter 5 and 8.2.1} and the published V_t data for pm-

ALM, whereupon the introduction of a (pyromellitoyl)$^{3-}$ moiety to the C-terminus triples V_t (Woolley *et al.*, 1994). This result is also in agreement with macroscopic measurements conducted on R_f = 30 ALM (where GLN18 is replaced with GLU) and on a truncated alamethicin analog with a C-terminus carboxyl (Hall *et al.*, 1984); Both of these peptides have a lower macroscopic channel formation propensity relative to ALM. Finally, Wada and coworkers compared the macroscopic behavior of trichocellins A-II (·····VAL-AIB-IVA-GLN-GLN-PHEOL) and B-II (·····VAL-AIB-IVA-GLU-GLN-PHEOL), in keeping with the results described above— the introduction of a negative charge onto the C-terminus increases V_t (Wada *et al.*, 1997).

The introduction of a hydrophobic metallocene moiety into the N-terminus (cxALM-NFc) reduces V_t relative to cxALM-Ac, this decrease correlates well with increased total hydrophobicity (F_{oct} = -113.2 for cxALM-Ac *vs.* -115.6 kcal/mol for cxALM-NFc). This result is consistent with the hypothesis that one terminus of a CFP must penetrate the bilayer before ion channels can assemble (Baumann & Mueller, 1974; Boheim, 1974; Oiki *et al.*, 1990; Sansom, 1992). A consummate experiment would be to synthesize and evaluate N-terminus ferrocenoyl alamethicin, (C-terminal OH) this would allow the effect of N-terminal modification to be compared in two systems. Unfortunately, no work has been published on structure-activity relationships between N-terminus modified CFPs so there is little basis for evaluating our results against a literature precedent.

Single channel conductance levels of cxALM-Ac are slightly lower than ALM and are spread over a wider range of conductance levels {see Table 4.1 and 5.1}. But, the gating kinetics of the two peptides are qualitatively very similar. In sharp contrast is the behavior of cxALM-NFc relative to cxALM-Ac and ALM. The cxALM-NFc peptide forms channels whose mean open lifetimes are approximately five-fold shorter compared

to cxALM-Ac and ALM. Perhaps the most revealing result is that, although cxALM-NFc has a lower activation threshold (V_t), the actual microscopic gating process is hampered relative to cxALM-Ac. This may be supporting evidence for the molecular models of cxALM-NFc discussed below– the N-terminus metallocene at the constricted end of the bundle has a great potential to impact the kinetics and mechanism of gating.

8.3.2. Redox studies on cxALM-NFc: Evidence for Switchable Ion Selectivity. Our initial experiments were essentially duplications of the redox experiments conducted with Fc-ALM and cxFc-ALM . . . investigating redox driven alterations in channel behavior. Table 8.1 summarizes the results of macroscopic measurements described in Chapter 5 {5.4}; the oxidized form of cxALM-NFc has a higher V_t value than reduced cxALM-NFc or cxALM-Ac. This shift is most likely due to the energy barrier imposed by the need to traverse the charged ferrocene moiety through the bilayer.

Next, I sought to prove the following hypothesis: if the helix-bundle model of ion channel formation is correct, (i.e. if the N-terminus of the peptide must traverse the bilayer before channels are formed) one might evoke persistent transbilayer orientation by oxidizing the ferrocene moiety from the *trans* side of the apparatus without effecting initial insertion. This is because the energy barrier in the peptide coming back out of the membrane is increased by a factor of the Born solvation energy. Based on this hypothesis, one would expect that an I-V curve obtained by *trans* addition of oxidizing agent would be equivalent to the *cis* addition curve but shifted to lower potentials. Results from the addition of oxidizing agent to the *trans* side of the PLB apparatus show that this is indeed the case (see Table 5.2). During these investigations more detailed measures of macroscopic channel behavior were sought, particularly with regard to hysteresis, so the 25 and 100 pA thresholds for

both the ascending (dV/dt > 0) and descending (dV/dt < 0) I-V curves were measured. The V_{25} index is particularly revealing in comparing *cis* versus *trans* addition of oxidizing agent. The slope of the *cis* CAN curve, approximated by (V_{t+} - V_{25+}) is much greater than the slope of the *trans* CAN curve (6 *vs.* 26 respectively), indicating differing insertion energetics.

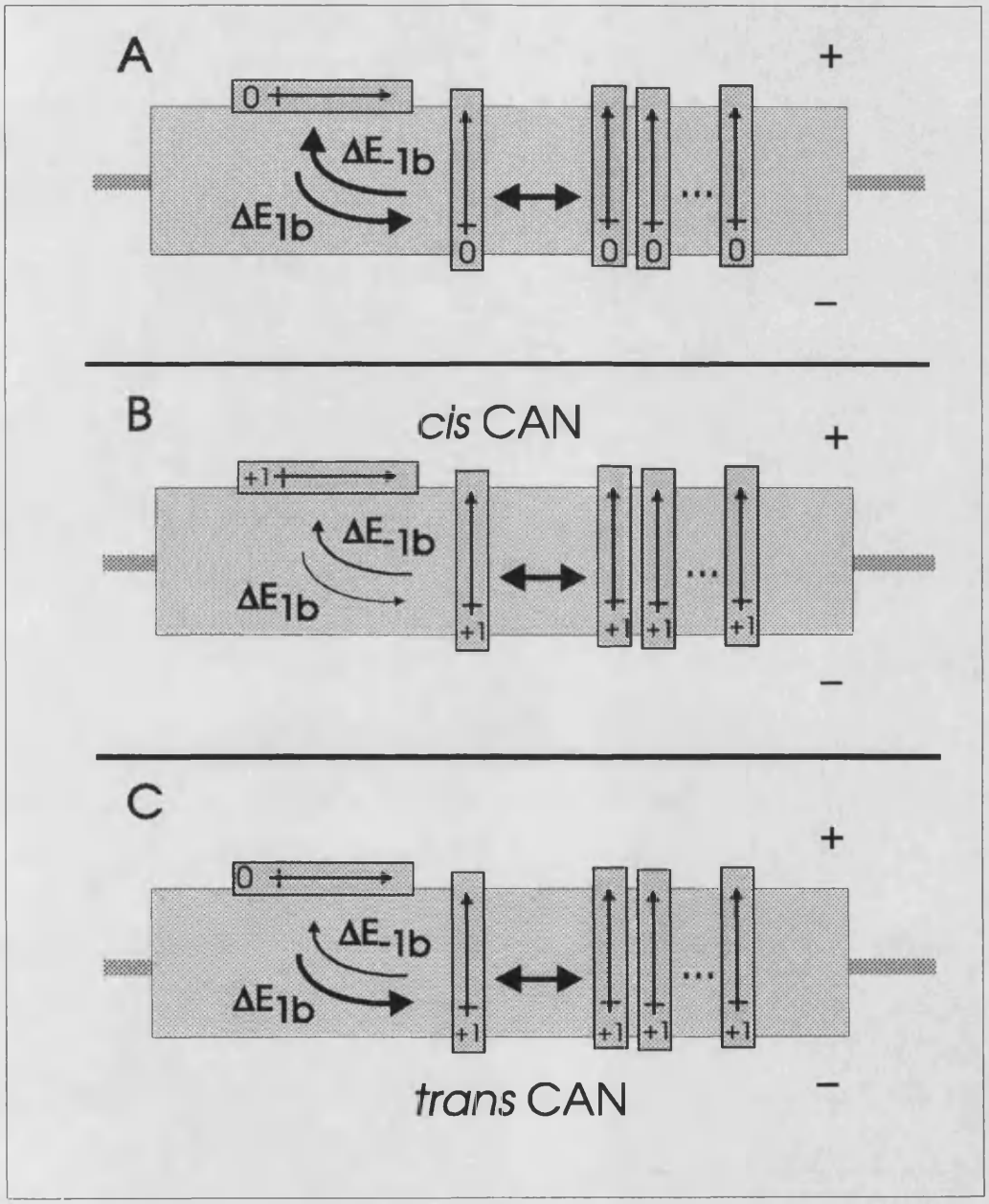

FIGURE 8.2. REDOX EXPERIMENTS WITH cxALM-NFc. A: Reorientation of cxALM-NFc from the bilayer surface due to an imposed potential, $|\Delta E_{1b}| = |\Delta E_{-1b}| = [\ |\Delta E_{bilayer\_penetration}| + |\Delta E_{desolvation}|\ ]$ (this nomenclature is used for the sake of consistency with discussions found later in the Chapter); B: The effect of oxidizing agent (CAN) added to the

cis well, $|\Delta E_{1b}| = |\Delta E_{-1b}| = [\ |\Delta E_{bilayer\_penetration}| + |\Delta E_{desolvation}| + |\Delta E_{Born}|\ ]$; C: The effect of oxidizing agent (CAN) added to the *trans* well. Imagine the scenario whereby the neutral ferrocene moiety of cxALM-NFc traverses the bilayer in response to an imposed *cis*-⊕ transbilayer potential and as soon as it contacts the oxidizing agent in the *trans* well it is oxidized, thus $|\Delta E_{1b}| < |\Delta E_{-1b}|$ and $|\Delta E_{-1b}| = [\ |\Delta E_{1b}| + |\Delta E_{Born}|\ ] = [\ |\Delta E_{bilayer\_penetration}| + |\Delta E_{desolvation}| + |\Delta E_{Born}|\ ]$. Arrow thickness' indicate probable weightings of the equilibria.

Single channel experiments indicate that oxidation of cxALM-NFc leads to channels with different conductance levels {Table 5.1 and 5.3} and enhanced channel lifetimes {Figure 5.6} relative to the reduced peptide. During the experiments where *trans* CAN was used as an oxidizing agent channels that persisted when the electronically generated transbilayer potential was brought to zero (V_E = 0 channels) were observed. This implied that the ionic excess in the *trans* side of the apparatus was creating a potential sufficient to sustain channel formation— an effect that could be eliminated by adding an equivalent amount of CAN to the *cis* side of the apparatus (data not shown). This effect was not observed when CAN was added to the *cis* side of the apparatus alone. The implication here is that channels formed by cxALM-NFc(ox) are exceedingly anion selective. To test this hypothesis a large organic oxidizing agent, DDBQ, was employed. DDBQ's predominate reduced form (a semiquinone) is devoid of charge {Figure 5.4}. *Trans* side oxidation of cxALM-NFc by DDBQ eliminated the V_E = 0 channels, but the addition of nitrate ion (as KNO_3) to the *trans* side (to a concentration equivalent to that in the CAN experiment) restored the V_E = 0 channels. This activity could in turn be eliminated by the addition of an equivalent amount of nitrate to the *cis* compartment.

At this point voltage-step experiments with asymmetric electrolyte concentrations were taken up to allow the ion permeability ratios (P_{M+}/P_{X-}) to be quantitated from reversal potentials of the various peptides. In these experiments I first established that CAN, added to the *trans* compartment, causes the formation of V_E = 0 channel ensembles (Figure

5.8, page 1). Once the system was equilibrated a value of V_{rev} = -65 mV was determined. Unfortunately, P_{M+}/P_{X-} could not be extrapolated from this experiment due to the impossibility of knowing the ionic makeup of the *trans* compartment. When DDBQ is used as an oxidizing agent one obtains a V_{rev} = -84.5 mV compared to -26 mV for reduced cxALM-Ac {Figure 5.9}. Application of the Goldman-Hodgkin-Katz equation yields a permeability ratio P_{M+}/P_{X-} = 0.90 for reduced cxALM-NFc and $P_{M+}/P_{X-} \cong$ 0.12 for the oxidized form. Note that $P_{M+}/P_{X-} \cong 1.5$ for ALM (Hall *et al.*, 1984). This striking change in selectivity is in accord with selectivity experiments conducted on various leucine-serine CFPs, (Lear *et al.*, 1997) these results are discussed in detail below {8.3.3}. It must be noted that the ratios described above may be somewhat inaccurate due to the impossibility of characterizing with precision the ionic makeup of the electrolyte milieu, we cannot rule out, for example, the presence of DDBQ-quinone (charge = -1) or the possibility of ionic species generated electrochemically at the Ag-buffer interface.

Finally, cxALM-NFc oxidized with DDBQ results in single channels with markedly different conductance and temporal character than those generated *via* CAN oxidation. The DDBQ oxidized peptide leads to larger channels, i.e. channels that posses stabilized higher conductance levels (n=4,6,7) whereas lower conductance levels (n=1,2) prevail upon CAN oxidation. This implies that the highly charged cerium ions (Ce^{+4} and Ce^{+3}) interact with the channel bundles beyond the oxidative capacity. One distinct possibility is that rings of hydrogen bonding atoms in the channels are acting as *pseudo*ligands for d/f-orbital coordination with the ceric or cerius ion.

8.3.3. <u>Modeling Studies</u>. The quicker gating kinetics (i.e. diminished stability) seen with cxALM-NFc relative to cxALM-Ac is borne out in the molecular modeling. Figure 7.4 shows the close proximity of the metallocene moieties. From this model, one might surmise that

considerable steric constraint and subsequent impact on bundle architecture may be elicited by the N-terminal ferrocences. It also appears that the ferrocene moieties may reside closer to the pore mouth, giving rise to additional peptide-peptide and peptide-ion interactions. Again, MD simulations are needed to rigorously explore the structural effects of the ferrocene moiety.

Despite the failed attempt at using Poisson-Boltzmann electrostatics to predict ion selectivity ratios, a simpler model developed by DeGrado's group (Lear et al, 1997; Kienker & Lear, 1995) produced encouraging results. The difference in ion selectivity ratio between the reduced and oxidized forms of cxALM-NFc is accurately predicted in these calculations, see Figure Appendix A. There are a number of possible explanations for the lack of accuracy in the prediction, these include: (1) lack of accuracy in characterizing the electrolyte's ionic makeup in the I-V experiments; (2) over simplification of the electrostatic profile due to the approximation of Lear *et al.* (1997); and inaccuracies in treating the asymmetric electrolyte concentrations.

It is important to mention that Lear and coworkers got similar encouraging results applying their electrodiffusion formulation to the so-called LS peptide (Lear *et al.*, 1997). They synthesized two variants of the LS peptide (Ac-[LSSLLSL]$_3$), one containing a negatively charged glutamic acid at the N-terminus (Ac-EW-[LSSLLSL]$_3$, the tryptophan was included as a spectrophotometerc reporter) and one containing a positively charged arginine at the N-terminus (Ac-RW-[LSSLLSL]$_3$). PLB experiments revealed that the introduction of a negative charge at the N-terminus changes the conductivity from nonselective to cation selective (deduced from permeability ratios, P_{K+}/P_{Cl-}). Similarly, addition of a positive charge makes the channels cation selective. To inform their findings they conducted calculations based on the dipole potential equations described in Chapter 1 (Section 1.7). Application of equation 1.8 to the LS peptide and its two charge variants successfully reproduces their I-V curves and also the ion permeability ratios. It must be noted that

their I-V curves and also the ion permeability ratios. It must be noted that the investigators used a rather dubious fitting procedure to weight the terms in their electrodiffusion equation to match the observed data (Kienker *et al.*, 1994).

8.4. BIOPHYSICAL AND MODELING STUDIES: MELITTIN ANALOGS

The nature of melittin's membrane interaction has been a long standing matter of debate (Hanke *et al.*, 1983; Toteson & Toteson, 1981; Toteson & Toteson, 1984; Toteson *et al.*, 1985; for review, see: Dempsy, 1990). In Chapter 6 the conjecture that melittin forms ion channels *via* a mechanism similar to alamethicin was explored — a hypothesis set forward by a number of investigators (Toteson & Toteson, 1981; Toteson *et al.*, 1985; Talbot *et al.*, 1987). While there exists a strong structural similarity melittin and other CFPs (Terwilliger & Eisenberg, 1992; Dempsy, 1988; Bazzo *et al.*, 1988; Campbell, 1988; Pastore *et al.*, 1989) the channel opening life-times are often so short as to be bandwidth limited and the conductance levels of longer bursts are difficult to ascertain. Additionally, high concentrations of melittin seem to elicit severe, nonspecific perturbative effects on lipid membranes (Dempsy , 1990). One of the distinguishing qualities of melittin is the excessive positive charge, located mostly at its C-terminus (sequence: ·····LYS-ARG-LYS-ARG-GLN-GLN-); It has been suggested that this charge density is the source of its perturbative effects (Hanke *et al.*, 1983). These investigators observed that melittin forms well resolved channels only at very high (~5M) electrolyte concentrations, implying a correlation with the screening effects of a decreased Debye length. One might surmise that melittin's positive character promotes association with, and subsequent disruption of, phospholipid headgroups; this supposition was extended to a testable hypothesis: if one were to reduce the positive character of the peptide would it be more prone to form alamethicin like (classical CFP)

channels? Also, if one were to accomplish this by cysteine mutation, would the resulting melittin dimers form more stable channels?

8.4.1. Macroscopic Characterization. The monomers MEL, MEL-K7Q, MEL-K23C and MEL-K23Q,Q25C were tested for their ability to induce macroscopic channel activity. The cysteine mutant MEL-K23C and MEL exhibit nearly identical macroscopic behavior {Figure 6.1}; Position 23 is on the hydrophilic face of the peptide, so the likelihood is that a mutation would have less impact then a replacement on the hydrophobic face of the helix. This is borne out by results obtained with the double mutant MEL-K23Q,Q25C. This peptide proved to be extremely lytic and either exhibited no channel forming activity or repeatedly broke the bilayer. The rationale in synthesizing the double mutant was based on conserving total charge between the cysteine mutants. Numerous attempts at varying peptide and electrolyte concentration failed to yield consistent results. It is important to stress the fact that lysine to cysteine mutation on the otherwise hydrophobic face of the peptide had a deleterious effect on channel formation; This indicates that factors beyond amphiapathicity are effecting channel formation. It has been proposed that the principal aggregate responsible for the low-conductance bursts of channel activity is the tetramer (Vogel & Jähnig, 1986; Talbot *et al.*, 1987). One might infer that the introduction of a hydrogen bonding moiety in the hydrophilic face of the peptide is occluding the channel assemblies *via* intermolecular hydrogen bonding.

Surprisingly, both of the dimeric analogs, $(MEL\text{-}K23C)_2$ and $(MEL\text{-}K23Q,Q25C)_2$ failed to render macroscopic I-V data with sufficient burst density to allow determination of threshold potentials. This is reflected in the results of single channel recordings, bursts of channel activity were separated by extended periods of inactivity (see below). Although it is impossible to ascertain why these peptides exhibit such behavior, one

might guess that dimerization severely limits the number of possible conformations which lead to channel activity.

8.4.2. Single Channel Characterization. All three monomeric peptides, MEL-K7Q, MEL-K23C and MEL-K23Q,Q25C form asymmetric single channels. MEL-K7Q appears to form two distinct types of channel bursts, characterized by differing conductance levels and lifetimes. Most frequently, alamethicin-like openings with multiple conductance levels are seen. These bursts have mean lifetimes of around 100 msec {Figure 6.3A} and open to five or six levels. MEL-K7Q also gives rise to bursts that are characterized by very rapid gating, 5-10 msec (bandwidth limited) to only two conductance levels {Figure 6.3B & C}. It is important to note that, within a single experiment, both types of bursts are observed. We believe that the two classes of channel are representative of an equilibrium population of melittin-like channels (5-10 msec) and alamethicin-like channels (100 msec). The single channel behavior of MEL-K23C mirrors its macroscopic behavior. This peptide, like MEL, is characterized by very rapid gating with hard to resolve conductance levels. Events that may be sustained openings (~100 msec) were frequently observed {Figure 6.4B}. The double mutant MEL-K23Q,Q25C produced similar, but more difficult to characterize channels {Figure 6.4C & D}. Occasionally, sustained and rapid bursts to one level {6.4C} were observed, but the lytic properties of this peptide along with the scarcity of events made this observation difficult to quantify.

Single channel characterization of the dimers, $(MEL\text{-}K23C)_2$ and $(MEL\text{-}K23Q,Q25C)_2$, produced very interesting results. $(MEL\text{-}K23C)_2$ forms channels with sustained and clearly defined conductance levels {Figure 6.7A & B}, the lowest observed conductance level (16-17 pS) appears to be particularly stable with openings as long as a few seconds. So, although macroscopic experiments indicate that fewer peptide interactions lead to channel formation, the channels that do form are very

stable. One unique property of $(MEL\text{-}K23C)_2$ is that some openings are 'noisy' and some are 'clean' {Figure 6.7A}. The 'noisy' openings are characterized by a rapid ±25 pS oscillation around the mean conductance level (The author admits to the rather imprecise use of the word 'oscillate', strictly speaking, oscillation implies periodicity, but here it is meant to describe fluctuation about a mean value). Whereas, the 'clean' openings appear to have the same ±7 pS level of noise as the baseline. The low conductance levels of the $(MEL\text{-}K23C)_2$ channels imply that rapid oscillatory events seen within some of the bursts may be due to sidechain-related gating (for a discussion of melittin channel gating mechanisms see: Toteson *et al.*, 1990; or for a more general discussion: Läuger, 1976; Hille, 1992) or to extensive disruption of boundary lipid surrounding the channels. The double-mutant dimer $(MEL\text{-}K23Q,Q25C)_2$ is the only melittin derivative studied that appears to form channels at *cis* positive and negative results in rapid bursts at two to three distinguishable conductance levels. The extremely quick nature of the gating precluded exact measurement of the conductance levels. The *cis* negative bursts are very similar to melittin— bandwidth limited and difficult to resolve. $(MEL\text{-}K23Q,Q25C)_2$ like the other dimer forms highly cooperative periods of activity followed by extended periods of inactivity. The data on the melittin dimers, taken together, imply that oligomer interactions that lead to channel formation are exceedingly rare. Conformational constrains imposed by the dimerized N-termini may contribute to this effect; there is also evidence that dimerization stabilizes the tetrameric form found in solution (Dempsy, personal communication), thus lowering the effective concentration of peptide available for membrane association. One additional possibility is that the dimeric forms of both peptides form non-conducting transbilayer oligomers, as it has been suggested that lipid associated melittin, in the absence of a transbilayer potential, forms tetrameric and possibly larger bundles (Talbot *et al.*, 1987).

8.4.3. Modeling and Simulation Studies. The use of molecular dynamics simulated annealing was a means of preliminary investigation of mellitin and mellitin mutant bundles. These simulations were intended to be a prefatory structure-property exploration. Investigations indicate that the formation of helix bundles, similar to those modeled for alamethicin (Breed *et al.*, 1997), are reasonable approximations of what is observed experimentally. Although it must be stressed that a comprehensive modeling study of melittin is beyond the scope of this thesis.

A number of observations that parallel these experimental results warrant deliberation. First, persistent intermolecular hydrogen bonding of glutamine-7 was observed in MEL-K7Q. It is proposed that this contributes significantly to the increased stability of these peptide channels relative to melittin. This is in keeping with experiments conducted on analogs of alamethicin with and without C-terminus hydrogen bonding groups (Mathew & Balaram, 1983a; Mathew & Balaram, 1983b; Molle *et al.*, 1996); These investigators provide supporting evidence, through experimental and modeling studies, that intermolecular rings of hydrogen bonds stabilize the channels. Electrostatics calculations also indicate that removing the cationic amino acid from the C-terminus mouth of the pore significantly reduces positive electrostatic character and thus may reduce intermolecular repulsion.

Dimerization of the cysteine mutants had significant impact on the bundle geometries. It was anticipated that MEL-K23Q,Q25C in a hexameric bundle configuration would not accommodate a disulfide bond without gross distortion of the channel geometry. However, MD simulations predicted that this dimerization is moderately well accommodated in MEL-K23Q,Q25C. One geometric consequence of dimerization, seen in both peptides, was a straightening of the overall bundle architecture, mediated largely by a reduction in the kink angle

joining the two α-helical domains of the peptides. This effect may be the source of the experimentally observed more highly defined conductance states especially with $(MEL\text{-}K23C)_2$— as a reduction in kink angle increases pore radius.

Perhaps the singly most informative modeling results are those from the electrostatics calculations. Here, an approach frequently used in small molecule structure-property modeling was taken: assess the impact of structural modification by comparing molecular variants that are conformationally as similar as possible (here a *sine qua non* is that the structures be conformationally and energetically realistic). Examination of electrostatic isopotentials highlights the impact of our mutations. In every case, changes in the degree of 'disfavored' electrostatic interaction mirror the observed behavior of the peptides.

8.5. CONCLUSIONS

8.5.1. <u>A Kinetic Model For The Formation Of Ion Channels: Melittin To Alamethicin</u>. Based on a survey of single-channel and macroscopic CFP data in the literature and on results described in this Thesis, a kinetic model for the formation of CFP ion channels is given.

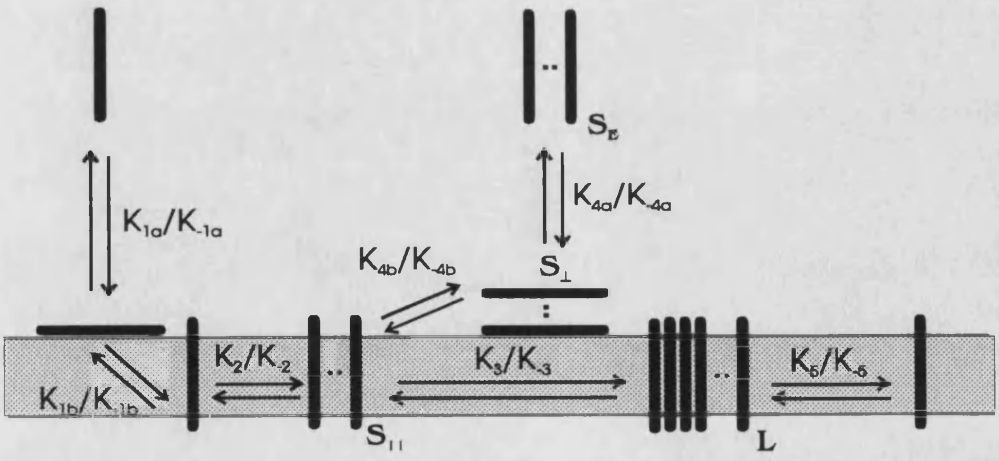

FIGURE 8.3. A KINETIC MODEL FOR CFP CHANNEL FORMATION. The rate terms are defined as follows: $\mathbf{K_{1a}/K_{-1a}}$, solvated monomer association/disassociation with bilayer surface; $\mathbf{K_{1b}/K_{-1b}}$, reorientation of

monomers from a surface to a transbilayer orientation; K_2/K_{-2}, monomer to oligomer bundle transition {possibly a nonlinear function of S_I size}; K_3/K_{-3}, bundle partitioning, small bundles **S** combine to form large bundles **L** and *vise versa*; K_{4a}/K_{-4a}, solvated aggregate association/disassociation with bilayer surface; K_{4b}/K_{-4b}, small bundle, $S_\perp$, transition to/from transbilayer orientation; K_5/K_{-5}, addition/subtraction of monomers from large bundles **L**. Positive rate terms point toward channel formation, negative terms point away. Small bundles, S_I, have size: n = 3, . . ., 12; $S_I \geq S_\perp$; Large bundles, **L**, have size $n \geq 12$, and in the case of melittin $n \geq S_I \times j$.

This model accounts for the diverse behavior of melittin and alamethicin and partitions the factors that are thought to contribute to channel formation into discernible kinetic steps. Figure 8.3 shows a schematic of the proposed mechanism. First, let us consider alamethicin and other peptaibols in light of this model. These peptides form channels with clearly defined conductance levels, that can be approximated by electrolyte-filled cylinders of varying diameters (Sansom, 1993). Numerous biophysical studies, outlined in Chapter one, indicate that peptaibol channels are formed by the following pathway: $K_{1a} \rightarrow K_{1b} \rightarrow K_2$. At all but very high concentrations, experimental results imply the following: $[S_E] = [S_\perp] = 0$, thus $K_{4a} = K_{4b} = 0$. Melittin, which forms tetramers in solution forms channels via the following pathway: $K_{4a} \rightarrow K_{4b}$ and $K_{4a} \rightarrow K_{4b} \rightarrow K_3$. Conductance states defined by the first pathway are small bundles n = 3, . . . ,5 with short bandwidth limited gating ($g \cong$ 5-500 pS); conductance states defined by the second pathway are the large ($g \geq$ 2 nS) bilayer disrupting events. This model implies that the large aggregates, **L**, are not limited to helix bundle geometries. One could envision that tetramer interaction is sufficiently strong to allow bundles-of-bundles to form. The melittin mutants described in this Thesis (Chapter 6), particularly MEL-K7Q and $(MEL\text{-}K23C)_2$, appear to sit in the middle of the peptaibol and melittin regimes. In fact, single recordings often show two distinct forms of gating behavior—one clean (peptaibol like) and one melittin like (spiky).

8.5.2. Hydrogen Bonding: A Hypothesis Relating Hysteresis and Channel Stabilization. This work shows two notable examples of an increase in hysteresis upon the incorporation of hydrogen bonding moieties into CFPs. Modeling results indicate that these moieties may participate in intermolecular H-bonding in the proposed CFP bundles. Therefore it is concluded that hysteresis reflects the establishment of stabilizing intermolecular forces within an ion channel once formed. If this hypothesis were confirmed then one could, in principal, design experiments that 'quantitatively' distinguish between the forces leading to channel assembly and forces that result in channel stabilization and gating.

8.5.3. Putative Contribution of Boundary Lipid to Ion Channel Kinetics. On a more speculative note I wish to propose a hypothesis that grew out of conversations with M.S.P. Sansom. Here we endeavor to explain some of the complexities in CFP gating kinetics not encompassed by current theory. This hypothesis is uncomplicated and can be described in context of the kinetic model described in Section 8.5.2 above. The bundles $\mathbf{S_I}$ and **L** will be surrounded by regions of boundary lipid at both the C- and N-termini. Being different from the bulk phase, this boundary lipid will have a lesser or greater tendency to support the process $\mathbf{K_{1b}/K_{-1b}}$ and $\mathbf{K_2/K_{-2}}$. It is likely that a concerted $\mathbf{K_{1b}}$--$\mathbf{K_{-2}}$ step may also contribute to the ion channel dynamics, whereby monomers go from a surface orientation directly to a bundle and *vise versa*. Careful experiments will need to be designed to establish to what extent this phenomenon occurs. One such experiment would be to synthesize tethered dimers, one monomer containing a spin label and the other containing a fluorescent sidechain. The spin depolarization profile in an equilibrated population of channels would, in principal, afford: (1) the percentage of tethers where both helices are in the bilayer, (2) the

percentage of tethers with only one helix is in the bilayer and (3) the relative rate of the transition process.

8.6. FUTURE DIRECTIONS

The results of investigations using redox-active ferrocenoyl peptides described in this thesis suggest a number of future experiments. The most pressing issue is to determine how to use Poisson-Boltzmann electrostatics calculations to predict the ion selectivity properties of the redox active channels. Two possible solutions come to mind: (1) conduct the calculations on larger (but realistic) bundle models and (2) to modify the dielectric model with a switch function that would allow smooth transition from the bulk to low dielectric enviornment.

The C-terminus ferrocenoyl alamethicin derivatives could also be further characterized using the large organic oxidizing agent DDBQ. The results could provide further evidence for the involvement cerium in specific coordination type interactions with the redox channels. Additionally, one would be able to characterize redox channel behavior in the absence of additional ions in the electrolyte solutions, thus allowing ion selectivity to be compared for the reduced and oxidized peptides.

One of the most promising aspects of this study has been that ferrocene, incorporated into peptides, allows one to probe the impact of site-specific charge variation in a pH independent manner. One might envision synthesizing a series of alamethicin analogs that contain ferrocenyl alanine at various positions. Biophysical characterization of these analogs would allow one to structurally map the impact of structural and electrostatic changes as a means of testing hypothetical channel models. On the same token redox active melittin derivatives could be synthesized and used as above.

Channel lifetime is one of the limiting factors in the biophysical characterization of CFPs and other ion channels. The synthesis of redox-active tethered alamethicin derivatives would, most probably, lead to channels with substantially longer open times. Ferrocene-1,1'-bis((α-keto)butyric acid) was synthesized with this in mind— standard carboxylate coupling methodology should provide a means to link an alamethicin to each of this tether's carboxylic acids. The synthetic chemistry described in this thesis has also lain the groundwork for the synthesis of other peptide dimers. These novel linkers, described above, may not only provide tools to probe the physical determinants of channel formation, but may also serve as prototype nanodevices.

The cysteine mutants of melittin also have great potential as probes for exploring charge-function relationships. One could easily oxidize the cysteine sulfhydryls to either the sulfinic acid (q = -1) or the sulphonic acid (q = -2) and thereby introduce negative charge into specific sites on melittin. Similarly, it would be easy to derivatize the CYS mutants with various size SH reactive agents, thus allowing one to probe the packing of bundle models. Results described in the molecular modeling chapter also indicate that mutation of lysine-7 to cysteine would lead to highly stabilized dimers.

As mentioned above, we hypothesize that macroscopic channel hysteresis and intermolecular hydrogen bonding (within the channel assembly) are linked. A study whereby hydrogen bonding amino acids are introduced into alamethicin and melittin, may afford a means which to deconvolute the relative contributions of *inter*- versus *intra*molecular forces in ion channel formation.

In the modeling and simulation dominion it would be very instructive to couple future redox active peptide experiments with rigorous simulation. This Thesis demonstrates that Density Functional

methodology is a robust approach to obtain detailed forcefield parameters needed for such work. The coupling of simulation and experiment, especially where exists a history of successful modeling, would greatly accelerate advances in our understanding of CFP biophysics. Finally, simulations of CFP bundles in explicit bilayers would be a penultimate test of the validity of the proposed models.

8.7. BIOLOGICAL SIGNIFICANCE

A significant motivation for this work has been to gain insight into the behavior and evolution of membrane associated proteins. What contribution can ion-channel biophysics make to our understanding of biology and evolutionary dynamics? In general, CFPs might be considered the first biological sensors, in that they 'respond' to environmental changes by altering the nature of their molecular associations. Since these changes occur at a boundary (or interface) a myriad of consequences become possible. Trial and error, in the Darwinian sense, then enables the evolution of operations we associate with cellular biology— selective transport of materials, control and maintenance of ionic gradients and signal transduction. The experiments described in this Thesis demonstrate that the underlying forces are calculable . . . electrostatic profiles determine ion selectivity, peptide channel stabilization is mediated by forces such as hydrogen bonding and ampiapathicity and that macro-dipoles, in the presence of the right force, are large enough to overcome thermal randomization forces (kT). The significance of the dipole and charge related effects cannot be overstated, because they lead to events that are essentially asymmetric. Asymmetric molecular events, especially those that occur at interfaces, are keystones of living systems for they allow a system to become dissipative as well as meta-stable (Kauffman, 1993; Prigogine 1984; Rayner, 1997).

Meta-stability may help to explain, beyond the obvious problem of hydropathy, why the structural characterization of membrane associated proteins is so difficult. Perhaps membrane associated proteins have evolved in such a way that a great variety of conformational states, separated by shallow energy barriers, are accessible. This meta-stability may afford these proteins a greater variety of 'responses' to changes in their environment, but may preclude standard methods of structural characterization.

8.8. CLOSING REMARKS

The results described herein further validate the helix bundle hypothesis of ion channel formation. Biophysical and modeling studies conducted on two different CFP systems, contributes to our knowledge of the basic forces underlying ion channel assembly and behavior. Structure-function comparison of various alamethicin and melittin analogs demonstrate that channel formation is modulated by a combination of factors, such as hydrophobicity, molecular dipole effects and hydrogen bonding. The redox-active peptide concept provides a significant addition to the arsenal of tools that may be used to unravel the relationship between structure and function in CFPs and ion channels. Our modeling and biophysical characterization of Fc-ALM, cxFc-ALM and cxALM-NFc is further confirmation that CFPs can be rationally designed to posses unique properties and responses to chemical and electrical environment.

8.9. REFRENCES: DISCUSSION AND CONCLUSIONS

Baumann, G., & Mueller, P. (1974) *J. Supramol. Str. 2*, 538-557.

Bazzo, R., Tappin, M.J. , Pastore, A. , Harvey, T.S. , Carver, J.A., & Campbell, I.D. (1988) *Eur. Biochem. J. 173*, 139-146.

Boheim, G. (1974) *J. Membr. Biol 19*, 277-303.

Breed, J., Biggin, P.C., Kerr, I.D., Smart, O.S., & Sansom, M.S.P. (1997) *Biochim. Biophys. Acta 1325,* 235-249.

Campbell, I.D.(1988) In: *Transport Through Membranes: Carriers, Channels and Pumps* (ed. B. Pullman *et al.*), *pp 91-101*, Dordrecht: Kluwer Academic Publishers, Berlin.

Dempsy, C.E. (1988) *Biochemistry 27,* 6893-6901.

Dempsy, (1990) *Biochim. Biophys. Acta 1031,* 143-161.

Dempsy, C.E., Bazzo, R, Harvey, T.S., Syperek, I., Boheim, G. & Campbell, I.D. (1991) *FEBS Lett. 281*, 240-244.

Dougherty, D. A., & Stauffer, D.A. (1990) *Science* 324, 1558-1560.

Dugast J.-Y., Helluin, O., & Duclohier, H. (1997) *Biochim. Biophys. Acta 1330,* 284-292.

Hall, J. E., Vodaynoy, I., Balasubramanian, T.M. & Marshall, G. M. (1984) *Biophys. J. 45*, 233-247.

Hanke W., Methfessel, D., Wilmsen., H.U., Katz, E., Jung, G., & Boheim., G. (1983) *Biochim. Biophys. Acta 727,* 108-114.

Hille, B. (1992) Ionic Channels of Excitable Membranes, 2nd. ed., Sinauer Assoc., Sutherland, Mass.

Kauffman, S. (1993) Origins of Order, Oxford University Press, Oxford UK.

Kienker, P.K., DeGrado, W.F., & Lear, J.D. (1994) *PNAS USA 91*, 4859-4863.

Lau, H. H., & Hart, H. (1959) *J. Org. Chem. 24*, 280-281.

Lauger, P. (1976) *Biochim. Biophys. Acta 455*, 493-509.

Lear J.D., Schneider, J.P., Kienker, P.K., & DeGrado, W.F. (1997) *J. Am. Chem. Soc. 119,* 3212-3217.

Mak, D., & Webb, W.W. (1993) *Biophys. J. 64* A95.

Mathew, M.K., & Balaram, P. (1983a) *FEBS Lett. 157,* 1-5.

Mathew, M.K., & Balaram, P. (1983b) *Mol. Cell. Biochem. 50,* 47-64.

Matsubara, A., Asami, K., Akagi, A., & Nishiono, N. (1996) *Chem. Commun. 46,* 1156-1163.

Molle, G., Dugast, J.-Y., Spach, G., & Duclohier, H. (1996) *Biophys. J. 70*, 1669-1675.

Montal, M. (1990) *FASEB J. 4,* 2623-2635.

Nagaraj, R. & Balaram, P. (1981) *Tetrahedron 37,* 1263-1265.

Nesmeyanov, N., & Reutov, O.A. (1957) *Proc. Doc. Chem. 115*, 763-765.

Oiki, S., Madison, V., & Montal, M. (1990) *Proteins: Str.Func. Genet. 8*, 226-236.

Pastore, A., Harvey, T.S., Dempsey, C.E., & Campbell, I.D. (1989) *Eur. Biophys. J. 16,* 363-367.

Pearlman, R.S. (1980) Physical Chemistry Properties of Drugs (ed. S.H. Yalkowski, *et al.*), *pp 125-141*, Dekker, New York.

Prigogine, I. (1984) Order Out of Chaos, Random House, New York.

Rayner, A.D.M. (1997) Degrees of Freedom: Living in Dynamic Boundaries, Imperial College Press, Cambridge UK.

Sansom, M. S. P. (1992) *Eur. Biophys. J. 21*, 281-298.

Sansom, M. S. P. (1993) *Quart. Rev. Biophys. 26*, 365-421.

Schmitt, J. D., Sansom, M.S.P., Kerr, I.D., Lunt, G.G., & Eisentlal, R. (1996) *Biochemistry 36,* 1112-1115.

Sheehan, D.R. & Hess, V. (1955) *J. Am. Chem. Soc. 77,* 1067-1072

Shubert, U., Henklein, P., Bour, S., Ferrermonteil, A.V., Oblattmontal, M., Montal, M., & Strebel, K. (1995) *AIDS Res. Human. Retrovir. 11,* 5114-5121.

Talbot, J.C., Faucon, J.F., & Dufourcq, J. (1987) *Eur. Biophys. J. 15,* 147-157.

Terwilliger, T.C., & Eisenberg, D. (1982) *J. Biol. Chem. 257,* 6016-6022.

Toteson, M.T., &. Toteson, D.C. (1981) *Biophys. J. 37,* 353-361.

Toteson, M.T., & Toteson, D.C. (1984) *Biophys. J. 45,* 112-114.

Toteson, M.T., Alvarez, O., & Toteson, D.C. (1985) *Regl. Peptides (suppl. 4) 8,* 39-45.

Wenschuh, H., Beyermann, M., Haber, H., Seydel, S., Krayuse, E., & Bienert, M. (1995) *60*, 405-410.

Toteson, M.T., Alvarez, O., Hubbell, W., Bieganski, R.M., Attenbach, Caporales, L.H., Levy, J.J., Nutt, R.F., Rosenblatt, M., & Toteson, D.C. (1990) *Biophys. J. 58,* 1367-1375.

Vogel, H., & Jähnig, F. (1986) *Biophys. J. 50,* 573-582.

Wada, S.-I., Iida, A., Asami, K., Tachikawa, E., & Fujita, T. (1997) *Biochim. Biophys. Acta 1325*, 209-214.

Wada, A. (1976) *Adv. Biophys. 9*, 1-63.

Wenschuh, H., Beyermann, M., Haber, H., Seydel, S., Krayuse, E., & Bienert, M. (1995) *60*, 405-410.

Woolley, G. A., Epand, R.M., Kerr, I.D., Sansom, M.S.P., & Wallace, B.A. (1994) *Biochemistry 33*, 6850-6858.

You, S., Peng, S., Lien, L., Breed, J. & Woolley, G.A. (1996) *Biochemistry 35,* 6225-6232.

APPENDIX A

A.1. Theoretical Analysis of I-V Curves of cxALM-NAc, cxALM-NFc(red) and cxALM-NFc(ox) According to Lear *et al.* :
a Continuum Electrodiffusion for Predicting Ion Selectivity Ratios.

The electrodiffusion equation described in Chapter 1 {eq1.8} for prediction of macroscopic I-V curves is:

$$I(V) = \frac{F\beta DAC(e^{\{VF/RT\}} - 1)}{\int e^{\{\Psi(x,V)F/RT\}} dx}$$

The potential with respect to position x along the channel axis, $\Psi(x,V)$, is the sum of three terms (x = 0 is taken to be the center of the channel):

$$\Psi(x,V) = \Psi_{app}(x,V) + 180\left[\Psi_{ec}(x) + \Psi_{img}(x)\right]$$

where $\Psi_{app}(x)$ is the electrical potential due to ionic gradient or transbilayer potential, $\Psi_{ec}(x)$ is the dipole potential extrapolation. As discussed in Chapter 1, the net helical dipole is approximated as two net charges at the ends of the helix. The final term, $\Psi_{img}(x)$ is the potential due to an ion passing from a high-dielectric region to a lower dielectric (passage into the channel). The weighting value of 180 mV/Å allows $\Psi(x)$ to be expressed in mV.

The potential arising from the ionic gradient and transbilayer potential is:

$$\Psi_{app}(x,V) = \frac{(x + L/2)}{L} + V_{app} = \frac{(x + L/2)}{L} + 24$$

Where V_{app} is the potential due to the asymmetry of the electrolyte solution (0.5M *cis*, 1.0M *trans*). The channel length is taken as L = 30 Å. The dipole potential is as follows:

$$\Psi_{ec}(x) = 6\left[z_c\left[a^2 + \left(x + L/2\right)^2\right]^{-1/2} + z_n\left[a^2 + \left(x - L/2\right)^2\right]^{-1/2}\right]$$

where, z_c is the effective charge at the N-terminus, z_n is the effective C-terminus charge, a is the distance of the end charge from the bundle center-axis and takes on the value of a = 4 Å. The image potential is a distance dependent exponential:

$$\Psi_{ec}(x) = \left[\left[\left(f(K)/a\right)\right] - \ln\left[\frac{2/1+K}{KL}\right]\right] e^{\left(-x^2/2\sigma^2\right)}$$

Where K is the ratio of bulk (water) to channel dielectric constants, K = $\varepsilon_w/\varepsilon_p$ = 6.67 (ε_w = 80, ε_p= 12); f(K) is a function that describes the effect of the induced image charge on the dielectric ratio (see, Parsegian, V.A. (1975) *Ann. N.Y. Acad. Sci. 264,* 161-174) this value was taken to be a constant, f(K) = 1.47 (Lear, J.D., Schneider, J.P., Keinker, P.K., & DeGrado, W.F. (1997) *J. Am. Chem. Soc. 119,* 3212-3217). The last term, σ = 12.4 (*ibid.* Lear *et al.* (1997)) describes the change in dielectric per unit space.

Results from dipole calculations described in Chapter 7 {Table 7.2} were used to calculate the effective N- and C-terminal charges, z_n and z_c, on the peptides using the following equations:

z_n[cxALM-NAc]= S(1.091D)= 0.240

z_n[cxALM-NFc(red)]= S(0.891D)= 0.196

z_n[cxALM-NFc(ox)]= S(1.801D)= 0.396

where S= 0.22 is a screening function due to the dielectric environment (*ibid.* Lear *et al.* (1997)).

Matlab was than used to numerically approximate the zero value of the master equation:

$$I(V) = \frac{F\beta DAC(e^{\{VF/RT\}} - 1)}{\int e^{\{(\Psi_{app}(x,V)+180[\Psi_{ec}(x)+\Psi_{img}(x)])/RT\}} dx}$$

Evaluation of I(V)= 0 gives the calculated reversal potential $V_{rev,calc}$ for the three peptides:

$V_{rev,calc}$[cxALM-NAc]= -28.1
$V_{rev,calc}$[cxALM-NFc(red)]= -27.3 mV
$V_{rev,calc}$[cxALM-NFc(ox)]= -66.9 mV

Finally, application of the Goldman-Hodgkin-Katz equation {eq M2} to calculate the permeability ratios gives:

P_k/P_{Cl}[cxALM-NAc]= 0.82
P_k/P_{Cl}[cxALM-NFc(red)]= 0.84
P_k/P_{Cl}[cxALM-NFc(ox)]= 0.23